University of Southampton

Faculty of Engineering and the Environment

Effect of Dissociation on the Properties of Hydrate Bearing Sediments

by

Amit Kumar Sultaniya

(B.Tech., M.Eng.)

Thesis for the Degree of Doctor of Philosophy

November - 2011

Thesis Submitted for the Degree of Doctor of Philosophy within the School of Civil Engineering and the Environment (Faculty of Engineering and the Environment) of the University of Southampton, Highfield Campus, Southampton (UK).

To my late Grandmother,
my parents, and my sisters.

UNIVERSITY OF SOUTHAMPTON

ABSTRACT

FACULTY OF ENGINEERING AND THE ENVIRONMENT
Civil Engineering and the Environment

Doctor of Philosophy

EFFECT OF DISSOCIATION ON THE PROPERTIES OF HYDRATE BEARING SEDIMENTS

by Amit Kumar Sultaniya

Gas hydrates are clathrate hydrates, which are solid, ice-like compounds. Gas hydrates exist where there is an ample supply of gas and water combined with high pressure and/or low temperature conditions. In nature these are found in sediments where permafrost is present, and in deep-marine sediments. The morphology of gas hydrate within a sediment has a large impact on the strength and stiffness properties of hydrate bearing sediments. Gas hydrates are metastable and they dissociate if the temperature and/or pressure conditions are sufficiently altered. The dissociation of gas hydrate and its potential as a submarine geohazard have become of increasing importance as oil and gas exploration activities extend into significant water depths on continental margins and seas where gas hydrates are known to exist. Such activities may lead to dissociation of hydrate, possibly increasing pore pressure, and altering the stiffness and strength of the sediment. Due to difficulty in performing field testing and obtaining undisturbed in-situ samples for testing, at present, hydrate dissociation in the natural environment and its effects are hypothesised on the basis of remote observations. Therefore, a series of well-controlled laboratory tests were conducted on laboratory-prepared methane hydrate bearing sand sediments.

The tests were undertaken with hydrate saturation ranging from 7% to 27% in the Gas Hydrate Resonant Column Apparatus (GHRC). Factors such as effective stress were also assessed with regard to specimen stiffness. Resonant column testing during hydrate formation and dissociation processes carried out for the first time, such that not only final change in specimen properties to be determined as a function of total hydrate saturation but also the change in specimen properties as function of the percentage of hydrate formation and dissociation. Test results showed that a rapid reduction in stiffness occurred for a minor change in hydrate saturation of sand specimens where dissociation was induced by temperature increase, but for specimens that were dissociated using the pressure reduction method a slower reduction occurred. In contrast, during hydrate formation stiffness increased more gradually. In addition, test results showed that the hydrate formation using the excess gas method led to higher increases in the shear stiffness compared to the flexural stiffness of specimens, and the linear stiffness threshold limit of hydrate bearing specimens were lower than the non-hydrate bearing sands.

In addition to laboratory tests, an analytical model was built to predict the increase in pore pressure under undrained conditions within hydrate bearing sediment during dissociation. The results obtained from the laboratory tests were used to compare the predicted results from the model. Analytical model showed that the rise in pore pressure within a sediment was dependent on a number of factors: Major factors were initial pore pressure, amount of hydrate dissociation, cage occupancy of gas within hydrate, stiffness of the sediment, and degree of water saturation; Minor factors were methane gas solubility in water, and methane hydrate density.

Contents

List of Figures

List of Tables

Declaration of Authorship

I Amit Kumar Sultaniya declare that this thesis entitled **"Effect of Dissociation on the Properties of Hydrate Bearing Sediments"**, and the work presented in it are my own and has been generated by me as the result of my own original research. I confirm that:

1. This work was done wholly while in candidature for a research degree at this University;
2. Where any part of this thesis has previously been submitted for a degree or any other qualification at this University or any other institution, this has been clearly stated;
3. Where I have consulted the published work of others, this is always clearly attributed;
4. Where I have quoted from the work of others, the source is always given. With the exception of such quotations, this thesis is entirely my own work;
5. I have acknowledged all main sources of help;
6. Where the thesis is based on work done by myself jointly with others, I have made clear exactly what was done by others and what I have contributed myself;
7. Parts of this work have been published as:

   Sultaniya, A., Clayton, C. R. I. and Priest, J. A. (2010). Assessing cross anisotropic of stiffness using the resonant column apparatus, *Fifth International Conference on Recent Advances in Geotechnical Earthquake Engineering and Soil Dynamics*, San Diego, California (USA).

   Sultaniya, A., Priest, J. A. and Clayton, C. R. I. (2010a). Hydrate dissociation around oil exploration infrastructure, *Frontiers in Offshore Geotechnics II*, Perth (Australia).

   Priest, J., Sultaniya, A. and Clayton, C. (2011). Impact of hydrate formation and dissociation on the stiffness of a sand, *Proceedings of the 7th International Conference on Gas Hydrates*, Edinburgh (UK).

Signed:.....
Date:.....

Acknowledgement

First of all, I would like to thank "Fugro Offshore Geotechnics (Netherlands)" and "School of Civil Engineering and the Environment (University of Southampton, UK)" for their financial support during this research.

I would also like to thank Harvey Skinner, Earl Peters, and Mike Rose from civil engineering laboratory for their technical support in solving electrical, plumbing problems in the Gas Hydrate Resonant Column (GHRC) apparatus during the course of this research.

I would like to give great thanks to my supervisors Prof. Chris Clayton and Dr. Jeffrey Priest, who gave me opportunity to study with them, and giving their support and encouragement throughout the period of this research. I would also like to thanks my supervisors for their comments to shape this thesis. I would like to thank my supervisors, in particular Dr. Jeffrey Priest, who helped me to understand and use the Gas Hydrate Resonant Column apparatus.

I wish to thanks my fellow research friends and my friends for the time we shared during and after long working hours in the office and in the laboratory. I would like to thanks Gleb Koloskov and Nicola Bicocchi for their helpful suggestions using LaTex document writing software.

Above all, I am very grateful to my parents for their constant support and encouragement throughout my study. They are always with me though they live far away in India. They always wish good health and good luck to me.

List of Notations

Symbols

ac	Acceleration of specimen
a, b	Peng-Robinson's constant
f	Frequency of vibration
g	Acceleration due to gravity
h_{0i}, h_{01}	Heights of bottom and top of mass m_i above specimen
k	Spring stiffness
l'	Distance of accelerometer from the centre axis of specimen
l	Length of specimen
m_T	Total mass of specimen
m_{hy}	Moles of hydrate
m_i	Added masses above specimen
m_s	Mass of soil solids
m_w	Moles of water
$n_{s:d}$, n_d, *and* $n_{e:d}$	Moles of methane at the start, during and at the end of hydrate dissociation respectively
$n_{s:f}$, n_f, *and* $n_{e:f}$	Moles of methane at the start, during and at the end of hydrate formation respectively
n	Moles of gas
q_{max}	Peak shear strength
r	Radius of specimen
t	Time

y_{ci}	Centre of gravity of mass m_i measured from top of specimen
$z_1,\ z_2$	Peak amplitutes at time t_1 and t_2 respectively
C_1, C_2	Arbitrary constants
D	Damping
E_{flex}	Flexural modulus
E	Young's modulus
G_s	Specific gravity of soil solid
G	Shear modulus
H_d	Percentage of total hydrate during dissociation
H_f	Percentage of total hydrate during formation
I_0	Mass moment of inertia of drive unit
I_{am}	Mass moment of inertia of added mass (including bar top disc)
I_b	Second moment of inertia of specimen
I_{yi}	Area moment of inertia of mass m_i
I	Mass moment of inertia of specimen
M_{hy}	Molar mass of hydrate
M_w	Molar mass of water
P	Pressure
Q^{-1}	Wave attenuation
Q	Quality factor
R	Universal gas constant
S_d	Hydrate saturation during dissociation
S_f	Hydrate saturation during formation
S_h	Total hydrate saturation
S_w	Water saturation
T	Temperature

V_{hy}	Volume of hydrate
V_p	Primary wave velocity
V_{soil}	Volume of soil solids
$V_{specimen}$	Volume of specimen
V_s	Shear wave velocity
V_{va}	Volume of voids for gas
V_v	Volume of voids
V_w	Volume of water
V	Voltage
Z	Accelerometer constant

α	Peng-Robinson's constant
δ	Logarithmic decrement
ϵ_{avg}	Average flexural strain
γ_{av}	Average shear strain
γ_{max}	Maximum shear strain
$\gamma_{x(outer)}$	Shear strain at outer surface of specimen
ω_n	Natural circular frequency
ω_d	Damped natural circular frequency under under-damped condition
ω_f	Natural circular frequency in flexural vibration
ϕ	Angular rotation
ρ	Density
ρ_{hy}	Density of hydrate
ρ_w	Density of water
σ_{dev}^{max}	Maximum deviatoric stress
θ	Angle of rotation

Abbreviations

BSR	Bottom simulating reflector
C_2H_4	Ethane
C_3H_8	Propane
CH_4	Methane
CO_2	Carbon dioxide
D	Drained
FVD	Free vibration decay
GHRC	Gas hydrate resonant column
H_2O	Water (Dihydrogen oxide)
H_2S	Hydrogen sulphide
HSZ	Hydrate stability zone
LBE	Leighton Buzzard Sand Grade-E
LVDT	Linear variable differential transformer
P-	Primary (compressional)
S-	Secondary
SDOF	Single degree of freedom
U	Undrained with varying effective stress
U-CES	Undrained with constant effective stress
U-PR	Undrained with varing effective stress through pressure reduction
p.u.	per unit

Prefixes

k	kilo (10^3)
m	milli (10^{-3})
M	mega (10^6)
n	nano (10^{-9})

Chapter 1

Introduction

1.1 Background

Gas hydrates are naturally occurring metastable compounds composed of gas molecules encapsulated within a water matrix to form an ice-like structure. These exist where there is an ample supply of gas within the sediment column and combined with high pressure and/or low temperature conditions. The most common gas found within gas hydrates is methane, although other gases such as CO_2, H_2S, C_2H_4 etc. are also found in naturally occurring gas hydrates. Methane hydrates are stable under a wide range of pressure and temperature combinations as shown in Figure 1.1. In nature these conditions exist within oceanic sediments on continental margins and deep within the sediments in Arctic regions below the permafrost.

1.2 Defining the problem

As gas hydrates are metastable they dissociate if the temperature and/or pressure conditions are sufficiently altered. This can change gas hydrates from an ice-like structure back to its constituent parts of gas and water. Therefore, gas hydrates have been a major topic of interest in three main areas; a potential future energy resource, a possible driver of global climate change, and a geotechnical hazard.

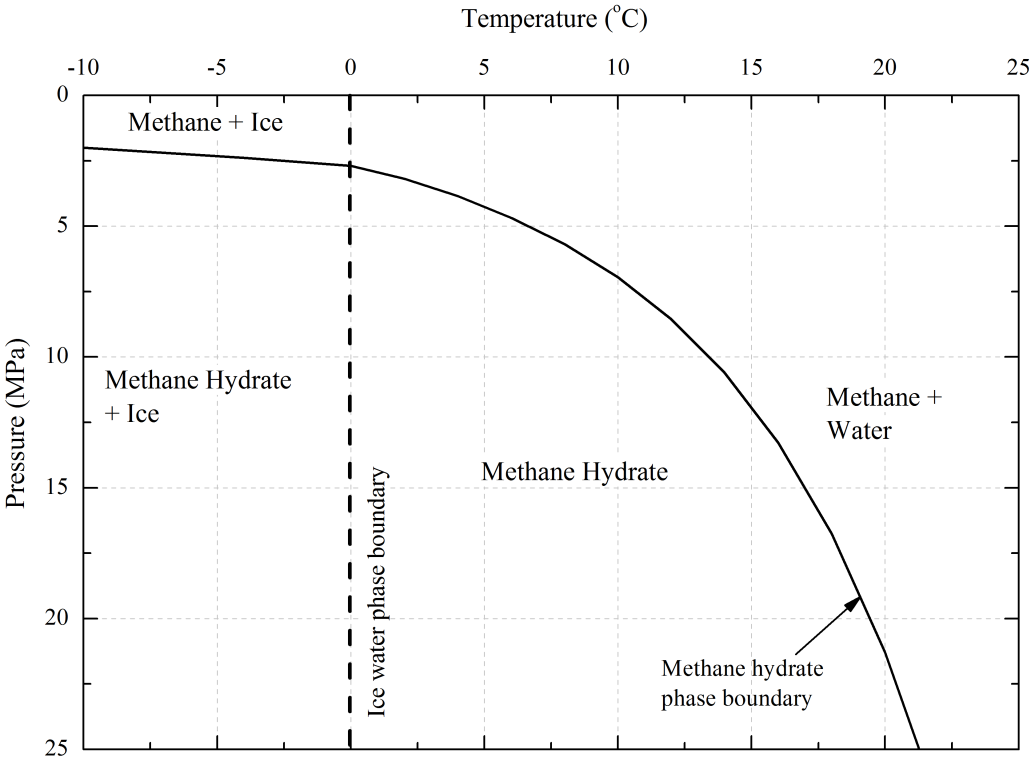

Figure 1.1: *Methane hydrate phase boundary with regards to temperature and pressure. Redrawn from Sloan (1998).*

Energy resource

In forming gas hydrates the gas is able to achieve a denser packing than it could occupy in its gaseous state ($1\,m^3$ of methane gas hydrate contains $164\,m^3$ of methane at Standard Temperature and Pressure (Kvenvolden, 1994)). Therefore dissociation of gas hydrate can release large volumes of methane gas, which apart from being a potential hazard may serve as a future energy resource.

The assessment of gas hydrate as an energy resource has often been based on the total amount of methane gas stored in form of methane hydrate. Currently, this is estimated at between 1×10^{15} to $20 \times 10^{15}\,m^3$, a figure nearly two orders of magnitude larger than the volume of conventional gas resource (Reagan and Moridis, 2007; Makogon et al., 2007). However exploitation of methane from hydrate will depend on different factors; such as hydrate morphology, physical properties, phase equilibrium condition of hydrate bearing sediment. For instance, will it be possible to commercially exploit hydrate from fissures or disseminated within sediment pores, will it be possible to extract gas from very low permeability sediments

like clay (Boswell and Collett, 2010; Demirbas, 2010), and will it be economically feasible to extract gas by destabilizing methane hydrate. Considering these issues may diminish the energy resource potential of gas hydrate (Beauchamp, 2004).

Global climate change

Methane is the most common gas found in natural gas hydrates and is 20 times more potent as a green-house gas than CO_2 (Kvenvolden, 1994; Sloan, 1998). Therefore the release of methane gas into the atmosphere through hydrate dissociation may trigger and/or escalate global climate change.

The possible role of gas hydrate as a factor in future climate change scenarios has often been overstated (Beauchamp, 2004). Although methane is a more potent green-house gas, much of the methane released may never reach the atmosphere, being converted into CO_2 and absorbed in the water column before reaching the atmosphere (Kvenvolden, 1999; Beauchamp, 2004). This will thus limit the influence that methane gas from gas hydrate will have on global climate change.

Geotechnical hazards

The change of an ice-like substance back to its constituent parts through hydrate dissociation may change sediment properties such as the sediment strength and permeability (Kvenvolden and Barnard, 1983; Waite et al., 2004). Therefore, the dissociation of gas hydrate may lead it to be a geotechnical hazard.

The dissociation of gas hydrate and its potential as a trigger for submarine geohazards (such as submarine landslides, slumps, sediment instability, possible tsunami, etc.) have become of increasing importance as oil and gas exploration activities have begun to extend into significant water depths (greater than 1000m) on continental margins and seas where gas hydrates are known to exist. Pumping of hot oil or gas through hydrate bearing sediments can induce hydrate dissociation by changing the temperature of the sediment. This may result in heave or subsidence around oil/gas wells depending on changes in strength and permeability of the sediment. As a consequence casing failure and, at the extreme, platform subsidence may occur (Makogon, 1981; Yakushev and Collett, 1992; Folger, 2008; Lachet and Behar, 2000). The consequences of hydrate dissociation on sediment

due to changes in sea level, or rise in ocean bottom temperature have been associated with large sea-floor failure causing devastating tsunamis and widespread flooding in the geologic past Carpenter (1981); Kayen and Lee (1991); Padden et al. (2001); Paull et al. (2003).

Numerical modelling can be used to assess the influence and the impact of drilling activities through hydrate bearing sediment (Freij-Ayoub et al., 2007). However, understanding the risk of drilling through gas hydrate sediments, using numerical models, can only be effective if a detailed knowledge of sediment behaviour during dissociation is available. Generally the effects of hydrate dissociation on natural sediments have been deduced on the basis of remote observations, such as theoretical hydrate stability criteria and well observation (Nimblett et al., 2005; Yakushev and Collett, 1992). To fully assess the impact of gas hydrate on sediments requires accurate prediction and measurement of the physical properties of hydrate bearing sediments. This can be achieved by using direct measurements from the field or performing laboratory tests either on in-situ or synthesised sample.

1.3 Aims and objectives

To accurately predict the effect of hydrate dissociation on in-situ sediment properties, a number of factors need to be known:

1. The amount of hydrate present within the pores of sediment during formation and dissociation processes.
2. The properties of hydrate bearing sediment as a result of hydrate concentration and effective stress.
3. Expected increase in pore pressure within the hydrate bearing sediment as a result of hydrate dissociation.
4. Expected change in the properties of the hydrate bearing sediment as a result of dissociation.

The aim of this research is therefore to investigate these factors on the physical properties of hydrate bearing sediments during dissociation.

This was achieved by conducting a series of tests on laboratory prepared specimens of methane hydrate bearing sands and determining the physical properties of these sands during formation and dissociation of gas hydrate. Factors such as the stress conditions during formation and dissociation of methane hydrate bearing sediments were also investigated. In addition, an analytical model was developed to investigate the pore pressure evolution within hydrate bearing sediment during dissociation. The results obtained from laboratory tests were compared with the results from the analytical model.

1.4 Overview

This thesis consists of the following chapters:

Chapter 2 presents a brief review of structure, types, formation and stability criteria of gas hydrate. A comprehensive review of current knowledge relating to the effect of gas hydrate dissociation on hydrate bearing sediments observed in the field and in the laboratory is presented. A review of numerical models, including the mechanisms responsible for the hydrate dissociation is also presented.

Chapter 3 gives a brief description of experimental apparatus used in the testing. The calibration and data reduction techniques used to derive the dynamic properties of the methane hydrate bearing sediments are discussed. In addition, the chapter outlines the methodology used to form hydrate in sediment and measure the properties of these sand sediments.

Chapter 4 highlights the results of a series of resonant column tests conducted on methane hydrate bearing sediments. The results are discussed in relation to the effect of methane hydrate formation and dissociation in sand sediments. In addition, the results from the analytical model are discussed with regard to the change in pore pressure during hydrate dissociation.

Chapter 5 draws together conclusions from each chapter. The chapter also outlines suggestions for further research.

Appendix A discusses formulations from literature to calculate shear wave velocity of sediments using different effective medium models.

Appendix B presents the results from numerical analysis to assess cross-anisotropy of small strain stiffness using a resonant column apparatus.

Appendix C outlines an analytical model to calculate increase in pore pressure within hydrate bearing sediment during dissociation.

Chapter 2

Literature Review

This chapter outlines the current knowledge on gas hydrate and its effect on sediments. It begins with a brief background to gas hydrate (mainly methane hydrate) including structure, type, stability, and formation criteria. Then the different physical properties of hydrate bearing sediments from laboratory and field measurements are discussed, followed by a discussion of the causes of hydrate dissociation and the effect of dissociation on both bulk hydrate and hydrate bearing sediments.

2.1 Structure and types of gas hydrate

Gas hydrate is a clathrate hydrate, which is a solid, non-stoichiometric, ice-like compound, in which water molecules are linked through hydrogen bonding to form a lattice which contains cavities. These cavities can enclose a large variety of gas known as guest molecules with no chemical bonding between the host water molecules and the guest gas molecules. The crystal structure of gas hydrate consists of 85% water molecules, so many of the mechanical properties of gas hydrate resemble those of ice (Sloan, 1998).

Gas hydrates commonly form in one of three crystallographic lattice type structures: Structure I (cubic), Structure II (cubic) and Structure H (hexagonal), although other lattice type structures are also known to exist (Udachin and Ripmeester, 1999). The type of crystalline structure is influenced by the size of the

Hydrate Property	Gas hydrate structure						
	I "cubic"		II "cubic"		H "hexagonal"		
Cavity	Small	Large	Small	Large	Small	Medium	Large
Description	5^{12}	$5^{12}6^2$	5^{12}	$5^{12}6^4$	5^{12}	$4^35^66^3$	$5^{12}6^8$
No. of cavity/unit cell	2	6	16	8	3	2	1
Average cavity radius (Å)	3.95	4.33	3.91	4.73	3.91	4.06	5.71
Ideal unit cell formula	$6x2y.46H_2O$		$8x16y.136H_2O$		$1x2y3z.34H_2O$		
Type of molecules are found in gas hydrate	CO_2, CH_4, H_2S, SO_2		O_2, N_2 C_3H_8		butane, higher hydrocarbons		

Table 2.1: *Different cage sizes of gas hydrate (Sloan, 1998).*

guest molecule encased within the cavity (Sloan, 1998; Koh, 2002; Kirchner et al., 2004). The basic building block for all types of hydrates is the pentagonal dodecahedron (5^{12}) lattice cage (Figure 2.1), which is the smallest available cavity. Table 2.1 shows that the structure-H and structure-II hydrates have the ability to encase larger guest molecules compared to structure-I hydrate, which can hold guest molecules of size less than 4.33Å. The most common naturally occurring gas hydrate is structure-I, with methane as the guest molecule. Therefore this research is mainly focused on structure-I hydrates.

2.2 Stability and occurrence of gas hydrate

Gas hydrate forms under certain thermobaric conditions. In nature these conditions are found in two regions; in sediments where permafrost (surface temperature is less than 0°C) is present (Figure 2.2(a)), and in deep ocean sediments on continental slopes and rises (Figure 2.2(b)) when sediment temperature and pressure are within the hydrate stability region.

As a major part of the earth surface is covered by oceans, the oceanic environment is thought to be the predominant place for gas hydrates. In the oceanic environment pressure increases with depth, and temperature decreases in sea water and increases in the sediment with depth as shown in Figure 2.2(b). The hydrothermal gradient coincides with the phase boundary above the sea bed (at $\sim 0.5\,km$ from the sea surface in Figure 2.2(b)), and the geothermal gradient coincides with the phase boundary below the sea bed (at $\sim 2.5\,km$ from the sea surface in Figure 2.2(b)). Gas hydrate can be stable in region to the left of the phase boundary,

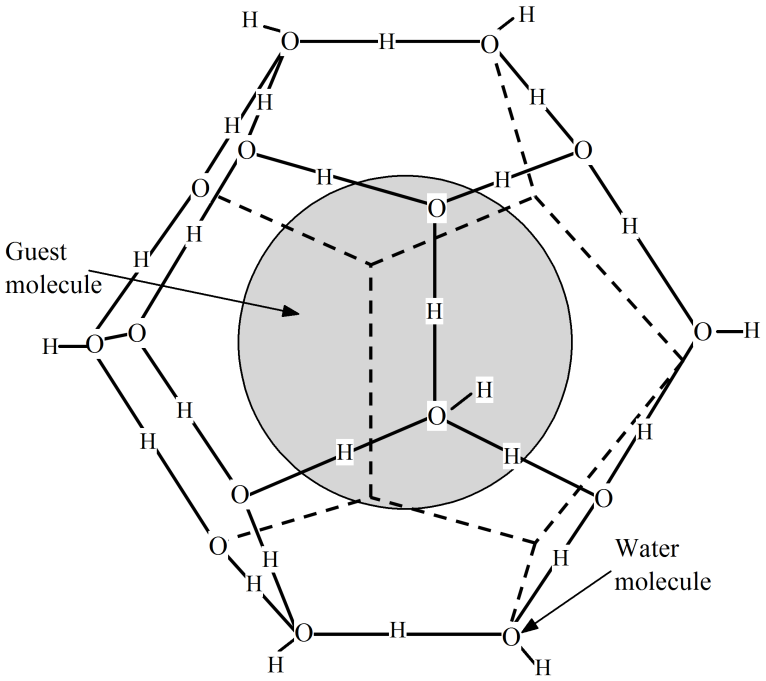

Figure 2.1: *Pentagonal Dodecahedron (5^{12}) structure in hydrate, showing water and guest molecules. Redrawn from Sloan (1998) after McMullan and Jeffrey (1965).*

bounded by the hydrothermal and the geothermal gradients above and below the sea bed respectively (Figure 2.2(b)). However, hydrate in sea water will float outside the hydrate stability region due to its low density compared to water. The region below the sea bed and to the left of the phase boundary is known as the hydrate stability zone (HSZ, Figure 2.2(b)). It can be seen in Figure 2.2 that small changes in temperature have more effect on the hydrate stability zone than the small changes in the pressure, thus hydrate stability is more susceptible to change in temperature than in pressure (Dillon and Max, 2003). There are also other factors which can affect hydrate stability.

- Guest molecules properties: The presence of a small fraction of ethane or propane will produce structure II hydrate, which is stable at higher temperatures than structure I at a given pressure (Dillon and Max, 2003).
- Gas solubility in the water : It has been observed that the hydrate begins to form only when the gas concentration in the fluid exceeds the gas solubility limit (Zatsepina and Buffett, 1997).
- Pore fluid properties: For instance, the CH_4 hydrate stability curve has an

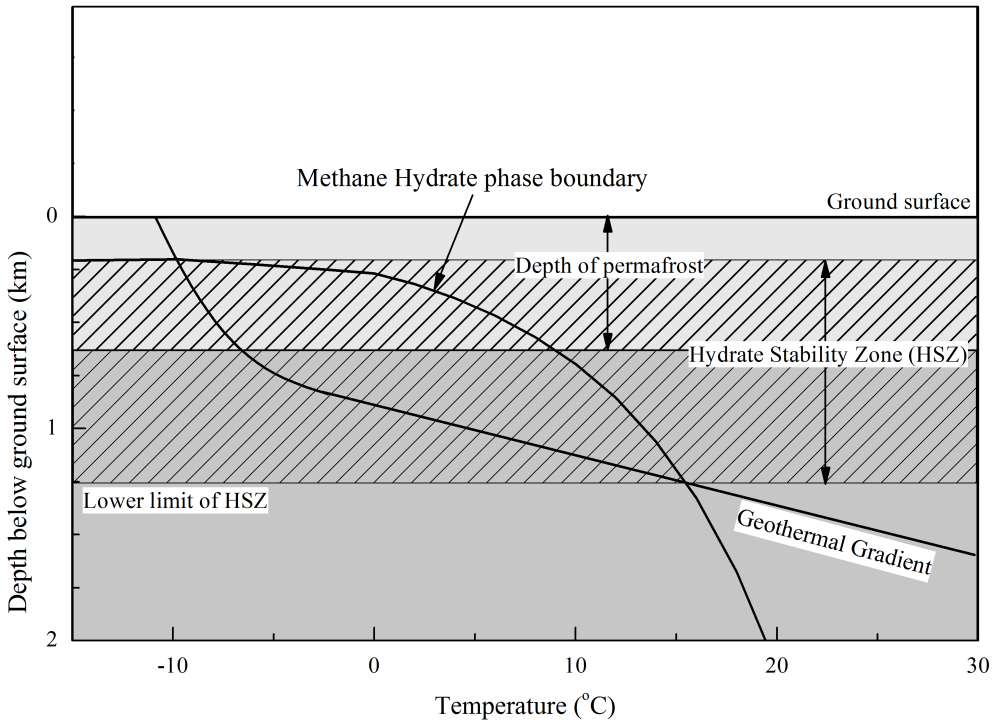

(a) *Stability region of methane hydrate in permafrost as defined by temperature (T) and pressure (P, indicated as water depth below ground surface in km). Redrawn from Kvenvolden (1988).*

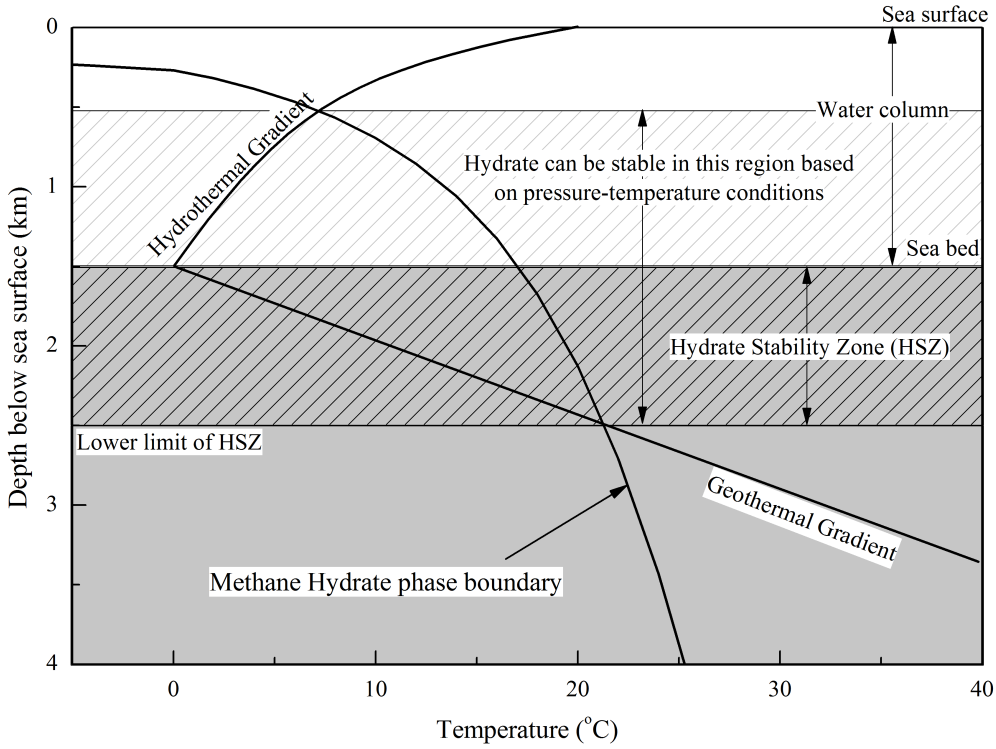

(b) *Stability region of methane hydrate in sea water as defined by temperature (T) and pressure (P, indicated as water depth below sea surface in km). Redrawn from Dillon and Max (2003).*

Figure 2.2: *Stability region of methane hydrate in (a) permafrost, and (b) seawater.*

offset of -1.1^oC in presence of 33.5% NaCl in pure water (Ruppel, 1997).

- Stability of gas hydrate bearing sediment also depends on the properties of the sediment (coarse or fine grained sediment). For instance, hydrate may be difficult to form in fine grained soils due to small pore sizes; methane and propane hydrate formation within 70Å silica gel pores requires 20-100% higher pressure than that for bulk hydrates (Handa and Stupin, 1992).

Natural occurrences of gas hydrate

Gas hydrate has been detected within both oceanic and permafrost (polar) sediments (Makogon, 1981; Dillon and Max, 2003). Permafrost associated gas hydrate has been detected within sample cores from Nerlerk, Koakoak, Ukalerk and Koponoar sites on the Beaufort sea shelf in northern Canada (Weaver and Stewart, 1982; Collett, 1994). Oceanic hydrate has been detected using well-logs and sample cores, and predicted using remote survey methods (Matsumoto et al., 1996; Shipboard Scientific Party, 2002; Uchida et al., 2004). The worldwide distribution of hydrate deposits in permafrost and oceanic sediments is shown in Figure 2.3. It can be seen that the gas hydrate occurs in almost all continental margins. Therefore, it is necessary to understand gas hydrate and its dissociation effect upon the properties of hydrate bearing sediments, given that oil/gas exploration activities are encroaching into these areas.

2.3 Formation and morphology of hydrate bearing sediments

Gas hydrate bearing sediment takes a number of forms and structures. Different morphologies of gas hydrate have been found in marine and permafrost sediments (Carson et al., 1993; Dallimore and Collett, 1995; Matsumoto et al., 1996, 2000; Shipboard Scientific Party, 2002; Uchida et al., 2004; Holland et al., 2008). Based on observations from numerous locations around the world and on the basis of laboratory tests, gas hydrate morphologies can be classified into different categories from sediment-scale to pore-scale level as shown in Figure 2.4.

At the sediment scale, gas hydrates typically occur in the form of segregated

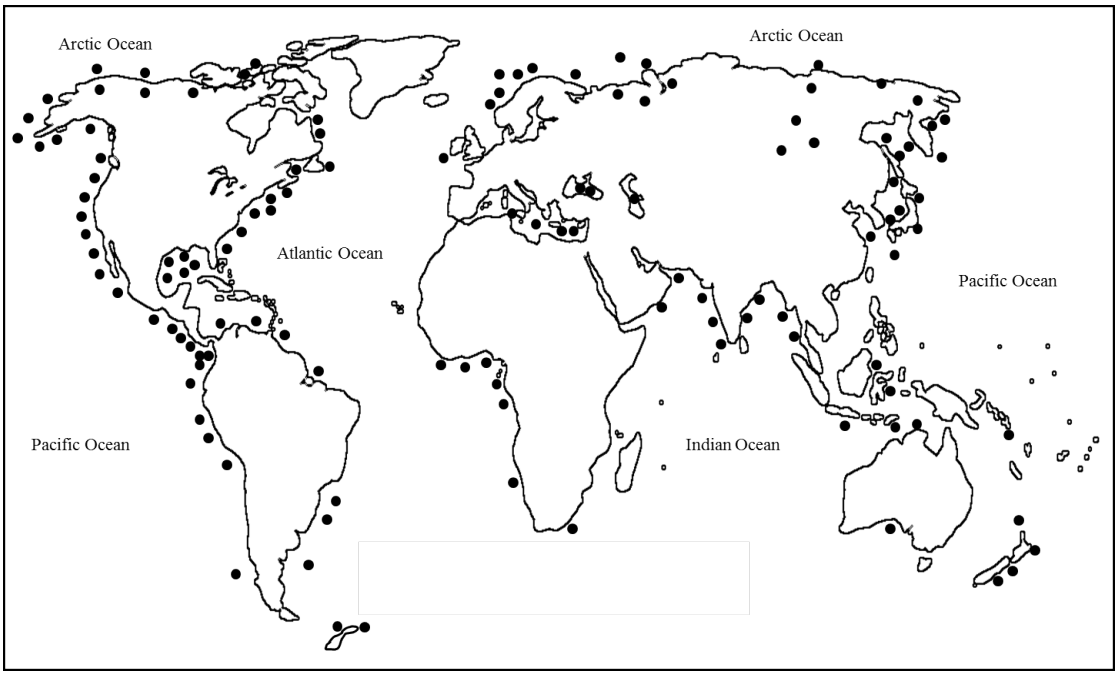

Figure 2.3: *Distribution of worldwide locations of known and inferred gas hydrate deposits in permafrost and in oceanic sediments. Redrawn from Kvenvolden (1993) and Makogon et al. (2007).*

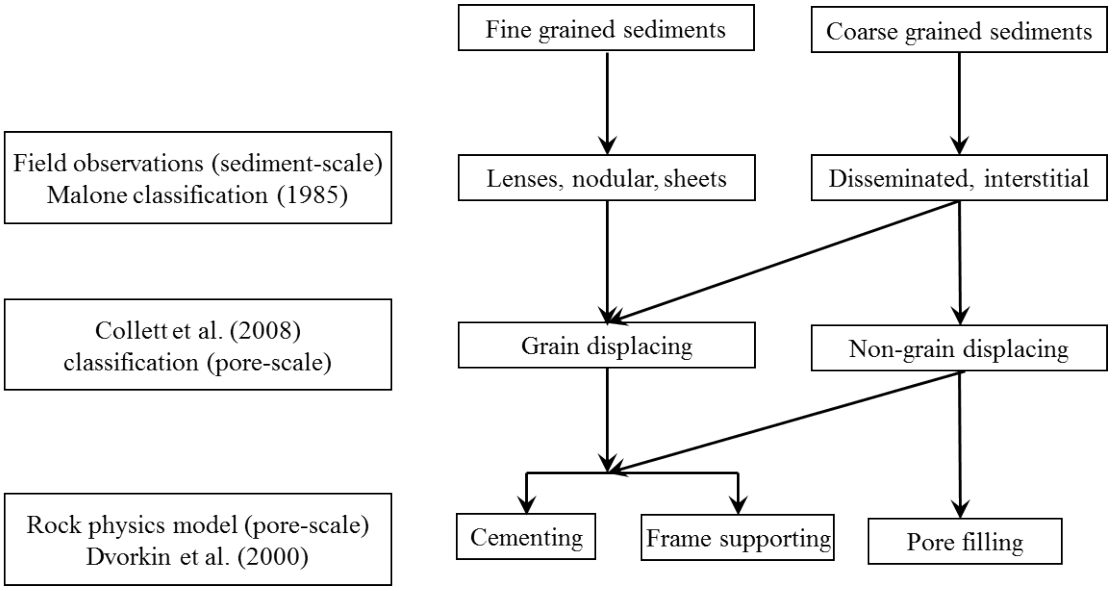

Figure 2.4: *Gas hydrate morphologies within sediment from sediment scale to pore scale.*

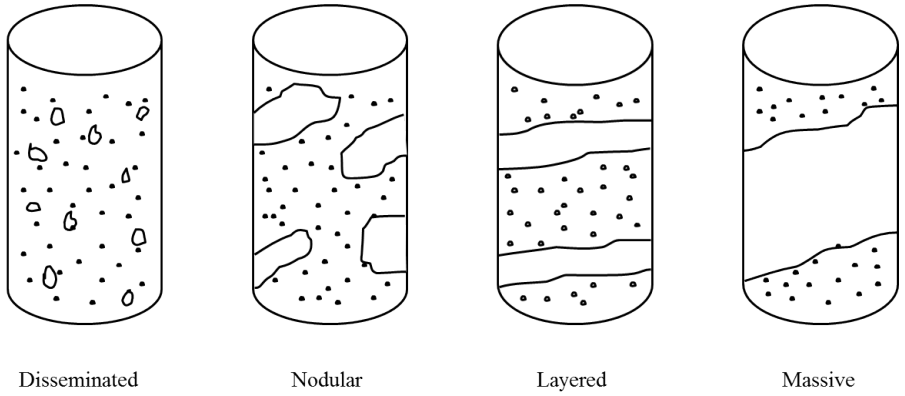

Figure 2.5: *Four types of natural gas hydrate deposits in the sediment. Redrawn from Malone (1985).*

bodies; lenses, nodules or sheets where the host sediment is fine-grained (clays and silts), and as interstitial or disseminated material in coarse-grained sediments (Brooks et al., 1994; Dallimore and Collett, 1995; Matsumoto et al., 2000; Uchida et al., 2004). In 1985 Malone (Sloan, 1998) suggested that interaction of gas hydrate can produce four types of morphologies as shown in Figure 2.5. Disseminated hydrate describes a material that is homogeneously distributed throughout a sediment. Nodular and layered morphologies are a bulk accumulation of pure hydrate in a sediment. If the supply of gas and water are sufficient then each of these hydrate morphologies can develop to massive hydrate morphology.

However, recent advances in natural hydrate sampling and imaging techniques have led to another classification system which describes hydrate in terms of two morphological types, grain displacing and non-grain displacing (Collett et al., 2008). Non-grain displacing morphology describes hydrate that forms in the pore spaces of a sediment, replacing the pore fluids (water and gas). Whereas grain displacing hydrate does not occupy the pore spaces instead forces grains apart, forming discrete nodules, layers, and lenses of the hydrate (Holland et al., 2008). In terms of Malone's classifications, grain displacing and non-grain displacing morphologies can occur for any of the morphologies (disseminated to massive, Figure 2.5).

To understand the hydrate morphologies and properties of hydrate bearing sediments, a number of researchers synthesised gas hydrate within sediments using different formation techniques. The hydrate formation techniques can be broadly classified into five categories, as discussed below;

1. Methane gas is injected into a partially water-saturated sediment to form methane hydrate. The volume of hydrate is calculated on the basis of water present within the specimen (Priest, 2004). This method of hydrate formation is refereed as the "excess gas" method.

2. Methane gas is injected into a sediment containing ice seed. Temperature is increased above the ice point to form hydrates. The volume of methane hydrate is calculated from the volume of ice added or on the basis of moles of methane gas consumed or evolved, respectively, during the formation or dissociation process (Stern et al., 2001; Waite et al., 2004). To avoid ice coating, the hydrate formation/dissociation needs to be performed above the freezing point of water.

3. A dry specimen is filled with methane gas at a defined pressure. Then water is injected into the specimen to form hydrate. The volume of hydrate is then calculated on the basis of number of moles of methane gas injected into the specimen (Rees, 2009). This method is refereed as the "excess water" method.

4. A fully water-saturated specimen is injected with methane gas until a pre-determined amount of water is pushed out. The volume of methane hydrate is calculated from the moles of methane gas consumed or evolved, respectively, during formation or dissociation process (Winters et al., 2004).

5. A pre-determined amount of gas is mixed with water. Then, temperature is lowered at high pressure to form hydrates (Tohidi et al., 2001). The volume of hydrate can be calculated from the amount of gas mixed in water. However, methane hydrate formation from this method has limitations due to low methane solubility in water (Chapoy et al., 2004). However, some researchers have used this method to form up to 100% of methane hydrate by continuous flowing methane through water (Spangenberg and Kulenkampff, 2003).

Results from laboratory formed methane hydrate in Leighton Buzzard sand showed that gas hydrate grown in gas saturated sands exhibits a cementing morphology (Priest, 2004). Results from laboratory formed methane hydrate in Ottawa sands using the excess gas method also showed that the sand exhibits a cementing morphology (Waite et al., 2004). However methane hydrate grown in water saturated

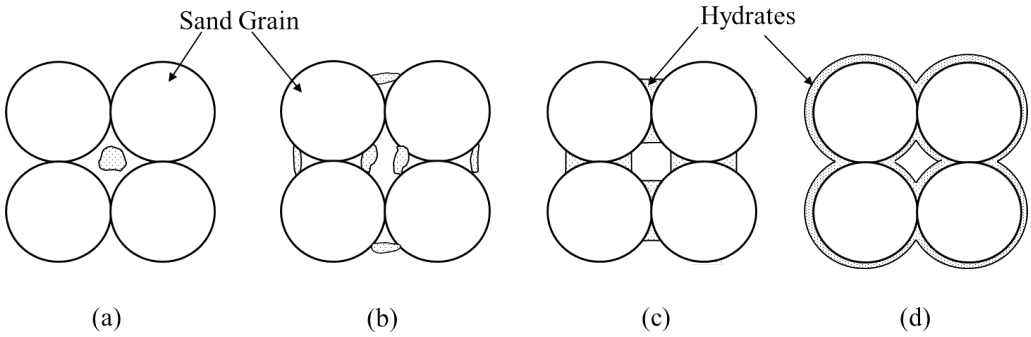

Figure 2.6: *Possible location of hydrate in a granular material. (a) hydrate as pore-filling in the pore space, (b) hydrate as frame-supporting between the grains, (c) hydrate as cementation to the grain contacts, and (d) hydrate as envelops to the grains. Redrawn from Dvorkin et al. (2000).*

sands exhibits a frame supporting morphology (Rees, 2009). Laboratory tests on different types of sediments (sand, silt and clays) suggested that up to 40% of THF (Tetrahydrofuran) hydrate saturation in the pore spaces forms a pore-filling morphology whereas above 40% hydrate saturation forms a cementation morphology (Lee et al., 2010). Figure 2.6 highlights the possible location of hydrate in the pore spaces of a sediment based on theoretical rock physics models (Dvorkin et al., 2000).

Comparison of laboratory results with theoretical rock physics models have suggested that the hydrate can exhibit different pore-scale morphologies in different sediments, depending on the methodology used for the hydrate formation (Priest et al., 2009). Similarly in nature, different morphological forms of hydrate are likely to result from how methane gas arrives at the hydrate stability zone. Currently there are three different hypotheses of how methane gas gets into the hydrate stability zone (HSZ).

1. Gas hydrate formation from in-situ methane: The gas is mainly derived from microbiological processes which reduce the organic matter within the sediment to methane gas (Kvenvolden and Barnard, 1983). Gas hydrate is formed directly as the quantity of methane becomes greater than the solubility of methane in the pore fluid (Sloan, 1998).

2. Gas hydrate formation by migration of free gas: Free gas migrates upward into the hydrate stability zone through fissured and permeable layers (Minshull et al., 1994). Methane gas may come from outside the HSZ

through biogenic or thermogenic sources (Sloan, 1998). Biogenic methane gases are from microbial transformation of organic matters, and thermogenic methane gases are from deep petroleum reservoirs.

3. Gas hydrate formation from gas dissolution from rising pore water: Gas solubility in pore water increases with depth, so as methane-saturated water rises through the sediment, methane gas comes out of solution and forms gas hydrate in hydrate stability region (Hyndman and Davis, 1992).

2.4 Properties of gas hydrate bearing sediments

Gas hydrate was first discovered in 1965 in the natural environment in the Siberian permafrost region by Makogon and co-workers (Makogon et al., 2007). It initiated an interest into how hydrate can affect the properties of the sediment. As discussed in Chapter 1 gas hydrate can be a geotechnical hazard, a driver of global climate change or a future energy resource. Therefore, many researchers have studied the properties of hydrate bearing sediments from field measurements using the seismic survey and analysis, laboratory measurement on in-situ or synthesised hydrate bearing sediments, and using effective medium modelling of the hydrate bearing sediments.

2.4.1 Laboratory measurements

A number of researchers have studied the effect of hydrate formation on sediment properties, such as seismic wave velocities and the shear strength of sediments, using synthesised and in-situ hydrate bearing specimens. It has been found that the presence of gas hydrate in sediment increases the shear wave velocity (Stoll, 1979; Whiffen et al., 1982; Lee and Collett, 2001; Waite et al., 2004; Winters et al., 2004; Priest, 2004; Rees, 2009; Lee et al., 2010) and the shear strength (Ebinuma et al., 2005; Masui et al., 2005; Yun et al., 2007; Santamarina and Ruppel, 2008; Song et al., 2010; Miyazaki et al., 2011). Different researchers have used different methodologies to synthesise gas hydrate; hydrate formation within gas or water saturated environments, or hydrate formation from dissolved

gas in water phase. After hydrate formation, the shear wave velocity has been measured using resonant column testing or the bender element method, and the shear strength has been measured using triaxial compression tests.

Table 2.2 gives a summary of laboratory measured P- and S- wave velocities obtained by various researchers from laboratory synthesised and in-situ hydrate bearing sediments. For comparison the seismic velocities of ice, bulk methane hydrate, and water are also given. Table 2.3 gives a summary of shear strength (q_{max}) obtained from various researchers. The shear strength (q_{max}) is half of the maximum deviatoric stress (σ_{dev}^{max}) obtained from the triaxial compression test; ($q_{max} = \sigma_{dev}^{max}/2$). For comparison the shear strength of bulk methane hydrate and non-hydrate sediment are also given.

It can be seen in Table 2.2 and 2.3 that the presence of hydrate increases the seismic velocities and the shear strength of sediment. However, measured increases in the velocities and strengths are different for different researchers. This could be due to a number of factors, such as type of hydrate, type of sediment, volume of hydrate, and hydrate formation methodology. Sediment with hydrate which was synthesised using the excess gas method exhibits higher seismic velocities (Priest, 2004; Waite et al., 2004) compared to the hydrate which was synthesised using the excess water or dissolve gas methods (Stoll, 1979; Rees, 2009). In general the sediment which has higher stiffness tends to have higher strength as observed in laboratory tests on cemented sands (Consoli et al., 2007) and on rocks samples (Hobbs, 1975). Therefore it is to be expected that the shear strength will be higher for the hydrate bearing sediment formed using the excess gas method compared to sediment formed using the excess water method (as seen in Table 2.3).

2.4.2 Seismic survey and analysis

Seismic surveys are geophysical techniques, these are routinely used to determine sediment properties remotely. Seismic surveys commonly use bottom simulating reflector (BSR) to estimate the depth of gas hydrate stability zone. The BSR is an acoustic reflection which mimic the sea floor within the oceanic sediment (Kvenvolden and Barnard, 1983). It is typically associated with a strong negative polarity reflector, indicating a large decrease in acoustic impedance (wave velocity $\times$ density), which is believed to be found at the interface between free gas and

Material	V_p (m/s)	V_s (m/s)
Ice Ih (Shaw, 1986)	3900	1900
Bulk methane hydrate (Whiffen et al., 1982)	3369	-
Propane hydrate (Stoll, 1979)	2360	-
Water (Helgerud et al., 1999; Winters et al., 2004)	1500	0
100% ice within Ottawa sand (Winters et al., 2004)	4230	-
37% methane hydrate within Ottawa sand (Winters et al., 2007)	3360	-
20% methane hydrate within Leighton Buzzard sand (Clayton et al., 2005)	2476	1423
20% methane hydrate within Leighton Buzzard sand (Rees, 2009)	1745	287
Krishna-Godavari basin, NGHP-01 (Winters et al., 2008)	1560 - 1900	-
Malik 2L-38, Mackenzie delta (Winters et al., 2004)	2900 - 3880	-
Ulleung Basin, Sea of Japan (Yun et al., 2011)	3000	1000

Table 2.2: *Primary (V_p) and shear (V_s) wave velocities of various materials measured in laboratory.*

the gas hydrate (Berndt et al., 2004). As discussed previously, the presence of hydrate increases sediment wave velocity, however even very small amount of free gas in the sediment will greatly reduce its wave velocity. Consequently, the acoustic impedance contrast between sediment containing hydrate and sediment containing free gas occurs (Kvenvolden and Barnard, 1983; MacKay et al., 1994). However, gas hydrate may not be present in the sediment above this boundary (MacKay et al., 1994).

Table 2.4 gives wave velocities deduced from well logging and seismic surveys. The presence of hydrate is hypothesised in sediment due to the wave velocity being unusually higher than the adjacent sediments. Measurement of sediment wave velocity may identify the presence of hydrate, but may not identify the concentration of the gas hydrate because sediment stiffness (or seismic velocity) depends on the hydrate morphology within the sediment. For example, a hydrate bearing sediment where pore spaces filled with 10% of hydrate as cement morphology likely to have higher shear and primary wave velocities compared to the sediment with 50% of the hydrate as pore-filling morphology (Priest et al., 2009).

Material	Hydrate formation technique	Hydrate (%)	q_{max} (MPa)
Sand @ $3\,MPa$ effective stress (Ebinuma et al., 2005)	excess water	0	1.6
		25	4.2
	excess gas	0	2.0
		25	7.0
Toyoura sand @ $1\,MPa$ effective stress (Masui et al., 2005)	excess gas	0	1.9
		55	4.0
Sand @ $1\,MPa$ effective effective stress (Yun et al., 2007)	dissolved gas	0	1.4
		50	2.7
Silt @ $1\,MPa$ effective effective stress (Yun et al., 2007)		0	0.9
		50	2.4
Kaolinite (Clay) @ $1\,MPa$ effective stress (Yun et al., 2007)		0	0.4
		50	1.2
Toyoura sand @ $1\,MPa$ effective stress (Miyazaki et al., 2011)	excess gas	0	1.9
		48	3.2
Ottawa sand @ $0.3\,MPa$ effective stress (Winters et al., 2007)	excess gas	70	10.4
Krishna-Godavari basin, NGHP-01 (Winters et al., 2008)	in-situ specimen		0.12 to 0.18
Malik 2L-38, Mackenzie delta (Winters et al., 2004)	in-situ specimen	44	0.8 to 1.6
Solid methane hydrate @ $1\,MPa$ confining pressure @ temperature of -5^0C (Song et al., 2010)			0.9

Table 2.3: *Shear strength (q_{max}) for various materials measured in laboratory.*

Location	V_p (ms^{-1})
Blake Outer Ridge, ODP Leg 76 (Kvenvolden and Barnard, 1983)	2000
Offshore Vancouver and Oregon, ODP Leg 146 (MacKay et al., 1994)	1700 - 1900
Blake ridge and Carolina rise, ODP Leg 164 (Matsumoto et al., 1996)	1850 - 2000
Offshore Peru and Costa Rica, ODP Leg 112 (Pecher et al., 1996)	2150
Makran continental margin, Arabic sea, NGHP-01 (Sain et al., 2000)	2200

Table 2.4: *Primary wave velocities (V_p) from various seismic survey and well logging.*

2.4.3 Numerical modelling predictions

A number of theoretical rock physics models have been developed to model the influence of gas hydrate on sediment properties and therefore its effect on wave velocities (Ecker, 2001; Fernandez and Santamarina, 2001; Lee and Collett, 2001; Carcione and Gei, 2004; Chand et al., 2004; Winters et al., 2004). Gas hydrate is a solid material which has higher stiffness than its constituents; water and gas. However, the increase in wave velocities depend on whether the hydrate is modelled as a cement, frame-supporting or pore-filling component of the sediment (Figure 2.6).

Figure 2.7 shows the shear (V_s) and primary (or compressional, V_p) wave velocities of water saturated sand sediment with a 40% porosity, calculated from different effective medium models (Appendix A), as a function of methane hydrate saturation. It can be seen in Figure 2.7 that the highest increase in the wave velocities occurs when the hydrate cements the sand grains thus strongly reinforcing the sediment (Dvorkin et al., 1999). Hydrate acting as a pore-filling component has no effect on the shear wave velocity of the sediment (Figure 2.7(a)), because hydrate does not interact with the sand grains. However, the pore filling component of solid hydrate will reduce the volumetric compressibility of the pore materials (Dvorkin et al., 2000), increasing the compressional wave velocity (Figure 2.7(b)). Hydrate acting as a frame-supporting component produces a small increase in the wave velocities (Figure 2.7). This is due to the fact that the hydrate becomes a part of load bearing structure, thus enhancing contact area within the sediment by providing additional grain-hydrate contacts along with grain-grain contacts (Figure 2.6b).

2.4.4 Attenuation properties of hydrate bearing sediment

Attenuation is another material property which has been used by a number of researchers to study hydrate bearing sediment (Guerin and Goldberg, 2002; Chand and Minshull, 2004; Matsushima, 2006). Attenuation could be defined as the loss of energy or amplitude in one cycle of wave oscillation. There are number of attenuation mechanisms proposed by several researchers:

- Macroscopic fluid flow attenuation mechanism; the loss of wave energy oc-

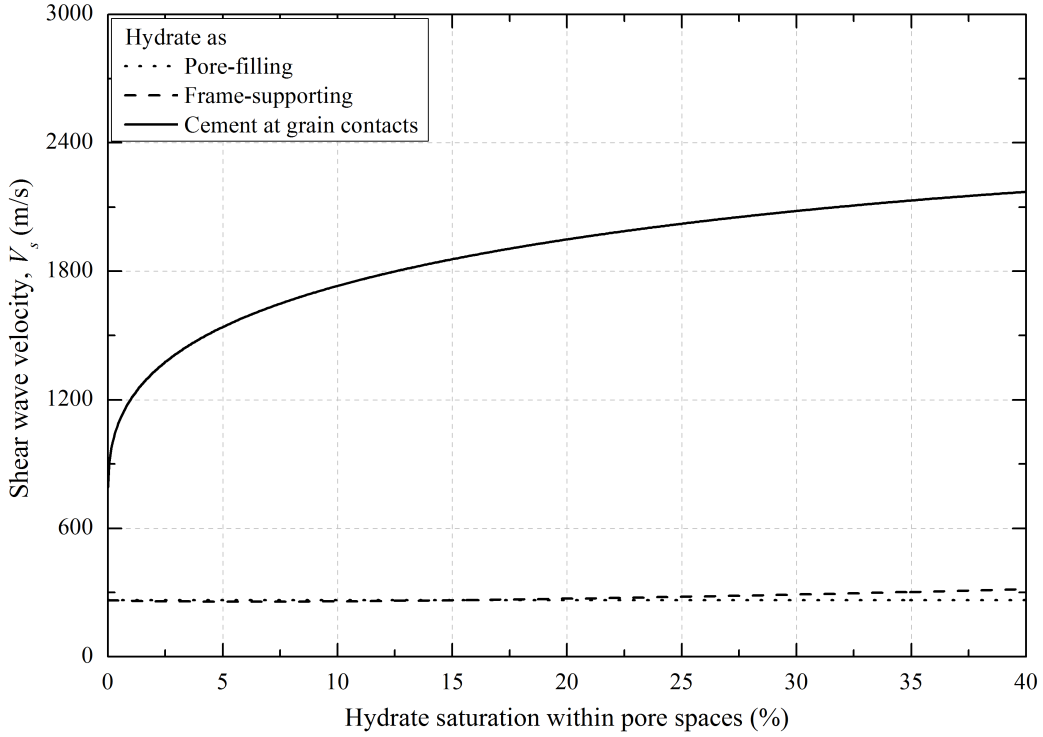

(a)

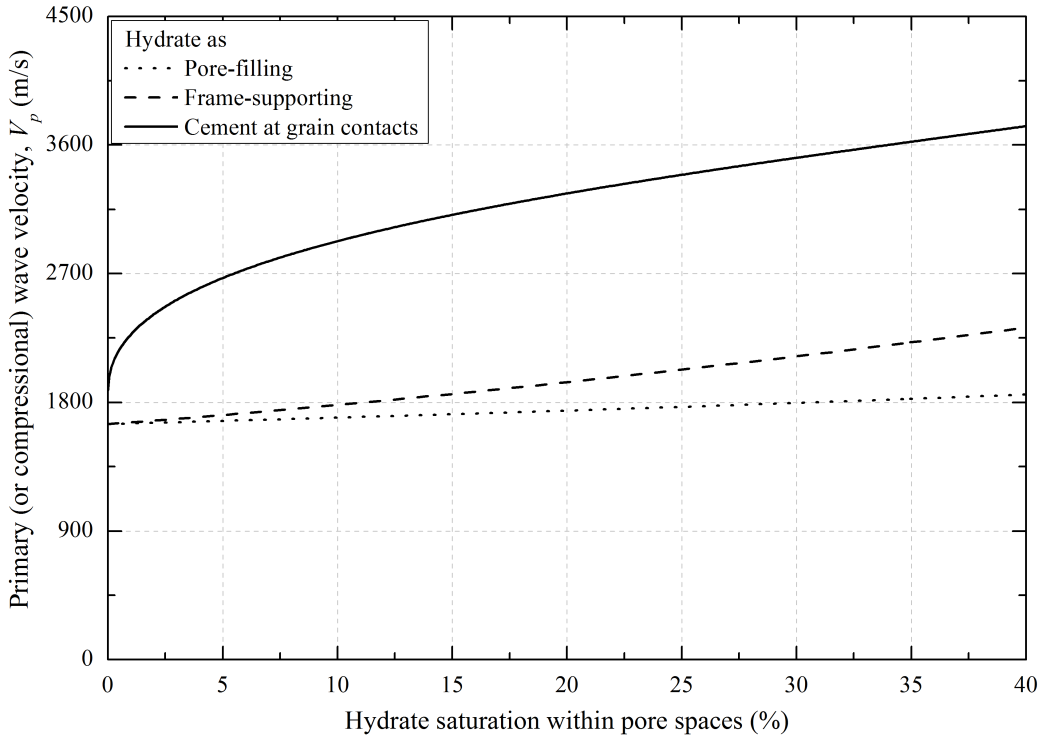

(b)

Figure 2.7: *Variation in (a) shear, and (b) primary wave velocities with hydrate saturation in pore spaces based on different theoretical rock physics models (Appendix A) of water saturated sediment with porosity 0.4 and density* $2000\,kg/m^3$.

curs due to relative motion of pore fluid and soil solid during passage of a seismic wave in a saturated sediment, where the soil solid and pore fluid are of comparable densities (Biot, 1956).

- Frictional dissipation between solid surfaces as they slide relative to one another during passage of a seismic wave (Walsh, 1966). Extending the work of Walsh (1966), Mavko and Nur proposed inter-crack squirt flow attenuation mechanism, in which fluid squirt flow from one pore to another as solid surfaces slide relative to one another during passage of a seismic wave within saturated sediments (Mavko and Nur, 1975) and partially saturated sediments (Mavko and Nur, 1979).

- Flow of water during passage of a seismic wave between total and partially saturated macroscopic regions within a patchy saturated sediment (White, 1975).

- Presence of water within pores reduces the friction coefficient between solid surfaces, facilitating sliding and thus increasing the attenuation during passage of a seismic wave (Johnston et al., 1979).

- Viscous shear relaxation; high viscous fluid within sediment will reduce the amplitude of passing seismic wave (Walsh, 1969).

- Scattering of wave amplitude; wave amplitude scatters during passage of a seismic wave in the small pore-spaces of a sediment, thus reducing the attenuation (McCann, 1969).

However, most of these mechanisms can be neglected for the case of seismic attenuation in hydrate bearing sediment (Chand and Minshull, 2004). Viscous fluid relaxation is significant for high viscosity fluids (Walsh, 1969), frictional attenuation is only significant at high strain level ($> 10^{-6}$, Walsh (1966)), and scattering is important only at wavelengths comparable to the size of the grains (McCann, 1969).

Microscopic fluid flow (the Biot (1956) mechanism) is a comprehensive theory of wave propagation in fully-saturated medium (Winkler and Nur, 1982). The Biot-squirt flow (BISQ) mechanism is a combination of Biot and squirt flow mechanisms. It has been used by many researchers to model seismic attenuation of sediment (Winkler and Nur, 1982; Dvorkin and Nur, 1993; Parra, 2000;

Guerin and Goldberg, 2002; Chand and Minshull, 2004). Guerin and Goldberg (2005) and Chand and Minshull (2004) have used the Biot-squirt flow (BISQ) mechanism to study Mallik 2L-28 well attenuation data at sonic frequency range $(1 - 20\,kHz)$. They found that the seismic attenuation increases with hydrate saturation. However, Matsushima (2006) used the Nankai Trough exploratory well data and observed that the seismic attenuation of the sediment was not affected by the presence of hydrate at seismic frequency range $(1 - 200\,Hz)$. This behaviour could be due to the fact that the attenuation is frequency dependent, the attenuation in hydrate bearing sediment may not necessarily translate from the sonic $(1 - 20\,kHz)$ to the seismic $(1 - 200\,Hz)$ frequency range (Guerin and Goldberg, 2002).

It has also been suggested that the presence of low concentration of free gas ($< 20\%$) may significantly increase seismic attenuation (Murphy III, 1982). The presence of gas within hydrate bearing sediment can occur from two reasons (Guerin and Goldberg, 2002): (1) pore water content may be insufficient for complete conversion of methane into hydrate, (2) gas may evolve from dissociation of hydrate in the vicinity of drilling operation.

2.5 Dissociation of gas hydrate

As shown in Section 2.2, gas hydrate remains stable within sediments under limited thermobaric conditions. If these conditions are sufficiently altered the hydrate dissociates, and will revert back to its constituent parts of water and gas. As discussed in Chapter 1, $1\,m^3$of methane gas hydrate contains $164\,m^3$of methane at standard temperature and pressure conditions. Therefore, release of gas and water may generate excess volume of fluids in the pores and may increase pore pressure within the sediment. The release of gas within pores may also increase pore fluid compressibility of the sediment. However, the increase in pore pressure will depend on the permeability of the hydrate bearing sediment and drainage condition. If dissociation of hydrate is fast compared to pore pressure dissipation, excess pore pressure will be generated and this will lead to a reduction in effective stress within the sediment. In addition, dissociation of gas hydrate from its ice-like solid structure to fluid materials may change the strength and stiffness of the sediment.

2.5.1 Causes of hydrate dissociation

Hydrate dissociation will occur if hydrate equilibrium pressure and temperature conditions are sufficiently altered. In general, there are two drivers for changes in temperature and pressure; natural changes (e.g. climate or sea-level change) or man-made activities (such as, exploration and exploitation activities).

Natural changes

Gas hydrate can dissociate as a result of natural changes such as a change in the environmental temperature and/or pressure conditions, due to global or regional temperature (Mienert et al., 2010) and sea-level change (Beauchamp, 2004). It is believed that global temperature rise may affect hydrate bearing sediment and may dissociate gas hydrate. However, any change in atmospheric temperature will have to transfer to the hydrate bearing sediment through the water column and sediment layer(s) above the hydrate bearing strata (Dillon, 2001; Paull et al., 2003; Nixon and Grozic, 2007). Due to the low thermal conductivity and high specific heat capacity of water, it will take thousands of years to alter the temperature of gas hydrate bearing sediment through changes in atmospheric temperature. Thus, the effect of atmospheric temperature changes are limited to hydrate at shallower depths or hydrate at the phase boundary (Glasby, 2003). Changes in sea-level can more readily alter the pressure condition within sediment (Dillon, 2001; Beauchamp, 2004); however change in sea-level occurs very slowly.

Therefore natural changes are slow processes, but their effect can cause large scale hydrate dissociation as they will affect the hydrate stability conditions over large areas (Figure 2.8). Such widespread dissociation in the sediment could lead to large areas of the sea floor sediment changing its properties and losing strength.

Exploration and exploitation activities

Oil and gas exploration activities could result in small scale or local hydrate dissociation that may endanger engineering projects in the immediate vicinity (Nixon and Grozic, 2007; Kvenvolden, 2000). For example, Figure 2.9 shows a methane hydrate bearing sediment that is stable in an oceanic environment, at a given pressure and temperature. Consider a well drilled through the hydrate

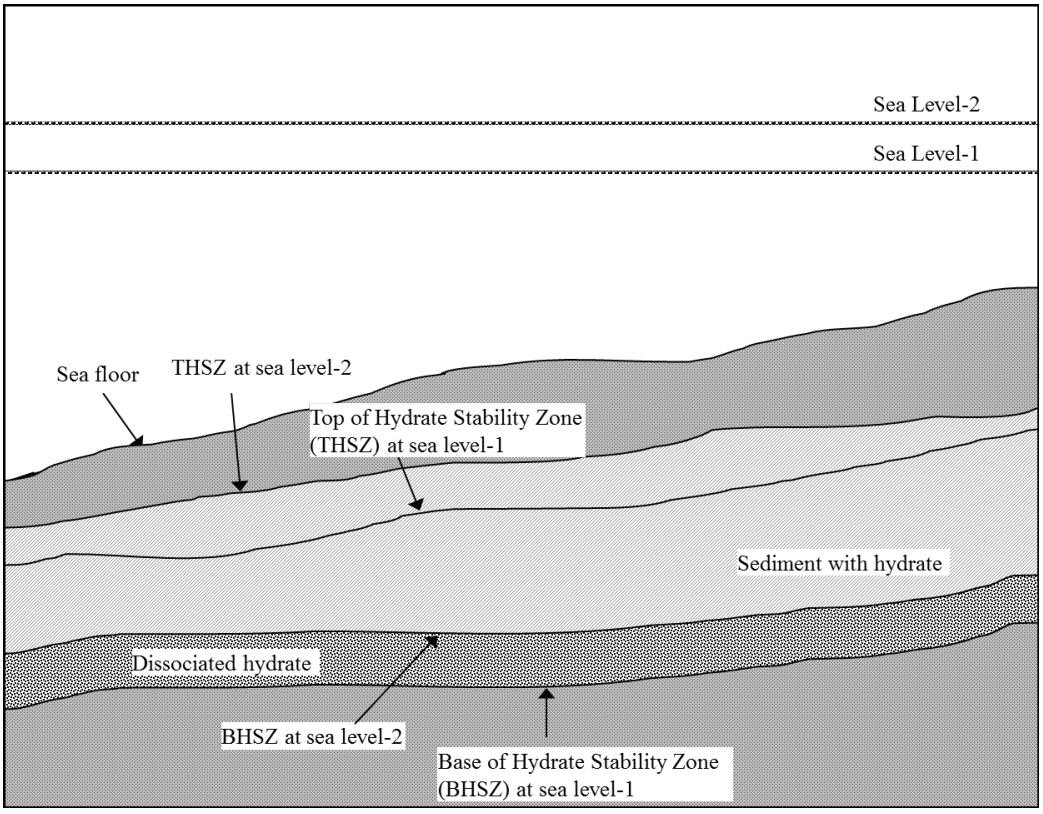

Figure 2.8: *Dissociation of gas hydrate in oceanic sediments due to change in sea level. Rise in sea level from 1 to 2 changes the pressure within the sediment thus raising the top and bottom of the hydrate stability region. Hydrate which is outside the new hydrate stability zone (at level 2) will dissociate. Redrawn from Kvenvolden (1999).*

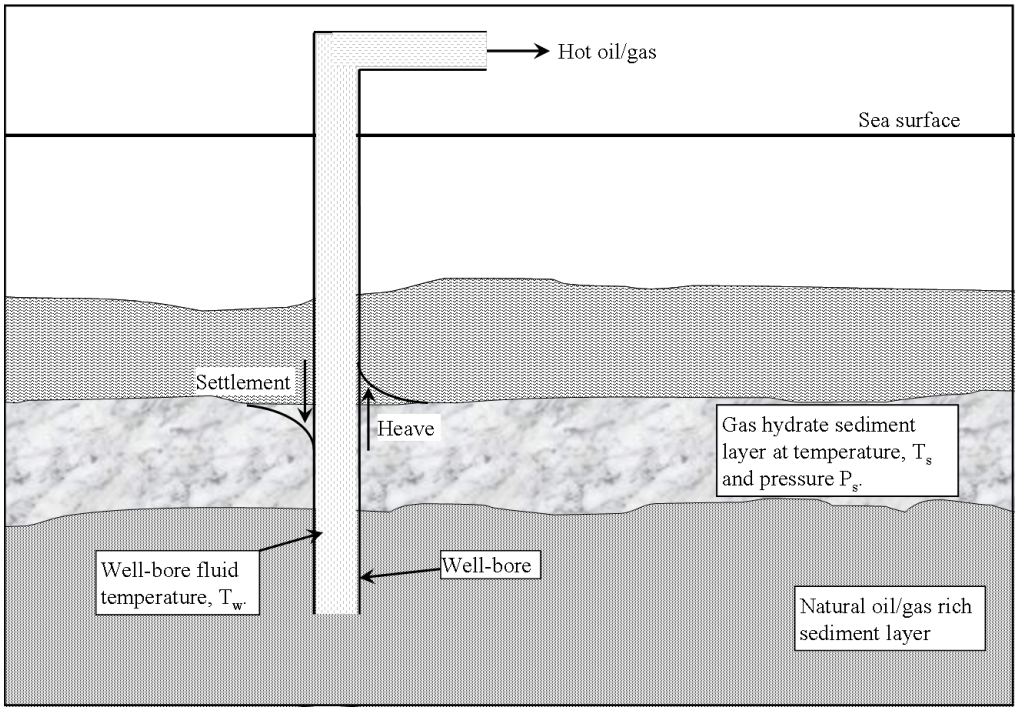

Figure 2.9: *Pumping of hot oil/gas from oil/gas rich strata through gas hydrate bearing sediment can transfer heat from the oil/gas into the sediment through heat conduction. If this is outside the pressure-temperature equilibrium condition for hydrate, then hydrate will dissociate and result in settlement, or heave, of the sediment.*

bearing sediment into an oil/gas rich strata which is at a higher temperature. As hot oil/gas is pumped through the hydrate bearing sediment, the temperature around the well increases through heat conduction. If the temperature is above the pressure-temperature equilibrium condition for the hydrate, then hydrate will dissociate within the vicinity of the well pipe. The hydrate dissociation may increase pore pressure within the sediment and may result in settlement or heave of the sediment (as shown in Figure 2.9). Thus platform subsidence or at the worst platform collapse may occur (Nimblett et al., 2005).

Other activities could also dissociate hydrates and affect engineering projects. For an instance, application of cement to well-bore casing can release heat and dissociate nearby hydrate, which may lead to inadequate casing or casing failure (Nimblett et al., 2005).

2.5.2 Field observation of hydrate dissociation

A number of slide scars left by submarine landslides have been observed along continental margins within marine sediments (Schwab et al., 1993). The size and shape of these scars suggest that the volume of material removed in these slumping events may involve tens and even thousands km^3 of material (Paull et al., 2003). Many researchers have suggested that hydrate dissociation may have caused submarine landslides and slope failures, producing tsunamis, in the past (Carpenter, 1981; Kayen and Lee, 1991; Popenoe et al., 1993; Field and Barber Jr, 1993; Paull et al., 2000).

The Storrega slide on the mid-Norwegian Continental Margin is one of the largest known submarine slides. It has a 290 km long head-wall scar, extends for over $800\,km$ down slope, and is estimated to have transported over $5,500\,km^3$ of sediment over the sea floor (Paull et al., 2000). The Storrega slide has been extensively studied, and it has been found that the slide scars coincide with the location of a BSR, suggesting the failure surface coincided with the base of gas hydrate stability before the slide occurred. It has also been suggested that a drop in overburden pressure may have caused lowering of the base of gas hydrate zone and may have triggered hydrate dissociation, which may have weakened the sediments and caused the Storrega slide (Paull et al., 2000; Berndt et al., 2002; Mienert et al., 2005). However, some researchers believed that the inherent properties of the build up of free gas and pressure beneath the gas hydrate stability zone (GHSZ) may have caused these slides (Beauchamp, 2004).

Studies of the Beaufort Sea continental slope have revealed a belt of massive bedding-plane slides and rotational slumps, coinciding with a region of hydrate bearing sediment (Kayen and Lee, 1991). They suggested that a reduction in sea level during the Pleistocene era (2.6 to 0.12 million years ago) may have initiated gas hydrate dissociation, causing excess pore fluid pressure and reducing slope stability of this region.

The Cape Fear landslide is one of a number of large scale submarine slope failures along the U.S. Atlantic continental margin (Carpenter, 1981; Paull et al., 2000). High resolution seismic reflection data show that the base of the hydrate stability zone, corresponding to the BSR, is associated with a zone of weakness and failure within the sediments (Popenoe et al., 1993; Paull et al., 2000). Based on these seismic reflection data, it has been suggested that the landslide could be related

to the liberation of free gas by hydrate dissociation thus weakening of sediments (Carpenter, 1981; Popenoe et al., 1993). However, Driscoll et al. (2000) proposed that the slow warming of ocean bottom water during interglacial periods could have caused gas hydrate dissociation and consequent weakening of the hydrate bearing sediment and caused slope failure.

Apart from these natural events, there are numerous examples of drilling activities which have been hampered during and/or post drilling operation in oceanic and Arctic environments (Yakushev and Collett, 1992; Collett and Dallimore, 2002; Nimblett et al., 2005). For example, conventional rotary drilling operations can cause sudden pressure and temperature changes in the surrounding sediment (Dillon and Max, 2003). The sediment temperature change could occur either due to hot drill bit or warm drilling fluids (Bagirov and Lerche, 1997). If the surrounding sediment contains gas hydrate, this temperature-pressure change may dissociate hydrate releasing large quantity of gas. This could result in gas kicks, blow-outs, and uncontrolled gas release in and around the well as observed in the Russian Yamburg field (Yakushev and Collett, 1992; Collett and Dallimore, 2002) and other locations (Nimblett et al., 2005; Folger, 2008). As methane is the most common gas in natural gas hydrate, its sudden release could result in fires during drilling operations as observed in the Russian Yamburg field (Yakushev and Collett, 1992).

Numerous drilling hazards have also occurred during drilling operations across several areas of the US and Gulf of Mexico (GoM), offshore south-east Asia, West Africa, the Norwegian Sea and other parts of the world where sudden water flows have disrupted drilling operations (Nations and Medley, 1997; Hardage et al., 2006). These hazards may be associated with hydrate dissociation caused by circulation of warm drilling mud (Hardage et al., 2006). In addition, the occurrence of flowing water in sediments during drilling activity can erode the structural support of the well, resulting in subsidence and buckling of casing, and subsequent casing failure (Alberty et al., 1997; Nations and Medley, 1997).

Furthermore, dissociation of gas hydrate can cause instability to an open-wellhole and oil-well platform due to reduction in shear strength of the sediment (Nations and Medley, 1997; Durham et al., 2003; Folger, 2008). In addition, the increase in pore water/gas pressure may result in inadequate cementation of the casing which may further reduce the casing stability (Nimblett et al., 2005).

2.5.3 Laboratory observation of hydrate dissociation

As discussed above the effect of hydrate dissociation in natural sediments are hypothesised on the basis of remote observations of sea floor or hydrate related drilling hazards. However, accurate prediction of the physical properties of hydrate bearing sediments during dissociation can only be gained from direct measurements in the field or in the laboratory (either on in-situ or synthesised samples). As discussed in Section 2.2, natural gas hydrate exists in deep oceanic sediments or permafrost sediments. Therefore it is often impractical to perform field testing and difficult to obtain undisturbed samples for laboratory testing. Therefore, a number of researchers have studied the properties of laboratory synthesised gas hydrate in its bulk form or within sediments.

Results from solid CO_2 hydrate have indicated that hydrate dissociates radially inwards (Uchida et al., 2000). Uchida et al. (2000) results show that hydrate dissociation below the CO_2 vapour-liquid equilibrium pressure is rapid, due to release of CO_2 gas, and breaks the hydrate into small pieces. Similarly, Circone et al. (2004) studied the effect of temperature on hydrate dissociation (solid CO_2 and CH_4) at low pressure (0.1MPa) and observed that the hydrate dissociation was mainly controlled by inwards flow of heat. Their results suggested that the rapid dissociation at a positive temperature and at pressure below the vapour-liquid equilibrium pressure of gas might be associated with faster gas transport pathways arising due to formation of free water during initial dissociation. It has also been observed that the increase in temperature of bulk hydrate is slow, due to endothermic process, until complete dissociation occurs (Pang et al., 2009; Circone et al., 2004).

Petres et al. (2000) have studied the properties of bulk methane hydrate during dissociation. Their experiment simulated the dissociation of methane hydrate plugs in a steel pipeline by the method of two-sided de-pressurisation, and their results indicated that dissociation of hydrate in a pipeline occurs radially inwards, rather than axially. In addition, their mathematical model describing hydrate dissociation radially in the pipeline was in quantitative agreement with the experimental data. The study of dissociation on bulk hydrate is important to help understand the basic processes involved in hydrate dissociation. However, bulk hydrates are mainly limited to the petroleum/chemical transportation industry.

The effect of methane hydrate dissociation in small pores was initially studied by Handa and Stupin (1992). They observed that after the initial dissociation at subzero temperature hydrate dissociated into ice and gas, encapsulating the remaining hydrate in the pores as the ice caps formed at the pore openings. Thus the remaining hydrate trapped in the interior of the pore remained stable until the pore ice melted (Handa and Stupin, 1992). Similarly, dissociation experiments conducted on bulk methane hydrate showed that up to 93% of the hydrate preserves for at least 24 hours at subzero temperature (between temperature $242\,K$ and $271\,K$, Stern et al. (2001)). A similar conclusion was deduced by Ershov and Yakushev (1992) where hydrate became stable due to formation of an ice film on its surface. They termed this phenomenon "self-preservation" behaviour. The self preservation of hydrate has also been visually observed by different researchers on natural samples (Dallimore and Collett, 1995) and on laboratory synthesised samples (Stern et al., 2001; Tohidi et al., 2001). The effect of self-preservation may be the result of ice forming an impermeable barrier on the surface of the remaining hydrate reducing release of gas and the resistance to heat transfer (Kamath and Holder, 1987). However the lack of self preservation in ethane hydrate (at temperature $268\,K$) suggests that the presence of ice as a gas shielding or sealing mechanism is insufficient to explain the behaviour of all type of hydrates (Stern et al., 2003).

Systematic dissociation measurements of methane hydrate in different pore sizes have revealed that at a given pressure the dissociation temperature is inversely proportional to the pore diameter (Uchida et al., 1999). Later Uchida et al. (2002) found that the dissociation temperature of different hydrates (CH_4, CO_2, and C_3H_8 hydrates) at a given pressure was lower than that for the bulk hydrate; for CH_4 hydrate the temperature shift was $-12.3\,K \pm 0.2\,K$ for $4\,nm$ pore diameter and the shift reduced to only $-0.5\,K$ for $100\,nm$ pores. The effect of pore size on dissociation have been studied for different types of gas hydrate and it has found that the "activity" of water has a major affect on the hydrate equilibrium condition (Uchida et al., 2002; Anderson et al., 2004). "Activity" is defined as the ratio of the vapour pressure within the pore spaces to the vapour pressure of pure water at the same temperature. Anderson et al. (2009) reported that the temperature shift of gas hydrate formation and dissociation in small pores are different; hydrate formation occurs at temperature significantly lower than the dissociation. This could be due to formation of high curvature phase interface (water-gas) during hydrate formation which can induce high capillary

pressure altering the stability condition compared to a negligible capillary interface (hydrate-gas) pressure during hydrate dissociation. Therefore, it would be expected that the different temperature shift characteristics of hydrate formation and dissociation would be observed in clay and sand sediment due to their different pore sizes.

A number of researchers have conducted laboratory experiments to simulate the transfer of hydrate bearing sediment core from a storage vessel into a laboratory measurement apparatus (Waite et al., 2008; Kneafsey et al., 2007; Rees, 2009). This was achieved by briefly de-pressurising the sample to $100\,kPa$ thereby inducing hydrate dissociation. The test results showed that redistribution of hydrate occurred within the sample. It was also observed that there was a loss of hydrate near the perimeter and a gain of hydrate in the centre of the sample. These observations suggest that even for a small change in temperature-pressure conditions outside the hydrate stability zone the properties of hydrate bearing sediment may change. Furthermore, using X-ray CT imaging, a comparison of the natural hydrate core sample under in-situ temperature-pressure conditions and after rapid de-pressurisation with subsequent freezing have revealed that during rapid de-pressurisation with subsequent freezing the structure of the hydrate cores become heavily disturbed (Priest et al., 2008). Therefore, to understand these changes the rate of hydrate dissociation at different temperature-pressure conditions is required.

Analysis of methane hydrate test data has indicated that the rate of hydrate dissociation is proportional to the particle surface area and the difference in fugacity of methane (the tendency of a gas to expand or escape) between the equilibrium pressure and dissociation pressure (Kamath and Holder, 1987; Kim et al., 1987). Similarly, the rate of ethane hydrate dissociation increases with temperature (Clarke and Bishnoi, 2000).

It has been found that the highest rate of dissociation for CO_2 hydrate occurred when pressure was reduced, rather than when temperature was increased (Uchida et al., 2000). This may be due to the low thermal conductivity of the hydrate (Warzinski et al., 2008). Similarly, X-ray CT scanning of natural hydrate bearing core sample has indicated that the pressure reduction was effectively transmitted within the sample through water, evolved from the initial dissociation (Mikami et al., 2000). In addition, the rate of hydrate dissociation can be considerably increased in the presence of an inhibitor such as methanol (Kawamura et al.,

2008).

Change in physical properties during dissociation

Few laboratory studies have been conducted to simulate the change in physical properties of hydrate bearing sediment during dissociation. The response of CO_2 hydrate bearing sands in a triaxial cell indicated that dissociation leads to an increase in pore gas pressure proportional to the volume of hydrate dissociated (Wu and Grozic, 2008). Similar results have been found in water-saturated fine-grained (Waite et al., 2008) and coarse-grained (Hu et al., 2010) hydrate bearing sediments. Test results on pressure cores of hydrate bearing sediment (Ulleung Basin, Sea of Japan) have also shown that hydrate dissociation increases the pore pressure within the sediment (Yun et al., 2011). These observations are due to the fact that in forming gas hydrates the gas is able to achieve a greater density than would have in its gaseous state (as discussed in Chapter 1).

The increase in pore pressure will lead to a reduction in effective stress, which may reduce the sediment strength (Yun et al., 2006; Francisca et al., 2005). In addition, Sakamoto et al. (2007) studied the change in permeability of hydrate bearing sand sediment during dissociation using laboratory experiments and numerical modelling. The experiment was carried out by injecting hot-water into the hydrate bearing sand sediment. The results indicated an increase in sediment permeability during hydrate dissociation. Similarly, Kumar et al. (2010) also observed the increase in permeability of hydrate bearing sediment during dissociation. This could be due to conversion of solid hydrate into gas and water.

The effect of dissociation varies with the type of hydrate present within a sediment. Dissociation of CO_2 hydrate produces a lower pore pressure change than CH_4 hydrate, due to higher solubility of CO_2 in water (Circone et al., 2003). As discussed in Section 2.1, in nature the most common hydrate is methane hydrate but many researchers have studied other type of hydrates such as CO_2, ethane, THF, etc. Therefore, these results may not be directly applicable to predict the effect of dissociation of methane hydrate bearing sediments.

2.5.4 Numerical modelling

A number of different numerical models have been developed to assess the effect of hydrate dissociation with respect to the rate of heat and mass transfer, and the change in properties of gas hydrate both in the bulk form and in hydrate bearing sediment.

A basic numerical model of hydrate dissociation through temperature increase was developed by Selim and Sloan (1985), which showed that heat transferred from an applied surface to the rest of the sample during hydrate dissociation as a moving boundary process. They assumed that the water evolved from dissociation is instantaneously drained out. Later Ullerich et al. (1987) showed that the Selim and Sloan (1985) numerical model of hydrate dissociation fits within 10% of their experimental data. These studies are only useful to model solid hydrate dissociation. For natural sediments, the rate of heat and mass transfer are strongly influenced by the presence of the surrounding sediments (Selim and Sloan, 1989). It should be noted that these models have not considered the kinetics of the hydrate dissociation. Since hydrate dissociation is endothermic, heat must be absorbed during dissociation process. On the basis of phase equilibrium of hydrate and kinetic theory of gases, Wilder and Smith (2002) developed a mathematical model to predict the heat flux necessary to keep the sediment temperature constant during hydrate dissociation for constant rate of gas production from hydrate.

Similarly, an one-dimensional numerical model of hydrate dissociation in marine sediments through de-pressurisation was studied by Ahmadi et al. (2004). They considered the heat and mass transfer within sediment released from the hydrate dissociation. Their results indicated that the rate of hydrate dissociation is not sensitive to small variation in the reservoir temperature. However, the results from an axisymmetric model indicated that the rate of dissociation is sensitive to reservoir temperature (Ahmadi et al., 2007). These different models show the importance of using the right type of model in predicting the rate of dissociation.

As discussed in Section 2.5.3, hydrate dissociation leads to an increase in pore gas pressure within sediment due to the gas being able to achieve a denser packing in gas hydrates than it could occupy in its gaseous state. A number of researchers have also developed numerical models to predict the pore pressure evolution due to hydrate dissociation (Xu and Germanovich, 2006; Ahmadi et al., 2007;

Kwon et al., 2008). It has been predicted that the rise in pore pressure is proportional to the rate of dissociation, and inversely proportional to the total stress and the permeability of the sediment (Xu and Germanovich, 2006). A parametric study of methane hydrate in oceanic sediments has also suggested that the rate of dissociation depends on the permeability of the dissociated hydrate bearing sediments and the adjacent sediments (Tsimpanogiannis and Lichtner, 2007). These models demonstrate that low permeability sediments, such as clays, may develop extremely high pore pressure during hydrate dissociation, which may lead to sediment fracturing.

A thermodynamic analysis was carried out to study temperature rise in hydrate bearing sediment caused by pumping hot oil through hydrate bearing sediment in ocean sediments (Briaud and Chaouch, 1999). The parameters considered were methane gas, methane hydrate with a liquid phase with different thermal properties such as thermal conductivity, specific heat capacity and thermal diffusivity. For the disseminated hydrates equivalent thermal properties were considered and it was assumed that these properties did not change with temperature or dissociation. It was found that the time to increase the temperature in hydrate is greater if latent heat is considered. This showed the importance of using latent heat of gas hydrate in numerical analysis, as the latent heat of hydrate represents an additional heat sink for the heat source.

It is important to note that all the above models are based on the assumption that hydrate bearing sediments are undeformable and remain unaffected during hydrate dissociation. Thus the influence of hydrate dissociation on the strength or deformation property of hydrate bearing sediments has been neglected. However, these effects may be important, especially if the stability of the oil/gas well pipeline or platform in a hydrate bearing sediment is to be correctly assessed.

Several numerical models have been developed to describe the change in stress or deformation of hydrate bearing sediments with dissociation. One such numerical formulation was described by Jayasinghe and Grozic (2008). The problem was modelled as a 'Stefan' like moving boundary problem considering heat transfer in form of conduction only in an axisymmetric cylindrical geometry. Their model calculates the change in stress and strain within the sediment on the basis of volumetric strain caused by dissociation of solid hydrate into gas and water. In addition, Kwon et al. (2010) modelled hydrate dissociation around a pipe carrying hot oil through a hydrate bearing sediment in a two-dimensional axisymmetric

model. The model considered compressibility of sediment and pore fluids to calculate pore pressure evolution during dissociation however they did not account for latent heat of hydrate dissociation. Similar to Kwon et al. (2010) model, Pallipurath (2007) modelled hydrate dissociation around a pipe in an axisymmetric model. The model considered latent heat of hydrate formation/dissociation and validated settlement of marine sediment. However, these models did not account for the effect of dissociation on the strength/stiffness properties of hydrate bearing sediment.

Freij-Ayoub et al. (2007) developed a numerical model of a well-bore stability in hydrate bearing sediment. The model coupled the thermodynamic stability of hydrates within porous media to thermal and fluid transfer and to mechanical deformation. The heat transfer, due to hotter fluid flow in the well-bore and induced hydrate dissociation, were modelled by Fourier's Law of heat conduction. The fluid flow, due to pressure gradient generated during dissociation, was described by Darcy's Law. Sediment formation was modelled as a poro-elastic material, and the failure criteria was represented by a Mohr-Coulomb model. As hydrate dissociates within the sediment pores, it was assumed that a linear reduction of the sediment strength occurred, and it was modelled as a linear reduction of the grain cementation (or, cohesion) with hydrate dissociation. However, it was considered that dissociation takes place under isothermal condition, thus the latent heat of hydrate was not considered, which reduces the rate of hydrate dissociation.

2.6 Summary

This chapter has presented a review of the literature of gas hydrate and its effect on sediment properties. It has been observed that the strength and stiffness properties of hydrate bearing sediments depend on the morphology of hydrate within the sediment. However, it can be seen that there is a lack of current understanding in the area of gas hydrate dissociation, in particular the effect of hydrate dissociation on the stiffness/strength properties.

At present, hydrate dissociation in natural environments and their effects are hypothesised from remote observation of sediments where scars left by natural events (landslides, etc.) or hazards occurred during drilling operations. Accurate prediction of the properties of hydrate bearing sediments during dissociation can

be gained from field testing or laboratory testing on in-situ samples. Due to difficulty in performing field testing most of researchers have conducted laboratory research. However, most of the laboratory research have been concerned with hydrate formation. Few research have been concerned with hydrate dissociation, in which most of the research have been conducted to study the rate of dissociation of bulk hydrates or hydrates in small pores.

Numerical modelling of hydrate bearing sediment can be used to assess the impact of drilling activities on sediment behaviour. Due to lack of experimental data, these numerical models have assumed that the hydrate bearing sediment properties are constant or vary linearly with the volume of hydrate dissociated. However understanding the risk of drilling through gas hydrate sediments, using numerical models, can only be effective if a detailed knowledge of sediment behaviour during dissociation is available, in particular stress/strain behaviour. At present, no detailed characterisation of hydrate dissociation and its influence on sediment properties are available.

To fully understand the effect of dissociation on the behaviour of methane hydrate bearing sediments with regard to the submarine slope stability, well-bore stability or oceanic petroleum platform stability requires well-controlled laboratory experiments to be conducted on methane hydrate bearing sediments. Such tests results can also be used to validate numerical models.

Chapter 3

Experimental Apparatus and Methodology

Chapter 2 highlighted that gas hydrates exist in deep-water oceanic sediments, or deep permafrost sediments. Therefore it is not possible or practical to perform field testing and it is also difficult to obtain undisturbed in-situ samples for testing. Therefore a series of tests have been conducted on laboratory-prepared methane hydrate bearing sand sediments to investigate the change in physical properties of these sands during formation and dissociation of methane hydrate.

This chapter begins with a brief description of the experimental apparatus used to synthesise and test gas hydrate bearing sediments. The calibration of the apparatus and data reduction techniques employed to enable the properties of the sediment to be derived are discussed. In addition a description of the different testing methodologies used in different experiment, where methane hydrate was formed using the excess methane gas in an unsaturated sand specimen, are given. These experiments were conducted to examine the formation and the dissociation characteristics of methane hydrate in sands under drained and undrained conditions.

3.1 Test apparatus and its calibration

The resonant column apparatus, which measures the small strain stiffness of soils and its material damping, is routinely used in soil mechanics. In its standard form it works under low stress conditions $<= 1\,MPa$ and at room temperature ($20°C$). Since gas hydrate exists under restricted thermobaric conditions, high pressures (up to $20\,MPa$) and/or low temperatures (down to $-20°C$) are required to form hydrate in the laboratory (Stern et al., 1996). The Gas Hydrate Resonant Column (GHRC) apparatus was developed at the University of Southampton, and is capable of performing resonant column testing under thermobaric conditions where gas hydrates are stable.

3.1.1 Gas Hydrate Resonant Column Apparatus (GHRC)

The Gas Hydrate Resonant Column (GHRC) was developed within the School of Civil Engineering with GDS Instruments Ltd, UK (Figure 3.1). The apparatus consists of an environmental chamber used to replicate gas hydrate stability conditions, and the resonant column drive system.

The environmental chamber houses the pressure cell within a temperature controlled chamber, allowing temperature control from -20^0C to $+50^0C$ with a resolution of 0.1^0C. The pressure cell allows gas cell pressure, gas and water back pressure, and suction to be applied to the specimen. The pressure cell is rated to $25\,MPa$, to allow for hydrate formation.

The resonant column apparatus has been successfully used for more than forty years, and has become a standard method (ASTM-D4015, 1992) to determine the dynamic shear stiffness, longitudinal stiffness and the corresponding damping of soil specimen at very small strains (between 10^{-6} and 10^{-2} *per unit* (*p.u.*)). Due to the non-destructive nature of the resonant column test the same specimen can be tested at different strain levels and at different confining pressures. The principle of the resonant column apparatus is based on the vibration of an elastic, homogeneous, isotropic cylinder by either torsional, flexural, or longitudinal vibration. By measuring the induced vibration, using an accelerometer and varying the applied frequency, the resonance frequency of the system can be determined.

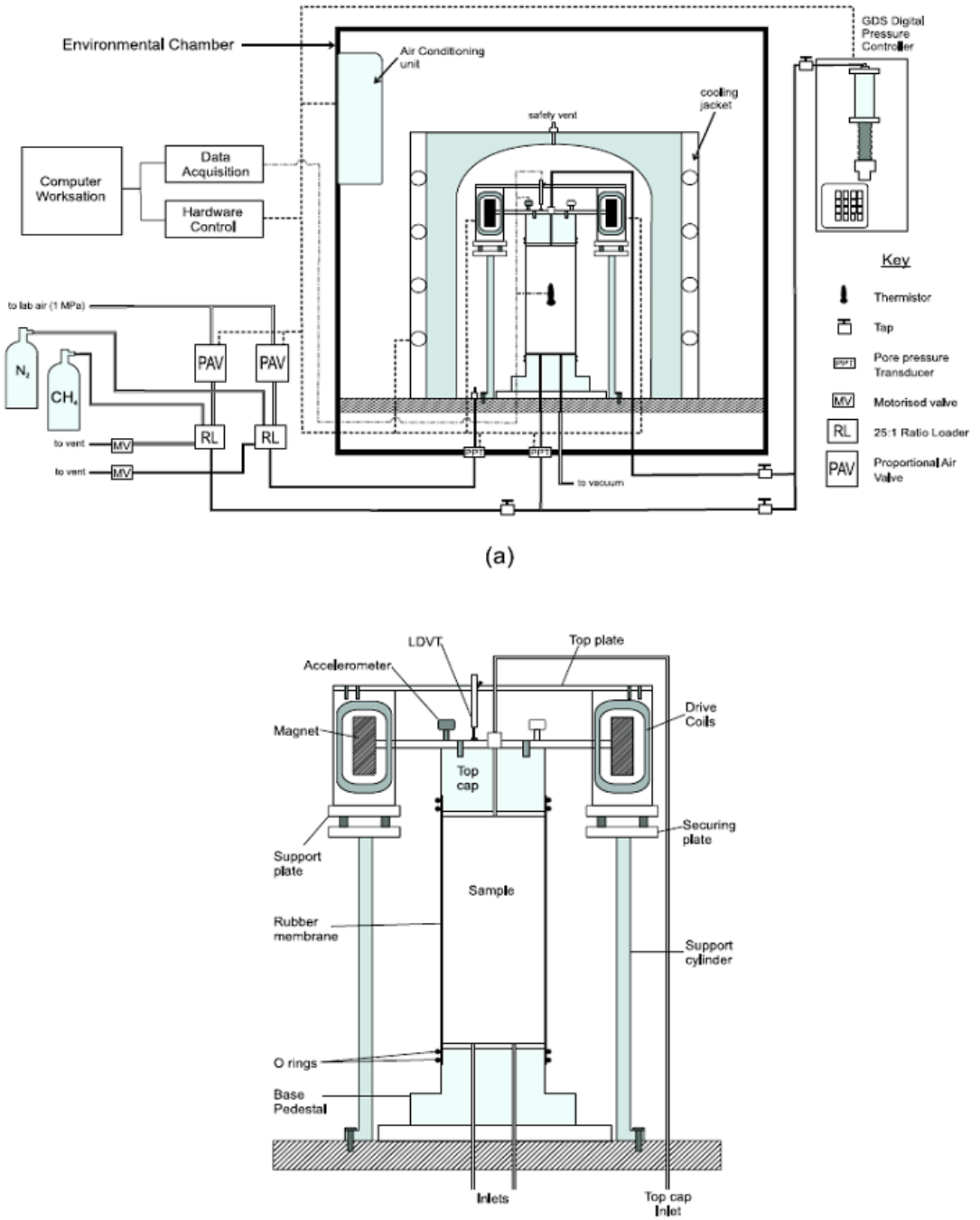

Figure 3.1: *(a) Schematic drawing showing the general layout of the gas hydrate resonant column (GHRC) apparatus including pressure and temperature control systems. (b) A close-up cross section of the resonant column drive system in the GHRC. Adapted from Clayton et al. (2005).*

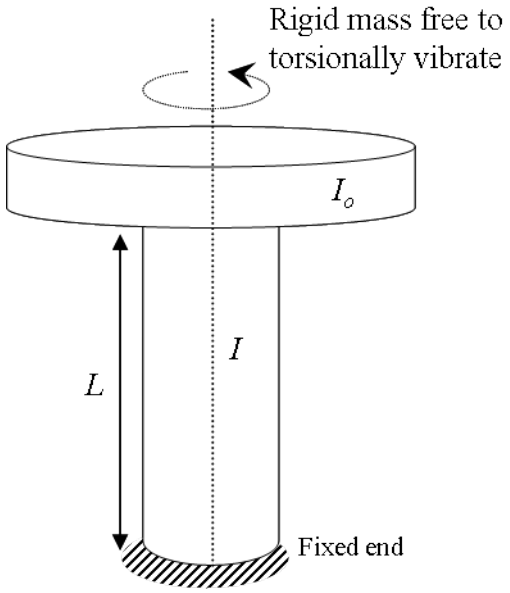

Figure 3.2: *Idealised representation for the Stokoe resonant column system. Redrawn from ASTM-D4015 (1992).*

Resonance frequency refers to the frequency at which the maximum amplitude of vibration is observed (Richart et al., 1970).

There are a number of different designs of the resonant column apparatus. The resonant column system in the GHRC is based on the Stokoe resonant column. In this device, one end of the specimen is held rigidly fixed at the base whilst the other end is free (Figure 3.2) and excited using an electromagnetic vibration system. For interpreting the fixed-free resonant column test data, the specimen is assumed to be homogeneous, isotropic and elastic. It is assumed that only the specimen and the attached drive mechanism vibrate. These are idealised as a single degree of freedom (SDOF) system. The GHRC drive system was modified to enable high stiffness material like gas hydrate to be tested by stiffening the base pedestal and the drive system. In addition to its torsional response, the flexural response of a specimen can be determined in the GHRC to calculate flexural stiffness of the specimen, as described by Cascante et al. (1998).

The following measurements were used in the resonant column apparatus:

- Resonant frequency in torsional vibration
- Resonant frequency in flexural vibration
- Torsional strain

- Flexural strain
- Damping ratio

Resonant frequency in torsional vibration:

In torsional excitation, the resonant column system is considered as a solid cylindrical bar subjected to pure torsion (Figure 3.2). The solution for the first mode of torsional vibration is given as (Richart et al., 1970):

$$\frac{I}{I_0} = \beta \tan \beta \tag{3.1}$$

where

$$\beta = \frac{\omega_n l}{V_s} \tag{3.2}$$

ω_n is the natural circular frequency in torsional vibration of the specimen; I_0 is the total mass moment of inertia at the free end of the specimen including mass moment of inertia of the drive system; l, I and V_s are length, mass moment of inertia and shear wave velocity of the specimen respectively.

The shear modulus (G) of a specimen can be computed from the known density (ρ) of the specimen,

$$G = \rho V_s^2 \tag{3.3}$$

Resonant frequency flexural vibration:

In flexural excitation, the resonant column system is considered as a flexing cantilever beam with a lumped mass attached at the free end. Figure 3.3 illustrates the idealisation of the resonant column as a cantilever beam. Utilising Rayleigh's energy method, Cascante et al. (1998) calculated equivalent mass of the lumped mass at the top of the specimen ($\sum m_i \, h(h_0, h_{1i})$), and showed that the natural frequency of the specimen in the flexural mode of vibration can be found from:

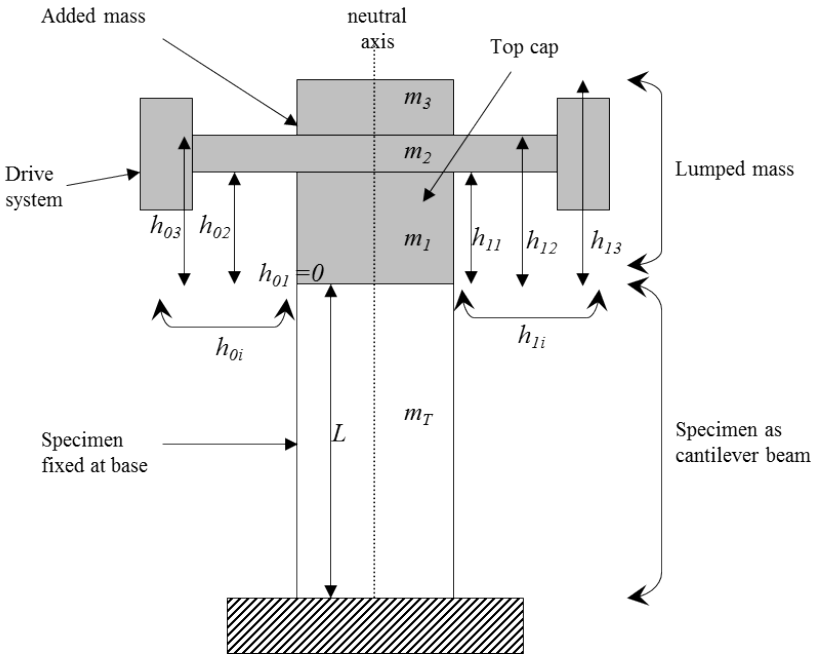

Figure 3.3: *Representation of the resonant column system as a cantilever beam. The specimen is idealised as a beam, and top cap, drive mechanism and added mass as a lumped mass attached at the top of the specimen.*

$$\omega_f^2 = \frac{3\,E\,I_b}{\left[\frac{33}{140}\,m_T + \sum m_i\,h(h_0, h_{1i})\right]\,l^3} \tag{3.4}$$

where,

$$h(h_{0i}, h_{1i}) = 1 + \frac{3\,(h_{1i} + h_{0i})}{2\,l} + \frac{3}{4}\,\frac{(h_{1i}^2 + h_{1i}h_{0i} + h_{0i}^2)}{l^2} \tag{3.5}$$

ω_f is the natural circular frequency in flexural vibration of specimen, I_b and E are the second moment of inertia and Young's modulus of the specimen respectively. h_{0i} and h_{1i} are the bottom and the top heights respectively of $i\,th$ mass (m_i), measured from the top of the specimen (Figure 3.3); and m_T is the mass of the specimen.

Torsional strain:

In the GHRC apparatus torsional strain is calculated by assuming a cylindrical shaped specimen subjected to pure torsion, with an angle of rotation (θ) as shown in Figure 3.4. Angle of rotation (θ) varies along the axis of the specimen such

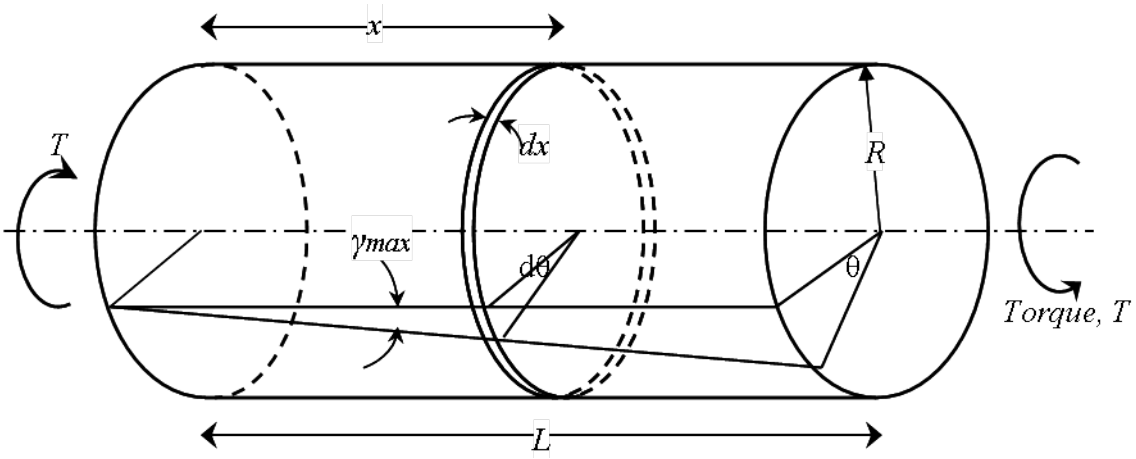

Figure 3.4: *Diagram showing a cylindrical bar subjected to pure torsion. Redrawn from Richart et al. (1970).*

that the angular rotation $\left(\phi = \frac{d\theta}{dx}\right)$ is constant. Using the theory of elasticity, shear strain at the outer surface of the specimen ($\gamma_{x(outer)}$) can be defined as:

$$\gamma_{x(outer)} = \frac{r\, d\theta}{dx} = r\, \phi \tag{3.6}$$

where r is radius of the specimen, θ is the angle of rotation and ϕ is the angular rotation during torsion.

Since the rate of rotation (ϕ) is constant for pure torsion, Equation 3.6 gives a constant strain for given R. Therefore in pure torsion, torsional strain is constant along the axis of rotation such that torsional strain is zero at the centre and maximum at the edge of the specimen (Figure 3.4). Using Equation 3.6, maximum strain can be calculated as;

$$\gamma_{max} = r\, \frac{\theta}{l} \tag{3.7}$$

where, l is length of the specimen.

To take into account of variation in torsional strain within the specimen, Chen et al. (1979) recommended using $4/5\, r$, instead of r, to calculate the average strain in the specimen, such that

$$\gamma_{av} = \frac{0.8\, r\, \theta}{l} \tag{3.8}$$

In the GHRC, an accelerometer is used to measure the acceleration (ac) of the specimen. Acceleration is calculated from the voltage output (V) multiplied by a constant Z ($ac = Z \times V$). For the GHRC accelerometer, Z is given as $\frac{2\sqrt{2}g}{5}$ (Priest, 2004), where g is the gravitational acceleration constant ($9.81\, m/s^2$). For simple harmonic motion, $ac = \omega^2 x = (2\pi f)^2 x$, where x is the rotational distance. Therefore,

$$(2\pi f)^2 x = \frac{2\sqrt{2}\, g}{5}\, V \tag{3.9}$$

For pure torsional vibration x is a function of angle of rotation and distance of the accelerometer from the axis of rotation ($= \theta l'$, where l' is the distance of the accelerometer from the centre axis of the specimen $= 0.03625m$ for the GHRC). Using Equation 3.9, the angle of rotation (θ) can be written as,

$$\theta = \frac{2\sqrt{2}\, g}{5} \frac{V}{(2\,\pi\, f)^2\, l'} \tag{3.10}$$

and substituting into 3.8 leads to

$$\gamma_{av} = \frac{1.56\, V\, d}{f^2\, l} \tag{3.11}$$

where d is the diameter of the specimen.

Flexural strain:

In flexural vibration it is assumed that the specimen undergoes pure bending. Using the theory of elasticity for pure bending of a cantilever beam with a circular cross section, the average strain can be defined (Priest, 2004) as,

$$\epsilon_{avg} = \frac{4}{\pi}\, r\, l\, \alpha_c \tag{3.12}$$

where r and l are radius and length of the specimen respectively, and α_c is a constant. For the GHRC, constant α_c can be derived (Priest, 2004) using,

$$\alpha_c = \frac{0.141\,V}{f^2\,l\,[2\,l + 3\,(x - l)]} \tag{3.13}$$

Therefore the average strain during flexural vibration in the GHRC can be calculated from,

$$\epsilon_{avg} = \frac{0.18\,V\,r}{f^2\,l\,[2\,l + 3\,(x - l)]} \tag{3.14}$$

Damping ratio

Damping ratio provides a measurement of the energy dissipated during vibration divided by the energy stored in the system. In the GHRC apparatus, damping can be calculated using the half-power bandwidth and the free vibration decay (FVD) methods. The half-power bandwidth method is based on the frequency response curve, and consists of obtaining the resonance frequency and two frequencies either side of the resonance frequency that have the response amplitudes equal to the maximum amplitude divided by $\sqrt{2}$ (Figure 3.5). The method assumes that the specimen damping is less than 20% for a single-degree-of-freedom system (Olmos and Roesset, 2010; Papagiannopoulos and Hatzigeorgiou, 2011). The free vibration decay (FVD) method considers the relationship between successive cycles of the peak amplitude when a specimen is allowed to vibrate freely at the resonance frequency. Figure 3.6 shows a typical plot of specimen response with time during FVD.

The value of maximum amplitude decreases as the specimen damping increases (Richart et al., 1970), and thus a broader frequency sweep is required to calculate specimen damping using the half-power bandwidth method. In contrast to the half-power bandwidth method, the free vibration decay (FVD) method requires the resonance frequency which can be obtained from a narrow frequency sweep. In this research FVD method is used to calculate specimen damping since this is suitable for quick measurement using the resonant column apparatus.

The FVD method is derived assuming free vibration of a single-degree-of-freedom

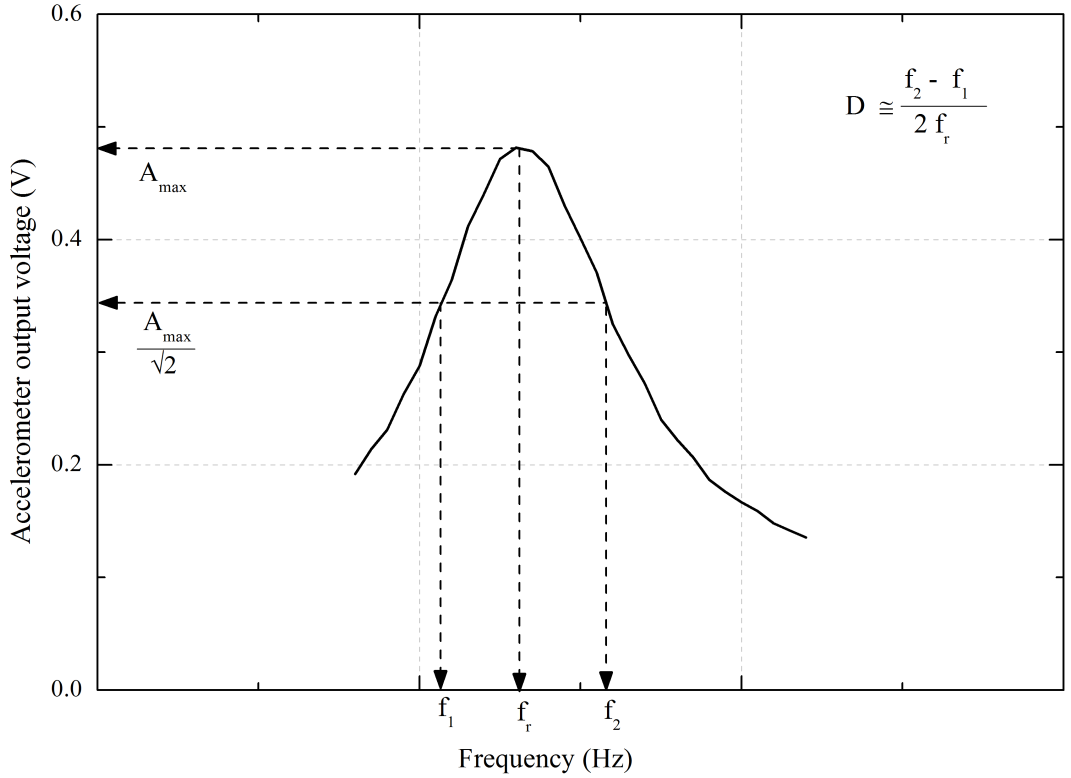

Figure 3.5: *Typical plot of the frequency sweep for a specimen. Also showing the resonance frequency at the peak amplitude (A_{max}) and two frequencies either side of the resonance frequency that has the response amplitude $A_{max}/\sqrt{2}$.*

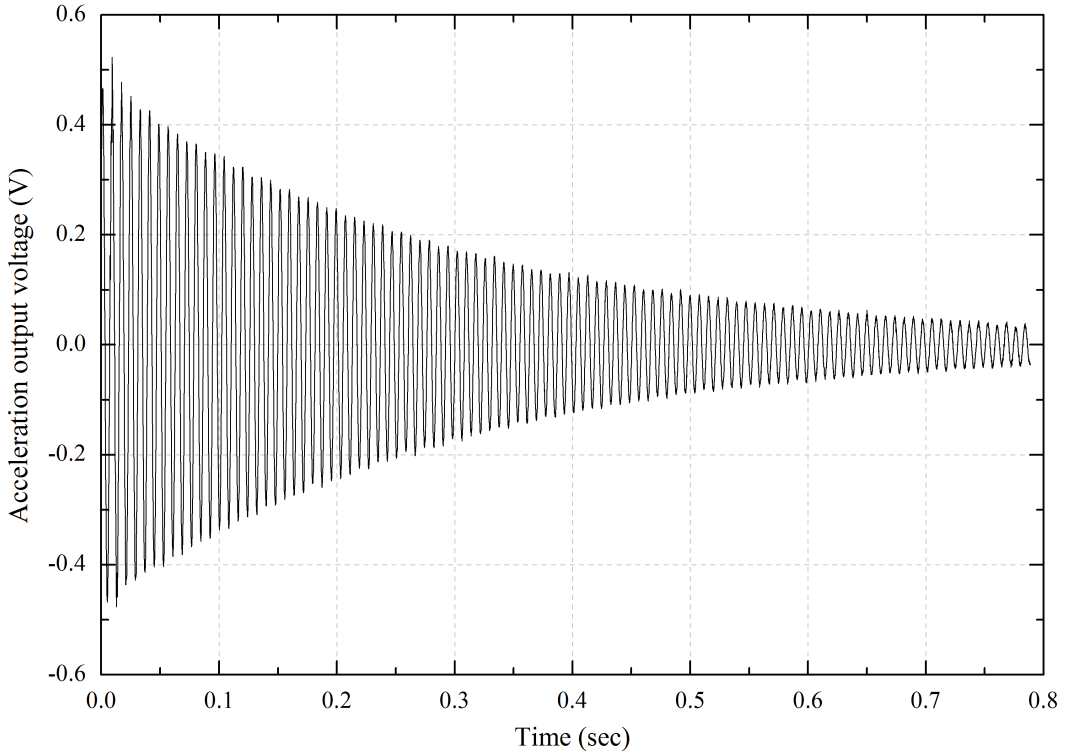

Figure 3.6: *Typical plot of specimen response (voltage amplitude) with time during free vibration damping decay.*

(SDOF) system in an under-damped condition. The displacement (z) of a SDOF system at any time (t) in an under-damped condition can be derived as (Richart et al., 1970);

$$z = e^{(-\omega_n D\, t)} \left(C_1\, sin\, \omega_n t \sqrt{1 - D^2} + C_2\, cos\, \omega_n t \sqrt{1 - D^2} \right) \tag{3.15}$$

where, C_1 and C_2 are arbitrary constants, D is damping, and ω_n is un-damped natural frequency of the system. Equation 3.15 is an equation for a harmonic oscillation with an amplitude $\left(e^{(-\omega_n D\, t)}\right)$ and natural frequency $\left(\omega_n \sqrt{1 - D^2}\right)$. This shows that the amplitude of the oscillation will decay exponentially with time (as shown in Figure 3.6). The natural frequency for an under-damped system (ω_d, damped natural frequency) and the natural frequency for a system in an un-damped condition are related as,

$$\omega_d = \omega_n \sqrt{1 - D^2} \tag{3.16}$$

The successive peaks of the oscillation in Figure 3.6 can be determined using Equation 3.15. Consider that the successive peaks z_1 and z_2 occur at times t_1 and t_2 respectively, such that

$$z_1 = e^{(-\omega_n D t_1)} \left(C_1 \, sin \, \omega_n t_1 \sqrt{1 - D^2} + C_2 \, cos \, \omega_n t_1 \sqrt{1 - D^2} \right) \tag{3.17}$$

$$z_2 = e^{(-\omega_n D t_2)} \left(C_1 \, sin \, \omega_n t_2 \sqrt{1 - D^2} + C_2 \, cos \, \omega_n t_2 \sqrt{1 - D^2} \right) \tag{3.18}$$

t_1 and t_2 are successive peaks so $t_2 = t_1 + 2\pi/\omega_d$, thus

$$sin \, \omega_d t_2 = sin \, (\omega_d t_1 + 2\pi) = sin \, \omega_d t_1 \tag{3.19}$$

$$cos \, \omega_d t_2 = cos \, (\omega_d t_1 + 2\pi) = cos \, \omega_d t_1 \tag{3.20}$$

Using Equations 3.17 to 3.20, the ratio of successive peaks can be represented as;

$$\frac{z_1}{z_2} = e^{\left(\omega_n D \frac{2\pi}{\omega_d} \right)} \tag{3.21}$$

and substituting Equation 3.16 into Equation 3.21 leads to,

$$\frac{z_1}{z_2} = e^{\left(\frac{2\pi D}{\sqrt{1 - D^2}} \right)} \tag{3.22}$$

The natural log of the ratio between two successive peaks ($= ln \, (z_1/z_2)$) is known as the logarithmic decrement (δ), and damping can be calculated by determining the logarithmic decrement. Richart et al. (1970) suggested that the logarithmic decrement (δ) can be calculated from any two consecutive peaks z and z_n through,

$$\frac{1}{n-1} \, ln \, \frac{z_1}{z_n} = \frac{2\pi D}{\sqrt{1 - D^2}} \tag{3.23}$$

and,

$$\delta = \frac{1}{n-1} \, ln \, \frac{z}{z_n} \tag{3.24}$$

$$ln \, z_n = -(n-1) \, \delta + ln \, z \tag{3.25}$$

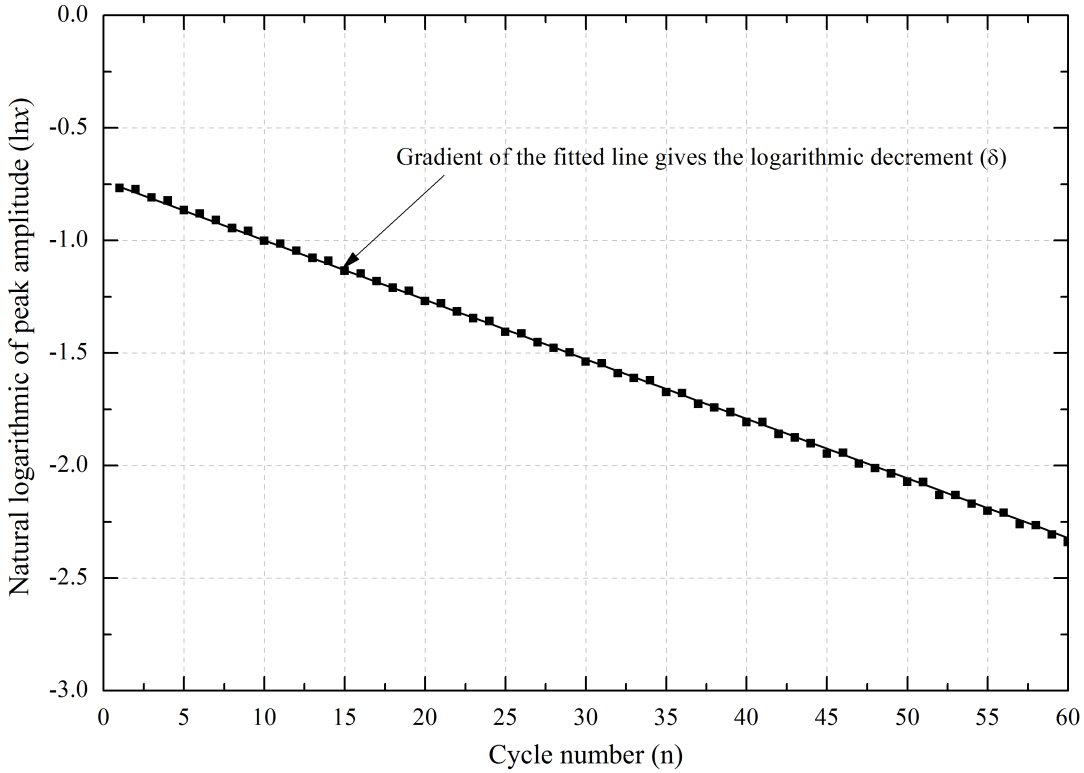

Figure 3.7: *Plot of natural logarithmic of peak amplitude against cycle number for a free vibration decay test for an aluminium calibration rod. Slope of the fitted line gives the logarithmic decrement for the specimen.*

It can be seen that Equation 3.25 is the equation of a straight line. Therefore, the logarithmic decrement (δ) can be calculated by fitting a straight line through log of peak amplitude vs cycle number as shown in Figure 3.7. Damping is then calculated by substituting Equation 3.24 into Equation 3.23, as:

$$D = \sqrt{\frac{\delta^2}{4\,\pi^2 + \delta^2}} \tag{3.26}$$

In geophysical surveys, the energy dissipation is mainly represented by the quality factor (Q). The quality factor is defined as ratio of the energy stored with the energy dissipated. The reciprocal of the quality factor is known as attenuation ($1/Q$), and is related to the damping as,

$$\frac{1}{Q} = 2\,D \tag{3.27}$$

3.1.2 Calibration of gas hydrate resonant column apparatus

To derive G and E in the resonant column apparatus using Equations B.2 and 3.4 respectively, several geometric properties of the apparatus, such as the mass polar moment of inertia, centre of gravity, and area moment of inertia of the drive system are required. The inherent apparatus damping is also required to calculate the true damping of the specimen. These geometric properties and damping can more easily be obtained experimentally using calibration bars because of the complex geometry of the drive system.

A total of four different aluminium calibration bars were used in the GHRC apparatus, to represent the range of the frequencies that may be expected when testing gas hydrate bearing sediments. Table 3.1 gives the geometrical properties of all the calibration bars, and Table 3.2 gives the properties of aluminium.

Calibration bar (No.)	Bar stem dimensions		Bar top-disc dimensions	
	Height (mm)	Diameter (mm)	Height (mm)	Diameter (mm)
# 1	100.00	22.02	15.12	69.99
# 2	100.12	27.99	15.06	69.99
# 3	99.99	31.99	15.10	69.99
# 4	100.02	35.93	11.11	70.09

Table 3.1: *Geometry of aluminium calibration bars used in the GHRC apparatus.*

Properties	source[a]	source[b]
Density (kg/m^3)	2699	2690
Young's modulus (GPa)	69.0	68.9 ± 0.7
Shear modulus (GPa)	25.7	25.6 ± 0.4
Poisson's ratio	0.34	~0.34

[a] Northern Aluminium Company Limited (1959)

[b] Billy (1980)

Table 3.2: *Properties of aluminium.*

Mass moment of Inertia (I_0) from torsional vibration

To derive the mass polar moment of inertia of the drive system, an aluminium calibration bar is placed in the resonant column (as shown in Figure 3.8) and its resonance frequency is obtained during torsional vibration. The test is then repeated by adding masses to the top of the drive system, and determining the resonant frequency with each added mass. The resonance frequency and the mass polar moment of inertia can be related using the following relationship:

$$\omega_n = \sqrt{\frac{k}{I_o + I_{am}}} \tag{3.28}$$

or

$$I_{am} = \frac{k}{\omega_n^2} + I_o \tag{3.29}$$

where k is stiffness of the calibration bar, I_0 is the mass moment of inertia of the drive system, and I_{am} is mass moment of inertia of the added mass (including top disc) at top of the calibration bar, and ω_n is natural circular frequency in torsional vibration of the bar. As noted in Equation 3.16, $\omega_n \backsimeq \omega_d$ for an under-damped system with small damping ($<= 10\%$).

Since Equation 3.29 is in the form of a standard linear equation, plotting the values of I_{am} as a function of $1/\omega_n^2$ for each calibration bar gives an intercept on the y-axis which gives I_0 (Figure 3.9) and the gradient of the fitted line is the stiffness of the bar. The shear velocity and shear modulus for the aluminium bar can then be obtained by using Equations B.2 to 3.3. Figure 3.9 shows the results obtained for each calibration bar. Using Equation 3.29, Figure 3.10 shows the values of I_0 obtained for all the calibration bars.

Table 3.3 shows the shear velocity and shear modulus for the aluminium bars obtained from Equations B.2 to 3.3 using I_0 from Figure 3.10. It can be seen in Table 3.3 that calculated shear modulus does not correspond to the shear modulus of aluminium ($25.2 - 26.0\,GPa$ in Table 3.2), and has an error of up to 13%. Also noted from Figure 3.10, the value of I_0 is not constant but increases as the stiffness of the calibration bar increases, although I_0 is a geometric property of the drive system and should be constant. A number of hypotheses have been given for the variation of geometric properties of the drive system with frequency

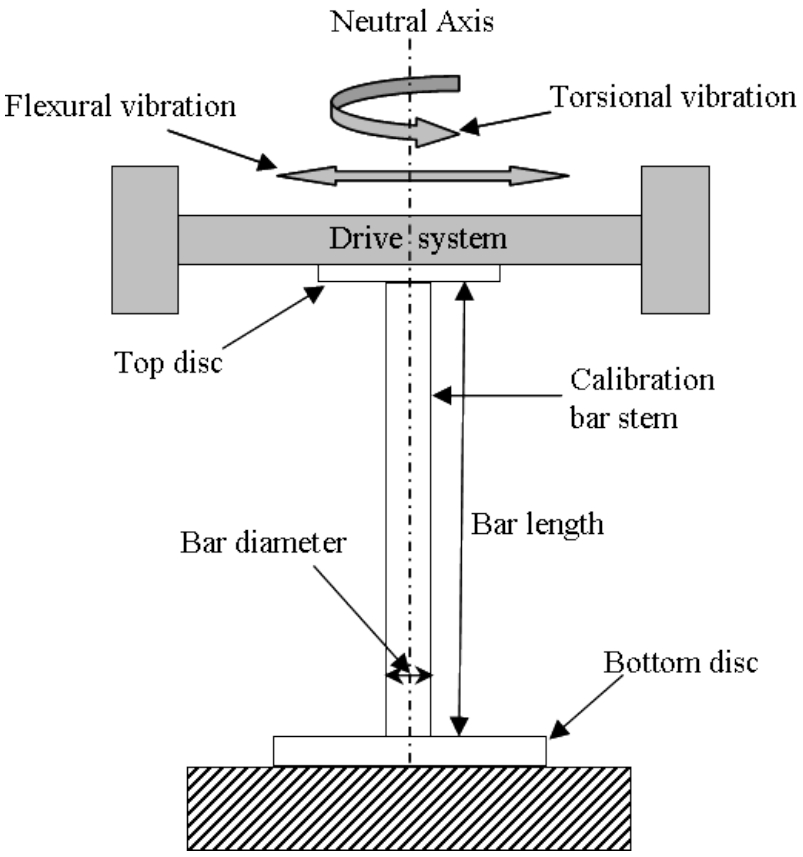

Figure 3.8: *Schematic drawing showing an aluminium calibration bar placed in the resonant column apparatus to conduct calibration test.*

Calibration bar no.	Frequency (Hz)	Intercept method (I_0 using equation in Figure 3.10)			
		$I_0\,(Kgm^2)$	$V_s\,(m/s)$	$G\,(GPa)$	error (%) in G
# 1	201	3.367×10^{-3}	2970.4	23.7	7.4 ± 1.4
# 2	310.2	3.631×10^{-3}	2947.8	23.4	8.8 ± 1.4
# 3	389	3.962×10^{-3}	2951.3	23.4	8.5 ± 1.4
# 4	461	4.366×10^{-3}	2902.4	22.7	11.6 ± 1.4

Table 3.3: *Shear velocity and shear modulus for aluminium calibration bars obtained using I_0 derived from equation of line given in Figure 3.10.*

of vibration (Clayton et al., 2009). Such as;

Effect of calibration bar design: Numerical analyses of the resonant column apparatus have shown that the ratio of diameter of the calibration bar stem and the metal plates at both ends of the bar considerably affect the torsional stiffness of the overall bar (Clayton et al., 2009). This is due to the stress distribution at the junction of the calibration bar and the metal plates. Clayton et al. (2009) showed that as the ratio of the diameter of the bar stem to the top (or bottom) disc increases the calculated stiffness decreases, and for the ratio ~0.4 the error is up to ~5%.

Compliance: The solutions of torsional (Equation B.2) and flexural (Equation 3.4) vibrations rely on the fact that only the calibration bar is deforming. If there is compliance between bar and the base pedestal, or bar and drive system, the resonant frequency obtained may not be the true resonant frequency. To ensure rigid fixity the GHRC apparatus was modified to increase base fixity by using eight M5 bolts (Priest, 2004), instead of four M4 bolts that was used in the standard Stokoe resonant column apparatus.

To eliminate the error in calculating the specimen stiffness, a regression analysis was carried out to calculate I_0 by substituting known material properties of aluminium (from Table 3.2) into Equations B.2 and 3.2 as suggested by Priest (2004). Figure 3.11 shows the values of I_0 with frequency derived using the regression method. Table 3.4 shows the error associated using the regression analysis (the value of I_0 is taken corresponding to the resonant frequency from Figure 3.11) which can be seen to be acceptably small.

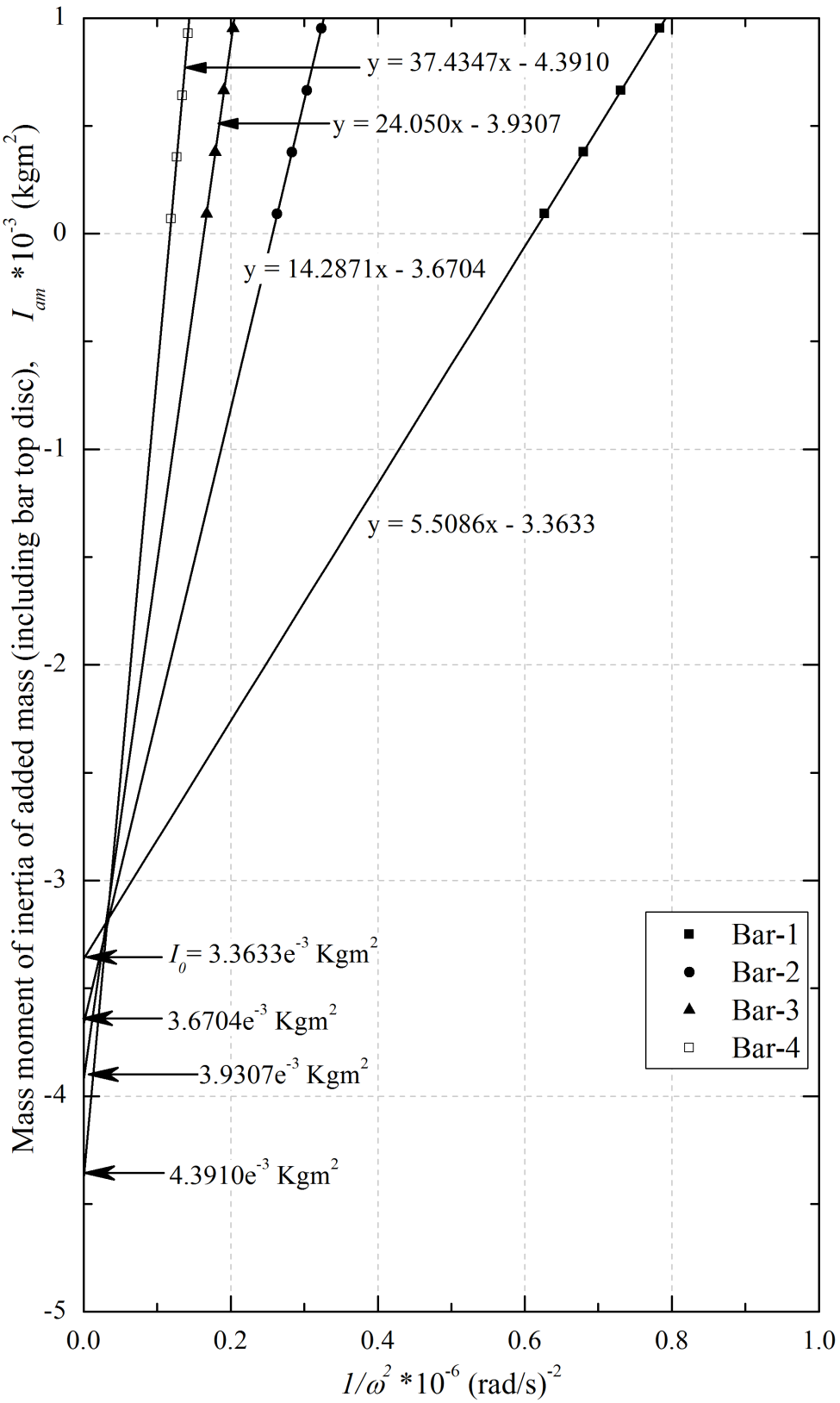

Figure 3.9: *Torsional calibration results of the GHRC using four aluminium bars, where intercept of each fitted line represents the value of I_o for the respective bars.*

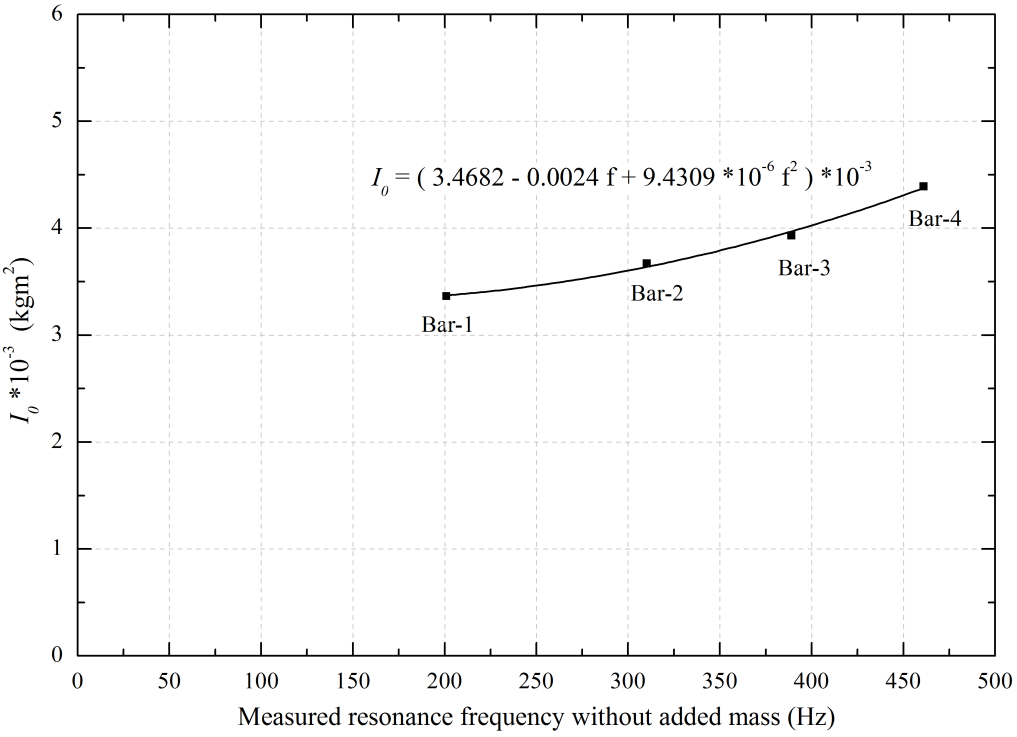

Figure 3.10: *The value of I_o for different resonant frequencies obtained using the added mass method from Figure 3.9.*

Calibration bar no.	Frequency (Hz)	Regression method (I_0 using equation in Figure 3.11)			
		$I_0\,(Kgm^2)$	$V_s\,(m/s)$	$G\,(GPa)$	error (%) in G
# 1	201	3.647×10^{-3}	3088.8	25.7	-0.3 ± 1.5
# 2	310.2	3.960×10^{-3}	3075.1	25.4	0.6 ± 1.5
# 3	389	4.390×10^{-3}	3102.6	25.9	-1.1 ± 1.5
# 4	461	4.932×10^{-3}	3081.7	25.5	0.2 ± 1.5

Table 3.4: *Shear velocity and shear modulus for aluminium calibration bars obtained using I_0 derived from equation of line in Figure 3.11.*

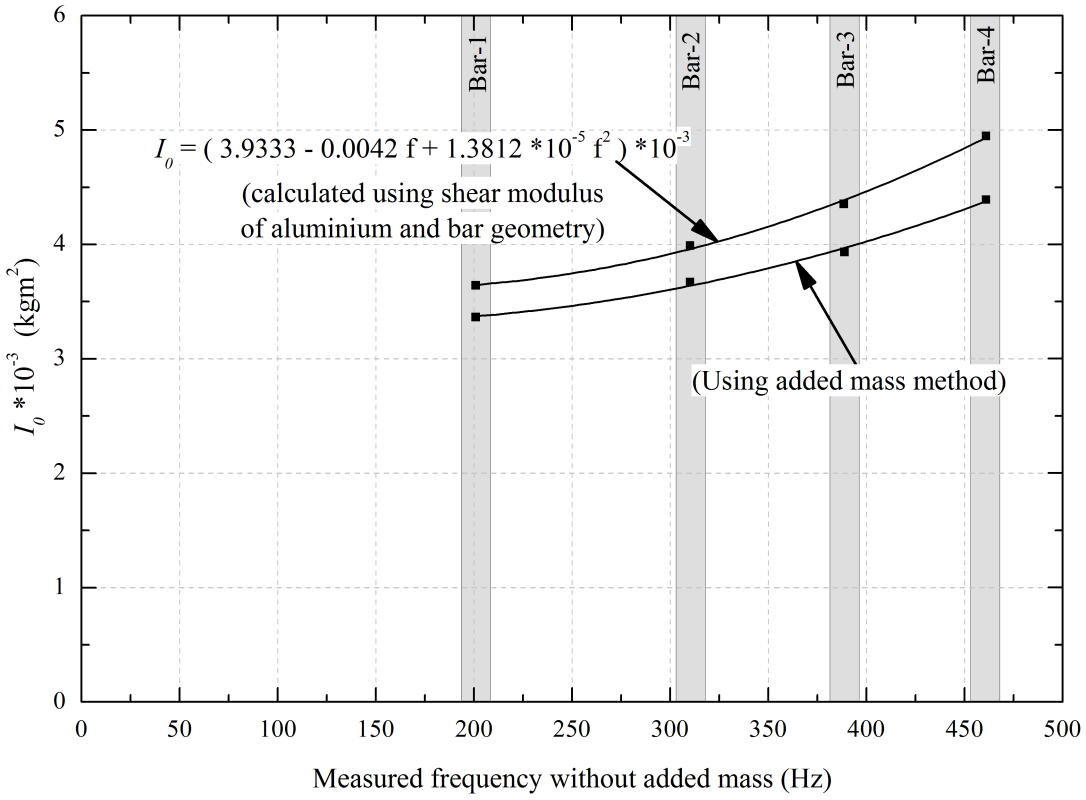

Figure 3.11: *The value of I_o for each calibration bar obtained using shear modulus $(= 25.6\,GPa)$ of aluminium and the bar geometry.*

Area moment of inertia (I_y)

Young's modulus in the resonant column is calculated from the flexural vibration of the specimen using Equation 3.4. The equation allows for the equivalent mass of the each component above the specimen to be represented in terms of equivalent height and mass. It is difficult to obtain equivalent height and mass of the drive system due to its complex geometry. So, Equation 3.4 can be rewritten to allow for masses of complex geometry by using the centre of gravity y_{ci} and the area moment of inertia I_{yi} of each component instead of the relative heights h_{0i} and h_{1i}.

$$h(y_{ci},\, I_{yi}) = 1 + \frac{3\, y_{ci}}{l} + \frac{9}{4\, l^2}\left[\frac{I_{yi}}{m_i} + y_{ci}^2\right] \tag{3.30}$$

To determine equivalent height of the drive system, values of m_i, y_{ci} and I_{yi} are required. m_i (mass) can be measured for the drive mechanism, y_{ci} can be taken as the geometric centre of the drive system and I_{yi} is then found using a similar calibration procedure to that for torsion.

As with the calibration value for I_0, the experimental value of I_y for each bar is not constant, but increases with the resonant frequency. Thus, in order to obtain the value of I_y a regression analysis was used to measure I_y, which uses known material properties of the calibration bars and measured frequency as shown in Figure 3.12. For the calculation of flexural modulus (E) using Equations 3.4 and 3.30, the value of I_y was determined from the measured resonant frequency from Figure 3.12.

Equipment damping

In order to calculate damping of the specimen, equipment damping must be deducted from the measured damping of the specimen. Material damping for each vibration mode is calculated using the free vibration decay (FVD) method by turning off the power to the drive coils when the system was vibrating at its resonant frequency. In the GHRC, open circuit is used during free vibration decay to prevent back e.m.f. being generated in the coils (Wang et al., 2003) which can lead to an overestimate of damping.

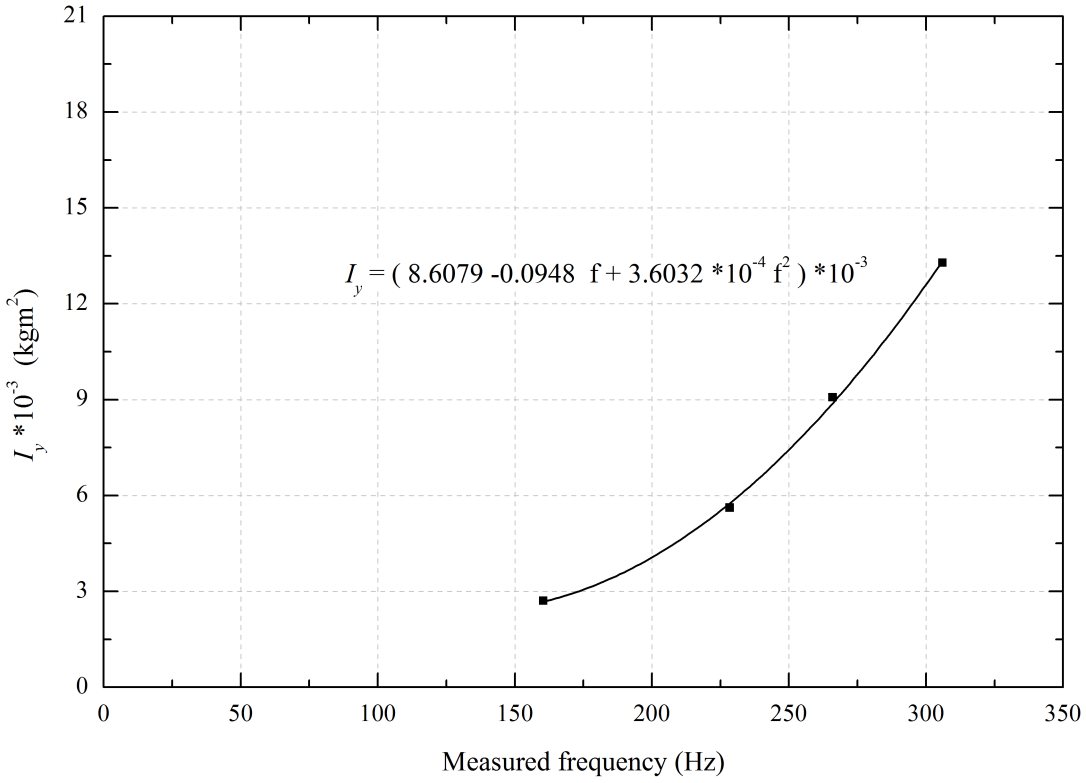

Figure 3.12: *The area moment of inertia of drive system, I_y, obtained from regression analysis plotted against resonance frequency for all calibration bars.*

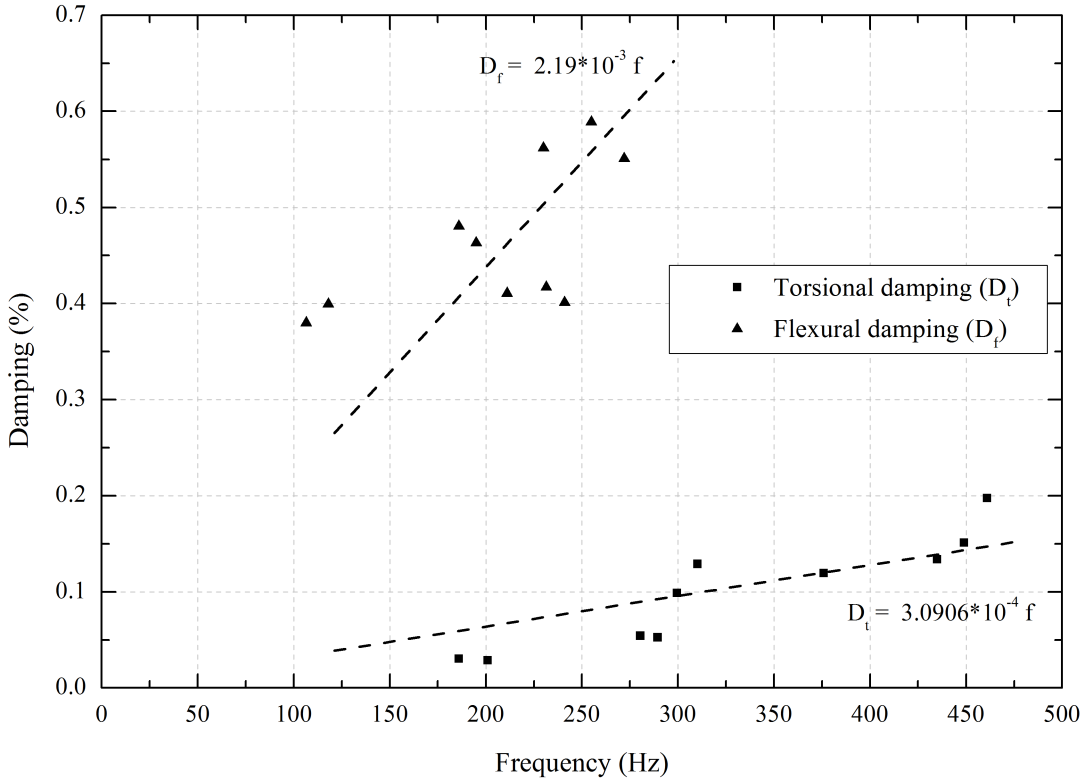

Figure 3.13: *Values of torsional and flexural GHRC equipment damping measured during calibration of aluminium bars, plotted against frequency.*

The equipment damping of the GHRC apparatus can be calculated from the damping measured for the aluminium bars when allowed to freely vibrate at their resonant frequencies. Since, aluminium can be considered to have negligible damping in both torsional and flexural vibration, the damping observed in the calibration test at small strain was assumed to be that of the apparatus (Figure 3.13). Best fit line is fitted to the data and the resultant equations are used to calculate damping of the apparatus (Figure 3.13).

3.1.3 Assumptions for data reduction

Several assumptions are made to calculate dynamic properties (shear and longitudinal wave velocity) of the specimen in the GHRC apparatus.

Young's modulus (E) from flexural vibration: To determine E from flexural vibration, it is assumed that the specimen has a constant cross-sectional area and behaves as a cantilever beam in pure bending. In addition, to derive Equa-

tion 3.4, Cascante et al. (1998) assumed that shear stiffness does not contribute significantly to deformations, and therefore to the resonant frequency in flexure. Classical elastic (Timoshenko) beam bending theory suggests that the contribution of shear stiffness is negligible where the length/diameter ratio of a beam is greater than 6. Since in a standard resonant column test the length/diameter ratio is of the order of 2, it was thought that significant errors might exist in the routine calculation of E_{flex}. Therefore, a numerical analysis was carried out to model both the Stokoe resonant column apparatus and specimen using the finite element software ABAQUS (version 6.8). The details of numerical analysis is given in Appendix B. It was found from the analyses (Appendix B) that slenderness ratio of an isotropic specimen affects the value of E calculated using Equation 3.4. The results from numerical analyses showed that the use of flexural vibration to derive E using Cascante equation (Equation 3.4) introduces an error of $\sim 10\%$ when the aspect ratio (length to diameter ratio) of the specimen is ~2 (Appendix B). This error occurs because no shear stiffness is considered in deriving Equation 3.4. Therefore in this research, stiffness from the flexural vibration is expressed as the flexural modulus (E_{flex}) rather than the conventional Young's modulus (E).

Material properties: To determine dynamic properties of the specimen using Equations 3.1 to 3.30, it is assumed that the material is homogeneous, isotropic and elastic. But in nature, sediments are rarely isotropic, containing some degree of anisotropy either due to inherent material characteristics or due to application of anisotropic stresses in the sediments. In this research, testing was performed on laboratory formed sand specimen and care was taken to ensure homogeneous preparation of the specimen. The specimen was prepared using a tamping method which may induce transverse anisotropy within the specimen; the specimen stiffness in the horizontal plane is assumed to be isotropic, and the vertical direction is the axis of anisotropy. However, numerical analysis in Appendix B showed that the calculated shear modulus from the torsional vibration is the shear modulus (G) in the vertical plane, and the calculated Young's modulus from the flexural vibration is within 10% of the Young's modulus (E) in the vertical plane for the specimen with E/G ratio <=2.7. Also in the GHRC, all the tests were conducted at low strain levels ($< 10^{-4} p.u.$), which was found to be below the elastic threshold. The elastic threshold is defined as the point when the calculated modulus values (G, E) are independent of applied strain (Saxena et al., 1988), and

the material can be considered as elastic below this point.

3.2 Experimental methodology

The GHRC apparatus has been successfully used for more than a decade to synthesise methane hydrates in sediments. Priest (2004) and Rees (2009) used the GHRC to synthesise methane hydrates within sediments using the excess gas (Priest, 2004) and the excess water (Rees, 2009) methods. In this research, the excess gas method was used to synthesis methane hydrates in sand sediments. Description of the material properties, the different steps for specimen preparation, and hydrate formation and dissociation used in this research are given in the following sections.

3.2.1 Material properties

All test specimens were prepared using Leighton Buzzard Sand Grade-E (LBE sand). This is a natural, uncrushed, uniform rounded to sub-angular silica sand, which is free from silt, clay or organic matter, with a nominal grain size between 90-150μm. Table 3.5 gives a summary of the different properties of LBE sand.

Leighton Buzzard Grade-E Sand	
Supplier	David Ball Group
Description	Natural, uncrushed, uniform rounded to sub-angular silica sand free from silt, clay or organic matter
Geological location	Lower Greensand sequence and outcrops at Leighton Buzzard, Bedfordshire, UK
Particle size	90 - 150 μm
Specific gravity (G_s)	2.65
Maximum dry density	1624 kg/m^3
Minimum void ratio	0.63
Minimum dry density	1331 kg/m^3
Maximum void ratio	0.99

Table 3.5: *The properties of LBE sand used to prepare test specimens (Priest, 2004).*

It is known that hydrate may be deposited in both coarse and fine grained sediments (Brooks et al., 1994; Dallimore and Collett, 1995; Clayton et al., 2008). The properties of natural hydrate bearing sediments may be different than the properties of laboratory synthesised hydrate bearing sand sediments. However the changes in pore pressure under undrained conditions will not be affected by the type of sediment. In the present research hydrate was formed in a disseminated morphology within sand sediments to evaluate its properties (stiffness, damping, and pore pressure) during methane hydrate formation and dissociation processes. Therefore, the measured pore pressure within laboratory synthesise hydrate bearing sediment will be representative that in natural hydrate bearing sediment under undrained conditions. As discussed in Chapter 2, in nature disseminated hydrates are mainly found in coarse sediments; such as sands. Therefore the stiffness and damping properties of laboratory synthesised hydrate bearing sand sediment may represent natural disseminated hydrate bearing sediments, or at least it may represent the trend of change in the properties of disseminated hydrate bearing sediment during formation and dissociation processes.

3.2.2 Apparatus preparation

The GHRC apparatus was prepared by following a sequence of steps.

1. Back pressure and cell pressure ports were checked for any blockage or any leak, and the top surface of the base pedestal of the GHRC apparatus was cleaned with a paper towel to remove any water or any foreign material.

2. A thin film of silicon grease was applied laterally to the base pedestal, and a clean butyl membrane was placed on it and sealed with a rubber O-ring.

3. A three-part split mould was used to make a specimen of height $140\,mm$ with diameter $70\,mm$. The split mould was fixed around the base pedestal and butyl membrane. The butyl membrane was stretched over the split mould such that it formed a smooth tube.

3.2.3 Specimen preparation

All soil specimens used in testing were prepared from LBE sand to synthesise hydrate in an excess gas environment by the following sequence of steps.

1. A known mass of de-aired water was added to a known mass of air-dried LBE sand ($\sim 850\,g$) in a seal-able plastic bag.

2. The sealed bag was kept at room temperature and pressure for at least 4 hours to allow for homogeneous distribution of water within sand.

3. The three-part split sample mould (as prepared in Section 3.2.2) was carefully filled in 8-10 equal layers with sand (as prepared in Stage-2). To ensure dense and uniform packing of the sand, each layer was tamped with 6 blows of a flat solid rubber bung of approximately $2\,cm$ diameter. Care was taken not to spill sand outside the mould, and if it was spilled it was collected carefully.

4. Once the specimen was at the required height a top-cap was placed on the top of the levelled specimen. A thin film of silicon grease was applied laterally to the top-cap. The butyl membrane was pulled up the top-cap and securely attached with a rubber O-ring.

5. Once the specimen was formed and sealed in the butyl membrane, a vacuum of $\sim 40\,kPa$ was applied to the specimen to remove air from the specimen and to allow the mould to be removed.

6. Once the vacuum has been applied and the split mould removed, the vacuum tap was closed off. The specimen was left for $30\,minutes$ to check for any leaks.

7. Additional O-rings were placed on the base-pedestal and top-cap to ensure a good seal.

8. Any leftover sand was weighed to determine the mass of sand and water in the specimen.

9. Specimen diameter (including membrane thickness) was measured at three different places, and specimen height (including top-cap and base pedestal) was measured at four different places. The average specimen dimensions

were calculated by subtracting the membrane thickness, and the top-cap and the base pedestal height from the measured diameter and height, respectively, of the specimen.

Once the specimen was securely placed and all dimensions were measured, the specimen was ready for various apparatus components such as thermistors, drive mechanism, axial transducer, and cell-top to be attached.

3.2.4 Instrumentation setup

1. Once the specimen was formed, the drive mechanism was carefully lowered onto the top-cap of the specimen and secured to it using six M5 countersunk screws.

2. In addition to an internal thermistor which was located inside the specimen near the base ($0.5\,cm$ from the metal base pedestal), an external thermistor was attached at mid height to the outside of the specimen using a soft rubber-band.

3. The accelerometer cable was connected to the accelerometer to measure vibration of the specimen during resonant column testing.

4. A LVDT axial gauge was attached to the specimen top-cap through the top-plate of the drive system and adjusted so that its output was within the linear range of the LVDT. The LVDT read-out was set to zero so that any change in specimen height could be read directly.

5. All four magnetic coil cables were connected to the respective electrical ports.

6. Once the above instrumentation was in place and correctly connected, the cell-top was slowly lowered and secured to the base with two steel C-clamps.

The specimen was now ready to test. Cell and back pressure could be applied and the hydrate formation process could be started.

3.2.5 Hydrate formation

Once the specimen was prepared (Section 3.2.3) and all the instrumentation was set-up (Section 3.2.4), hydrate was formed by raising cell and back gas pressure, then reducing the temperature of the specimen. In all tests, only the methane gas as back pressure was applied to raise the pore pressure within the specimen during hydrate formation process. Since, applied methane gas pressure was higher than the pore pressure within the specimen it can be assumed that the water drainage did not occur. Water and gas drainage were fully prevented when the tests were performed under undrained conditions (back pressure isolated conditions).

In the present research, hydrate was formed under two different conditions; a drained condition with back gas pressure applied, and undrained under constant effective stress conditions with back pressure isolated. The following sequence of steps were followed to synthesis methane hydrates under these two different conditions.

Drained condition (D)

1. Cell pressure was applied up to the chosen net stress (250kPa or 2000kPa) whilst back gas pressure was in vacuum at $\sim 40\,kPa$ (as applied in Stage 5 in Subsection 3.2.3) at room temperature (at point A in Figure 3.14). It was left at this pressure until the axial gauge showed that displacement had stabilised. The net stress is the difference between total and pore gas pressure. In the GHRC, the applied net stresses (cell pressure minus methane pore/back pressure) were significantly greater than the expected matric suction within the specimen (in general matric suction is in the range of $0 - 20\,kPa$ for sands for degree of water saturation $\geq 2.5\%$ (Fredlund and Xing, 1994)). Therefore it can be assumed that the net stress is the only stress controlling the mechanical response of the unsaturated sands, and therefore it was assumed that the applied net stress was approximately equal to the effective stress within the specimen.

2. Methane back pressure was applied to the specimen and raised to $6\,MPa$ whilst maintaining the net (or, effective) stress applied to the specimen (point B1). Overnight the temperature of the GHRC was lowered to $\sim 15^oC$ (point C1).

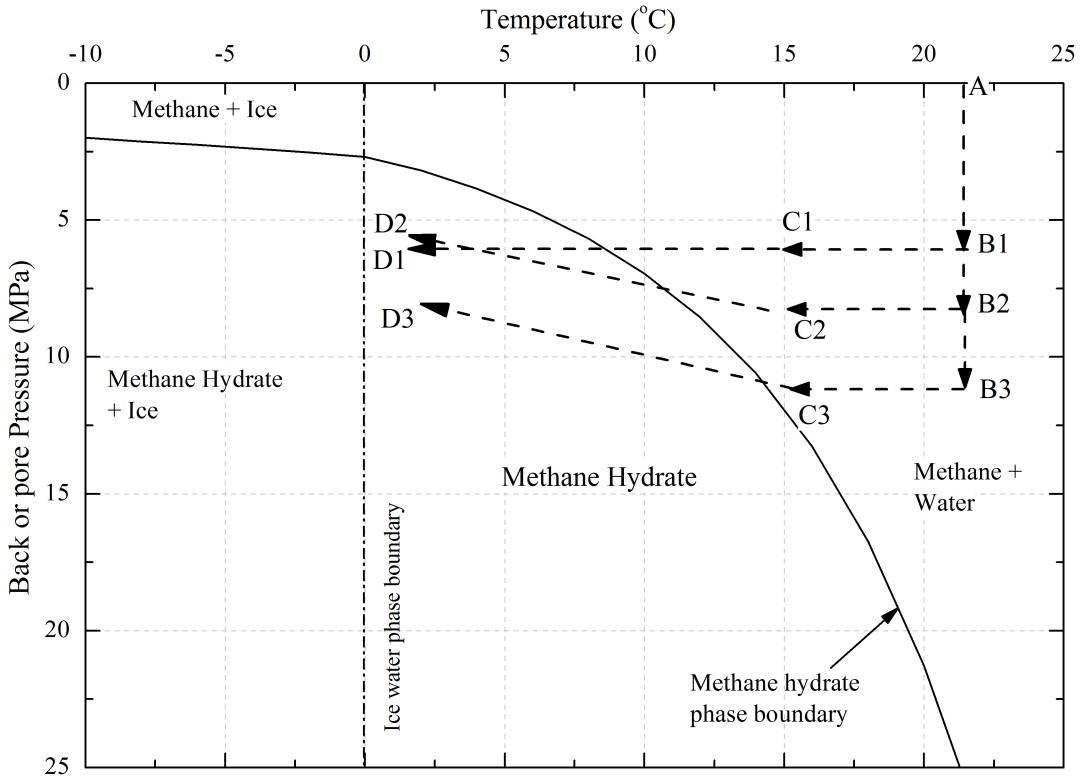

Figure 3.14: *Testing stages for hydrate formation. A-B(1,2,3) represents back pressure increase stage; B1-C1-D1 represents hydrate formation stages in drained condition; B2-C2-D2 and B3-C3-D3 represent hydrate formation in the undrained condition with constant effective stress.*

3. After the specimen temperature and pressure had stabilised overnight the temperature of the GHRC was lowered to $\sim 2^oC$ (point D1), well within the hydrate stability zone, leading to hydrate formation.

4. Temperature and pressure were maintained at point D1 for at least 48 hours to allow complete hydrate formation.

During the hydrate formation steps, cell and back air pressures were maintained at the initial pressure. Thus this process was idealised as drained hydrate formation and denoted with a symbol "D".

Undrained with constant effective stress (U-CES)

1. An net (or, effective) stress (250kPa or 2000kPa) was applied to the specimen by increasing cell pressure (at point A in Figure 3.14). It was left at this level until axial displacement stabilised.

2. Methane back pressure was applied to the specimen and raised to the chosen pressure (8.5 MPa or 11 MPa) whilst maintaining the effective stress on the specimen (point B2 or B3). Overnight the temperature of the GHRC was lowered to $\sim 15^oC$ (point C2 or C3).

3. Once the required temperature ($\sim 15^oC$) was attained the methane back pressure valve was closed off and the specimen was allowed to rest at these temperature and pressure conditions (point C2 or C3) until changes in pore pressure and axial displacement were stabilised.

4. The temperature of the GHRC apparatus was lowered to $\sim 2^oC$ (point D2 or D3) within the hydrate stability zone thereby inducing hydrate formation. As the pore pressure fell, the effective stress was maintained by reducing the cell pressure.

5. Temperature and effective stress were maintained at these levels (point D2 or D3) for at least 48 hours to allow complete hydrate formation.

During the hydrate formation steps the effective stress was maintained by varying the cell pressure whilst back gas pressure was isolated. This process achieved hydrate formation at constant effective stress under undrained conditions is denoted

with the symbol "U-CES". During hydrate formation process, resonant column tests were conducted at very small strains ($\leqq 5e^{-5}\,p.u.$) in regular intervals.

3.2.6 Stress and strain response

Once hydrate was fully formed at the chosen initial effective stress, resonant column tests were conducted at different effective stresses and at different strain levels ($<1e^{-4}\,p.u.$). The level of effective stress on the specimen was increased to $2000\,kPa$ or reduced to $250\,kPa$ through the intermediate level of effective stress at $500\,kPa$ and $1000\,kPa$, and then reduced/increased to the same pressures back to its initial value of effective stress. Each effective stress was maintained until changes in axial displacement, as measured by the axial LVDT transducer, were negligible.

3.2.7 Hydrate dissociation

Once methane hydrate was fully formed, and the stress and strain response tests had been conducted, hydrate was dissociated by either increasing temperature or reducing pore pressure within the specimen (points D(1-3) to F(1-3) in Figure 3.15).

To understand the effects of hydrate dissociation, three sets of hydrate dissociation tests were conducted with various hydrate saturations of the pore spaces;

- undrained conditions with varying effective stress: Back pressure was isolated, and cell pressure was kept constant.
- undrained conditions with constant effective stress: Back pressure was isolated, and cell pressure was varied to maintain the effective stress.
- undrained conditions with varying effective stress through pressure reduction: Methane back pressure was quickly reduced such that the specimen was outside the hydrate stability region, then the back pressure was closed off. The cell pressure was kept constant throughout the dissociation stage.

In all dissociation tests, water and gas drainage were prevented so that any change

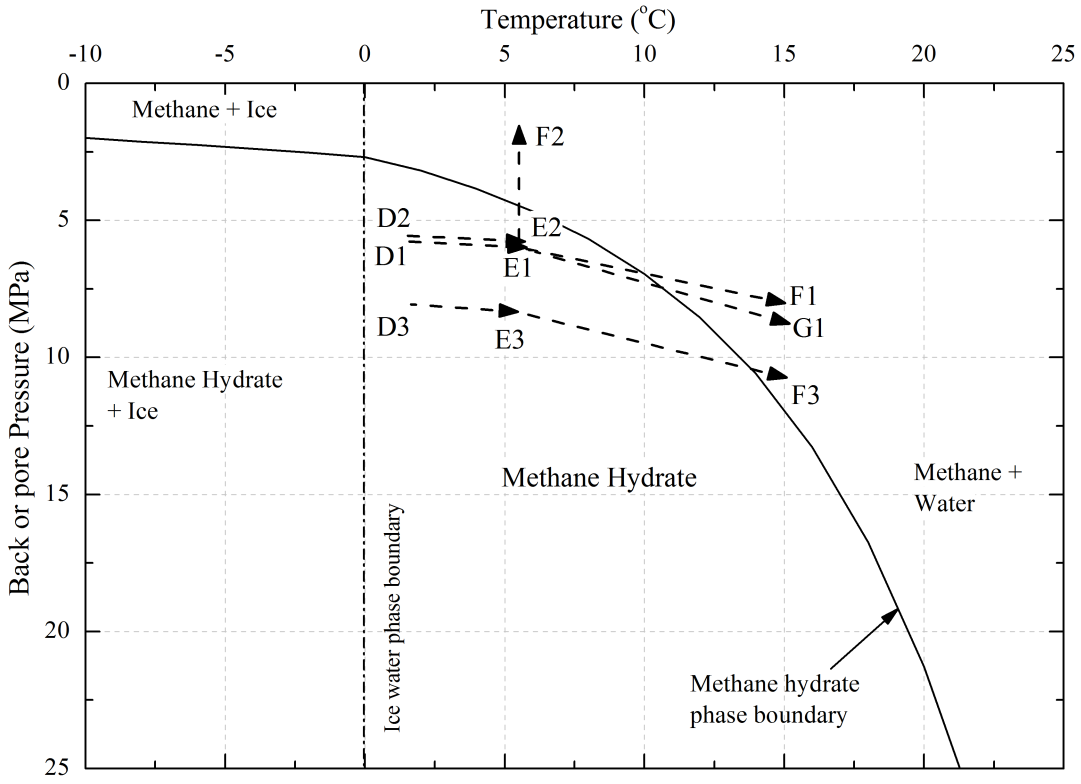

Figure 3.15: *Testing stages for hydrate dissociation. D(1,2,3)-E(1,2,3) represents temperature increase to* $\sim 6^0C$*; E1-F1, E1-G1, and E3-F3 represent hydrate dissociation stages through temperature rise; E2-F2 represents hydrate dissociation through pressure reduction.*

in pore pressure would be measured. The following sequence of steps were followed to dissociate methane hydrate under these three conditions.

Undrained with varying effective stress (U)

Methane hydrate was dissociated under undrained conditions with varying effective stress, through the following steps:

1. The methane back pressure was isolated and the temperature of the GHRC was increased to $\sim 6^oC$ (within the hydrate stability zone, point E1 in Figure 3.15), whilst maintaining the cell pressure at its initial value such that the effective stress on the specimen was allowed to change

2. Once the required temperature was attained the specimen was allowed to rest at this temperature (point E1) until the pore pressure and axial dis-

placement readings stabilised.

3. At this point the temperature of the GHRC was increased to $\sim 15^oC$, which was outside the hydrate stability zone (point F1), whilst maintaining the cell pressure with the back pressure isolated.

Undrained with constant effective stress (U-CES)

Methane hydrate was dissociated under undrained conditions with constant effective stress, following the steps below.

1. Overnight the temperature of the GHRC was increased to $\sim 6^oC$ (within the hydrate stability zone, point E1 or E3 in Figure 3.15), whilst maintaining the effective stress on the specimen.
2. Once the required temperature was attained methane back pressure was isolated and the specimen was allowed to rest at this temperature (point E1 or E3) until changes in pore pressure and axial displacement readings were stabilised.
3. At this point the temperature of the GHRC was increased to $\sim 15^oC$ (outside the hydrate stability zone, point G1 or F3 in Figure 3.15), whilst maintaining effective stress on the specimen by changing the cell pressure.

Undrained with varying effective stress through pressure reduction (U-PR)

Methane hydrate was dissociated using pressure reduction under undrained conditions with varying effective stress, through the following steps:

1. The methane back pressure ($\sim 5.75\,MPa$) was isolated and the temperature of the GHRC was increased to $\sim 6^oC$ (within the hydrate stability zone, point E2 in Figure 3.15), whilst maintaining the effective stress at $\sim 250\,kPa$ on the specimen by changing the cell pressure.
2. Once the required temperature was attained the specimen was allowed to rest at this temperature (point E2) until the axial displacement readings stabilised.

3. At this point the back pressure was reduced from $\sim 5.75\,MPa$ to $\sim 2.3\,MPa$ in ~6 seconds, which was outside the hydrate stability region (point F2). Then the back pressure was closed off whilst maintaining the cell pressure at $\sim 6\,MPa$ so that the rise in pore pressure during dissociation would be measured.

During the dissociation process, resonant column tests were conducted at very small strain ($\leqq 5e^{-5}\,p.u.$) in regular intervals.

3.3 Calculating the volume of hydrate within the specimen

In the GHRC apparatus the total volume of hydrate, for the excess gas tests, can be calculated either from the total change in methane pore pressure during dissociation or the amount of water added in the specimen. The percentage of total hydrate formed (or dissociated) within the specimen can be calculated from the change in pore pressure with respect to the total change in pore pressure after complete formation (or dissociation).

3.3.1 Hydrate calculation from added water

The total hydrate volume after hydrate formation was calculated from the added water, and is based on the assumption that all the added water was converted into methane hydrate; such that 5.75 moles of water (H_2O) produced 1 mole of methane hydrate ($5.75\,H_2O.CH_4$) within the specimen. The volume of methane hydrate was calculated from the initial water saturation ($S_w = \frac{V_w}{V_v}$). Where, V_w is the volume of added water and V_v is the total volume of the voids in the specimen which is calculated from,

$$V_v = V_{specimen} - V_{soil} \tag{3.31}$$

where $V_{specimen}$ is the volume of the specimen ($= \pi/4 \times d^2 \times l$; d and l are diameter and length of the specimen), and V_{soil} is the volume of the soil solids ($= m_s/G_s$; m_s is mass of the added dry sand and G_s is the specific gravity of the sand

grains (2.65)). The moles of water and methane hydrate within the specimen were calculated as,

$$n_w = \frac{V_w \, \rho_w}{M_w} \tag{3.32}$$

and therefore,

$$n_{hy} = \frac{n_w}{5.75} = \frac{V_w \, \rho_w}{5.75 \, M_w} \tag{3.33}$$

where, n_w and n_{hy} are moles of water and methane hydrate respectively; ρ_w and M_w are the mass density ($= 1000\, kg/m^3$) and the molar mass ($= 18.015\, g/mol$) of water respectively.

The volume of hydrate (V_{hy}) and total hydrate saturation (S_h) can be calculated from,

$$V_{hy} = \frac{n_{hy} \, M_{hy}}{\rho_{hy}} = \frac{V_w \, M_{hy} \, \rho_w}{5.75 \, M_w \, \rho_{hy}} \tag{3.34}$$

$$S_h = \frac{V_w \, M_{hy} \, \rho_w}{5.75 \, M_w \, \rho_{hy} \, V_v} \tag{3.35}$$

where, ρ_{hy} and M_{hy} are the mass density ($= 917\, kg/m^3$) and the molar mass ($= 119.63\, g/mol$) of methane hydrate respectively.

3.3.2 Hydrate calculation from pore pressure change

In tests where back pressure was locked off during hydrate formation/dissociation, the amount of methane hydrate in the specimen at any moment in time was calculated from the methane pore pressure change during hydrate formation/dissociation.

As methane is a non-ideal gas, the number of moles of methane gas present in the pore-space of the specimen at a given temperature and pressure can be calculated from the Peng-Robinson gas equation (Peng and Robinson, 1976):

$$P = \left(\frac{R\,T}{V_m - b}\right) - \left(\frac{a\,\alpha}{V_m^2 + 2\,b\,V_m - b^2}\right) \tag{3.36}$$

where $V_m (= \frac{V_{va}}{n})$ is available molar volume for gas; V_{va} is the volume of voids for gas; n is number of moles of gas in the voids; P is pressure (Pa); T is temperature (^oK); R is the universal gas constant (8.314472 Pa/K/mole); and a, b and α are Peng-Robinson's coefficients relating to critical pressure, critical temperature, and acentric factor of the gas. For methane gas these coefficients are:

$a = 0.24663$, $b = 2.64804 \times 10^{-5}$, and $\alpha = 1.391264925\ \left(1 - \sqrt{\frac{T}{190.6}}\right)^2$

The volume of hydrate present in the pore spaces of the specimen was calculated from the change in number of moles of the methane gas during hydrate formation and dissociation.

$$S_f = \left[1 - \left(\frac{n_f - n_{e:f}}{n_{s:f} - n_{e:f}}\right)\right] \tag{3.37}$$

$$S_d = \left[1 - \left(\frac{n_d - n_{s:d}}{n_{e:d} - n_{s:d}}\right)\right] \tag{3.38}$$

where S_f and S_d are the hydrate saturation in the pores of the specimen during formation and dissociation process; $n_{s:f}$, n_f and $n_{e:f}$ are moles of methane at the start, during and at the end of hydrate formation calculated using Equation 3.36; similarly $n_{s:d}$, n_d and $n_{e:d}$ are moles of methane at the start, during and at the end of hydrate dissociation.

Thus the percentage of total hydrate saturation during formation and dissociation within the specimen is calculated from;

$$H_f\ (\%) = \frac{S_f}{S_h} \times 100 \tag{3.39}$$

$$H_d\ (\%) = \frac{S_d}{S_h} \times 100 \tag{3.40}$$

where H_f and H_d are percentage of the total hydrate during formation and dis-

sociation respectively; and S_h is the total hydrate saturation calculated using Equation 3.35.

Chapter 4

Results and Discussion

This chapter discusses the results from laboratory tests. It begins with a discussion of typical measurement during hydrate formation and dissociation, then reports the effect of hydrate formation and dissociation on the stiffness, pore pressure, and material damping of sediments. In addition, an analytical model is developed to predict the pore pressure rise during hydrate dissociation.

A number of different sets of tests were undertaken with hydrate saturation ranging from 7 to 27% of the pore spaces. In the first set of tests, hydrate was formed under drained condition (D) under an effective (or net) stress of $250\,kPa$ and dissociated under the same effective stress (by increasing cell pressure to compensate for the increase in pore pressure during dissociation). This dissociation process was termed a "constant effective stress condition" (U-CES). In the second set of tests, hydrate was also formed under drained conditions but at higher effective stress ($\geq 2000\,kPa$) and was dissociated under undrained conditions. In these tests the cell pressure was not changed and so effective stress reduced during hydrate dissociation. These tests are described as "undrained" (U). In one specimen "14H-3", hydrate was formed and dissociated under constant effective stress condition (U-CES) of 250kPa whilst back pressure was isolated. In addition, two tests were conducted where hydrate was formed under a constant effective stress condition (U-CES) of 2000kPa whilst back pressure was isolated, and hydrate was dissociated by applying a reduction of pore pressure to take the specimen outside the hydrate stability region. Initial properties and test conditions for all specimens are presented in Table 4.1.

Specimen number	Specimen Properties								
	Dry density (kg/m^3)	Void ratio	Moisture content (%)	Hydrate content[a] (%)	Effective stress (kPa)		Type of test performed		Initial methane pressure at the start of hydrate formation stage (MPa)
					during formation	during dissociation	during formation	during dissociation	
7H-1	1547.6	0.71	1.5	7.0	250	250	D[b]	U-CES[c]	6.0
13H-1	1509.0	0.76	3.0	13.4	250	250	D	U-CES	6.0
14H-1	1529.2	0.73	3.0	13.7	250	-	D	Nodiss[d]	6.0
21H-1	1536.0	0.73	4.6	21.0	250	250	D	U-CES	6.0
27H-1	1520.3	0.74	6.0	27.3	250	250	D	U-CES	6.0
7H-2	1542.7	0.72	1.5	6.9	2000	2000	D	U[e]	6.0
13H-2	1492.8	0.78	3.0	13.1	2000	2000	D	U	6.0
27H-2	1519.7	0.74	6.0	27.3	2800	2800	D	U	6.0
14H-3	1525.2	0.74	3.0	13.7	250	250	U-CES	U-CES	11.0
21H-4	1524.0	0.74	4.8	21.5	2000	3700	U-CES	U-PR[f]	8.5
26H-4	1494.5	0.77	6.1	26.2	2000	3800	U-CES	U-PR	9.5
0H	1643.8	0.61	dry sand	0.0	-	-	-	-	-

Table 4.1: *Initial properties of the specimens used in the GHRC laboratory tests.*

[a] calculated from moisture content
[b] Drained condition
[c] Undrained with constant effective stress condition
[d] No dissociation stage was performed
[e] Undrained condition
[f] Hydrate dissociation through pressure reduction under undrained condition

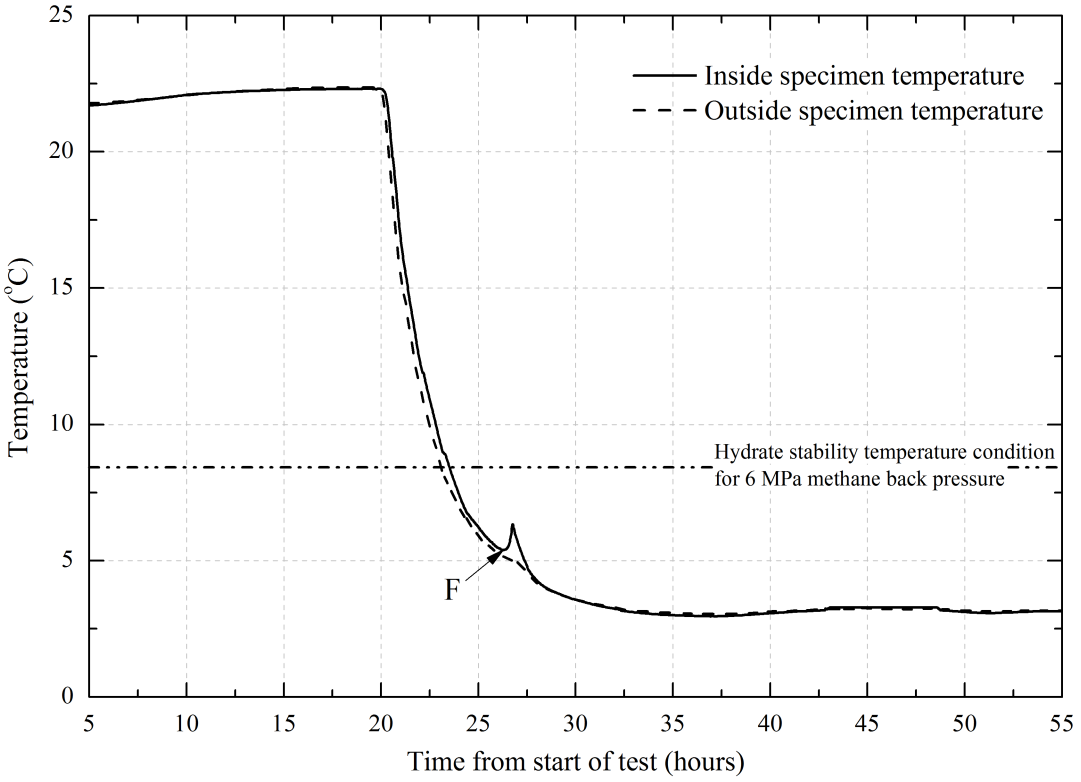

Figure 4.1: *Variation in specimen temperature with time for the specimen "14H-1" during temperature drop stage.*

4.1 Initiation of hydrate formation and dissociation

As discussed in Chapter 3, methane hydrate was formed by lowering the specimen temperature into the hydrate stability zone. Hydrate formation is an exothermic process, where heat is released from the specimen as hydrate starts to form. Figure 4.1 shows a plot of temperature change with time where system temperature was reduced from $\sim 22^oC$ to $\sim 3^oC$. It can be seen from Figure 4.1 that after $\sim$ 26 hours from the start of test the specimen temperature started to rise (point F), even though the temperature outside the specimen continued to fall towards the target temperature of 3^oC.

The rise in specimen temperature is thought to have occurred due to the heat liberated from the exothermic reaction during hydrate formation. Therefore this highlighted the starting point of hydrate formation in the specimen. However the point "F" at which the rise in specimen temperature was observed does not

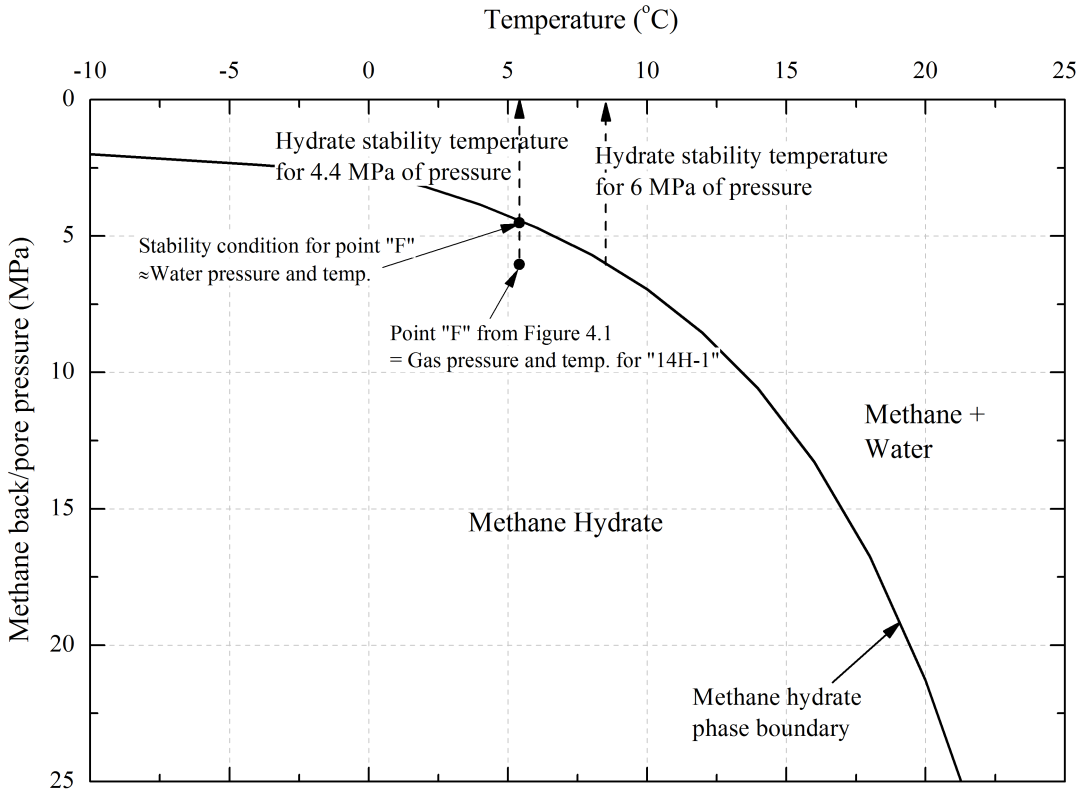

Figure 4.2: *Hydrate stability temperature for different pressures (Sloan, 1998).*

correspond to the temperature and pressure conditions from the methane hydrate stability curve (Figure 4.1) for formation but is well inside the hydrate stability zone. The observed difference in the temperature might be due to one or more of the following reasons;

- The small pore size of the specimen: In general, hydrate stability curves are based on the dissociation of hydrate in its bulk form (Figure 4.2 show the bulk methane hydrate stability curve by Sloan (1998)). However, a driving force (such as temperature below the equilibrium temperature) is required to initiate hydrate formation within a reasonable time scale (Anderson et al., 2003). Similar behaviour was also observed for specimen "14H-3" (Figure 4.3), that was formed at a higher back pressure. The temperature shift characteristics for hydrate formation in small pores (up to $100\,nm$) has been observed in the past by different researchers (Handa and Stupin, 1992; Uchida et al., 1999, 2002; Anderson et al., 2004, 2009). In addition for an unsaturated soil, the presence of gas within the pore space forms the curvature of menisci at the gas-liquid interface. As a result,

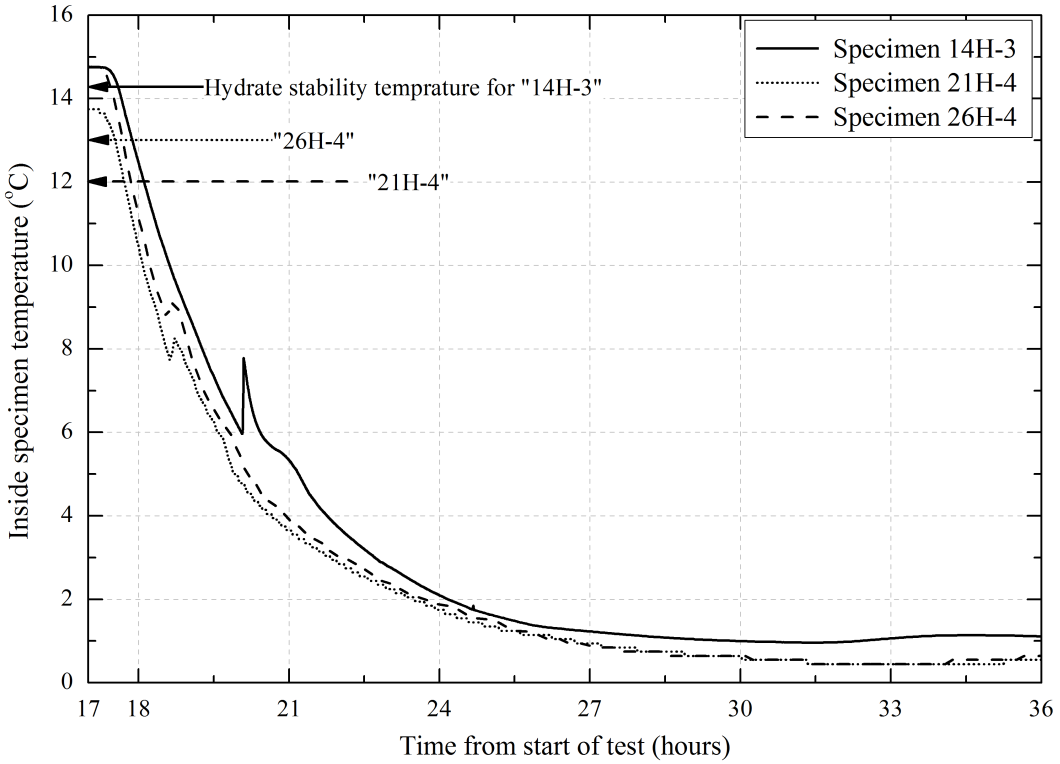

Figure 4.3: *Variation in inside specimen temperature during temperature drop stage with time for specimens that were formed at higher back pressures.*

pressure-temperature conditions within water may be closer to the hydrate stability curve compared to the pressure-temperature conditions within the methane gas (as shown in Figure 4.2). However, the inferred difference in water and methane gas pressure within the specimen appears to be unrealistically high ($1.6\,MPa$, Figure 4.2) compared to the pressure difference at the menisci for sands which is in the order of $\leq 0.01\,MPa$ when the degree of water saturation $\geq 5\%$ (Fredlund and Xing, 1994; Fredlund, 2000).

- Heat liberated during the initial stages of hydrate formation is insufficient to counteract the loss of heat caused by the lowering of the system temperature: As discussed in Chapter 3 two thermistors were used to measure specimen temperature. One thermistor was attached at mid height to the outside of the specimen, and the second thermistor was situated inside the specimen near the base ($0.5\,cm$ from the metal base). In the GHRC, the system temperature was set to a target temperature $\sim 2^oC$ and so heat was removed all the time. If there is a small amount of hydrate formation in the specimen it may not be possible for the thermistor to detect

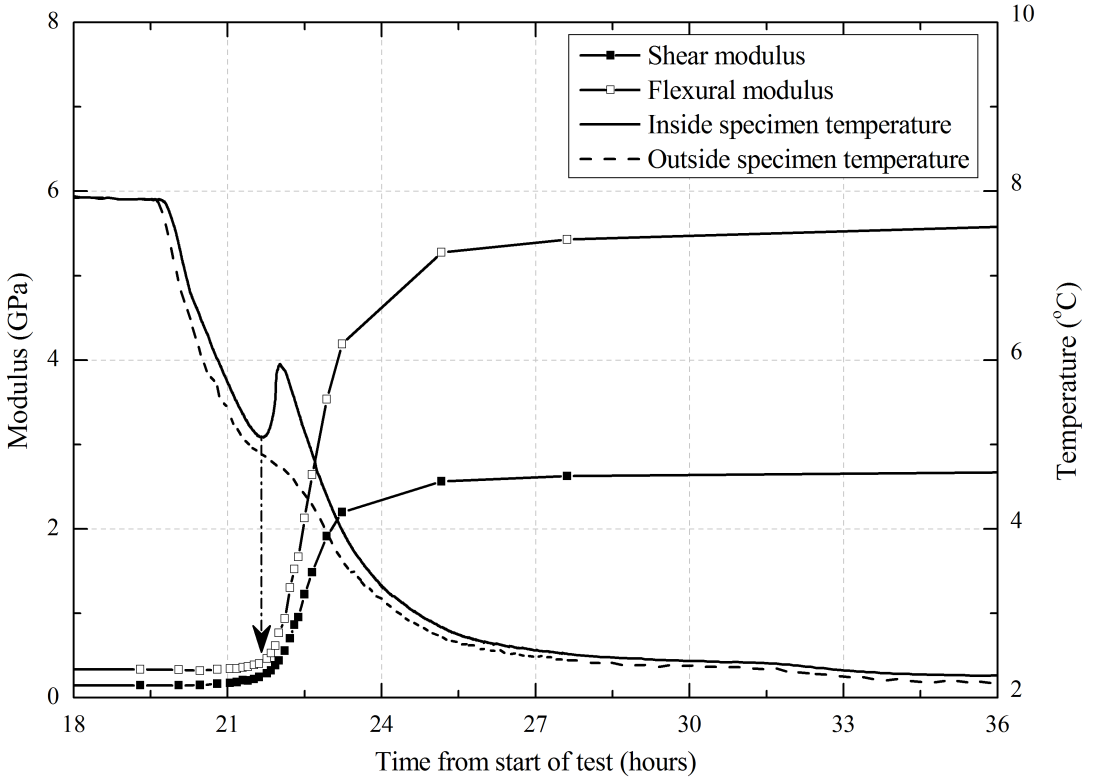

Figure 4.4: *Variation in calculated shear modulus (G_{max}), flexural modulus (E_{flex}), and specimen temperature with time for the specimen "13H-1" during temperature drop stage.*

the change in specimen temperature. Therefore, it might be possible that hydrate formation started before the change in the specimen temperature trend was observed.

Figure 4.4 shows the typical variation in stiffness (G_{max} and E_{flex}) with time calculated from the resonant column tests, along with corresponding specimen temperature during the system temperature being lowered. Both G_{max} and E_{flex} increase rapidly as the specimen moves into the hydrate stability field. Since the effective stress is constant and the temperature is above the freezing point of water, the increase in the stiffness can only be due to the formation of methane hydrate within the specimen. It can be seen in Figure 4.4 that a small increase in stiffness occurs before the rise in the specimen temperature.

To locate the start point of the hydrate formation, the test on specimen "14H-3" was carried out under constant effective stress (of 250kPa) whilst the back pressure was isolated. Change in pore pressure results from a decrease in temperature of the gas or methane gas consumption during hydrate formation. The percentage

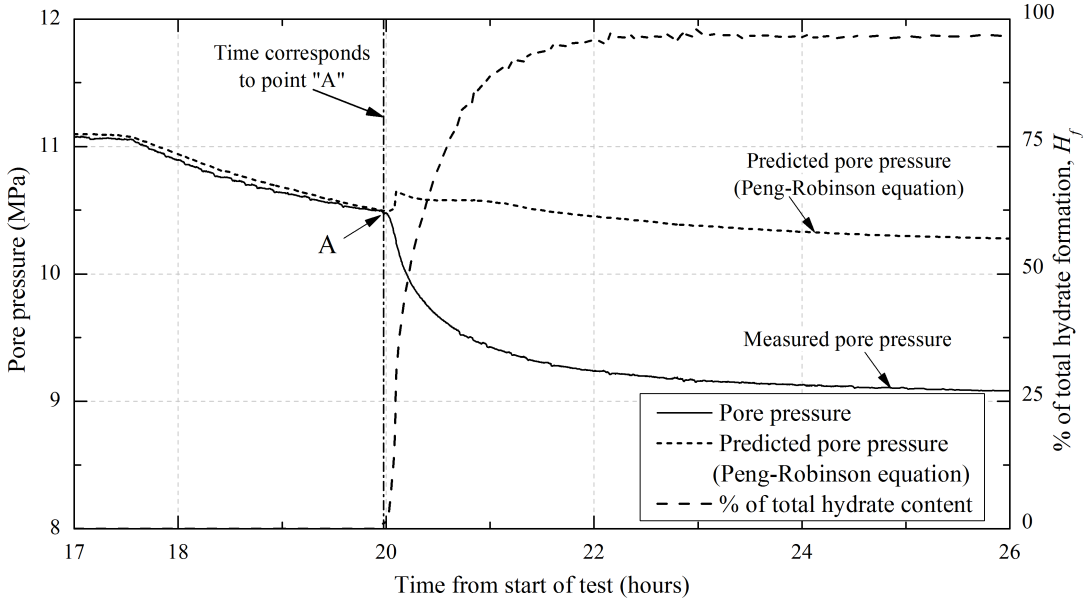

(a) *Variation in pore pressure and % of hydrate formation (H_f) with time.*

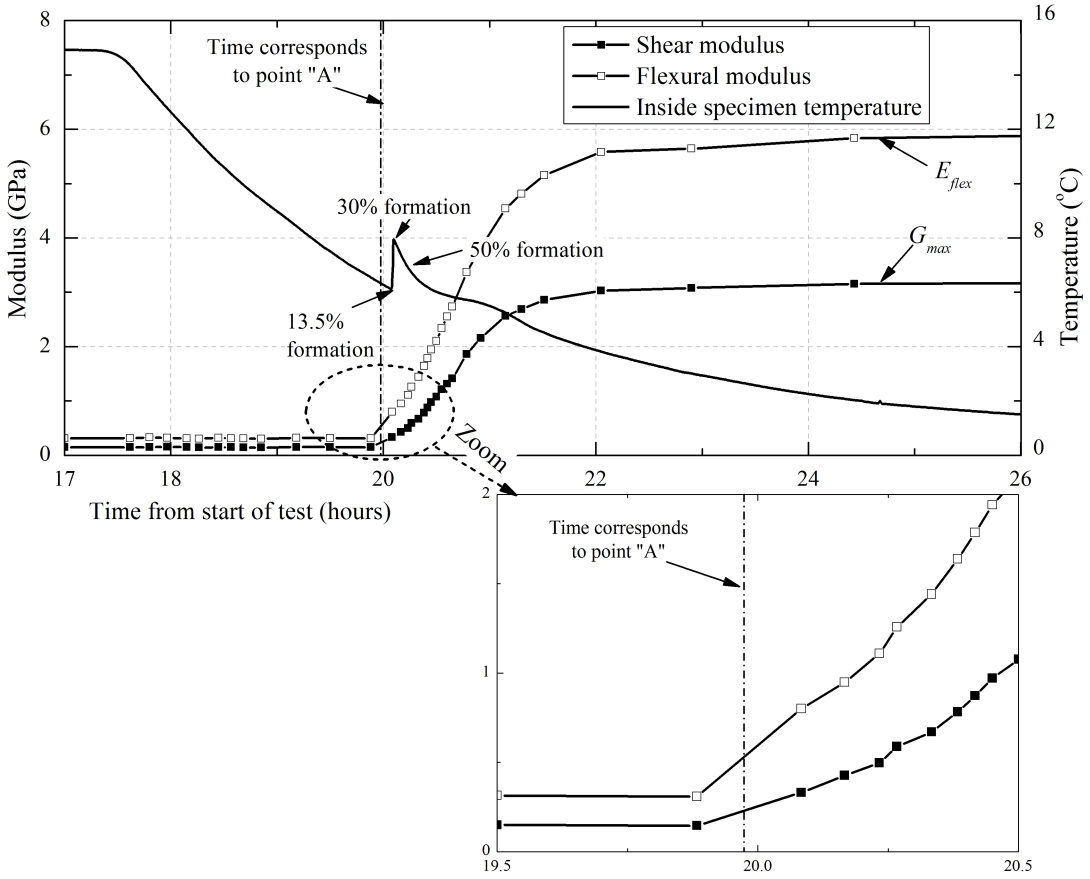

(b) *Variation in shear modulus (G_{max}), flexural modulus (E_{flex}), and specimen temperature with time.*

Figure 4.5: *Variation in various parameters with time for specimen "14H-3" during temperature drop stage.*

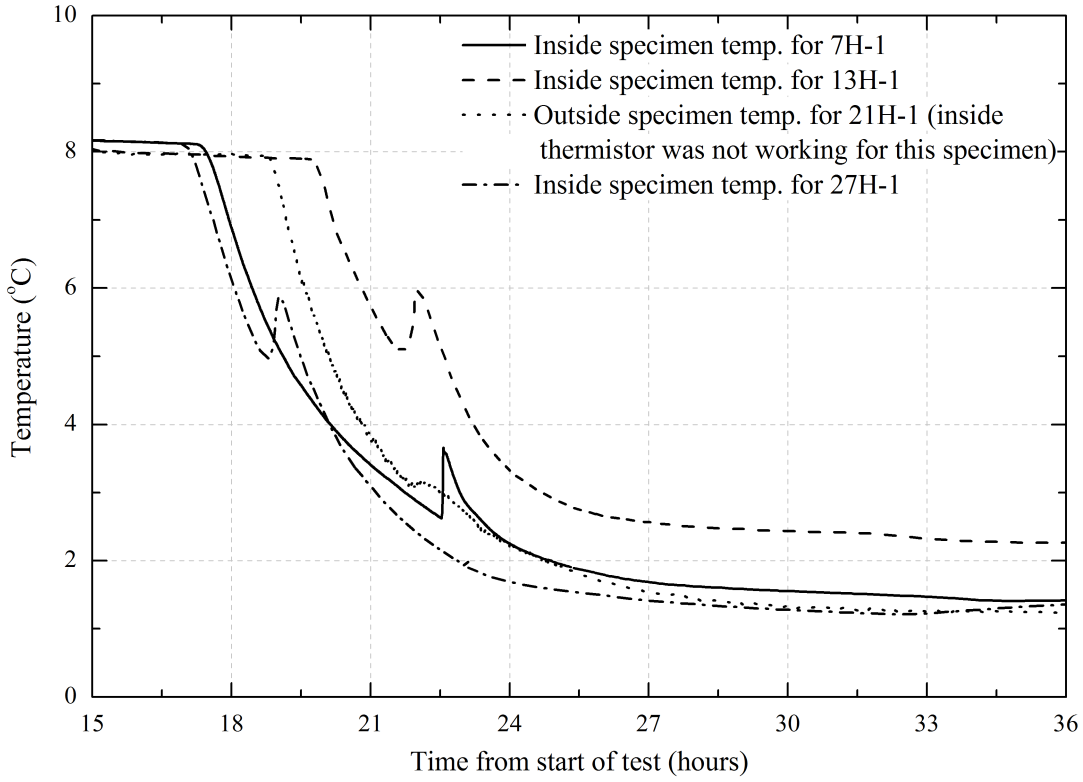

Figure 4.6: *Variation in specimen temperature with time for a number of specimens.*

of hydrate formed was calculated from the resulting pore pressure change using Equation 3.39. Figure 4.5(a) shows the % of hydrate formed and the change in pore pressure with temperature drop. The expected decrease in pore pressure resulting from the temperature drop (calculated using Peng-Robinson Equation 3.36) is also shown. It can be seen from Figure 4.5(a) that initially the pore pressure in the specimen follows the Peng-Robinson equation curve, caused by a reduction in specimen temperature and then the rate of change increases rapidly. This is due to the conversion of methane gas into the hydrate. As noted in Figure 4.5(a) the point "A" at which a sudden drop in the pore pressure was observed approximately corresponds to an increase in the specimen stiffness (in Figure 4.5(b)). It can also be seen in Figure 4.5(b) that the bottom of the temperature spike corresponds to ~13.5% of total hydrate formation. This suggests that the point "A" approximately corresponds to the start of hydrate formation. Therefore, for all tests, the start of hydrate formation was considered to occur at the point where an increase in specimen stiffness and/or sudden drop in pore pressure were measured.

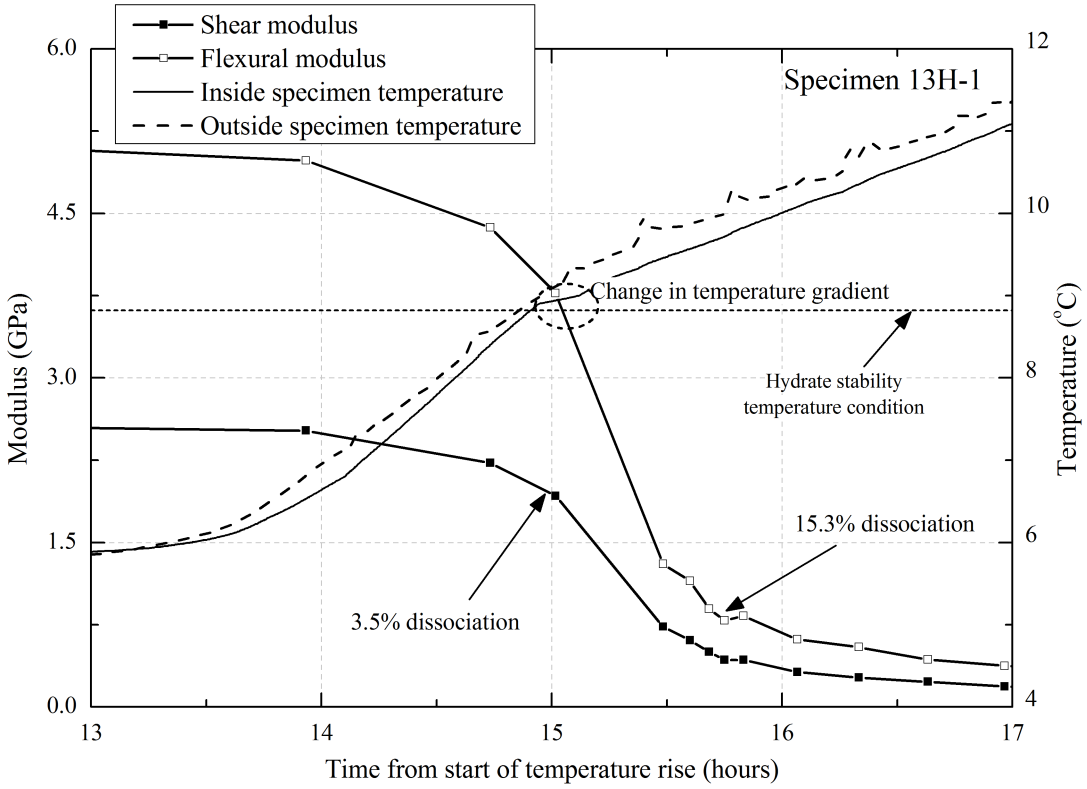

Figure 4.7: *Variation in specimen stiffness and temperature for specimen "13H-1" with time during temperature rise. Also shows change in temperature gradient corresponds to hydrate dissociation.*

It can be seen in Figure 4.5(b) that the specimen temperature increased shortly after hydrate formation started and reached a maximum value. Similarly, Figure 4.6 shows the change in specimen temperature trend for a number of specimens formed under drained conditions at $\sim 250\,kPa$ effective stress. For specimen "14H-3", the temperature spike occurred when ~30% of total hydrate was formed (Figure 4.5(b)). It is hypothesised that as the hydrate forms it produces a skin (cover of hydrate) encapsulating the remaining water and forms a barrier at the gas-water interface. Therefore, further hydrate growth depends on the diffusion of gas through this hydrate rind. Thus the rate of hydrate growth reduced, and so the heat liberated was insufficient to counteract the loss of heat caused by the lowering of the system temperature.

In contrast to formation, hydrate dissociation is an endothermic reaction. Figure 4.7 shows the typical response observed for specimen stiffness and temperature with time during dissociation caused by raising the system temperature. The presented plot is for specimen "13H-1" where hydrate was dissociated under a

constant effective stress of 250kPa by increasing cell pressure whilst back pressure was isolated. It can be seen from Figure 4.7 that the outside specimen temperature data has small identifiable spikes. These are due to the fact that the cell pressure applied to the specimen was raised by allowing nitrogen gas from a compressed gas cylinder located at room temperature to enter the cell. However, it can also be seen in Figure 4.7 that the inside specimen temperature was not noticeably affected. During the rise in specimen temperature, a change in temperature gradient was observed at $\sim 8.9^oC$ which approximately corresponds to the location on the hydrate stability curve at the given methane back pressure (Figure 4.7). However, it can be seen from Figure 4.7 that a small volume of hydrate dissociation had already occurred before the change in the temperature gradient (3.5% for specimen "13H-1" from Figure 4.7). This small volume of hydrate dissociation may result from a time lag in the specimen temperature between the outside of the specimen and the middle of the specimen at its base where the internal thermistor was located.

As discussed hydrate formation occurred at a temperature well-inside the hydrate stability curve. However, hydrate dissociation was observed to correspond to the hydrate stability curve for the measured temperature and pressure (Figure 4.8). This may be due to the different mechanisms of hydrate formation and dissociation. Hydrate formation occurs at the gas-water interface within the hydrate stability zone, but hydrate dissociation may occur as soon as hydrate stability region is crossed. More details of these mechanisms of hydrate formation and dissociation are discussed in Section 4.2.2.

4.2 Sediment stiffness

As hydrate forms water and gas convert into solid hydrate which is stiffer than the constituents (water and gas), and thus an increase in the specimen stiffness may occur. In addition, conversion of fluids into solid hydrate may reduce the specimen void ratio. The reduction in void ratio may increase the specimen stiffness (Seed et al., 1984). Figure 4.9 shows the change in shear modulus (G_{max}), and flexural modulus (E_{flex}) with time during hydrate formation process for specimens with different ultimate hydrate contents (7 to 27 %). As discussed in Chapter 3, the overnight system temperature was reduced from room temperature to 8^oC (from 0 to $\sim 18\,hours$). The system temperature was then further lowered to

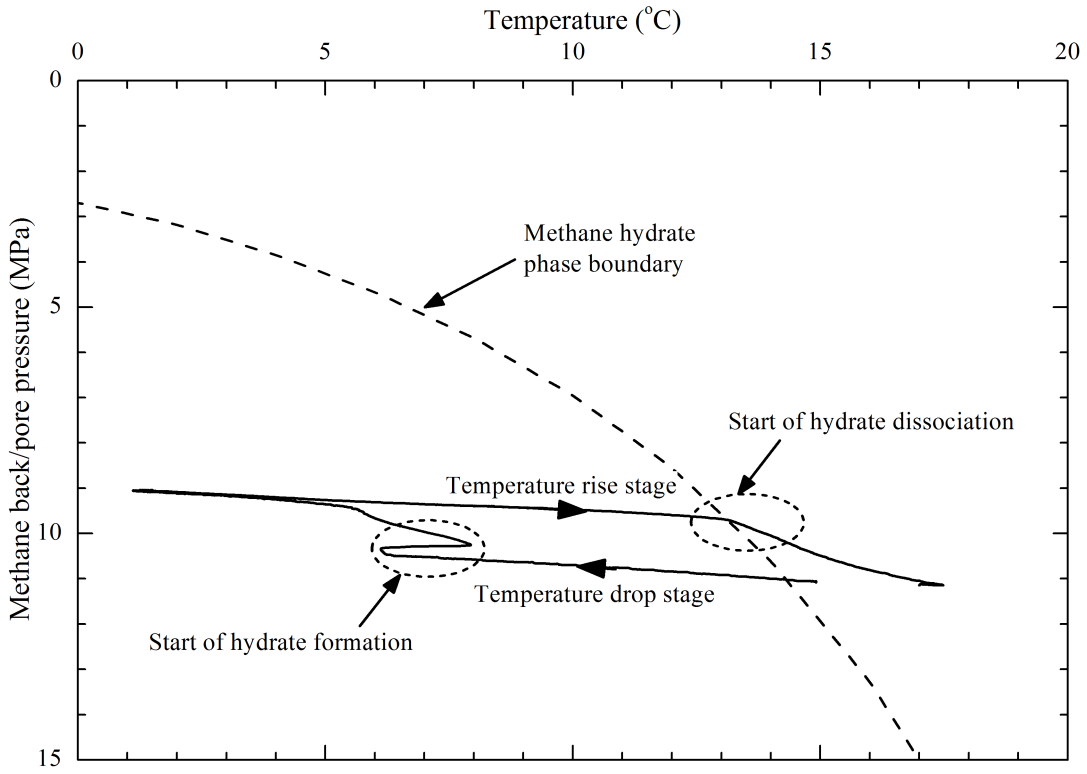

Figure 4.8: *Variation in temperature and pressure during temperature drop and rise stages for specimen "14H-3".*

2^oC to induce hydrate formation. Shear and flexural modulus were measured throughout the working day, which at the end of was sufficient for ~97% of the eventual increase in G_{max} and E_{flex} to have occurred for specimens contain 7% and 14% of hydrate saturation. For higher hydrate saturations (21% and 27%) ~75% of the eventual increase in G_{max} and E_{flex} occurred during this time. After $\sim 40\,hours$ no further increase in G_{max} and E_{flex} was measured for the 7% and 14% hydrate saturated specimens, whilst for the higher saturation around ~98% of the eventual increase in G_{max} and E_{flex} was measured. No further increase in G_{max} and E_{flex} was evident after ~50 hours for any specimen.

Conversely, hydrate dissociation results in the conversion of hydrate back to its constitutive parts of water and gas, so a decrease in specimen stiffness with dissociation is expected. Figure 4.10 shows calculated values of G_{max} and E_{flex} with time during the hydrate dissociation process for specimens at different hydrate saturations (7 to 27 %). As discussed previously the overnight system temperature was increased to 6^oC, which was within the hydrate stability region. The system temperature was then further raised to 15^oC to induce hydrate dissociation. It can be seen from Figure 4.10 that the eventual decrease in G_{max} and E_{flex} for all specimens was measured to occur within $5\,hours$ of the temperature rise (6^oC to 15^oC).

The changes in specimen stiffness that were observed depend upon a number of factors:

- Change in void ratio
- Change in hydrate saturation
- Effective stress
- Cyclic strain
- Dissociation methodology

4.2.1 Effect of change in void ratio

It has previously been hypothesised that growth of hydrate occurs at contacts between sand grains, and so may jack the grains apart when the excess gas

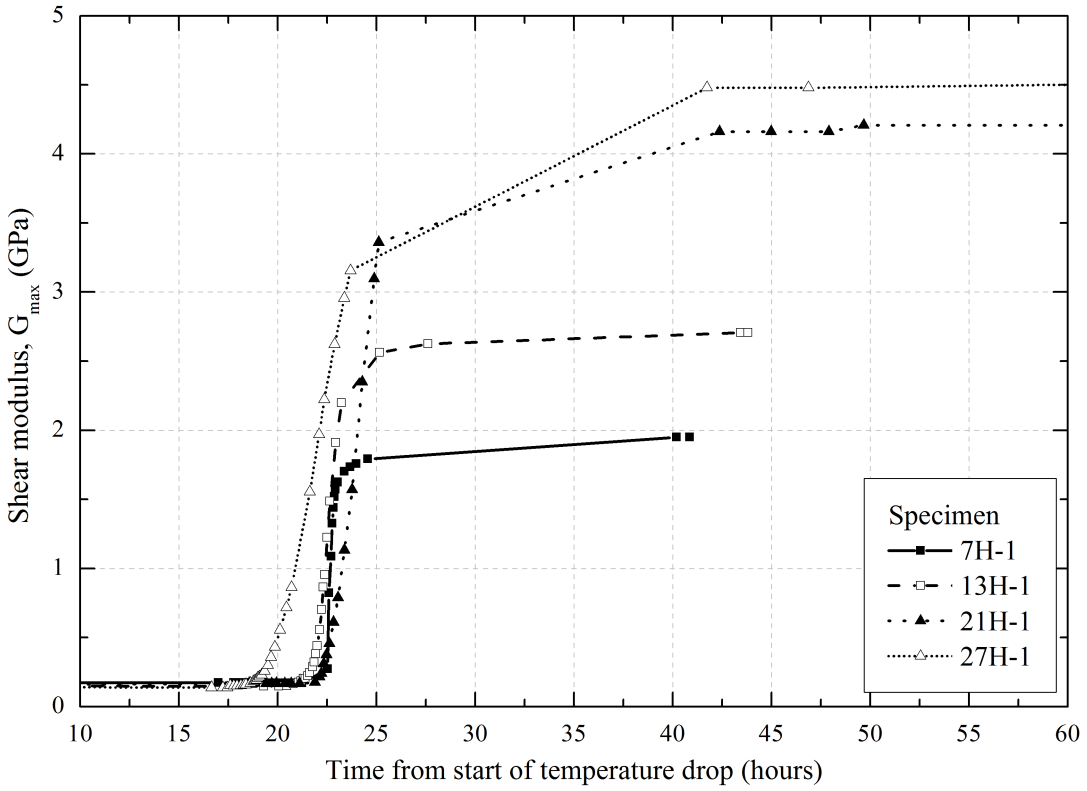

(a)

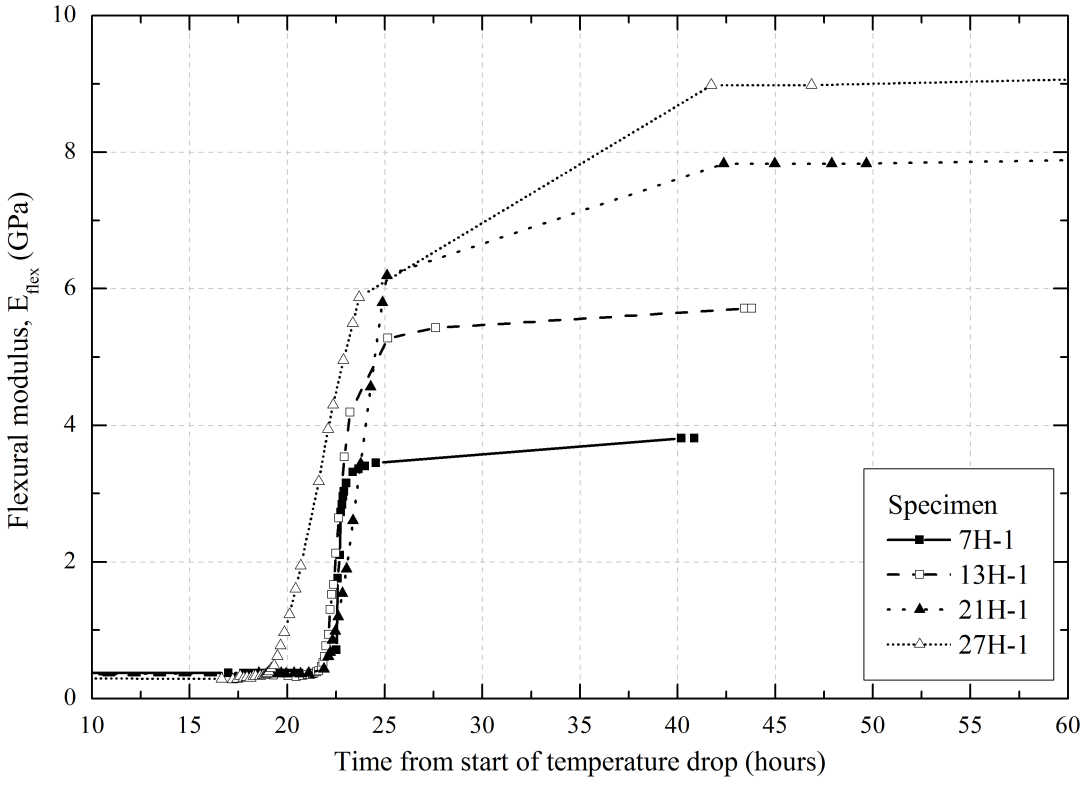

(b)

Figure 4.9: *Change in (a) shear modulus, and (b) flexural modulus during hydrate formation with time.*

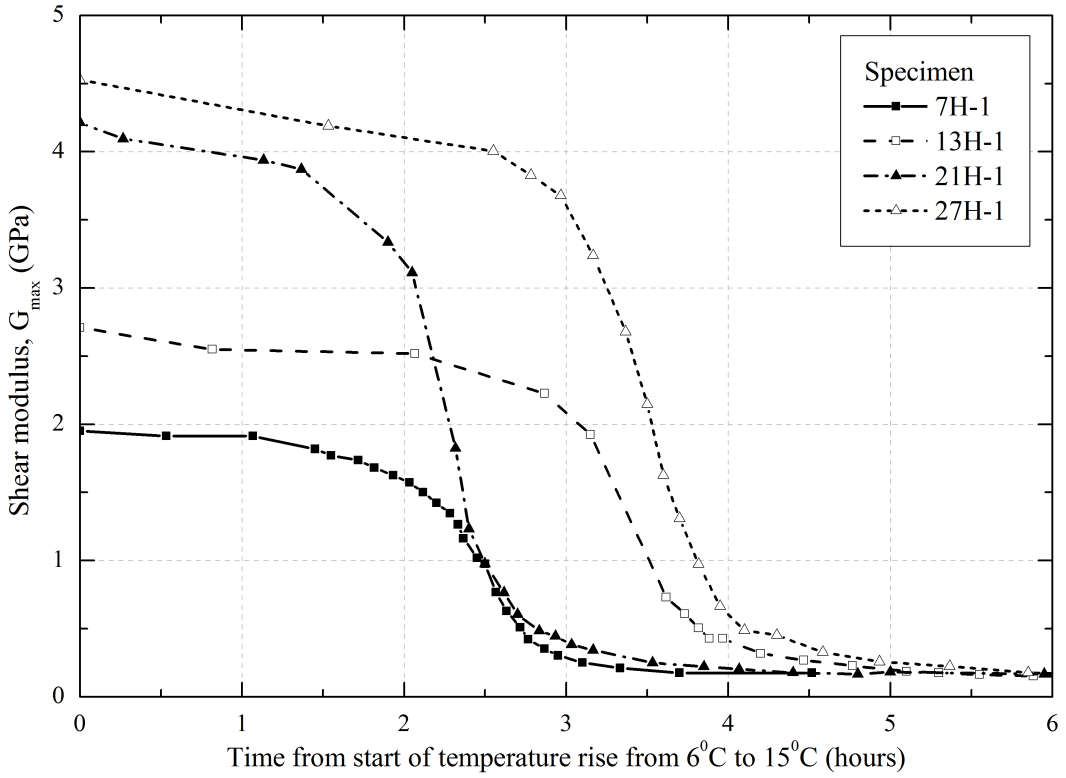

(a)

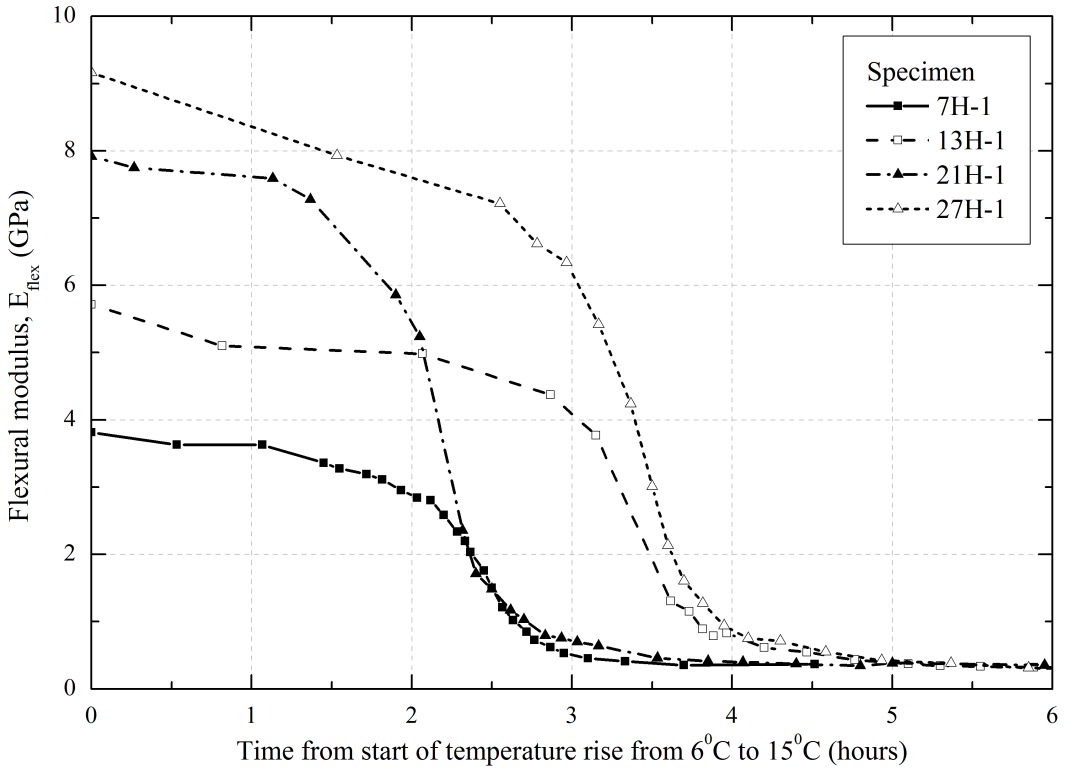

(b)

Figure 4.10: *Change in (a) shear modulus, and (b) flexural modulus during hydrate dissociation with time. Time "0" represents the time at which system temperature was set to increase* 15^oC *from* 6^oC.

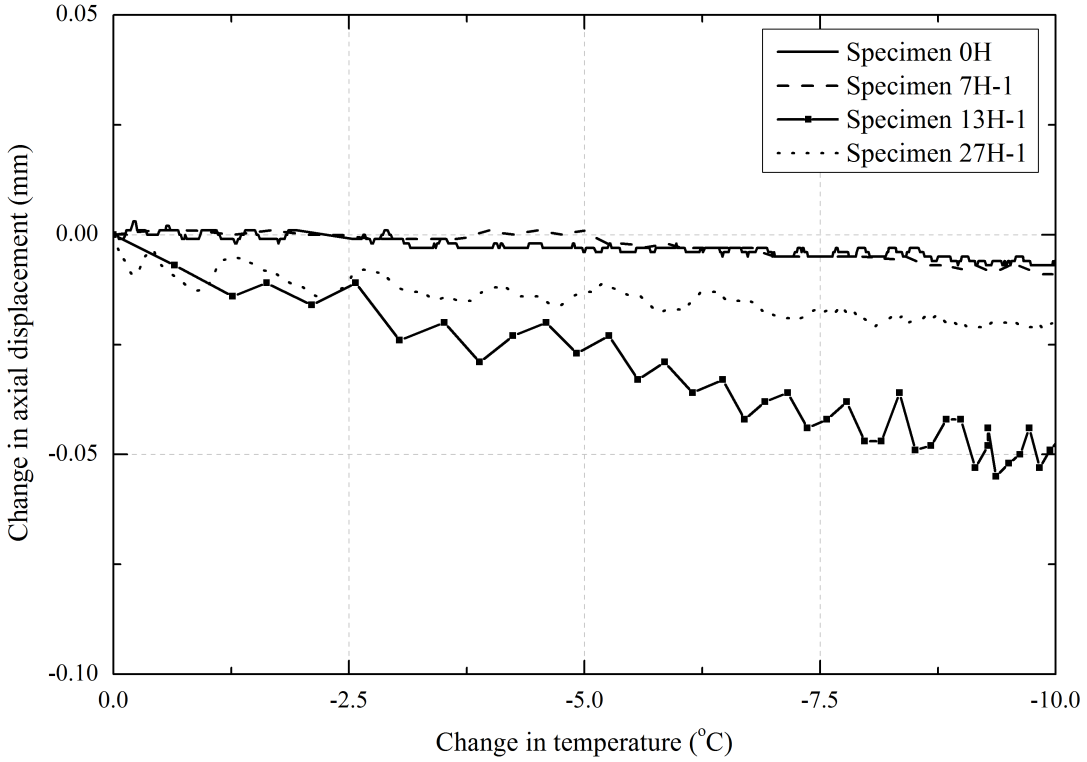

Figure 4.11: *Variation in axial displacement during temperature drop before the start of hydrate formation. Negative value represents expansion of the specimen.*

technique is used (Priest, 2004). However, Rees (2009) observed that hydrate formation did not jack the grains apart, when using the excess water technique. To measure the change in specimen height during hydrate formation a LVDT was mounted on the top of the supporting plate and resting on the top cap of the specimen. Figure 4.11 shows the change in axial displacement during a drop in temperature before the start of hydrate formation for a number of specimens. It can be seen that the change in axial displacement is very small ($< 0.05\,mm$ for 10^0C temperature drop; ~0.03% axial strain for the $140\,mm$ high specimen). These changes could be due to apparatus contraction during temperature drop as suggested by Rees (2009). Table 4.2 shows the change in axial displacement and strain due to hydrate formation and dissociation. It can be seen from the Table 4.2 that hydrate formation (or dissociation) does not significantly affect the axial displacement. This suggests that hydrate formation does not jack the grains apart.

As discussed the hydrate forms at grain contacts using the excess gas technique and becomes part of soil solids, thus a change in void ratio occurs. Similarly, a change in void ratio occurs during dissociation due to conversion of hydrate

Specimen number	Change in axial displacement and axial strain			
	during hydrate formation from temperature 8^oC to 1^oC		during hydrate dissociation from temperature 6^oC to 14^oC	
	displacement (mm)	strain (%)	displacement (mm)	strain (%)
7H-1	-0.009	-0.01	-0.002	0.00
13H-1	-0.014	-0.01	-0.002	0.00
14H-1	-0.007	0.00	-	-
21H-1	0.051	0.04	-0.044	-0.03
27H-1	0.103	0.07	-0.055	-0.04
7H-2	-0.015	-0.01	-	-
13H-2	-0.025	-0.02	-	-
27H-2	0.028	0.02	-	-
14H-3	0.017	0.01	0.018	0.02
21H-4	-0.005	0.00	-	-
26H-4	0.017	0.01	-	-

Table 4.2: *Axial displacement and strain values during formation and dissociation stages for all tests performed under drained (D) or constant effective stress (CES) conditions. Negative value represents expansion of the specimen.*

back into constituents (water and gas). In general, void ratio has a significant affect on the moduli of particulate materials (Hardin and Black, 1966; Seed et al., 1984), such as LBE sands. It has been suggested that the primary factors affecting the moduli of cohesionless soil under isotropic pressure at very small strain amplitude (within the linear threshold limit) are; effective stress ($\sigma^{'}$), void ratio (e), and particle characteristics (e.g. specific gravity, size, and shape) (Hardin and Drnevich, 1972b; Seed et al., 1984). Taking account of these parameters, a number of empirical equations for estimating G_{max} have been suggested by different researchers. The simplest form of these empirical equation can be represented as (Hardin and Drnevich, 1972a; Seed et al., 1984; Bui, 2009),

$$\left(\frac{G_{max}}{\sigma_r}\right) = A \times F(e) \times \left(\frac{\sigma^{'}}{\sigma_r}\right)^n \tag{4.1}$$

or,

$$(G_{max}) = A \times F(e) \times \sigma_r^{1-n} \times \left(\sigma^{'}\right)^n \tag{4.2}$$

where, $F(e)$ is an empirical void ratio function; n is the stress exponent; $\sigma^{'}$ is effective stress in kPa; and σ_r as a reference pressure makes to satisfy dimensions

(=1 kPa, Jovicic and Coop, 1997; Rampello et al., 1997) ; A is a material coefficient reflecting the influence of particle characteristics; and G_{max} is maximum shear modulus in MPa.

Bui et al. (2010) studied experimental data from the literature and theoretically derived a void ratio function ($F(e) = (1 + e)^{-3}$) with stress exponent ($n = 0.5$) to calculate small strain shear modulus. Their theoretical functions fitted well to the experimental data for both sands and clays over a wide range of void ratio, and therefore they suggested that this void ratio function could be considered as a universal void ratio function. Using the Bui et al. (2010) void ratio function and stress component Equation 4.2 can be written as:

$$G_{max} = \frac{A}{(1+e)^3}\,\sigma_r^{1-n} \times \left(\sigma^{'}\right)^n \tag{4.3}$$

In this research during hydrate formation and dissociation stages, the resonant column was used to derive specimen moduli at very small strain which was found to be within the linear elastic threshold limit (discussed later in Section 4.2.4). Therefore, Equation 4.3 can be used to calculate the anticipated change in shear modulus with void ratio. Equation 4.3 requires the material coefficient parameter (A) for specimen tested. This can be obtained using the specimen properties at the starting effective stress (e, $\sigma^{'}$, G_{max}) before hydrate formation. The material coefficient can be calculated from rearranging Equation 4.3; $A = G_{max} \times (1 + e)^{-3} \times \sigma_r^{0.5} \times (\sigma^{'})^{0.5}$; average material coefficient (A_{av}) was found to be 48 (shown in Table 4.3).

Figure 4.12 shows the variation in shear modulus with void ratio at different effective stresses for non-hydrate bearing LBE sand specimens. Trend lines were obtained using average material coefficient (A_{av} from Table 4.3). Figure 4.12 also shows the shear modulus of specimens after hydrate formation. It can be seen from the trend line that the shear modulus increases with reduction in void ratio at a given effective stress (Figure 4.12). As hydrate formation reduces the void ratio a small increase in specimen stiffness should occur. However it can be seen from Figure 4.12 that the increase in shear modulus due to hydrate formation is an order of magnitude larger than that due to a reduction in void ratio.

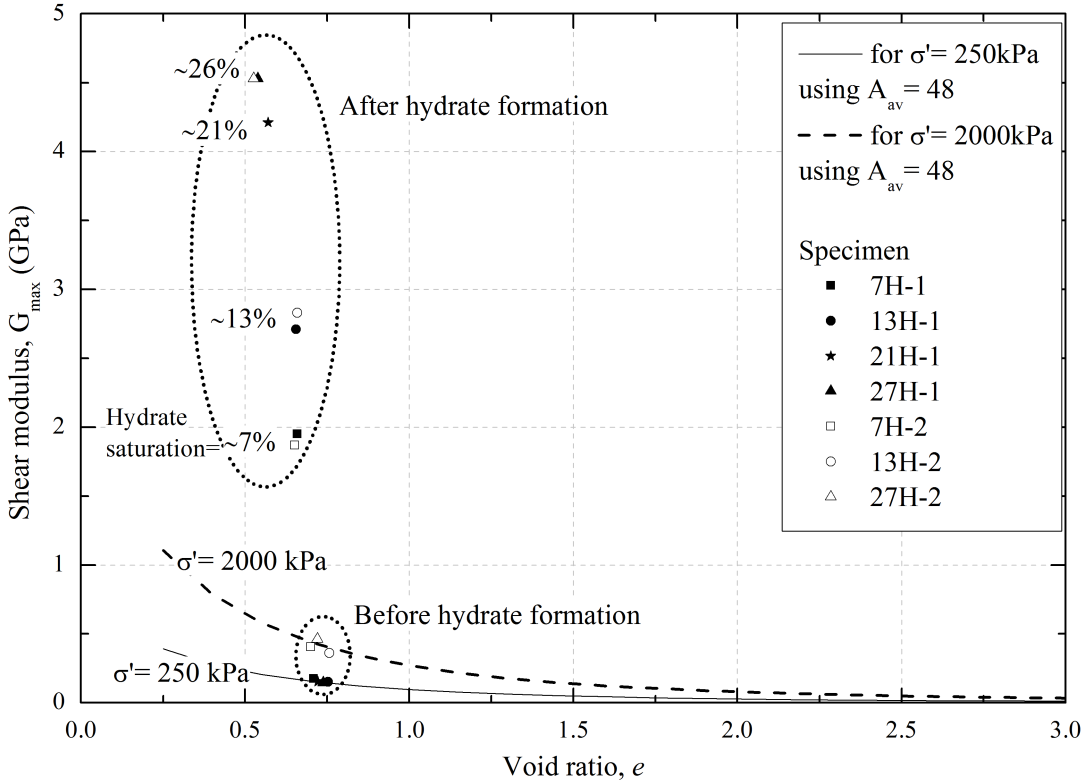

Figure 4.12: *Variation in shear modulus with void ratio for different effective stress (250kPa and 2000kPa) derived using Equation 4.3. Also shown is the change in shear modulus and void ratio due to hydrate formation for a number of specimen.*

Specimen number	Initial specimen properties before the start of hydrate formation			
	Void ratio (e)	Effective stress ($\sigma^{'}$, kPa)	Shear modulus (G_{max}, MPa)	Material coefficient (A)
7H-1	0.71	250	176	56
13H-1	0.75	250	153	52
14H-1	0.73	250	156	49
21H-1	0.72	250	154	50
27H-1	0.74	250	145	48
7H-2	0.70	2000	406	45
13H-2	0.76	2000	361	44
27H-2	0.72	2800	461	44
14H-3	0.74	250	146	48
21H-4	0.74	2000	370	44
26H-4	0.77	2000	343	43
0H	0.61	250	196	52
Average value of material coefficient				A_{av}= 48

Table 4.3: *Average value of material coefficient (A_{av}) derived using Equation 4.3 and initial material properties (e, $\sigma^{'}$, G_{max}) of specimens.*

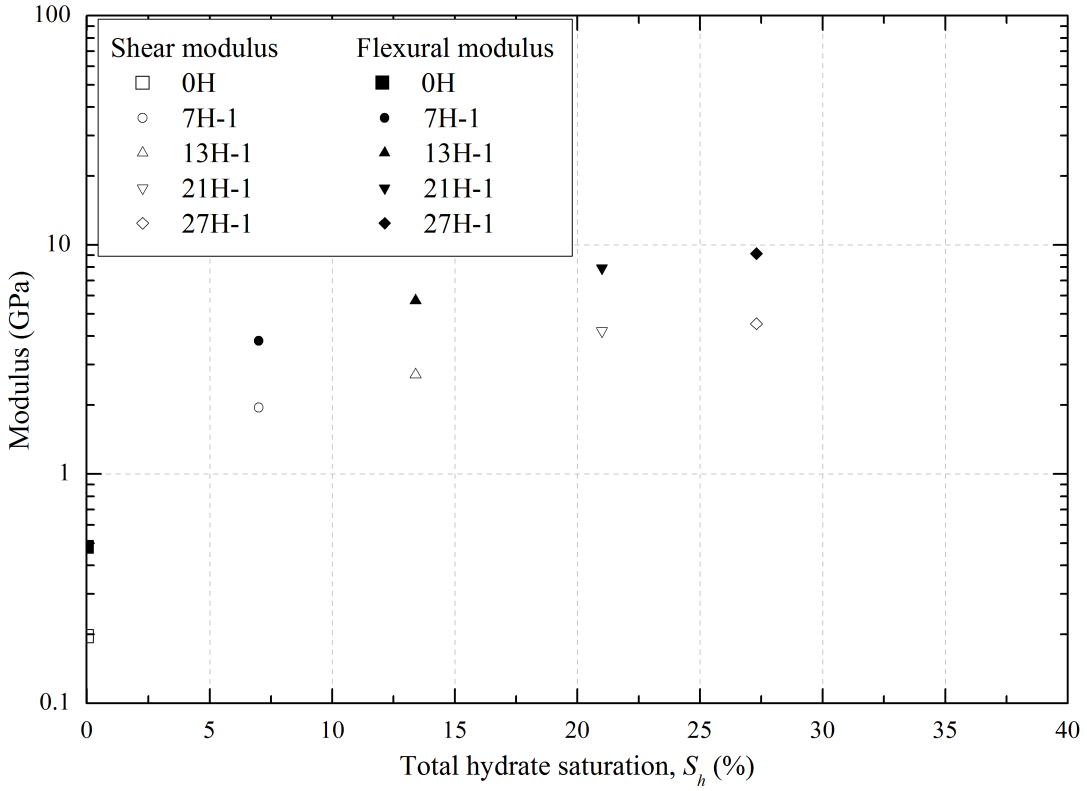

Figure 4.13: *Variation in shear and flexural modulus with total hydrate saturation (S_h) within pore spaces.*

4.2.2 Effect of hydrate saturation

As discussed, hydrate saturation has a significant affect on the specimen stiffness compared to the change in void ratio due to hydrate formation. This can be more clearly see in Figure 4.13 which shows the calculated values of G_{max} and E_{flex} as a function of total hydrate saturation (S_h). Also included are results for specimen number "0H", a dense sand with no hydrate. The results show that the inclusion of the hydrate within the pore space increases the stiffness approximately ten times when compared to the non-hydrate bearing dense sand. This behaviour has been observed previously when the hydrate was formed using the 'excess gas' method (Waite et al., 2004; Clayton et al., 2005).

However, results show that the increase in the stiffness is not linear during hydrate formation (Figure 4.14). It can be seen that when 50% of the hydrate is formed (equivalent to ~7% hydrate saturation for "14H-3") an increase of ~30% in the specimen stiffness is measured. This is somewhat less than the total increase in stiffness for a specimen with 7% hydrate saturation, which has G_{max} and E_{flex}

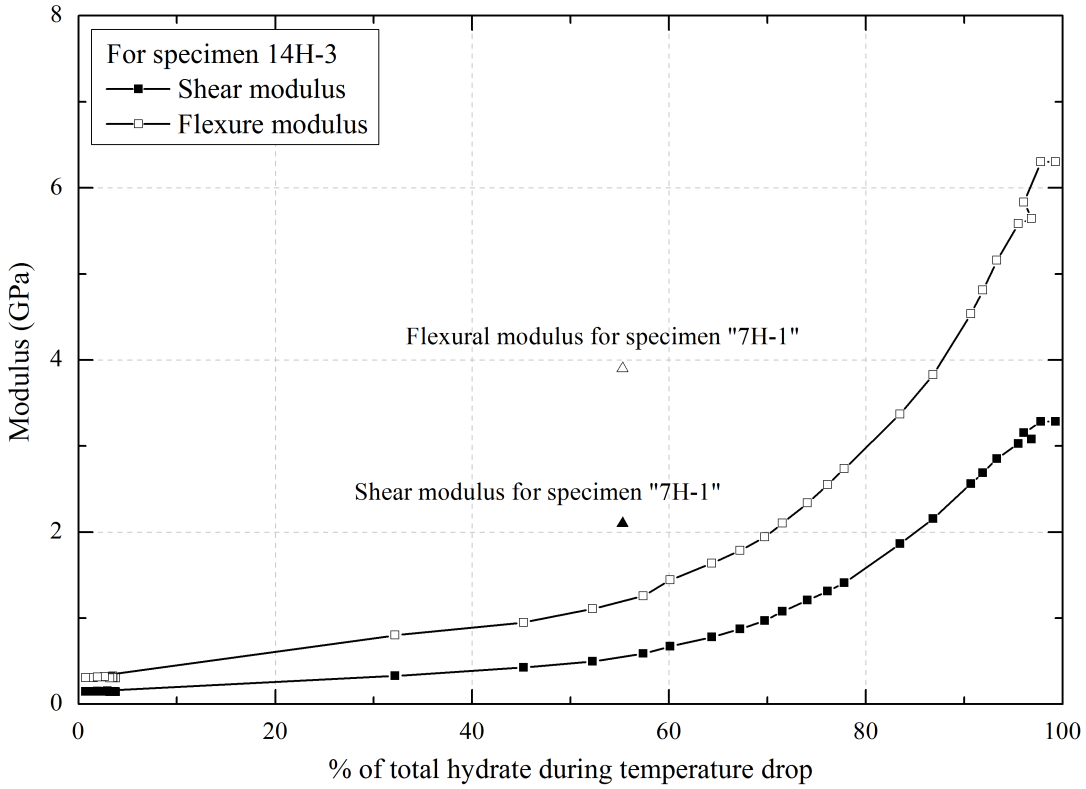

Figure 4.14: *Variation in shear and flexural modulus with % of total hydrate formation (H_f).*

of ~2.1GPa and ~3.9GPa respectively (from Figure 4.13).

In addition, it was found that the hydrate formation led to different increase in the shear and flexural stiffness for sand specimens. This can be clearly seen in Figure 4.15 which shows the variation in flexural modulus (E_{flex}) with shear modulus (G_{max}) for a number of specimens before the start of formation and after complete formation. X-axis and Y-axis values represent, respectively, shear and flexural modulus for the specimens before the start of hydrate formation (without hydrate). Due to large increase in stiffness after complete formation (Figure 4.13), the overall stiffness is normalised by 10 to fit the data within X and Y axis ranges in Figure 4.15, such that the X and Y axis represent, respectively, one tenth of the shear and flexural modulus of the specimens after complete hydrate formation. It can be seen in Figure 4.15, after complete formation stiffness ratio (E_{flex}/G_{max}) was reduced from 2.24 to 2.06 (using best fit lines). This shows that the overall increase in the shear stiffness was more than the overall increase in the flexural stiffness of specimens.

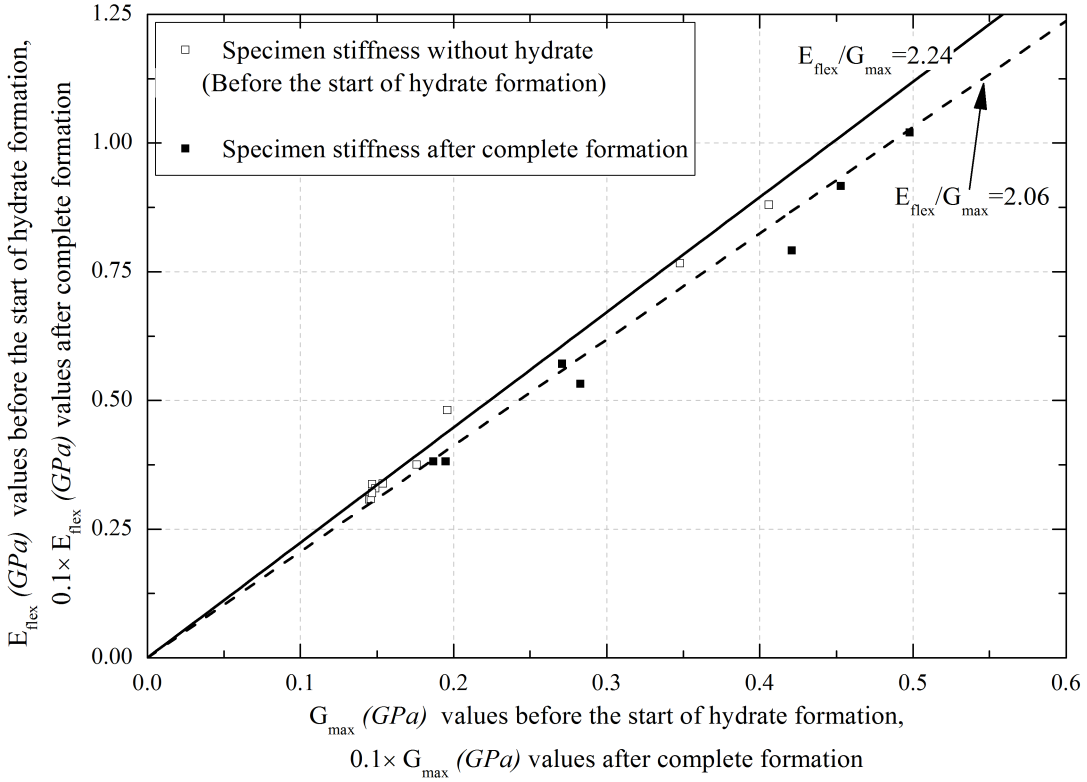

Figure 4.15: *Variation in E_{flex} with G_{max} for a number of specimens.*

The Poisson's ratio (ν) of the specimen can be calculated from the stiffness ratio. However, it should be noted that E_{flex}/G_{max} ratio may not give true Poisson's ratio of the specimen, because using the Cascante equation to derive Young's modulus from the flexural vibration introduces an error ($\sim 10\%$) for the specimen aspect ratio (l/d) of ~ 2 (Appendix B). After correcting the error associated with E_{flex} suggests that the Poisson's ratio ($\nu = \frac{1.1\times E_{flex}}{2\times G_{max}} - 1$) of the specimens after complete formation was reduced to 0.13 from 0.23. The decrease in Poisson's ratio has been observed in different sediments, such as dense sand sediments with increasing effective stress (Saxena and Reddy, 1989), carbonate sands after artificial cementation (Huang and Airey, 1998), and hydrate bearing sediments where hydrate was modelled as cement (Poisson's ratio can be derived using V_p/V_s (Waite et al., 2004)).

In contrast to formation, during hydrate dissociation a decrease in the specimen stiffness was measured. As shown in Figure 4.7, a sharp reduction in the specimen stiffness occurs for a small reduction in hydrate saturation, with specimen stiffness reducing by up to 80% of its value for only a 15% change in the hydrate saturation (for the specimen "13H-1" it is equivalent to a reduction from 10% to 8.5% total

hydrate saturation). This can be more clearly seen in Figure 4.16, which shows the change in G_{max} and E_{flex} with respect to % of hydrate dissociated. It can be seen in Figure 4.16, for ~5% reduction in hydrate saturation about 50% reduction in stiffness occurs while at ~10% of hydrate dissociation about 70% reduction in stiffness occurs. Comparing these values with those obtained during hydrate formation, it can be seen that stiffness is much more sensitive to changes in hydrate saturation during dissociation than during formation (Figure 4.17).

The changes in specimen stiffness during hydrate formation and dissociation suggest that the stiffness is dependent not only the hydrate saturation but also the way it forms and dissociates within the specimen. Using the excess gas method, water initially resides at grain contacts. As hydrate forms at the gas-water interface the hydrate grows inwards into the contact, and as such forms a bridge between the grain contacts which slowly increases in thickness until all the hydrate is formed (Figure 4.18). Thus the early stiffness of the specimen is dependent on the buckling resistance of the hydrate bridge. However during hydrate dissociation, the hydrate shrinks inwards across the whole of its surface area. Since the thermal conductivity of the sand grain is higher than that of the methane hydrate or methane gas (Cortes et al., 2009), it is postulated that dissociation starts at the grain contacts. Thus the cementing effect of the hydrate on grain contacts is lost almost immediately (Figure 4.18). Therefore stiffness of the specimen is derived from the interaction of the sand and hydrate grains, and it becomes more "frame supporting" rather than cementing.

The difference between formation and dissociation can be clearly seen in Figure 4.19, which shows the change in shear modulus with respect to the hydrate saturation for a range of specimens. Also shown for comparison, is the calculated shear modulus obtained from different effective medium models (EMM, using Appendix A). It can be seen from Figure 4.19 that when hydrate is fully formed the increase in shear modulus is such that the hydrate cements the grains. Although, measured shear modulus is less than the calculated shear modulus from EMM (~0.55 times the EMM cementing model). The difference in stiffness suggests that the interaction of gas hydrate with grains may not be adequately described by these models. This might result from the "hydrate cover" not having a smooth surface but rather contains cracks, similar to cemented sandstone (Murphy III et al., 1986). Therefore hydrate bearing sediment stiffness may be a combination of cementation and frame-supporting models (Chand et al., 2004; Clayton et al.,

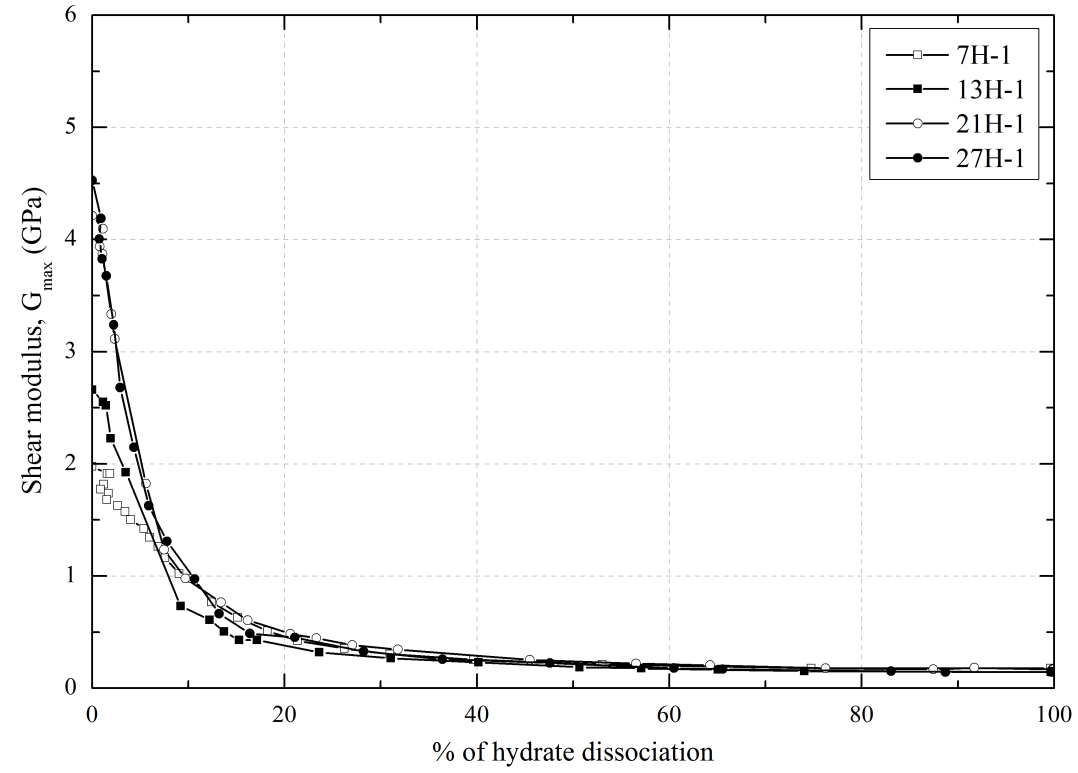

(a)

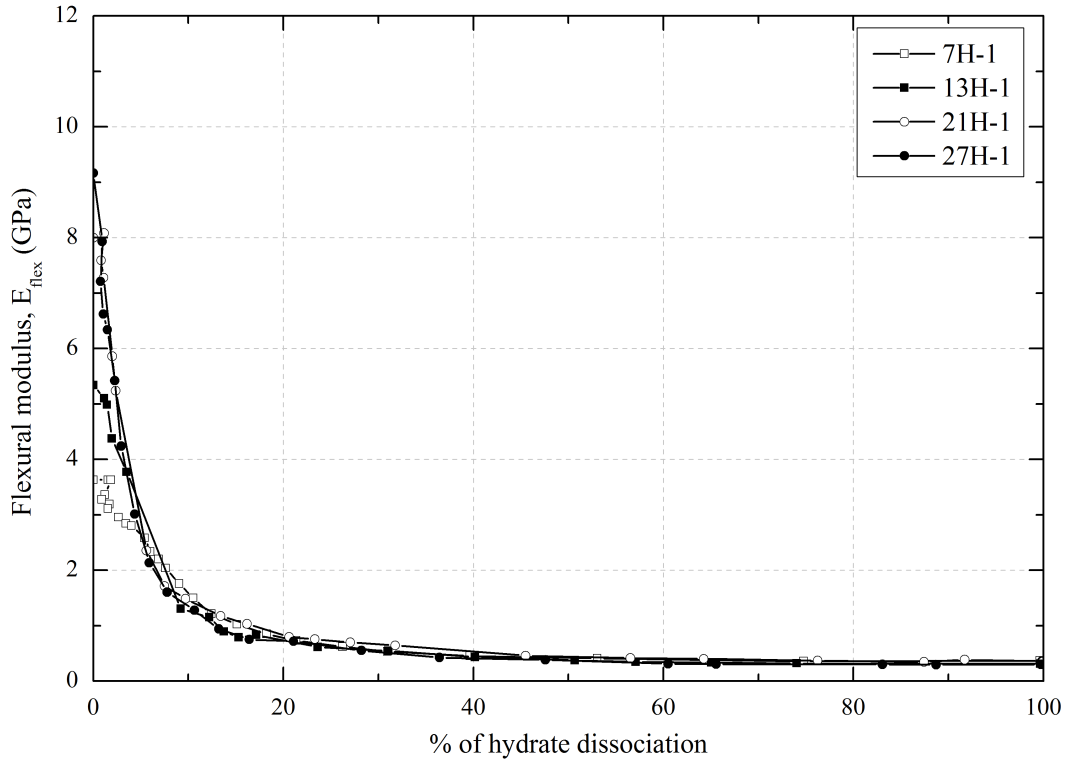

(b)

Figure 4.16: *Variation in (a) shear modulus, and (b) flexural modulus with respect to % of hydrate dissociation (H_d).*

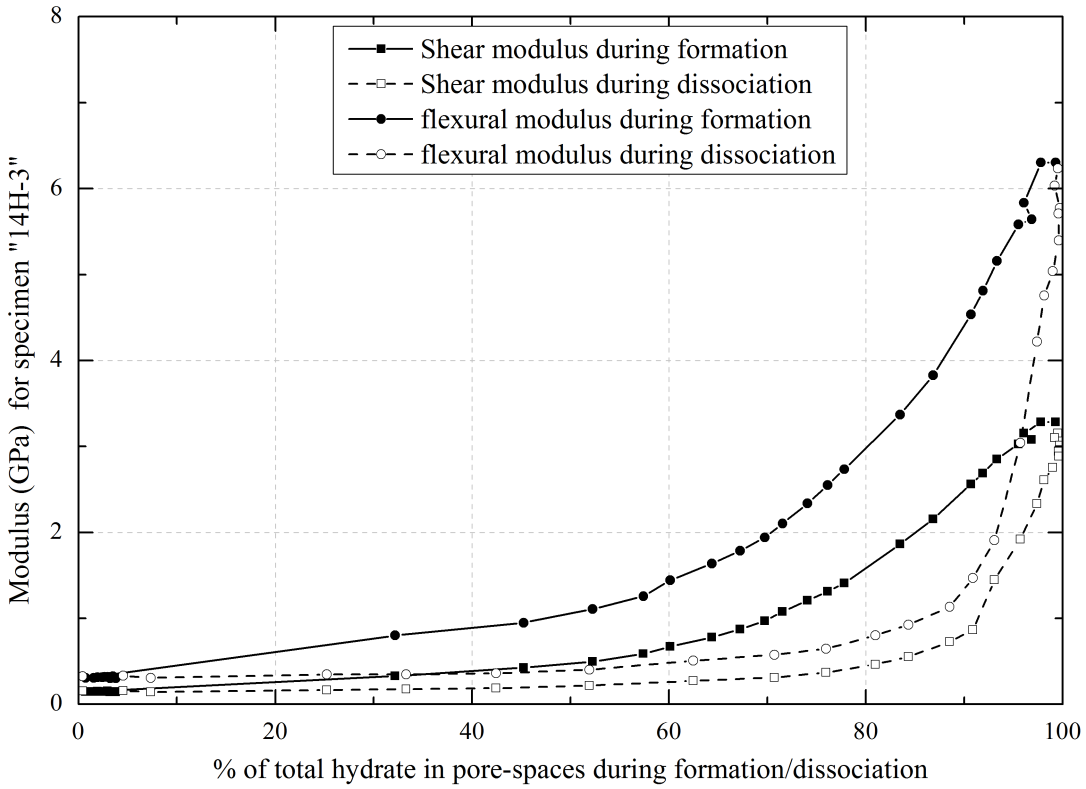

Figure 4.17: *Variation in G_{max} and E_{flex} with % of total hydrate during formation (H_f) and dissociation (H_d) for the specimen "14H-3".*

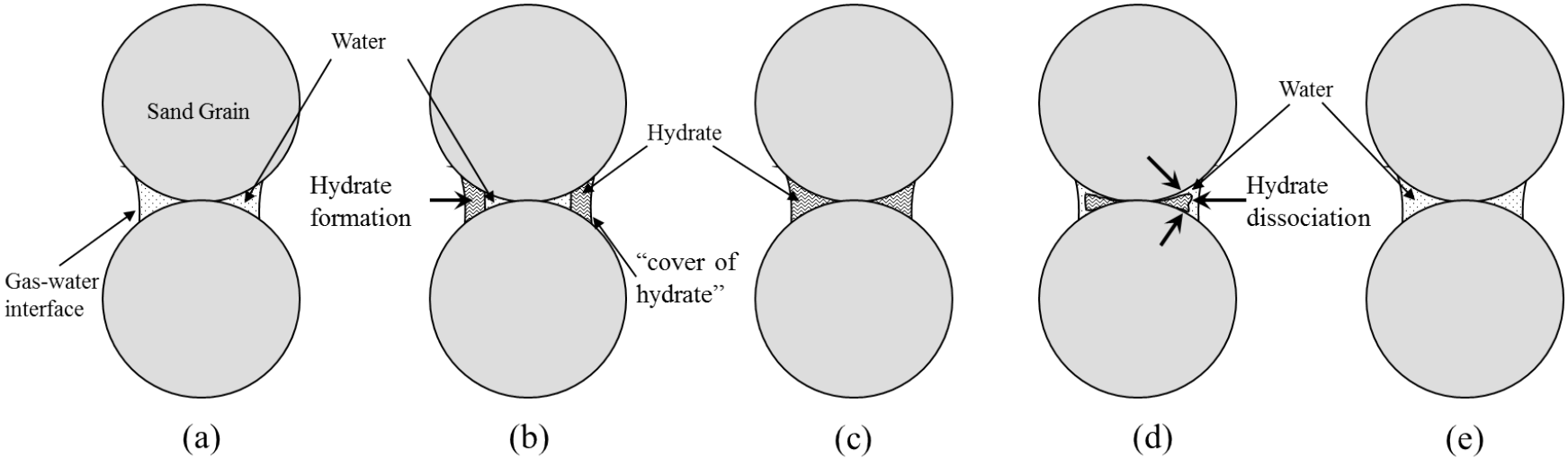

Figure 4.18: *Hypothesised morphological growth of hydrate within specimen during formation and dissociation induced by temperature change; (a) sand grains with water in its pores at thermobaric conditions outside hydrate stability zone, (b) start of hydrate formation that proceeds at water-gas interface with formation of "hydrate cover", (c) at the end of hydrate formation sand grains cemented with hydrates inside the stability zone, (d) start of hydrate dissociation due to temperature rise, and (e) at the end of hydrate dissociation.*

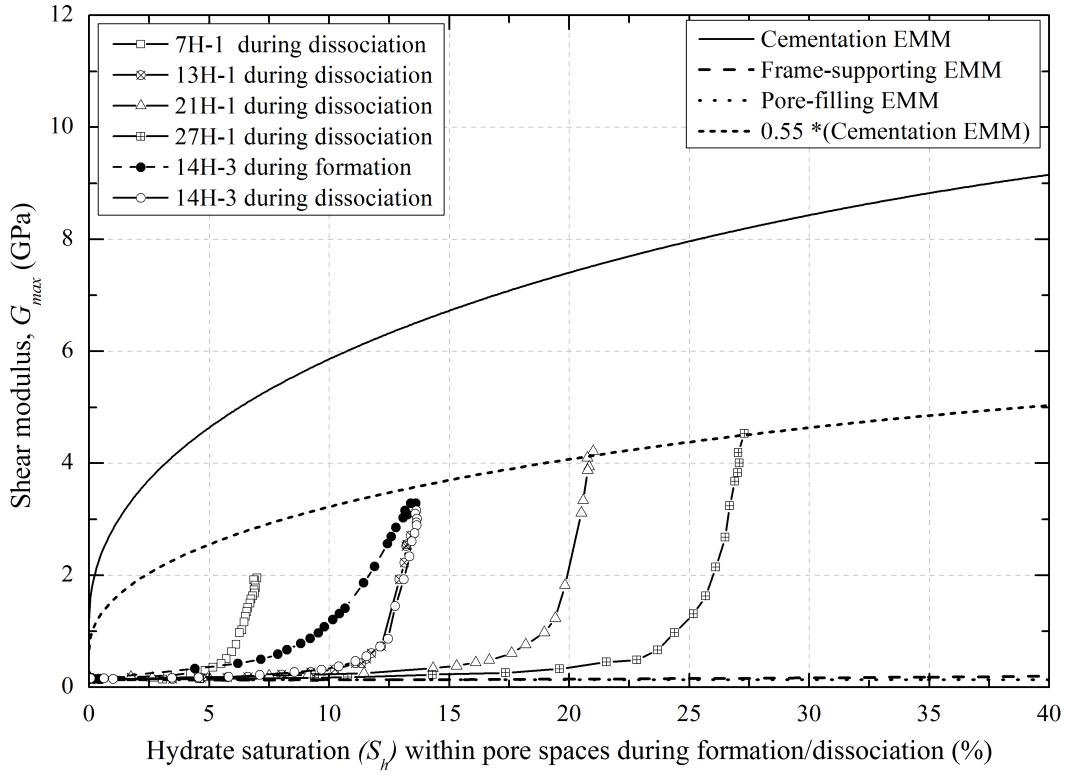

Figure 4.19: *Variation in shear modulus (G_{max}) with amount of hydrate present within the specimen during formation and dissociation stages.*

2005).

Hydrate formation followed by dissociation has no significant effect on the stiffness of dense sand specimen at a given effective stress (Figure 4.20); after complete dissociation stiffness properties of the sediment are similar to the sediment with 0% hydrate content. This is due to the fact that hydrate dissociation converts the hydrate into its constituents (water and gas) without any residual affect on sediment stiffness.

4.2.3 Effect of effective stress

Once hydrate was fully formed at the initial effective stress, resonant column tests were conducted at different effective stresses (250kPa, 500kPa, 1000kPa, and 2000kPa). Figure 4.21 shows the calculated values of G_{max} and E_{flex} as a function of isotropic effective confining pressure. Also included are results for the dense sand with no hydrate (specimen "0H"). It can be seen in Figure 4.21, for the dry sands specimen, $\sim$ 230% increase in stiffness was measured with increasing

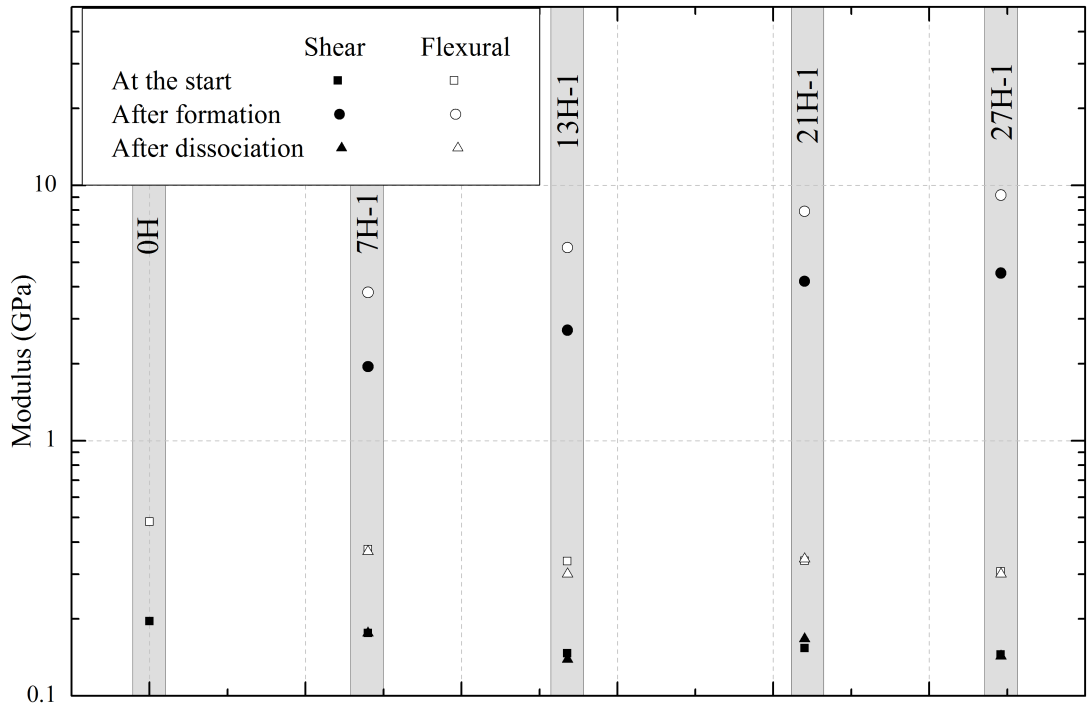

Figure 4.20: *Shear (G_{max}) and flexural (E_{flex}) modulus at the start of test, after hydrate formation, and after dissociation for a number of specimens.*

isotropic confining pressure from 250 to 2000 kPa. However for hydrate bearing sands, the increase in stiffness was $\leq 10\%$ for confining pressure up to $\sim 2000\,kPa$. It can also be seen in Figure 4.21 that hydrate saturation above 21% does not have significant effect on the specimen stiffness. This behaviour can also be seen in EMM cementation model (Figure 4.19) where the increase in cementation from 21% to 27% has little effect on the specimen stiffness.

To investigate the influence of the initial effective stress on the stiffness of hydrate bearing sand sediments, a number of specimens were formed at different effective stresses (2000 to 2800kPa, see Table 4.1). It can be seen in Figure 4.21 that the increase in specimen stiffness during hydrate formation is unaffected by the initial effective stress. This is due to the fact that a large increase in the specimen stiffness occurs by forming hydrate in pore spaces, compared to the minor changes in the stiffness as a function of effective stress (up to 2800kPa). However, it can be noted in Figure 4.21 that the specimen stiffness for the specimens formed at higher effective stress is slightly less compared to the specimens formed at lower effective stress. This could be due to their different densities, void ratios, and hydrate saturations (Table 4.1).

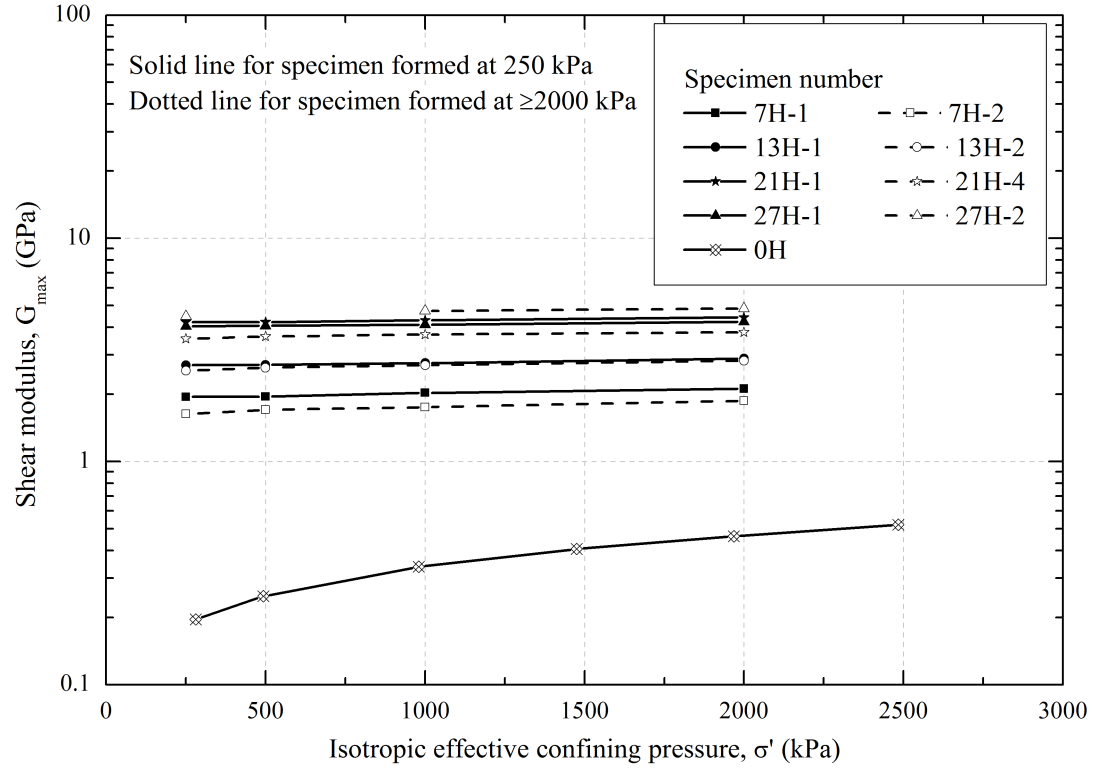

(a)

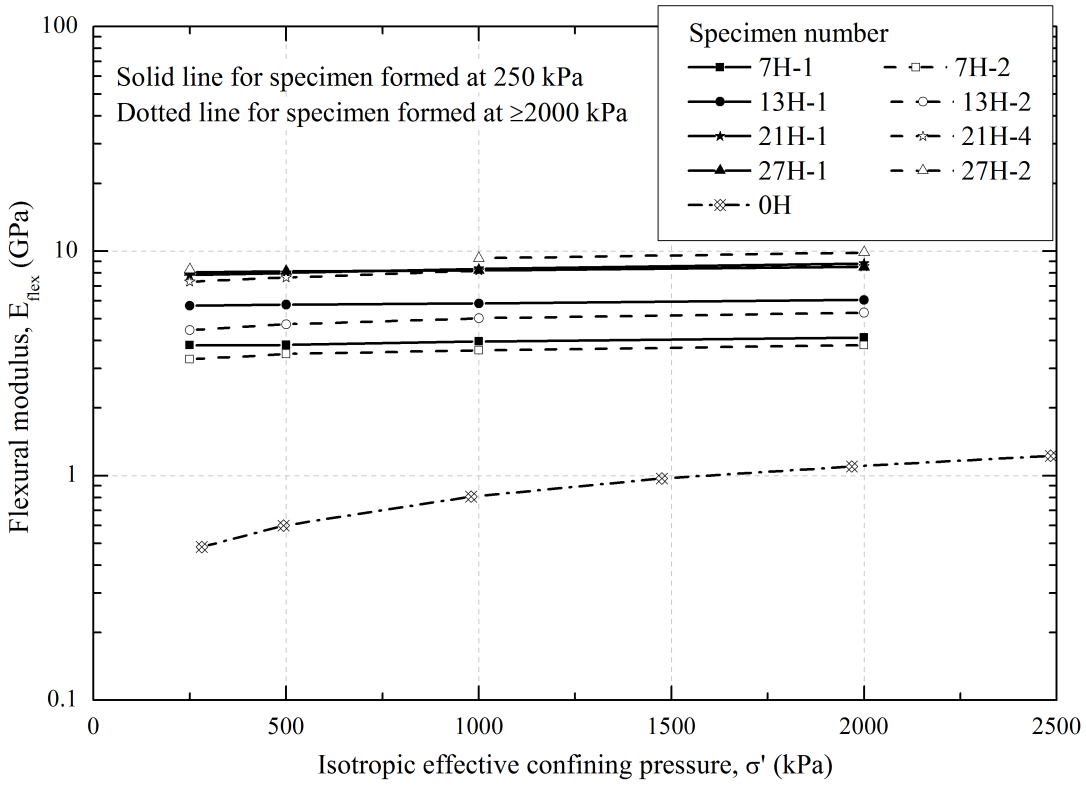

(b)

Figure 4.21: *Variation in (a) shear modulus, and (b) flexural modulus with isotropic effective confining pressure.*

4.2.4 Effect of cyclic strain

As discussed in Chapter 3, after complete hydrate formation resonant column tests were conducted at different strain levels. Figure 4.22 shows the calculated values of normalised shear and flexural modulus as a function of shear strain (γ) and flexural strain (ϵ_{flex}) respectively for the range of specimens listed in Table 4.1. It can be seen in Figure 4.22 that the stiffness degradation is less than 1% for strains $< 5e^{-5}\,p.u.$ for specimen without hydrate and $< 2e^{-6}\,p.u.$ for specimen after complete hydrate formation. To calculate G_{max} and E_{flex} from the shear and flexure resonance frequencies, the lowest strain was applied during formation and dissociation stages; such that during the formation stage, strain was decreasing from $\sim 5e^{-5}$ to $\sim 2e^{-6}\,p.u.$, and during dissociation stage the strain was increasing from $\sim 2e^{-6}$ to $\sim 5e^{-5}\,p.u.$ (Figure 4.22). Therefore it is a reasonable assumption that the stiffness measured during these stages (formation and dissociation) was within 1% of the maximum stiffness, and it can be considered that the strain applied was within the linear threshold limit.

It can also be seen in Figure 4.22 that the linear threshold limit for hydrate bearing sands is at a lower strain than the non-hydrate bearing sands. A number of researchers have also reported that cemented soils have a lower linear threshold limit compared to uncemented soils (Saxena et al., 1988; Pestana et al., 2006). This is due to the fact that the hydrate cements the grains which makes the specimen brittle (Pestana et al. (2006) after Saxena et al. (1988)), and therefore stiffness begins to degrade at a lower strain level.

4.2.5 Effect of dissociation methodology

In general, hydrate dissociation can be induced by increasing temperature or reducing pressure in order to take the hydrate outside the stability field. Therefore to investigate the influence of dissociation methodology, two hydrate bearing specimens ("21H-4" and "26H-4") were formed through a temperature drop under a constant effective stress condition ("CES") of 2000kPa. After $\sim 52\,hours$, the effective stress within the specimen was reduced to $\sim 250\,kPa$ and then the dissociation was induced by quickly (in $\sim 6\,seconds$) reducing the back pressure to $\sim 2300\,kPa$ at $\sim 5.5^oC$, which was outside the hydrate stability field. Back pressure was isolated whilst maintaining a cell pressure of $\sim 6\,MPa$ so that the

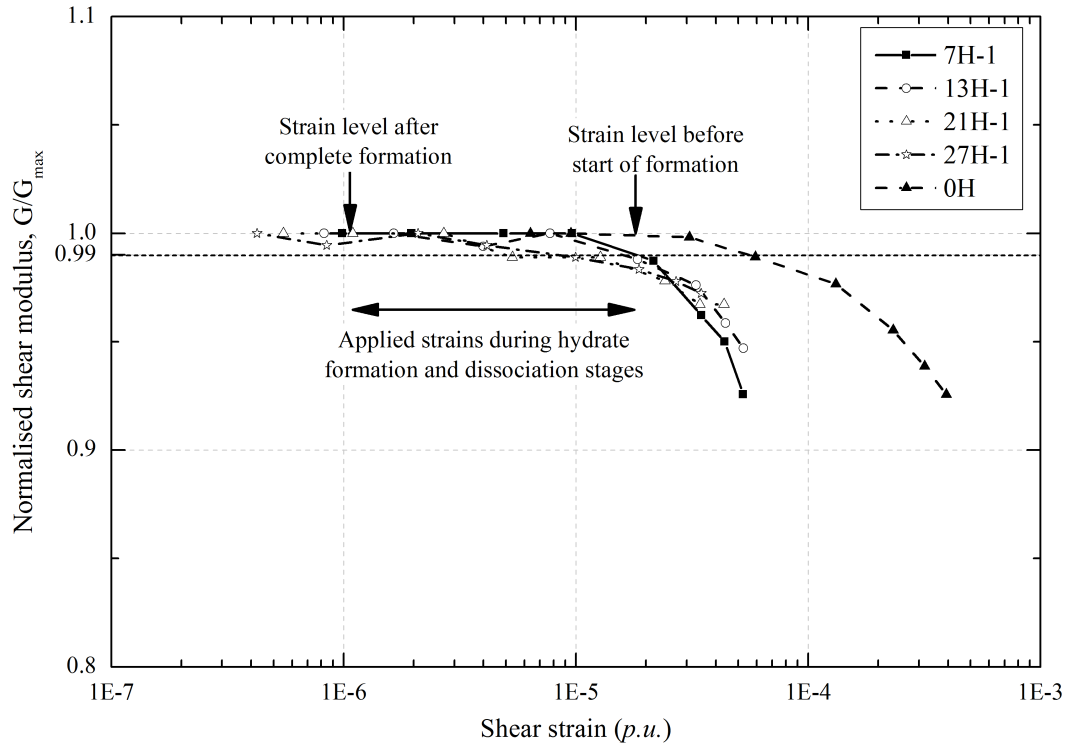

(a)

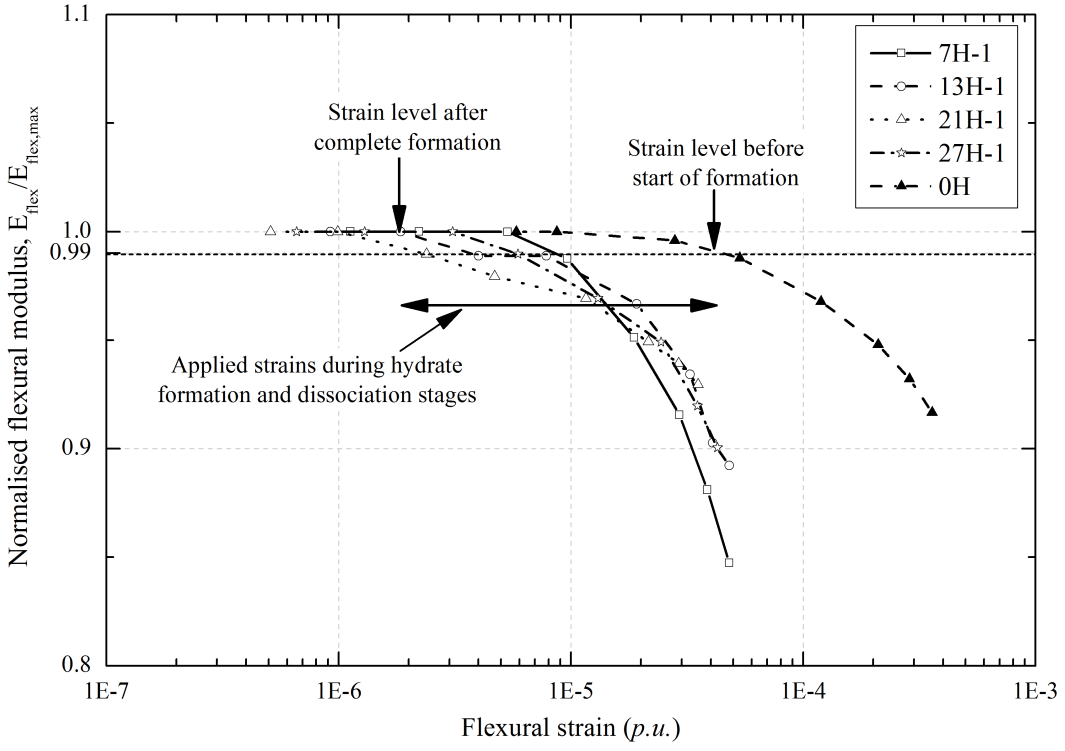

(b)

Figure 4.22: *Variation in normalised (a) shear modulus, and (b) flexural modulus as a function of strain.*

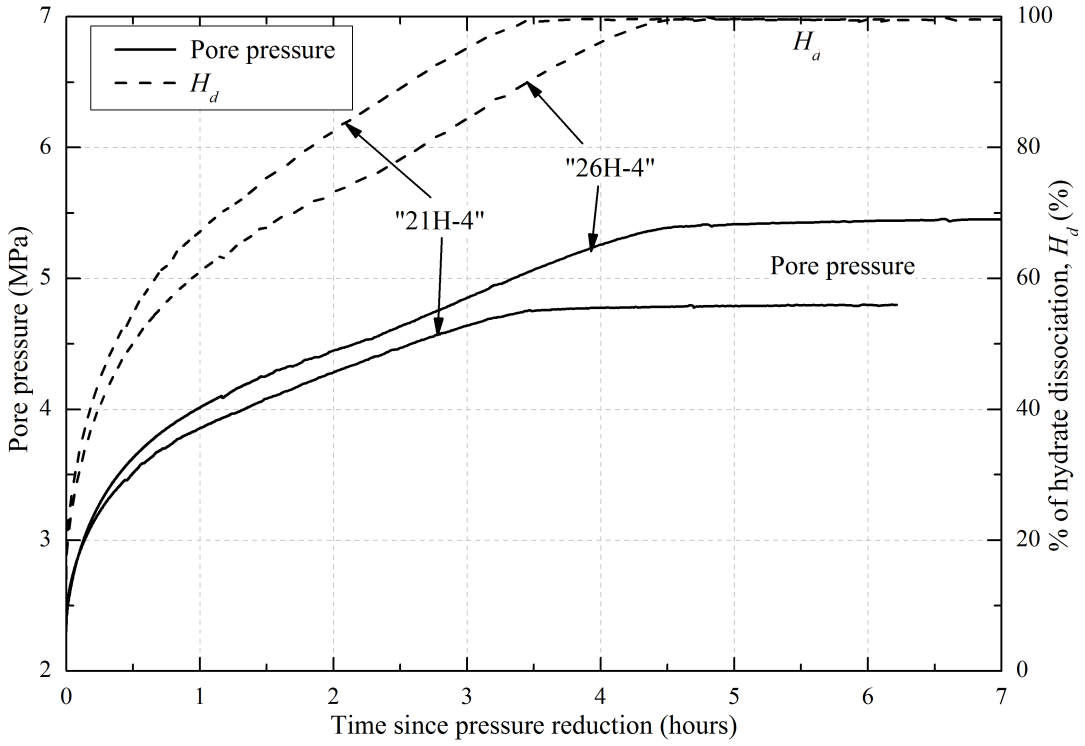

Figure 4.23: *Variation in cell pressure, back pressure, and % of hydrate dissociation for specimens "21H-4" and "26H-4" during dissociation stage.*

rise in pore pressure during dissociation could be measured (Figure 4.23).

Figure 4.24 shows the variation in shear modulus with the degree of hydrate formation and dissociation. As discussed, the volume of hydrate dissociated is calculated from the associated rise in pore pressure using the Peng-Robinson Equation 3.36. For specimens "21H-4" and "26H-4", the pore pressure was reduced to $\sim 2300\,kPa$ in $\sim 6\,seconds$, and during this short period up to ~13% of the hydrate was calculated to have dissociated (Figure 4.23). The percentage of total hydrate dissociated is calculated from the associated rise in moles of methane gas during dissociation with respect to the total moles of gas consumed during formation. The first resonant frequency after pressure reduction was measured when ~20% of hydrate had dissociated (Figure 4.24(b)).

It can be seen in Figure 4.24(a) that the increase in G_{max} with % of hydrate formed is gradual for all three specimens. This may be due to the hydrate formation starting at the water and gas interface and then grows inwards (Figure 4.18). In contrast during dissociation a rapid decrease in G_{max} with initial changes in hydrate saturation was measured for all specimens where dissociation occurred

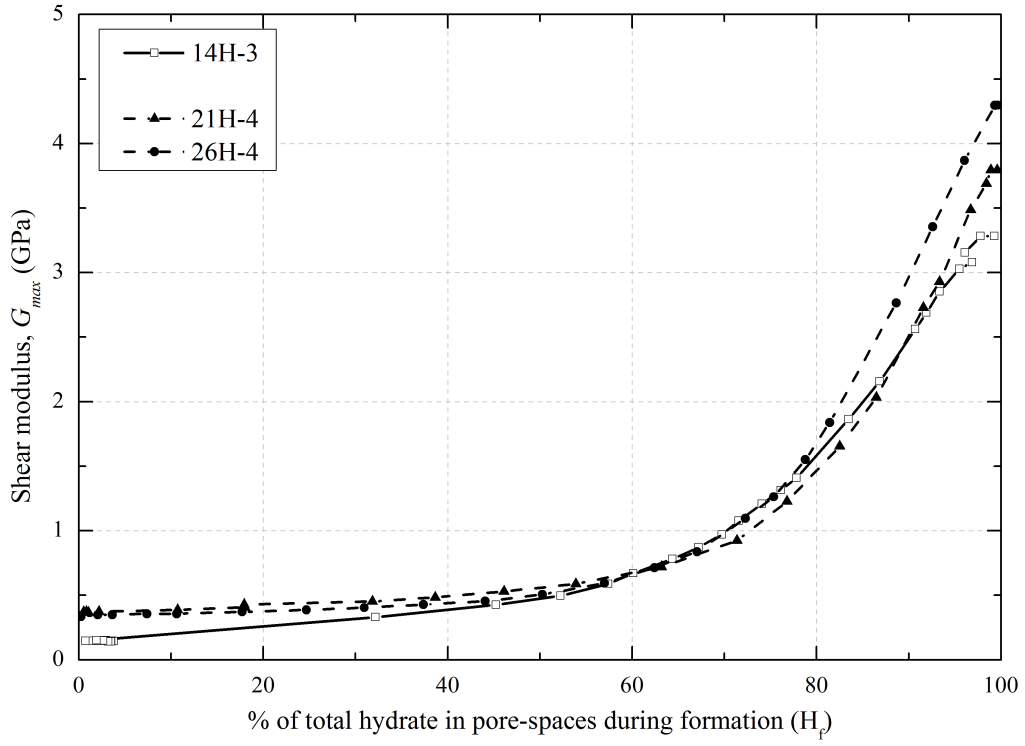

(a)

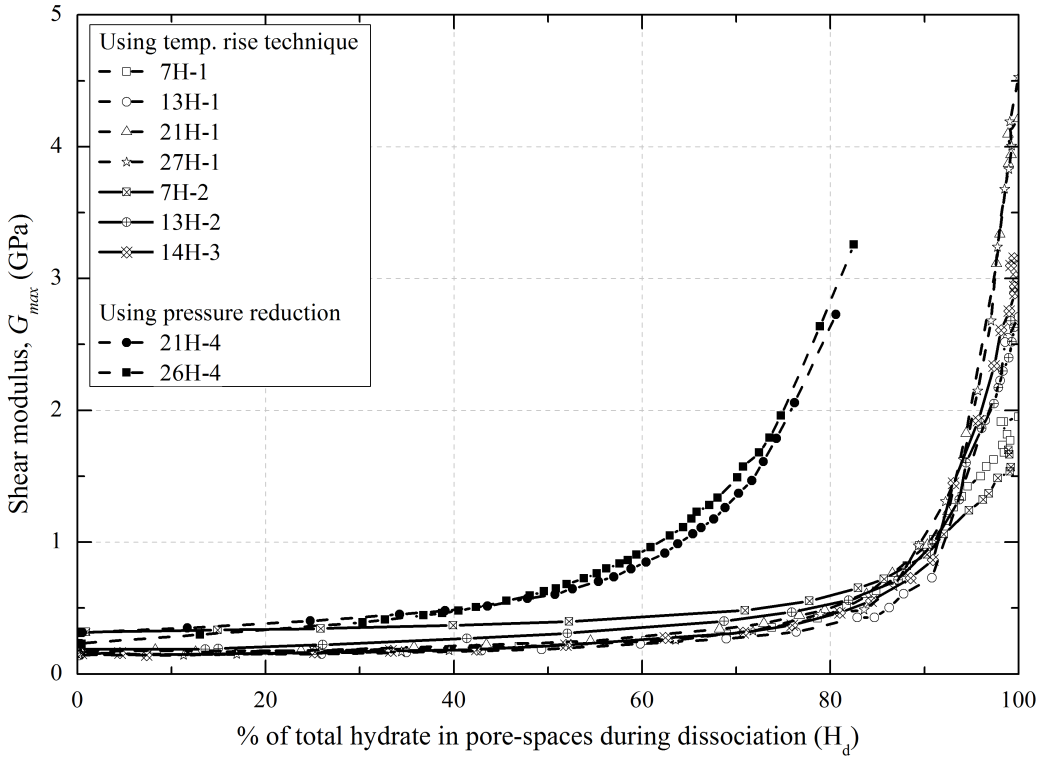

(b)

Figure 4.24: *Variation in G_{max} with % of total hydrate for a number of specimens dissociated through temperature rise and pressure reduction techniques during (a) formation, and (b) dissociation stages.*

due to temperature rise (Figure 4.24(b)), but for specimens ("21H-4" and "26H-4") that were dissociated using pressure reduction technique a slower reduction occurred (Figure 4.24(b)).

This can be more clearly seen in Figure 4.25, which shows the shear modulus (G_{max}) with % of hydrate dissociated for two specimens "21H-1" and "21H-4" that were dissociated using temperature rise and pressure reduction techniques respectively. For a comparison the normalised G_{max} values are also shown. Normalised G_{max} is a ratio of the shear modulus measured during dissociation to the shear modulus measured before the start of dissociation. It can be seen in the Figure 4.25 that for ~20% reduction in hydrate saturation about ~90% reduction in shear modulus occurred for specimen "21H-1", whereas ~20% reduction in shear modulus occurred for specimen "21H-4" for the same amount of dissociation (~20%). This could be due to the higher initial effective stress at the start of dissociation for specimen "21H-4" (~3700 kPa) compare to ~250 kPa effective stress for specimen "21H-1". However, similar to specimen "21H-1", a large reduction in the shear modulus occurred for specimens "7H-2" and "13H-2" that were dissociated at higher initial effective stress (~2000kPa) using temperature rise technique (Figure 4.24(b)).

The observed behaviour could be due to different fundamental mechanisms for these two dissociation methods. As discussed, hydrate dissociation starts at grain contacts through increase in temperature (Figure 4.26) due to the fact that the thermal conductivity of sand grains is high compared to the methane hydrate or gas. Therefore, a sharp reduction in specimen stiffness occurred during dissociation. On the other hand, when dissociation was induced through pressure reduction the change in the stability condition might have occurred at solid-fluid interfaces (in this case hydrate-gas and grain-gas interfaces) within the pore space, such that dissociation started at the interface of hydrate and gas (Figure 4.26). Therefore a gradual loss of cementation occurred, thus gradual reduction in specimen stiffness. However, at the end of dissociation specimen stiffness was measured to be equal to a non-hydrate bearing sand specimen irrespective the dissociation methodology was used.

To understand the reduction in stiffness within 20% of hydrate dissociation for specimens "21H-4" and "26H-4", the stiffness degradation curves are tentatively extrapolated as shown in Figure 4.27. It can be seen in Figure 4.27 that ~5% reduction in specimen stiffness occurs for ~10% of hydrate dissociation. This may

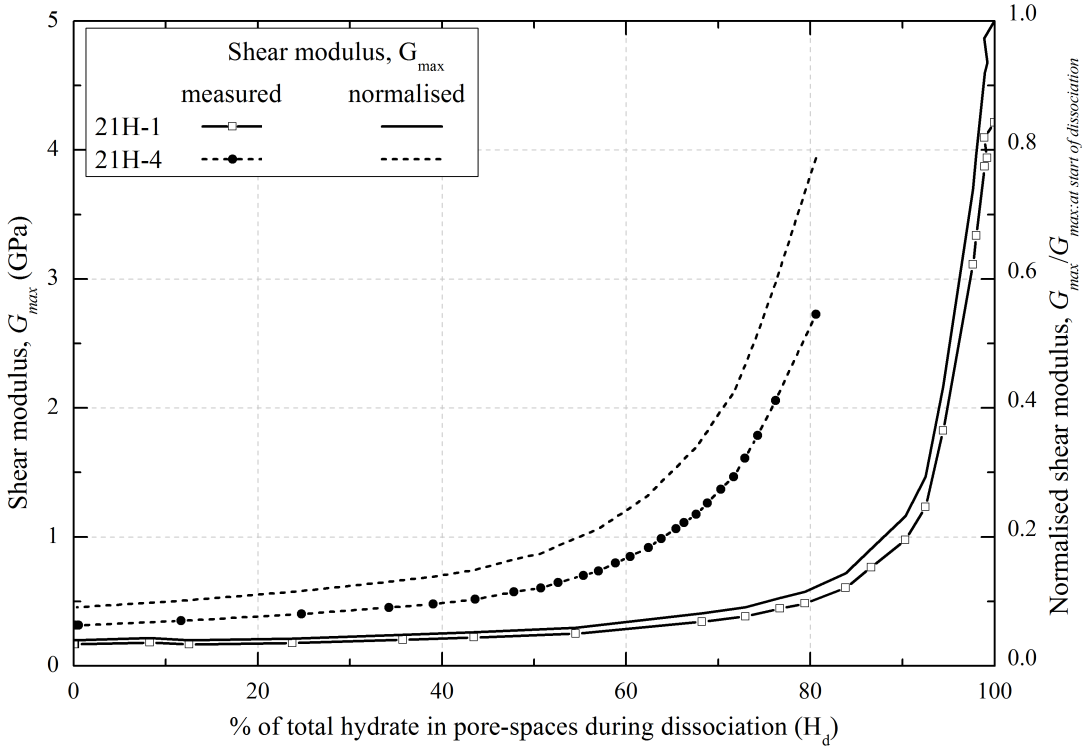

Figure 4.25: *Variation in measured and normalised shear modulus with % of hydrate dissociation for specimens "21H-1" and "21H-4".*

be due to the higher initial effective stress ($\sim 3700\,kPa$) just after the start of dissociation which compensates the reduction in specimen stiffness due to the loss of a thin layer of hydrate at the edge of hydrate-gas interface.

4.2.6 Comparison with previous literature

As discussed in Chapter 2, the hydrate morphology within a specimen depends on the hydrate formation methodology. For example, the excess gas method produces a cementing morphology, whilst the excess water method produces a frame supporting morphology (Waite et al., 2004; Clayton et al., 2005; Priest et al., 2009). In the GHRC, both these methodologies have previously been used to synthesise methane hydrate in sand sediments (Priest, 2004; Rees, 2009). Figure 4.28 shows the variation in specimen stiffness with hydrate saturation for specimens that were formed at $\sim 250\,kPa$ effective stress under drained condition. For a comparison previous researchers data are also shown (from Priest (2004); Rees (2009)). It can be seen in Figure 4.28 that the present research results are comparable to the previous results which used the excess gas method. Also

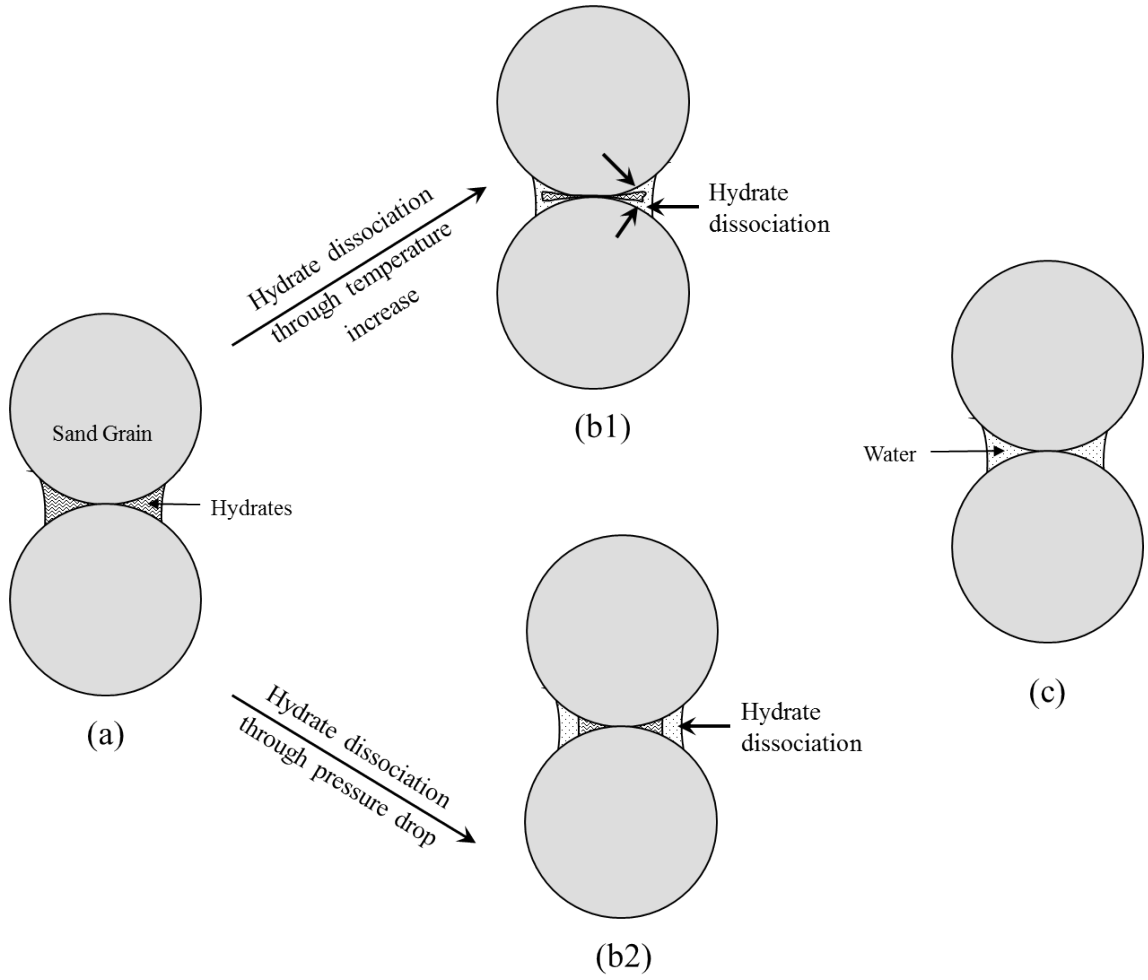

Figure 4.26: *Hypothesised morphological growth of hydrate within specimen during dissociation; (a) at the end of hydrate formation sand grains cemented with hydrates inside the stability zone, (b1) start of hydrate dissociation due to temperature rise (from Figure 4.18), (b2) start of hydrate dissociation due to pressure drop, and (e) at the end of hydrate dissociation.*

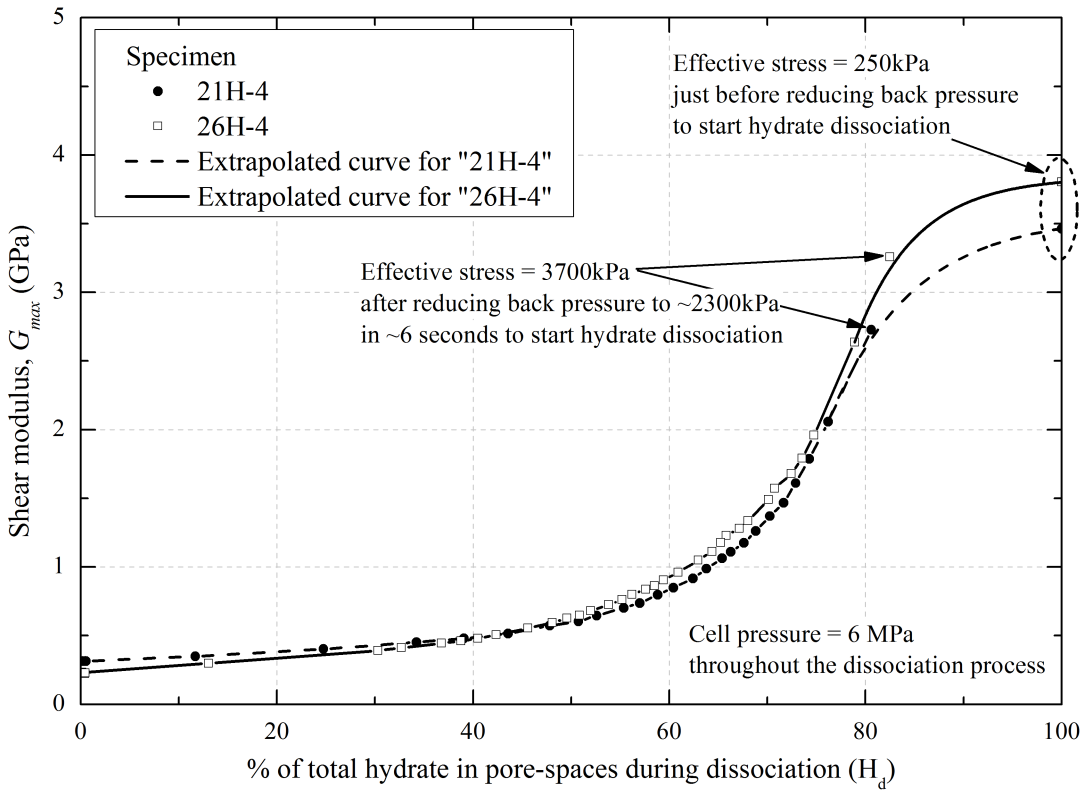

Figure 4.27: *Variation in measured and extrapolated shear modulus with % of hydrate dissociation for specimens "21H-1" and "21H-4".*

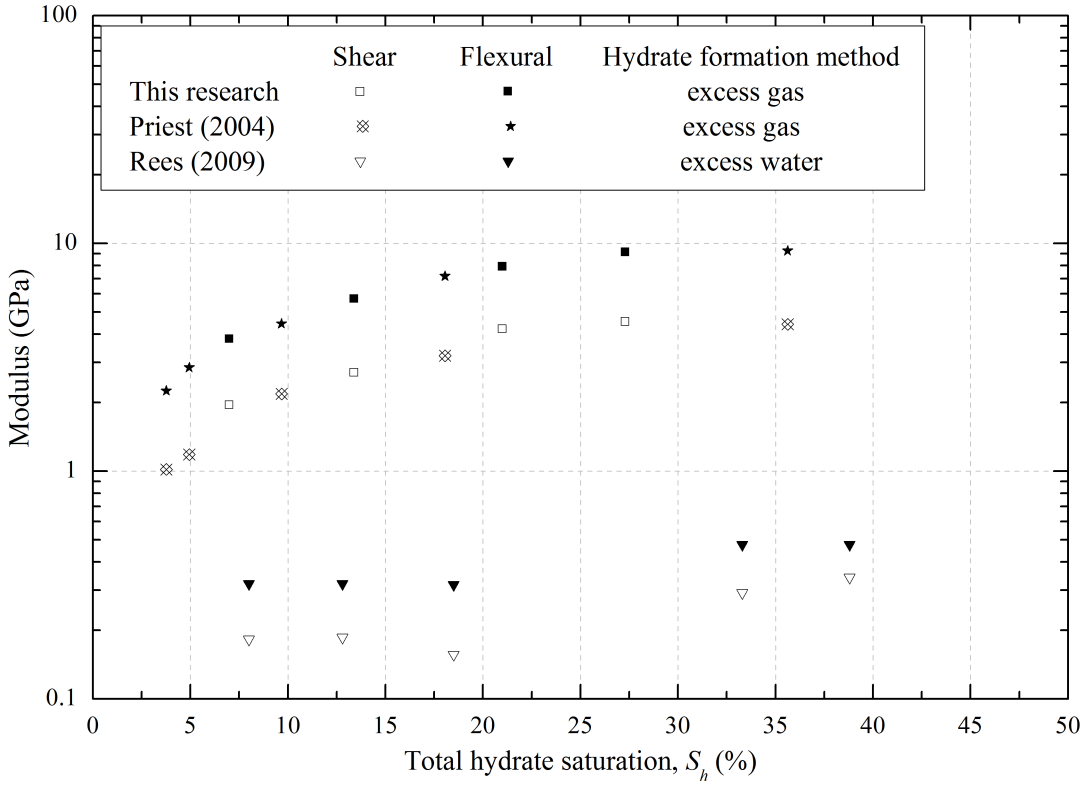

Figure 4.28: *Variation in shear and flexural modulus with hydrate saturation from this research (Figure 4.20) and previous researches (Priest, 2004; Rees, 2009).*

noted in Figure 4.28, the excess gas formation results in a significant increase in sediment stiffness (up to ~35% of total hydrate saturation) compared with a negligible change in sediment stiffness through the excess water method.

As discussed in Chapter 2, natural oceanic sediments may have different hydrate morphological growth. However, natural hydrate bearing sediment properties are remotely inferred from higher seismic velocities compared to the adjacent sediments. To attribute higher wave velocities within a disseminated hydrate bearing sediment, hydrate should have interacted with grains such that it exhibits frame supporting and/or cementing morphologies. The interaction of natural hydrate within a sediment as frame supporting and/or cementing morphologies has also been suggested through comparison of field data (from Mackenzie Delta and Black Ridge sites) to numerical models (Chand et al., 2004). As discussed in Subsection 4.2.2, hydrate dissociation through temperature change starts at grain contacts. Therefore, sediment with significantly higher stiffness in the presence of hydrate may lose significant stiffness even for small amounts of dissociation.

In general, sediment with higher stiffness will be associated with higher peak shear strength. This has been observed in cemented sand (Consoli et al., 2007) and hydrate bearing sediment (Masui et al., 2005; Yun et al., 2007). Higher peak shear strengths have been measured for hydrate bearing sediments that were formed using the excess gas method compared to these sediments formed using the excess water method (Table 2.3 in Chapter 2). Natural oceanic hydrate bearing sediments exhibit higher stiffness therefore it is expected to exhibit higher peak shear strength. Therefore, hydrate dissociation induced by temperature rise may result in a sharp reduction in shear strength of a natural sediment even for a small amount of dissociation.

4.3 Pore pressure change

As discussed in Chapter 1, $1\,m^3$ of methane hydrate contains $164\,m^3$ of methane gas under standard temperature and pressure conditions. Therefore, hydrate dissociation may generate excess volume of pore fluids increasing pore pressure within the sediment under undrained conditions. This section discusses the measured change in pore pressure within specimens during hydrate dissociation process, and compares the values with an analytical model.

4.3.1 Experimental results

To investigate the effect of dissociation on pore pressure, a number of tests were conducted whilst back pressure was closed off during the hydrate dissociation stage. As discussed in Chapter 3, dissociation tests were performed either under undrained ("U") or at constant effective stress ("U-CES") conditions, such that any change in pore pressure would result from the change in system temperature and/or hydrate dissociation. Figure 4.29 shows the typical variation in pore pressure and effective stress under undrained conditions with respect to increase in specimen temperature. For reference, the expected rise in pore pressure resulting from the expansion of free methane gas is also shown. It can be seen in Figure 4.29 that as the specimen temperature rises a minor change in pore pressure occurs due to the expansion of free methane gas. As the specimen temperature reaches the hydrate stability curve a rapid increase in pore pressure occurs due

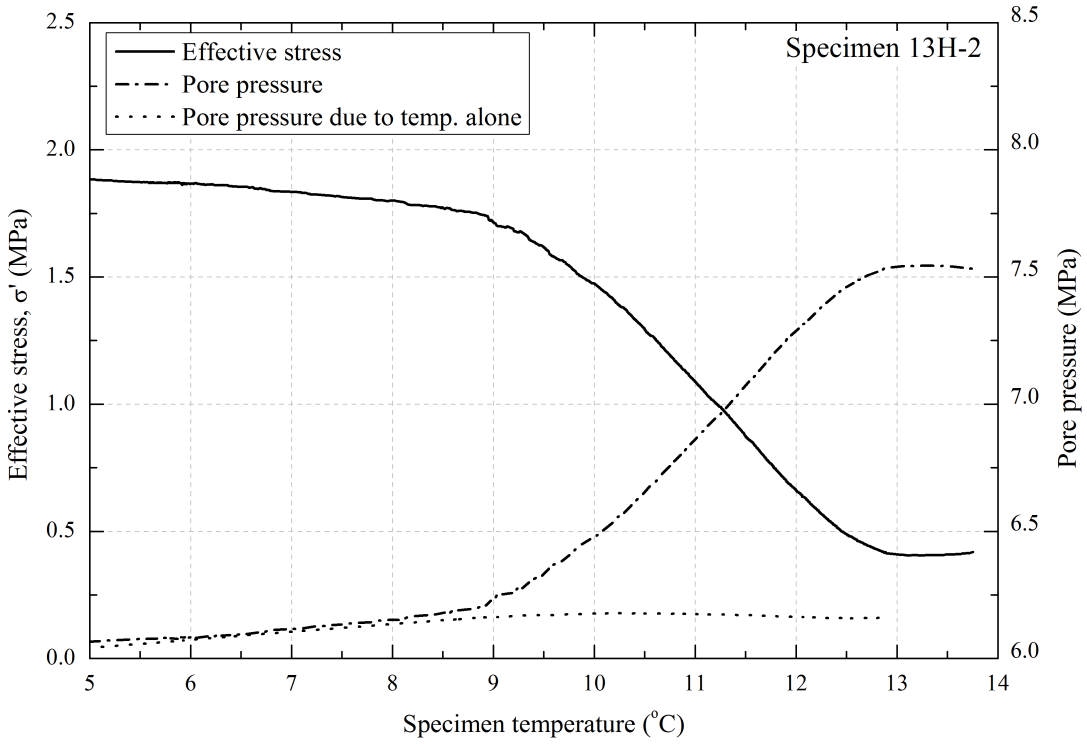

Figure 4.29: *Variation in pore pressure and effective stress for specimen "13H-2" with temperature rise.*

to dissociation of the hydrate, causing a large reduction in effective stress (Figure 4.29).

Figure 4.30 shows the increase in pore pressure due to hydrate dissociation for a number of specimens. The test data are slightly scattered for the specimen "21H-1" because the external thermistor temperature data are used due to failure of the internal thermistor. As discussed, the external thermistor was located at the mid height of the specimen on its outer surface, and nitrogen gas (located at room temperature) was used to raise the cell pressure to maintain the effective stress. Therefore as the cell pressure was raised it effected the temperature of the gas, and fluctuation occurred at the external thermistor. It can be seen in the Figure 4.30 that hydrate dissociation under undrained conditions can significantly increase the pore pressure within a sediment. It can also be seen that the overall increase in pore pressure depends on the volume of hydrate dissociated within the specimen.

The reduction in effective stress may result in a decrease in sediment stiffness. Figure 4.31 shows the variation in shear modulus, G_{max}, and effective stress with

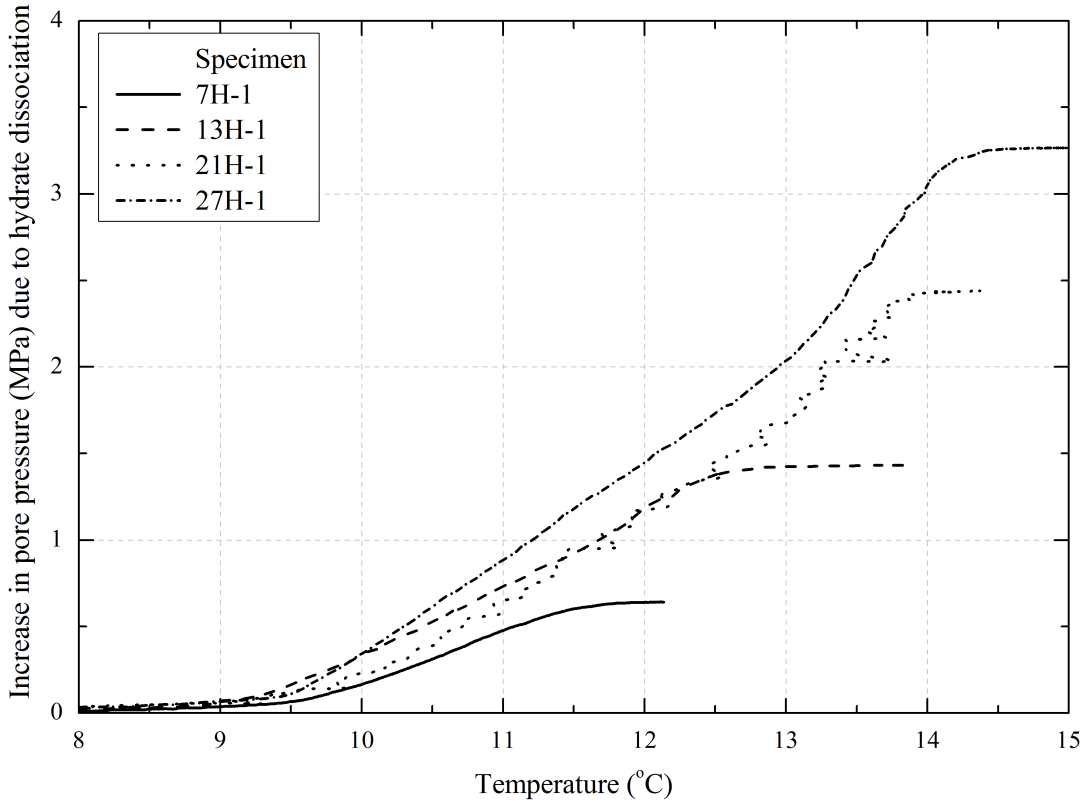

Figure 4.30: *Variation in increase in pore pressure due to hydrate dissociation during temperature rise stage.*

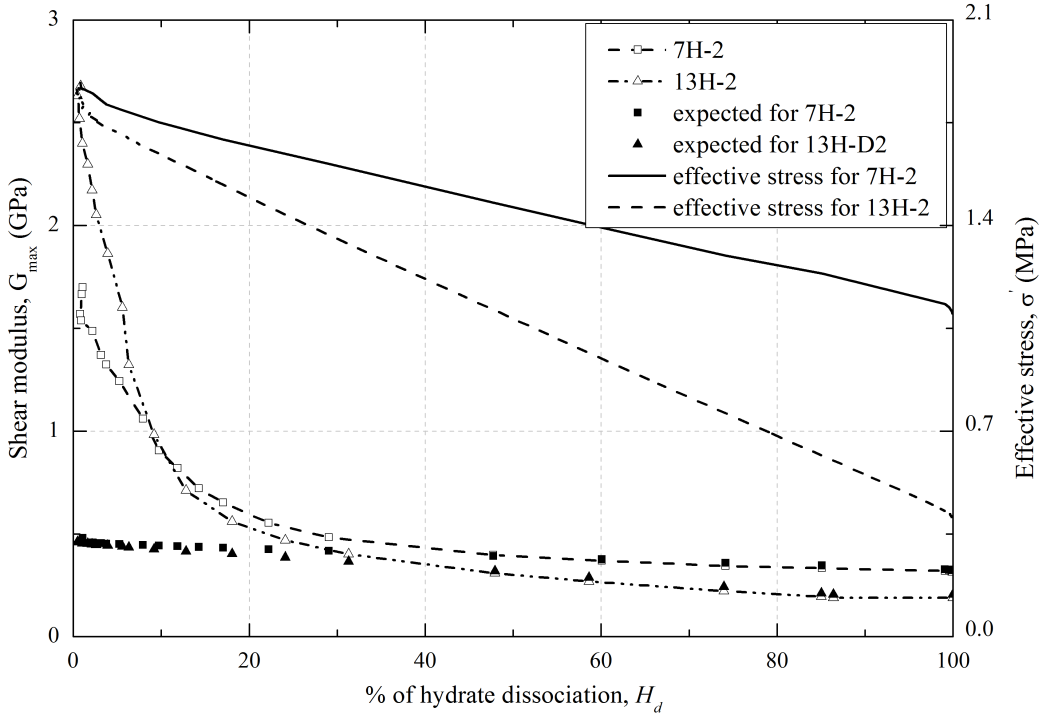

Figure 4.31: *Variation in shear modulus and effective stress with % of hydrate dissociation. Also included the expected G_{max} derived using Equation 4.3.*

% of hydrate dissociation for specimens that were dissociated under undrained ("U") conditions. For a comparison the expected values of G_{max} as a function of change in effective stress are also shown. The expected values of G_{max} are derived using Equation 4.3 and material coefficient, A_{av} from Table 4.3. It can be seen from Figure 4.31 that after $\sim$ 10% of initial dissociation the stiffness is the same for specimens "7H-2" and "13H-2". Similar behaviour was also observed for specimens that were dissociated under constant effective stress ("U-CES") conditions (Figure 4.16). This is due to the loss of cement at the grain contacts. However, as the cementation is lost the specimen stiffness depends on the effective stress (for $\geq$ 50% of hydrate dissociation in Figure 4.31).

4.3.2 Comparison with analytical model

An analytical model was developed to compare the experimental pore pressure evolution during hydrate dissociation. In the model, it was considered that all the water was converted into methane hydrate. The model descriptions are presented in Section C.2 (Appendix C).

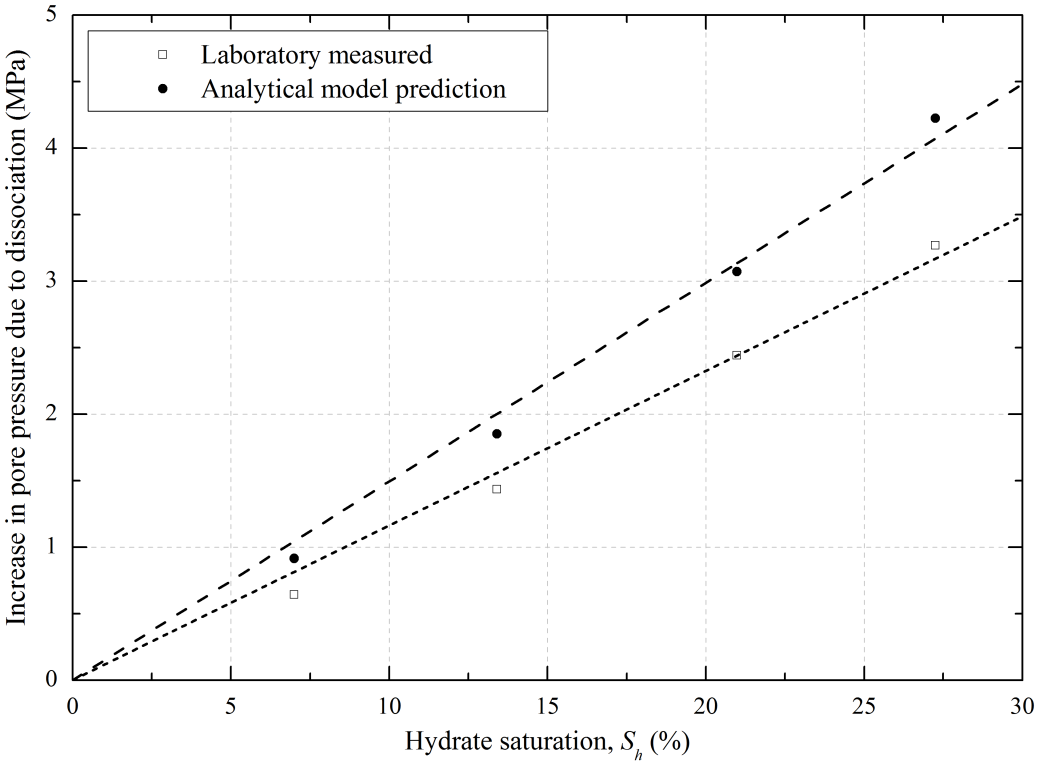

Figure 4.32: *Variation in measured (from Figure 4.30) and predicted pore pressure rise due to hydrate dissociation. The predicted pore pressure rise is calculated using analytical model with the assumption that all water was converted into hydrate of* 100% *methane cage occupancy.*

Figure 4.32 shows the predicted increase in pore pressure due to hydrate dissociation based on the initial water content and specimen dimensions for a number of specimens. It can be seen in Figure 4.32 that the measured increase in pore pressure during dissociation is smaller than the expected pore pressure rise. These differences in pore pressure change could be due to;

- Hydrate saturation: All the water in pore space was not converted into hydrate during the formation process thus reducing hydrate saturation.
- Cage occupancy: Methane molecules did not fill all the hydrate cages and so hydrate structure did not have 100% cage occupancy.

As discussed in Chapter 2, hydrate is a non-stoichiometric material, and thus all cages may not necessarily be occupied by methane gas. A number of researchers have also reported lower cage occupancy of methane in artificial and natural methane hydrate samples (Sloan (1998, p. 223); Huo et al. (2003); Sun and Duan

(2005)). During testing negligible changes in pore pressure (Figure 4.33(a)) and stiffness (Figures 4.33(b) and 4.9) were evident after $40-50\,hours$. This suggests that the water to hydrate conversion process had ceased. Therefore the hypothesis with regard to methane cage occupancy appears the most likely.

Comparison of laboratory measured pore pressure evolution during dissociation with the results from the analytical model suggests that the methane within the hydrate occupied $\sim 77\%$ of available cages (Figure 4.34). To investigate the effect of initial starting pore pressure on methane cage occupancy, specimen "14H-3" was prepared at higher initial back pressure (~11 MPa, Figure 4.33(a)). However it can be seen in Figure 4.34 that the specimen "14H-3" also had $\sim 77\%$ methane cage occupancy.

4.3.3 Sensitivity analysis of material properties

Comparison of analytical and experimental data suggest that methane cage occupancy may have a significant influence on the pore pressure rise during dissociation. However, there are a number of other factors which can also affect pore pressure evolution during dissociation, such as water saturation, methane solubility in water, methane hydrate density, initial pore pressure within sediment, bulk modulus of sediment, and hydrate saturation. If a specimen is water saturated, it would be expected to produce higher pore pressure during dissociation due to less pore volume being available for methane gas. The effect of such parameters on the pore pressure evolution due to hydrate dissociation are discussed.

As noted in the analytical model (Appendix C), fourteen different material properties are required to calculate pore pressure change due to hydrate dissociation (P_{diss}) using Equations C.1 to C.11. Out of these fourteen properties, two properties can be considered as constant; density of water ($\rho_w = 1000\,kg/m^3$), and molar mass of water ($M_w = 18.015\,g/mol$). Molar mass of hydrate can be calculated as,

$$M_{hy} = 5.75 \times M_w + cage \times M_{methane}, \tag{4.4}$$

Where, $M_{methane}$ ($= 16.04\,g/mol$) is molar mass of methane gas, and $cage$ is cage occupancy of the methane in hydrate. For 100% cage occupancy, molar mass of methane hydrate (M_{hy}) is $119.63\,g/mol$. The pore pressure rise is calculated

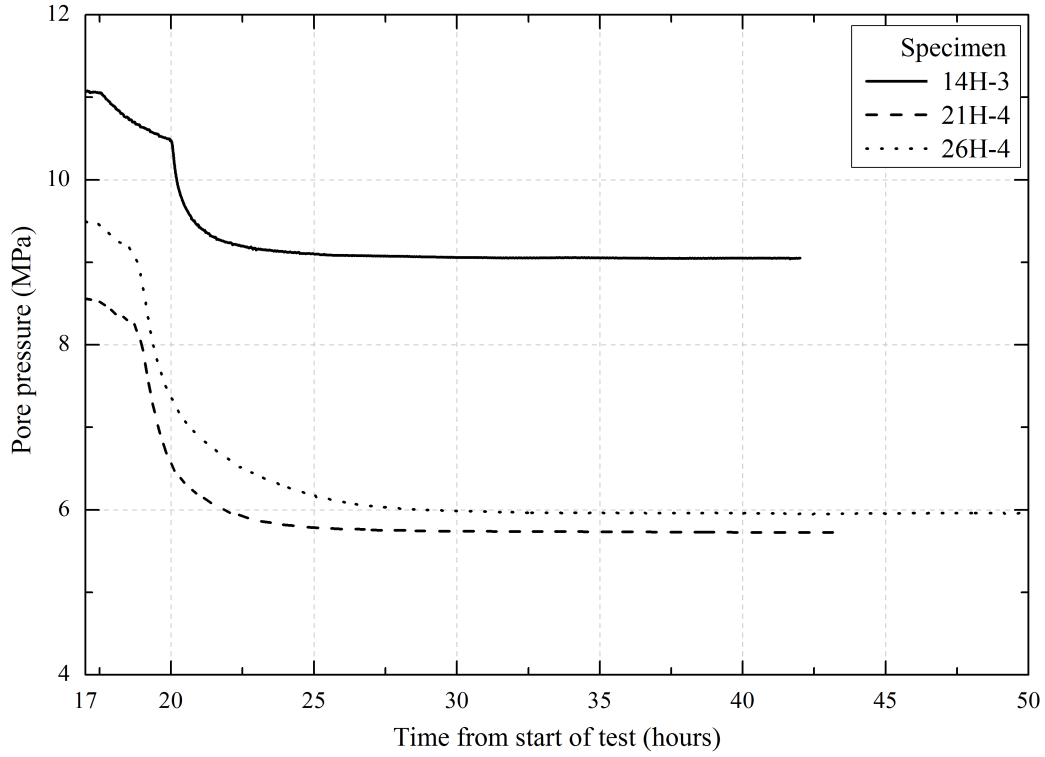

(a)

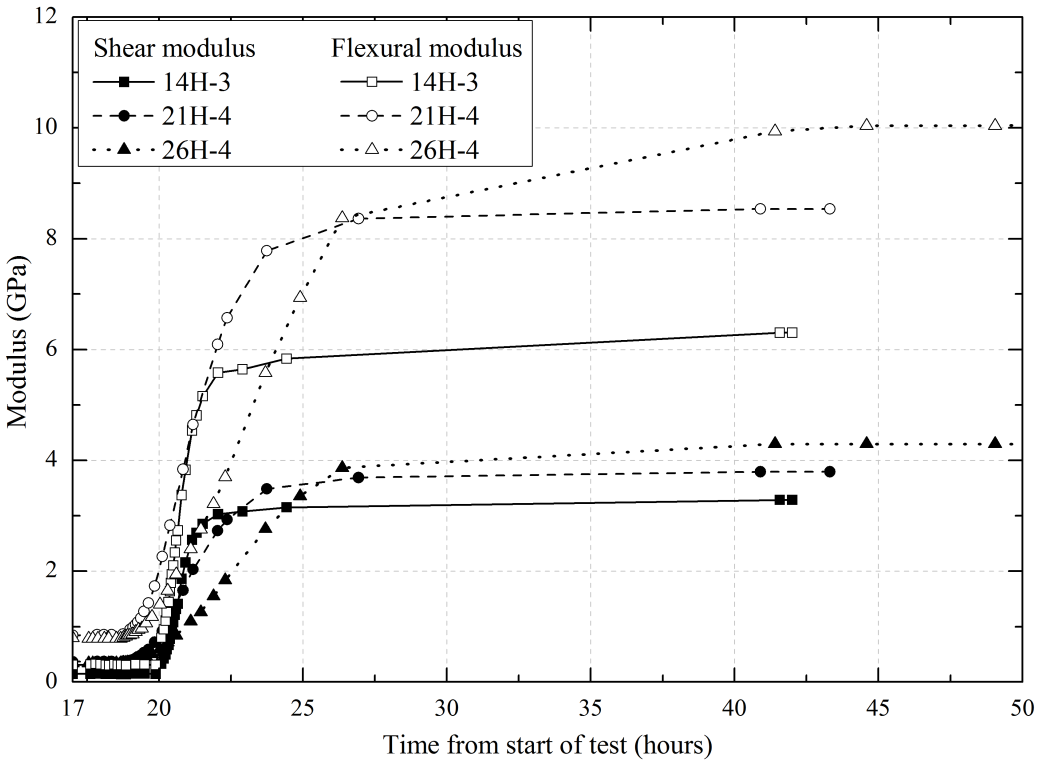

(b)

Figure 4.33: *Variation in (a) pore pressure, (b) shear and flexural modulus for all tests performed under constant effective stress conditions ("CES") during formation stage.*

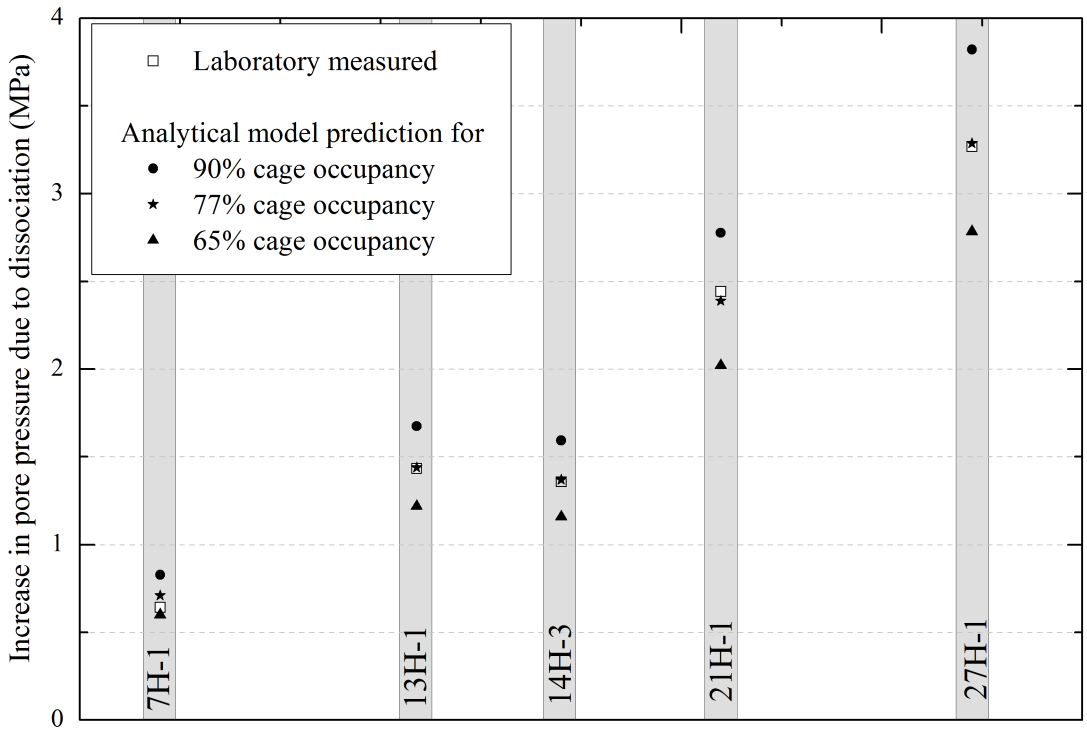

Figure 4.34: *Predicted pore pressure rise due to hydrate dissociation assuming various methane cage occupancy, for a number of specimens. Also shown the measured pore pressure rise for the specimens.*

Material properties	Analytical model (A) parameters for gas and water saturated sediment				
	A_{sol}	A_{cage}	$A_{\rho_{hy}}$	$A_{P_{in}}$	A_K
Hydrate density, ρ_{hy} (kg/m^3)	917	917	900 to 920	917	917
Bulk modulus, K (GPa)	0.30	0.30	0.30	0.30	0.30 to 2
Cage occupancy, $cage$ (%)	100	60 to 100	100	100	100
Initial pressure, P_{in} (MPa)	6	6	6	6 to 30	6
Hydrate content, S_h (%)	0 to 100	0 to 100	0 to 100	0 to 100	0 to 100
Gas solubility in water, sol_m (mol/mol)	0 to 0.005	0	0	0	0

Table 4.4: *Different sets of material properties used in different sets of analytical models.*

for hydrate dissociation using Equation C.11 (Appendix C), therefore it is not affected by the initial and final sediment temperatures (T_{in}, T_{fin}).

To determine the sensitivity of various material properties to the increase in pore pressure during dissociation, a number of analyses were carried out by varying different material properties. In the analyses, it was assumed that a soil sediment had initial volume, V_{in} $(= 1m^3)$ with initial porosity ϕ_{in} $(= 0.4)$ at initial temperature T_{in} $(= 4^0C)$. Hydrate was dissociated under undrained conditions by increasing the sediment temperature to T_{fin} $(= 14^0C)$. To calculate the increase in pore pressure due to complete hydrate dissociation within the sediment, it was considered that all the hydrate was dissociated during temperature rise (4^0C to 14^0C). Table 4.4 presents the various material properties which were used in the analyses. Each column represents a set of material properties that are used in the analyses for gas saturated, and water saturated sediment. Gas saturated hydrate bearing sediments are sediments in which all the pore spaces are filled with methane hydrate and methane gas ($S_{w:in} = 0$) before the start of hydrate dissociation. And for the water saturated sediments, all the pore spaces are filled with methane hydrate and water ($S_h + S_{w:in} = 1$).

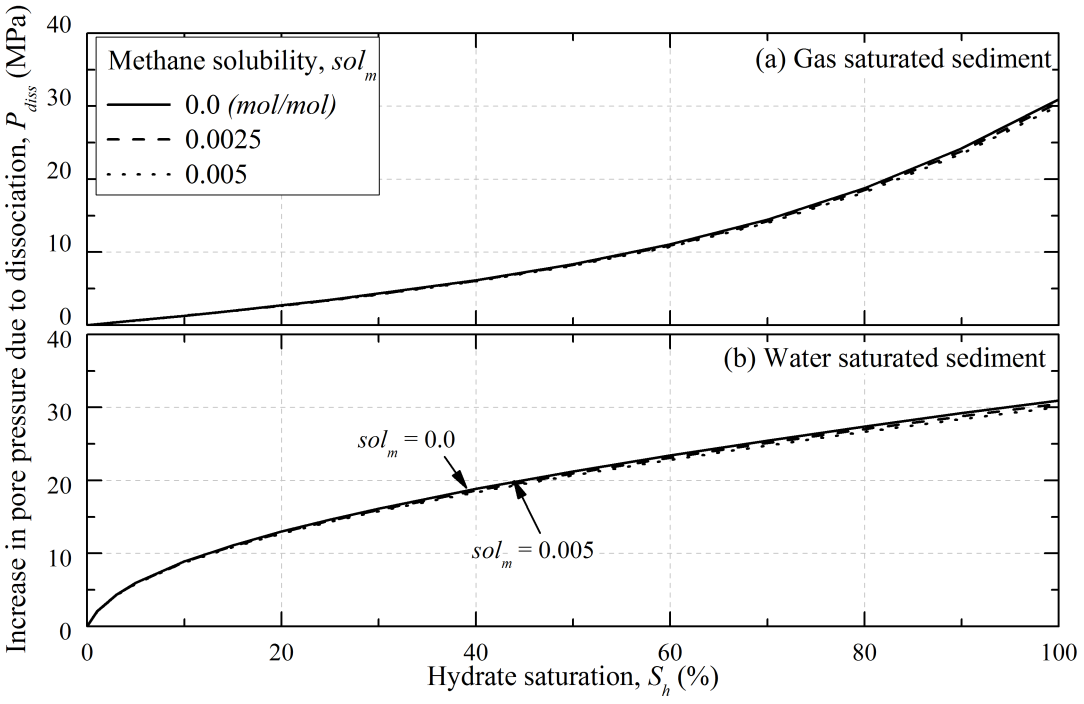

Figure 4.35: *Variation in P_{diss} with S_h for different gas solubility values (sol_m). Initial material properties of sediment are used from Table 4.4 (of column A_{sol}) for (a) gas saturated, and (b) water saturated sediment.*

Methane solubility

In general, methane gas solubility in water varies from 0 to 0.0025 mole fraction for a wide range of temperature and pressure conditions (Chapoy et al., 2004; Hashemi et al., 2006). For this range, the analytical model shows that pore pressure rise is not significantly affected by the gas solubility (<=0.0025) for both water and gas saturated sediments (Figure 4.35). Therefore methane gas solubility can be neglected in the analyses ($sol_m = 0$).

Methane cage occupancy

Figure 4.36 shows the increase in pore pressure during dissociation under undrained conditions using material properties highlighted in Table 4.4 (Column A_{cage}). It can be seen that methane cage occupancy has a significant effect on the pore pressure rise for both water and gas saturated sediments. This is due to the fact that the hydrate with higher cage occupancy yields large amount of gas within the sediment, and thus large increase in pore pressure occurs under

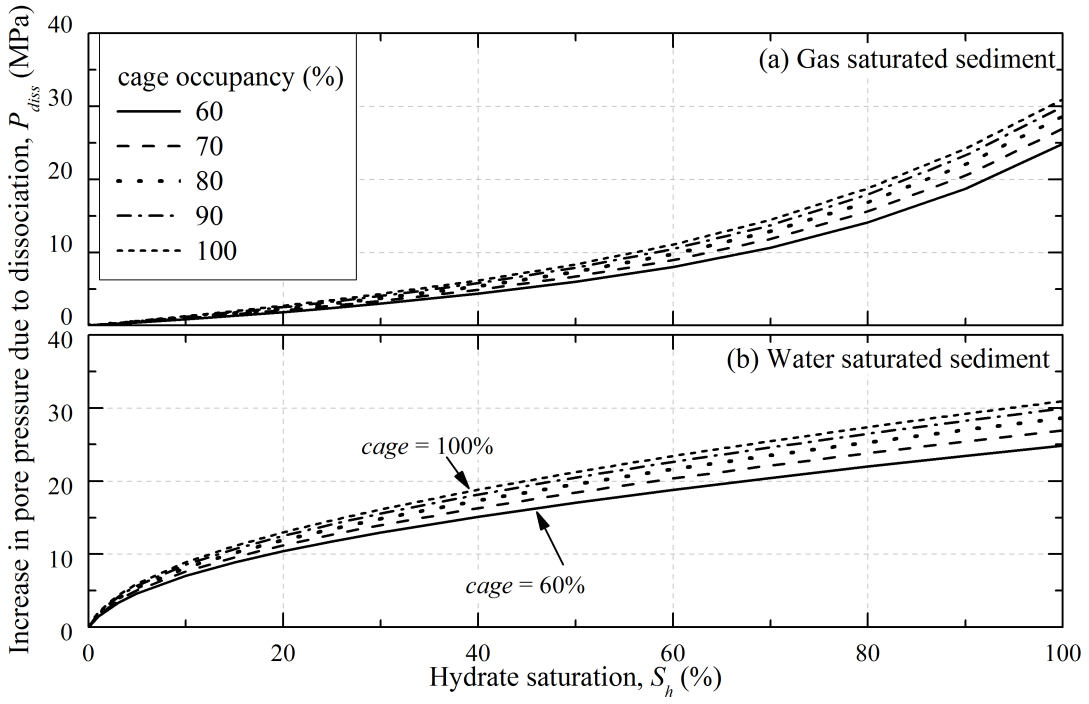

Figure 4.36: *Variation in P_{diss} with S_h for different methane cage occupancy (cage). Initial material properties of sediment are used from Table 4.4 (of column A_{cage}) for (a) gas saturated, and (b) water saturated sediment.*

undrained conditions.

Methane hydrate density

Methane hydrate density depends on the pressure and temperature conditions, in general it varies between 910 to 930 kg/m^3 (Sloan, 1998; Helgerud et al., 2009). Figure 4.37 shows the increase in pore pressure during dissociation under undrained conditions using material properties highlighted in Table 4.4 (Column $A_{\rho_{hy}}$). It can be seen in Figure 4.37 that the hydrate density has very little affect (<8.5%) on the pore pressure rise compared to the other parameters for both water and gas saturated sediments.

Initial pore pressure within sediment

Initial pore pressure within a saturated sediment represents the depth below the ground surface. Figure 4.38 shows the increase in pore pressure during dissociation under undrained conditions for both water and gas saturated sediments

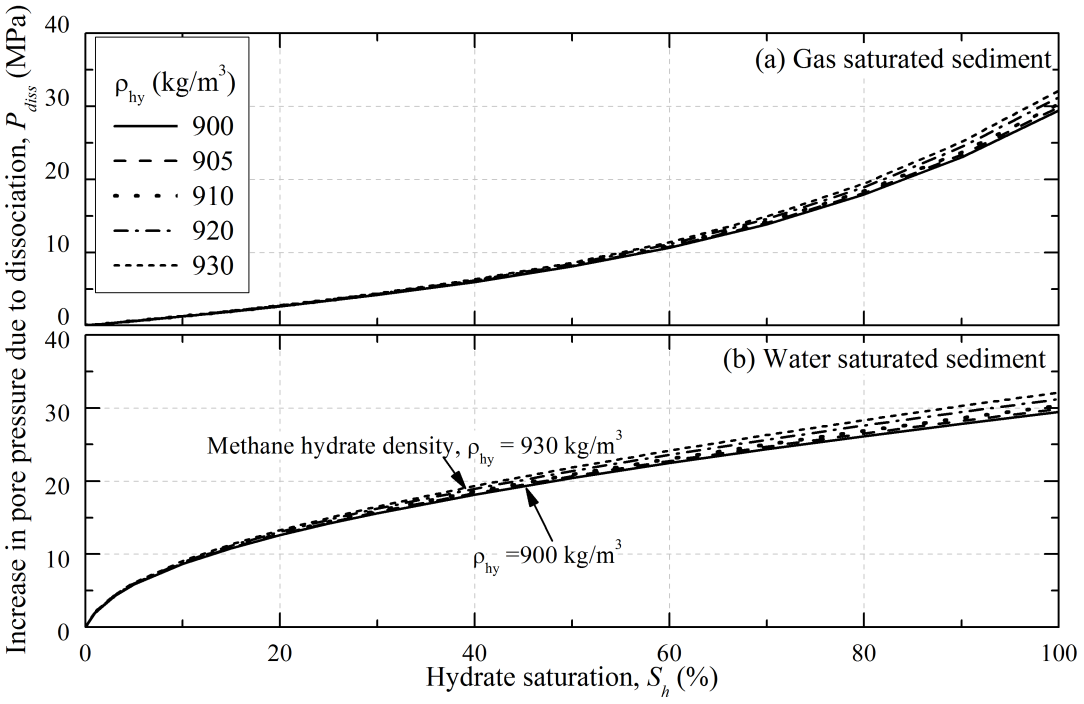

Figure 4.37: *Variation in P_{diss} with S_h for different methane hydrate density (ρ_{hy}). Initial material properties of sediment are used from Table 4.4 (of column $A_{\rho_{hy}}$) for (a) gas saturated, and (b) water saturated sediment.*

using material properties highlighted in Column $A_{P_{in}}$ of Table 4.4. It can be seen that the initial pore pressure has very little affect on the pore pressure rise for gas saturated sediments for S_h up to 60% (Figure 4.38). This is due to high compressibility of methane gas within pore spaces which acts as a cushion for pore pressure rise. However for water saturated sediments the rise in pore pressure is smaller for higher initial pore pressure (P_{in}). Similar behaviour is observed for gas saturated sediment at higher S_h (>60%, Figure 4.38). This is due to the fact that higher P_{in} provides higher confining pressure and higher offset for pore pressure rise. Therefore it might be expected to observe higher pore pressure rise in sediments at shallower depths compared to the deeper sediments.

Bulk modulus of sediment

Bulk modulus of a sediment represents the sediment resistance to deform under isotropic compression or expansion. In the analyses a range of sediment bulk modulus (0.3 to 2 GPa) were used in order to determine the bulk modulus sensitivity to pore pressure rise. Figure 4.39 shows the increase in pore pressure during

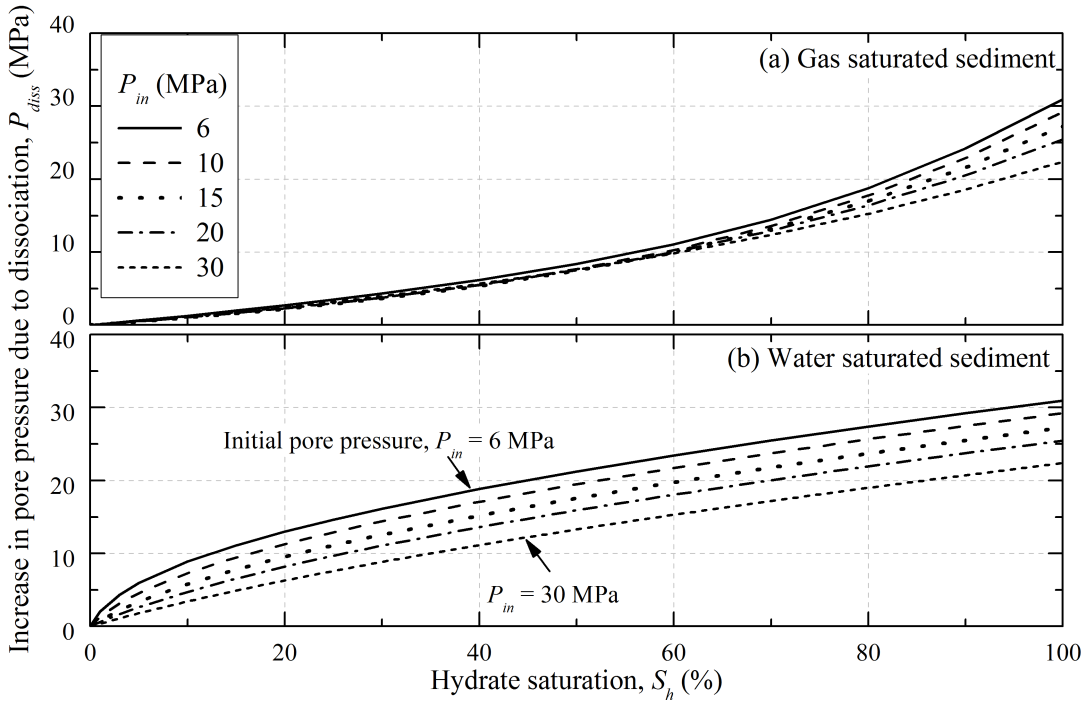

Figure 4.38: *Variation in P_{diss} with S_h for different initial pore pressure (P_{in}). Initial material properties of sediment are used from Table 4.4 (of column $A_{P_{in}}$) for (a) gas saturated, and (b) water saturated sediment.*

dissociation under undrained conditions for both water and gas saturated sediments using material properties highlighted in Table 4.4 (Column A_K). Similar to initial pore pressure, the bulk modulus has very little affect on the pore pressure rise for gas saturated sediments for S_h up to 60% (Figures 4.39). This is due to the fact that high compressibility of methane gas within pore spaces acts as a cushion for pore pressure rise. However, the bulk modulus of a water saturated sediment has significant affect on the total increase in pore pressure (Figure 4.39). This is due to the fact that the sediment with higher bulk modulus has less volumetric expansion upon increase in sediment pore pressure, thus less volume available for gas to expand.

Water saturation

Figures 4.35 to 4.39 show the rise in pore pressure under undrained conditions using the different material properties highlighted in Table 4.4. As noted in the figures the water saturated sediments have significant higher pore pressure rise compared to the gas saturated sediment, such that the rise in pore pressure is a

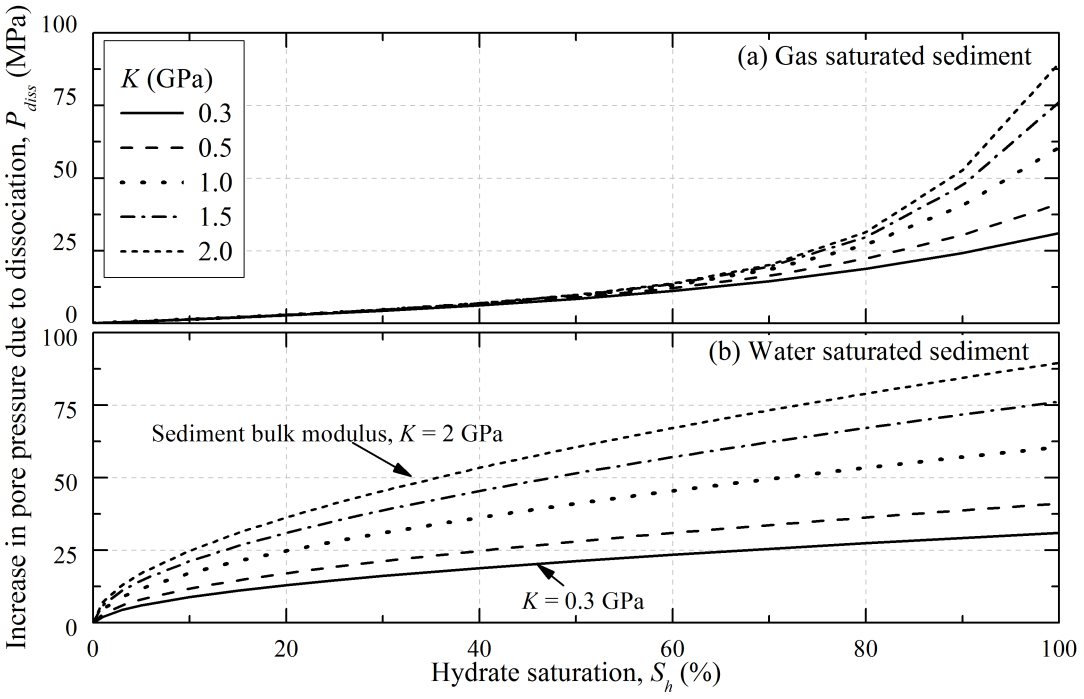

Figure 4.39: *Variation in P_{diss} with S_h for different sediment bulk modulus (K). Initial material properties of sediment are used from Table 4.4 (of column A_K) for (a) gas saturated, and (b) water saturated sediment.*

logarithmic function of hydrate saturation (S_h) for gas saturated sediments, and exponential function of hydrate saturation (S_h) for water saturated sediments. This is due to small pore volume available in water saturated sediment for methane gas to expand into during dissociation.

These results suggest that hydrate dissociation under undrained conditions will increase pore pressure within the sediment, thus decrease the effective stress and sediment stiffness irrespective of hydrate morphology. The increase in pore pressure due to hydrate dissociation depends on the cage occupancy of methane in hydrate, initial pore pressure within the sediment, bulk stiffness of the sediment, amount of hydrate dissociated, and water saturation within the sediment. Methane gas solubility and methane hydrate density have very little effect on the pore pressure rise within sediment. For sediments that are water saturated prior to dissociation pore pressure increase will be very large under undrained conditions. The change in sediment volume during dissociation, as a function of sediment stiffness and initial pore pressure, has a large influence in pore pressure rise.

In general oceanic sediment stiffness and pore pressure tend to increase with depth, therefore pore pressure rise during dissociation will not only depend on

sediment stiffness, but also initial pore pressure along with methane cage occupancy and amount of hydrate dissociates. Hydrate dissociation in oceanic sediment can result in hydraulic fracture, in particular for a sediment that has a higher air entry value such as clayey sediments. In addition, water evolved from dissociation can sweeten the pore water within oceanic sediment. The sweetening of pore water can decrease the undrained shear strength of the sediment (Clayton et al., 2008; Naioni and Jahanfar, 2011).

4.4 Material damping

Hydrate formed by the excess gas method has a cemented morphology (Section 4.2). However natural gas hydrate sediment can have different hydrate morphological growth (as discussed in Chapter 2). These differences make it difficult to identify and assess the presence of hydrate or hydrate dissociation through remote surveying, which rely on seismic wave velocities. However, seismic wave attenuation (or damping) may be affected by hydrate presence and hydrate morphologies. Thus for all the specimens, damping was also measured during the hydrate formation and dissociation stages.

4.4.1 Effect of hydrate saturation

Figure 4.40 shows the typical corrected damping values for a specimen in torsional (D_t) and flexural (D_f) vibration during a reduction in temperature to induce hydrate formation. It can be seen that both D_t and D_f increase rapidly as the specimen moves into the hydrate stability zone and reaches a maximum corresponding to the temperature spike, but further hydrate formation results in decrease in damping of the specimen. This behaviour is assumed to relate the formation of hydrate rind. It can hypothesise that as hydrate start to grow it produces a "cover of hydrate" encapsulating the remaining water, however the hydrate cover may not have a smooth surface but rather it contains cracks, similar to cemented sandstone (Murphy III et al., 1986), which allows the remaining free water to move within these cracks (squirt flow, Figure 4.41(a)). The squirt flow phenomenon causes wave energy to dissipate in the pore spaces and results in higher damping (Mavko and Nur, 1975). The squirt flow phenomenon reduces

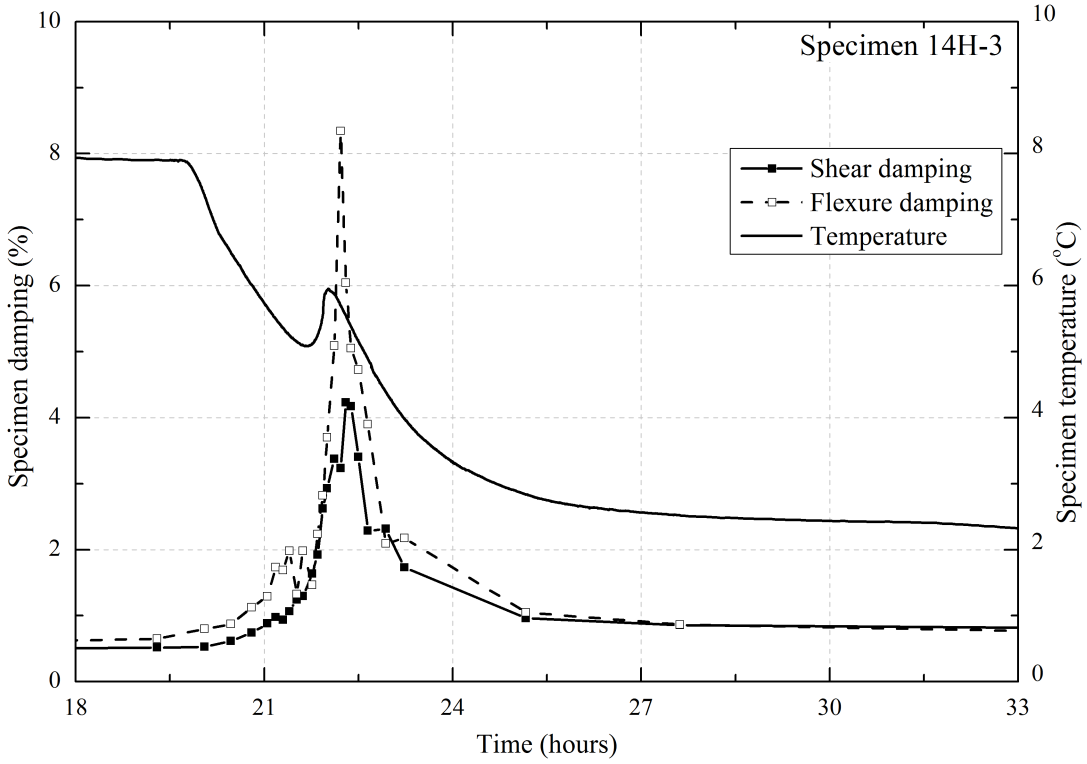

Figure 4.40: *Variation in torsional and flexural damping with time for the specimen "14H-3" during temperature drop.*

as conversion of water into hydrate proceeds, due to less availability of free water, thus specimen damping decreases. After complete hydrate formation, the volume of hydrate (7-26% of hydrate saturation) had no significant affect on the specimen damping (Figure 4.42), however Priest et al. (2006) observed unexpected higher specimen damping for 3-5% of hydrate saturation. Also noted in Figure 4.42 damping of the specimen without hydrate is slightly less than the specimen with hydrate even when all water is converted in to hydrate. This could be due to the presence of cracks in the "hydrate cover" (Figure 4.41(a)).

Figure 4.43(b) shows the typical corrected damping values during hydrate dissociation for a number of specimens, for both torsional (D_t) and flexural (D_f) vibration from resonant column tests. It can be seen that both D_t and D_f increase rapidly as the specimen moves out of the hydrate stability zone and reach a maximum. The maximum damping was observed to occur between $5 - 20\%$ of the total hydrate was dissociated (Figure 4.43(b)), which corresponds to the large drop in specimen stiffness (Figure 4.16). Although, similar behaviour was observed during hydrate formation, maximum damping was observed after ~70% of the total hydrate was formed (Figure 4.43(a)). The observed difference in

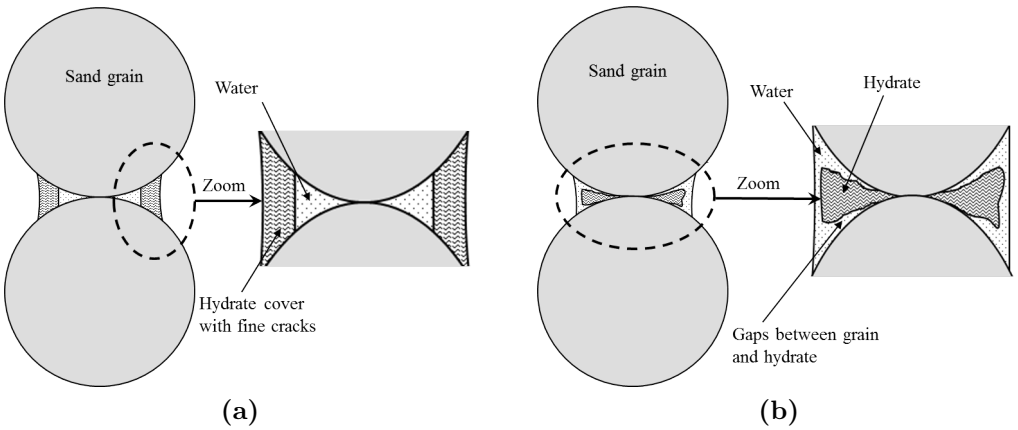

Figure 4.41: *Hypothetical hydrate growth during hydrate formation and dissociation. (a) Hydrate formation produces cover of hydrate with fine cracks (from Figure 4.18), and (b) hydrate dissociation produces fine gaps. These allow the free water to squirt and causes wave energy to dissipate resulting higher damping.*

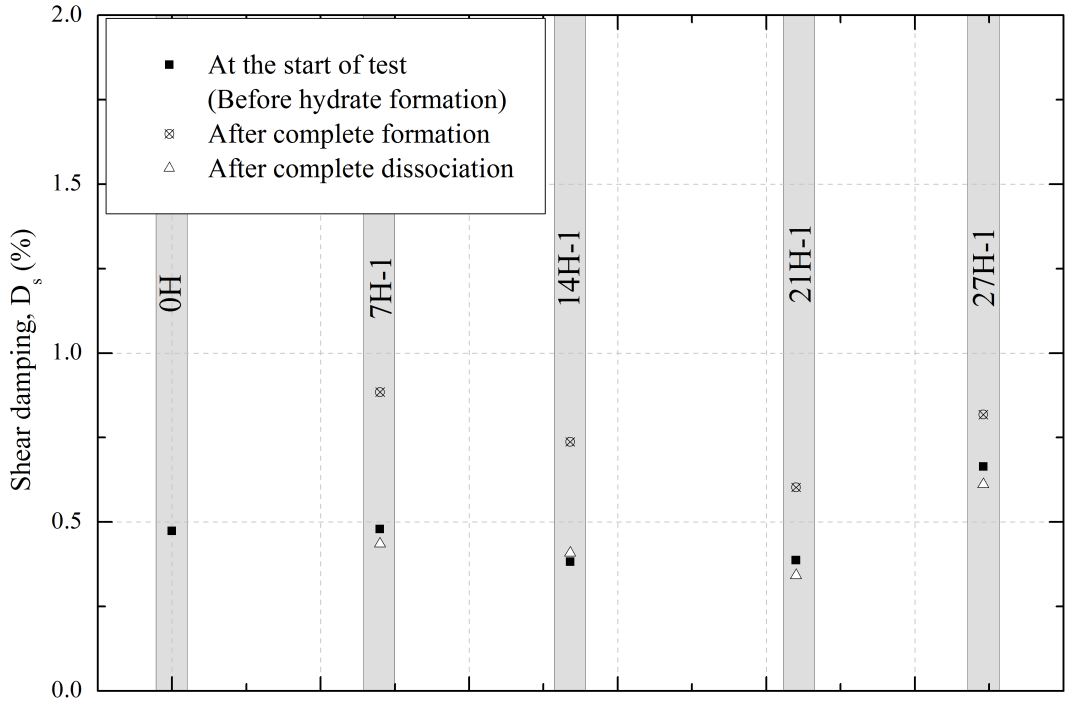

Figure 4.42: *Variation in shear damping at the start of test, after hydrate formation, and after dissociation for a number of specimen.*

damping could result from different processes during hydrate formation and dissociation. It can be hypothesised that as hydrate starts to dissociate it produces long channel, or fine gaps, between grains and the remaining hydrate (Figure 4.41(b)). This allows the free water (freed from dissociation) to squirt along these gaps and causes wave energy to dissipate, resulting in higher damping. As hydrate dissociation proceeds the gap between hydrate and grains increases such that squirt flow reduces, leading to reduction in damping. Similar to the stiffness, hydrate formation followed by dissociation had no significant affect on the specimen damping (Figure 4.42).

4.4.2 Effect of effective stress and cyclic strain

Once hydrate was fully formed at an initial effective stress, resonant column tests were conducted at different effective stresses and strain levels to determine resonance frequencies of the specimen, and specimen damping was also measured corresponding to these resonance frequencies. Figure 4.44 shows the variation in shear (D_s) and flexural (D_f) damping with respect to effective stress, and strain. It can be seen in Figure 4.44(a) that the effective stress does not have any significant affect on the specimen damping. Similar behaviour was also observed for the specimen without hydrate (Figure 4.44(a)). This could be due to the fact that these damping were measured at very small strain which was within the linear threshold limit (as discussed in Subsection 4.2.4). In general damping of soil sediment is at its lowest value below the linear threshold strain (Kramer, 2004). It can be more clearly seen in Figure 4.44(b) that specimen damping increases with strain level.

4.4.3 Comparison with previous literature

As discussed, after complete formation the volume of hydrate had no significant affect on the material damping of specimen. Figure 4.45 shows the variation in shear (D_s) and flexural (D_f) damping with hydrate saturation. For a comparison, previous researchers damping data (from Priest (2004) and Rees (2009)) are also shown where hydrate was formed using the excess gas method (Priest, 2004) and using the excess water method (Rees, 2009). It can be seen that similar damping behaviour was observed by Priest (2004) when using the excess gas technique

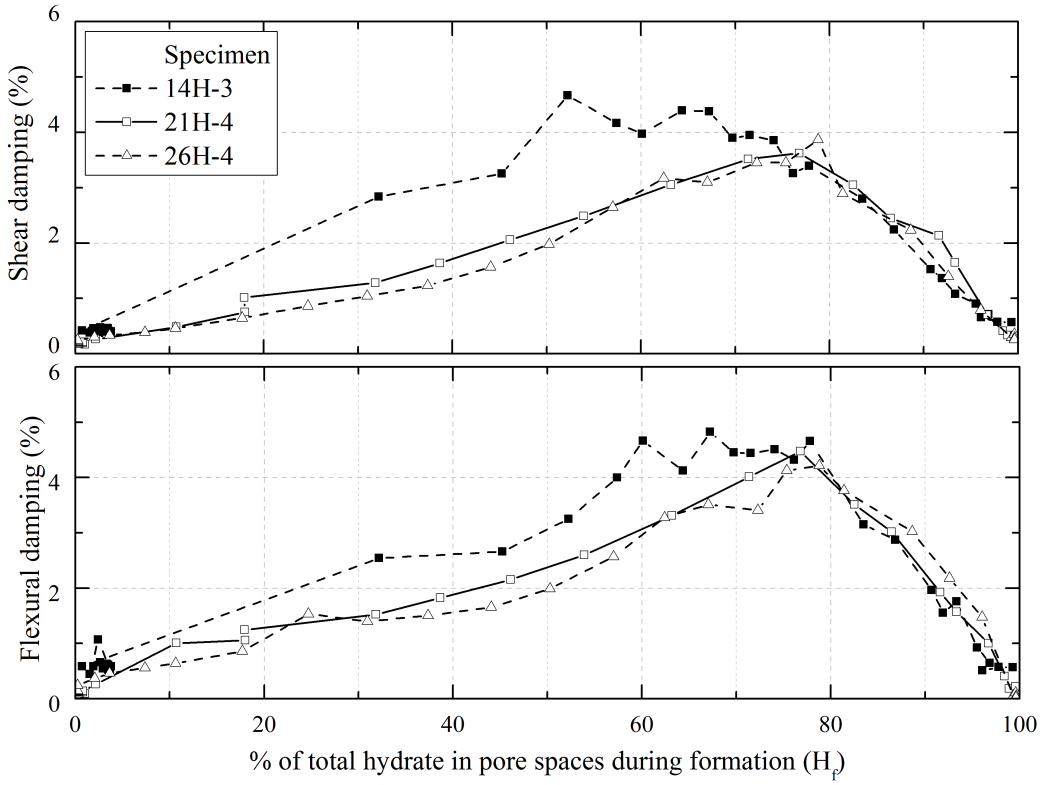

(a) *During hydrate formation.*

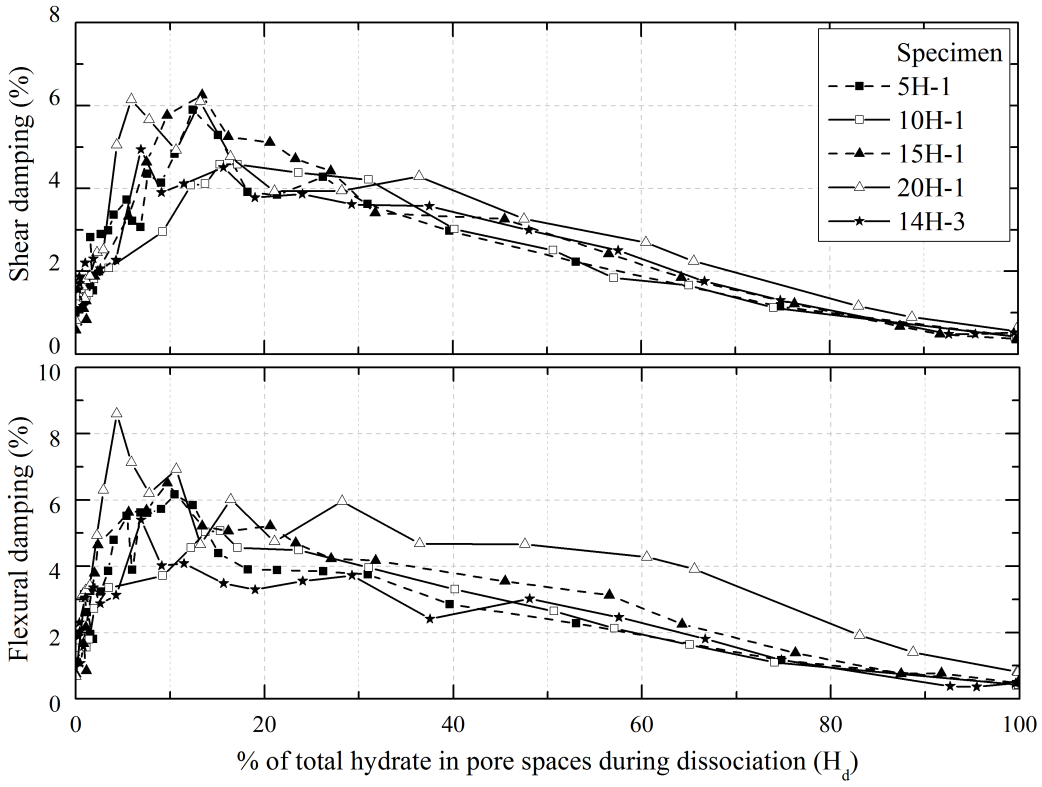

(b) *During hydrate dissociation.*

Figure 4.43: *Variation in shear and flexural damping with % of total hydrate saturation during (a) formation, and (b) dissociation stages for a number of specimens.*

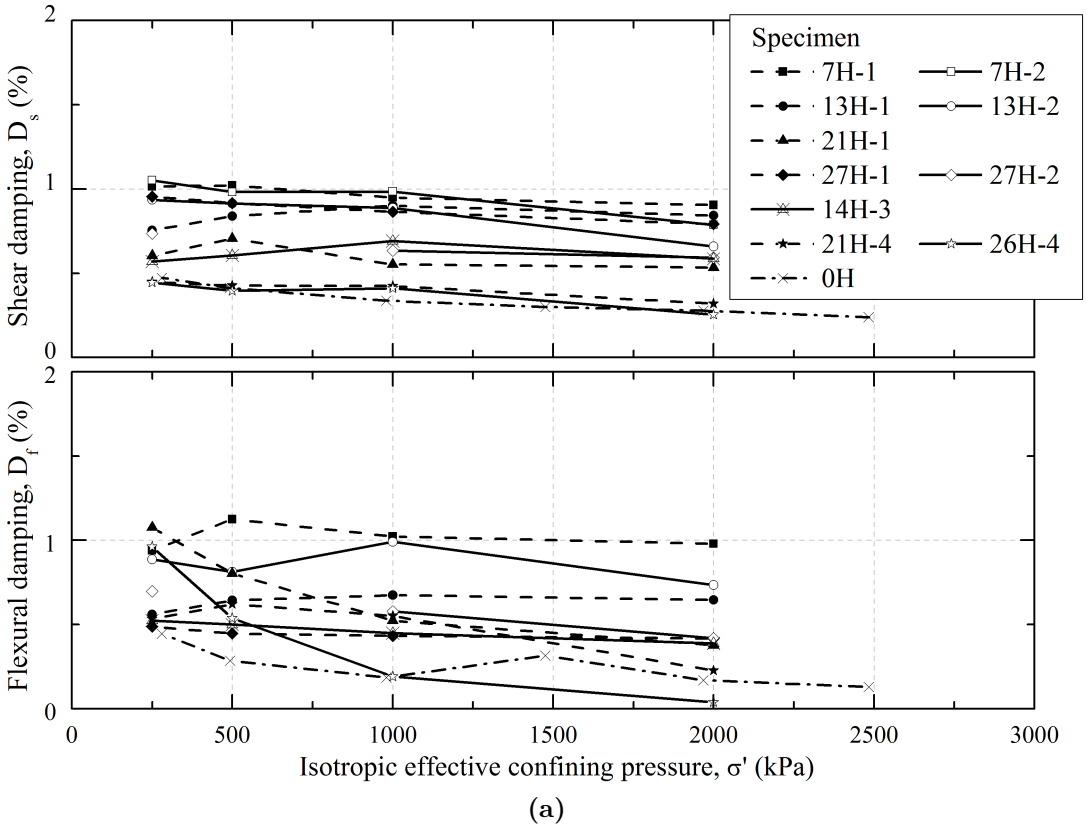

(a)

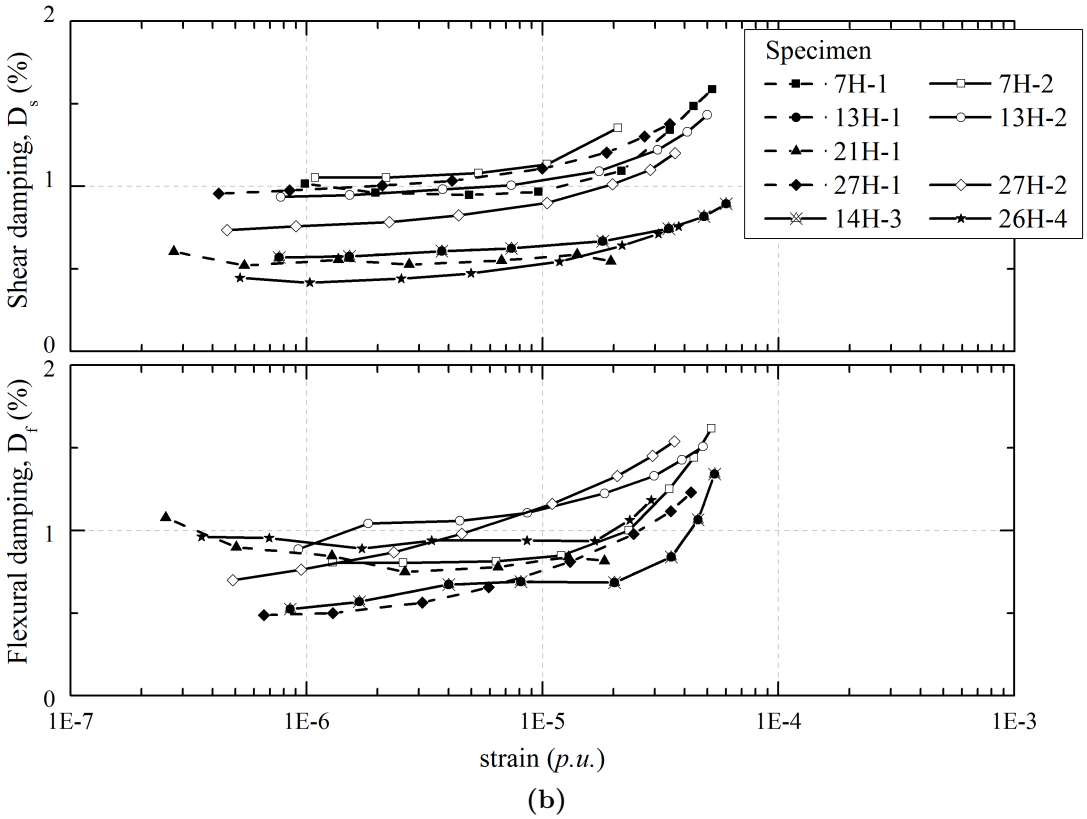

(b)

Figure 4.44: *Variation in shear and flexural damping with (a) effective confining stress, and (b) strain (at 250kPa of effective stress).*

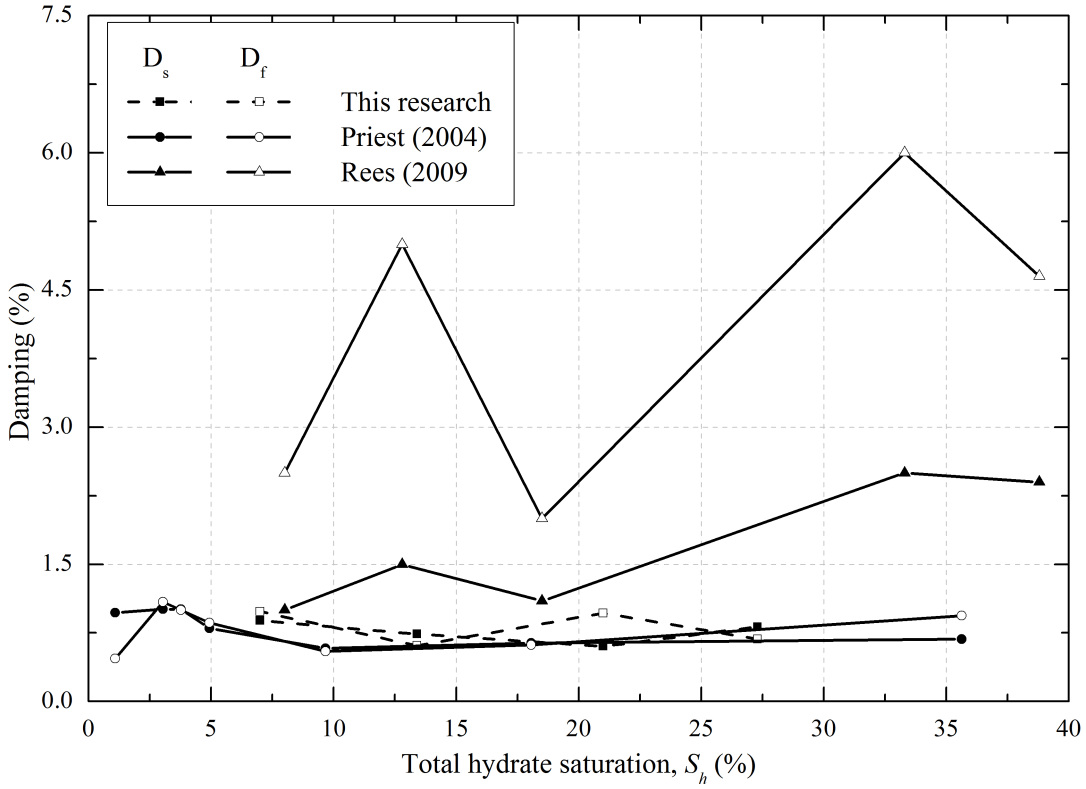

Figure 4.45: *Variation in shear (D_s) and flexural (D_f) damping with hydrate saturation from this research and previous researches.*

(Figure 4.45). However, when the excess water technique was used, Rees (2009) observed that material damping increased with hydrate saturation (Figure 4.45). The increase in specimen damping with hydrate saturation has been hypothesised to occur through a combination of Biot and squirt flow attenuation mechanisms. As discussed in Chapter 2, the Biot flow mechanism is a relative motion of fluid and solid within pore spaces of a sediment (Biot, 1956), and squirt flow mechanism is pore fluid flow from one pore to another (Mavko and Nur, 1975). Biot-squirt flow mechanism has also been used to study Malik 2L-28 attenuation (or damping) data, and it has been found that seismic attenuation increases with degree of hydrate saturation (Guerin and Goldberg, 2002; Chand et al., 2004).

In this research, it was observed that the specimen damping increased during hydrate formation (Figure 4.43(a)), probably due to squirt flow of the remaining free water within the pore spaces. The hydrate was formed using the excess gas method, therefore as the availability of free water reduced the squirt flow phenomenon would be expect to reduce, and thus the specimen damping (Figure 4.43(a)). In contrast natural hydrate bearing sediments may contain free water.

The presence of free water within the sediment may occur due to two reasons: (1) free gas content may be insufficient for complete conversion of all the water into hydrate, or (2) the hydrate conversion process may not be complete. The availability of free water in hydrate bearing sediments can enhance the sediment damping due to squirt fluid flow within the pore spaces as suggested by other researchers (Pecher and Holbrook, 2000; Guerin and Goldberg, 2002; Chand et al., 2004). This suggests that the change in damping (or attenuation) may allow an alternate method to detect the presence of hydrate within sediments where it may have not been detectable using standard seismic velocity method (Rees, 2009); such as when hydrate acts as frame-supporting or pore-filling morphology within a sediment, and very little changes in velocity occur.

Chapter 5

Conclusions and Suggestions for Further Work

This chapter presents the main conclusions drawn from each chapters along with suggestions for further research required to understand dissociation behaviour.

5.1 Conclusions

To understand current knowledge of gas hydrate and the effect of dissociation on sediment properties a literature review was conducted (Chapter 2). This review highlighted shortfalls in our understanding of the effect of dissociation on the stiffness, strength, and damping of hydrate bearing sediments. To improve our understanding of the effects of dissociation, an analytical mode was built (Appendix C) and a series of well-controlled laboratory tests were conducted on laboratory prepared specimens of methane hydrate bearing sands (Chapter 3). Resonant column testing during hydrate formation and dissociation processes carried out for the first time. The results from the laboratory tests were analysed with respect to the effect of formation and dissociation on the stiffness, pore pressure and damping of these sediments (Chapter 4). The main conclusions drawn from the research undertaken are presented in the following subsections.

5.1.1 Conclusions from literature review

- Gas hydrate is a solid, non-stoichiometric, metastable compound, in which gas is able to achieve a greater density than would have in its gaseous state. Therefore hydrate dissociation can lead to a large increase in pore pressure within hydrate bearing sediment under undrained conditions. The dissociation of gas hydrate and its potential as a submarine geohazard have become of increasing importance as oil and gas exploration activities extend into significant water depths on continental margins and seas where gas hydrates are known to exist. Such activities may dissociate hydrate and may induce failure of the sea floor.

- A number of numerical models have been developed to predict the effect of dissociation around a well-bore. Due to lack of experimental data, these numerical models have assumed that the sediment stiffness is a constant or varies linearly with volume of hydrate dissociated.

- To date, much of the research on gas hydrate has been concerned with hydrate formation within sediments. Little research has been conducted on hydrate dissociation. Most of this has been concerned with extraction of the methane gas from hydrate bearing sediment, and has not considered the effect of dissociation on the mechanical (stiffness/strength) properties of hydrate bearing sediments.

- The influence of hydrate formation on the strength and stiffness of hydrate bearing sediment depends on the morphology of hydrate within the sediment. Hydrate morphology in which hydrate acts as a cement has a larger influence on strength and stiffness compared to hydrate which exhibits a pore-filling morphology. The influence of hydrate dissociation may therefore be dependent on the morphology of the hydrate within the sediment.

- A number of researchers have studied the attenuation (or damping) of hydrate bearing sediment to quantify hydrate content within sediment. Most of these studies have been based on theoretical models, such as the self consistent approximation (SCA) and differential effective medium theory (DEM).

- To date, most of the research using attenuation have been done to quantify or identify hydrate within sediment. No research has been done to study

the effect of dissociation on the attenuation/damping properties of hydrate bearing sediments.

5.1.2 Conclusions from modelling

- Numerical analysis showed that the derivation of Young's modulus (E) of an isotropic material using Cascante equation introduces significant error (approximately 10%) when the aspect ratio (l/d) of the specimen is 2. It was shown that this error in E occurs due to the fact that no shear stiffness is considered in deriving the Cascante equation.

- A simple formulation was developed to quantify the amount of hydrate within the specimen during hydrate formation and dissociation process, based on the changes in pore pressure within the specimen during formation and dissociation.

- Through the development of an analytical model for hydrate dissociation it was shown that the rise in pore pressure within a sediment was dependent on a number of factors: Major factors were initial pore pressure, amount of hydrate dissociation, cage occupancy of gas within hydrate, stiffness of the sediment, and degree of water saturation; Minor factors were methane gas solubility in water, and methane hydrate density.

- For sediments that are water saturated prior to dissociation pore pressure increase under undrained conditions will be very large and the change in sediment volume during dissociation, as a function of sediment stiffness and initial pore pressure within sediment, has a large influence on the changes in pore pressure. Therefore, hydrate dissociation in oceanic sediment can be expected to result in hydrate fracture within the sediment, in particular if the sediment that has higher air entry value such as clayey sediments.

5.1.3 Conclusions from experimental results

- Resonant column testing during hydrate formation and dissociation processes carried out for the first time, such that the change in stiffness and material damping for sand specimens could be measured with the amount of hydrate formed/dissociated during formation/dissociation processes.

- It was shown that the initiation of hydrate formation and dissociation can be identified by measuring change in pore pressure, stiffness, and damping. The exothermic reaction was observed as in specimen temperature spike, and endothermic reaction was observed as a change in temperature gradient. These occurrence in temperature changes did not correspond to initiation of hydrate formation and dissociation as determined from changes in pore pressure and stiffness.
- For uniform sand specimens where hydrate (up to 27%) was formed using the excess gas method, it was shown that hydrate formation occurred within the pore spaces and did not displace the sand grains.

Effect on stiffness

- The increase in sediment stiffness due to hydrate formation was shown to result from the strong cementing effect of the hydrate at the grain contacts and to a lesser extent the decrease in void ratio as a result of the hydrate growth, where hydrate was formed using the excess gas method.
- Test results showed that the increase in sediment stiffness was a function of hydrate saturation within the pore spaces of sand specimens. The increase in stiffness was the same order of magnitude as measured by previous researchers, using the excess gas method.
- It was shown that the overall increase in sediment stiffness was dependent on the final hydrate saturation value rather than the quantified value during hydrate formation. For example, a specimen with 10% hydrate saturation at the end of the formation process had a higher stiffness compared to a specimen which had formed 10% hydrate saturation of the pore during the formation process.
- The stiffness of uncemented granular materials such as sands is strongly affected by effective stress. Using the excess gas method, it was observed that cementation of the grain contacts by the hydrate significantly reduced this stress dependency. Changes in effective stress (up to $2800\,kPa$) had no appreciable influence on the measured stiffness of methane hydrate sand sediments.

- It was shown that the linear threshold limit of hydrate bearing specimens were lower than the non-hydrate bearing sands. This is due to effect of hydrate as cement, which makes the specimen brittle.
- Test results showed that the hydrate formation using the excess gas method led to higher increases in the shear stiffness compared to the flexural stiffness of specimens; the specimen stiffness ratio (E_{flex}/G) after complete hydrate formation was lower than the specimen before the start of hydrate formation (without hydrate).
- During hydrate dissociation a rapid reduction in stiffness was measured for a minor change in hydrate saturation of sand specimens where dissociation was induced by temperature increase, but for specimens that were dissociated using the pressure reduction method a slower reduction occurred. In contrast, during hydrate formation stiffness increased more gradually.
- It is shown that the change in stiffness during hydrate formation and dissociation processes can be described by pore-scale conceptual model based on the interaction between hydrate and the sand grains.
- Using the excess gas method, hydrate formation followed by dissociation had no significant affect on the stiffness of dense sand specimen at a given effective stress; after complete dissociation the stiffness properties of the sediment were similar to those of the sediment without hydrate.

Effect on pore pressure

- Test results showed that the pore pressure evolution was a linear function of the volume of hydrate (up to 27% of the pore space) dissociated.
- The observed rise in pore pressure during hydrate dissociation was smaller than that calculated from the analytical model based on the volume of water present within the pore space. This was due to the hydrate in the pore space did not have 100% methane cage occupancy (non stoichiometry of methane hydrate).

Effect on material damping/attenuation

- Test result showed that the volume of hydrate had very little to no effect on the material damping of specimens after complete formation using the excess gas method. In contrast, previous researchers had observed that the material damping of hydrate bearing sediment increases with volume of hydrate when hydrate was formed using the excess water method.
- During hydrate dissociation a rapid increase in damping was measured for minor changes in the hydrate saturation of sand sediments. In contrast during formation damping increased more gradually, such that during dissociation the maximum damping was measured between 5 to 20% of the total hydrate had dissociated, while during formation maximum damping was measured when ~70% of the total hydrate had formed. A conceptual model was developed to describe lack of reversibility of change in the material damping of sand specimen during the hydrate formation and dissociation processes.

5.2 Suggestions for further research

- Hydrate formation using the excess gas method produces a cemented morphology. However natural gas hydrate sediment may have different hydrate morphological growth. This difference makes it difficult to identify, and assess the presence of hydrate, or hydrate dissociation, through remote surveying that rely on seismic wave velocity. However, seismic wave attenuation (or damping) may be more susceptible to hydrate presence and hydrate morphologies. Therefore, it may be useful to measure attenuation along with seismic wave velocities to identify and assess the presence of hydrate bearing sediments.
- A number of numerical models have been developed to predict the effect of dissociation around a hot well-bore. In general, these numerical models have considered that the sediment stiffness is a constant or a linear function of hydrate dissociation. However, the test results have shown that the stiffness reduces exponentially with hydrate dissociation. Therefore, the inclusion of this non-linear behaviour in a numerical model is required to better predict the deformation behaviour of hydrate bearing sediments during dissociation.

- As shown, using the Cascante equation to derive Young's modulus from the flexural vibration introduces an error ($\sim 10\%$) for the generally used specimen aspect ratio (l/d) of 2. To overcome this error, a longitudinal resonance frequency can be determined using longitudinal drive system in the resonant column apparatus. This will allow true vertical stiffness measurement and direct comparison with the flexural stiffness. In addition, longitudinal and torsional modes of vibration can be used to evaluate stiffness properties of a cross-anisotropy material using the developed equations (Appendix B).

- Little research has been conducted to study the strength of hydrate bearing sediments and no researcher has looked at the strength of sediment during dissociation. In general destructive tests are used to evaluate strength of a sediment. Therefore, it would not be possible to evaluate strength of hydrate bearing specimen during dissociation on the same specimen. However, using stiffness degradation data from the present research combine with strength of non-hydrate and hydrate bearing sediment, a simple formulation might be developed to assess the sediment strength during dissociation.

Appendix A

Effective medium models (EMM)

This appendix discusses different rock physics models to calculate the stiffness and wave velocities of a hydrate bearing sediment, where hydrate modelled as a pore-filling, frame-supporting, or cement component of the sediment.

A.1 Pore-filling model

In this case, gas hydrate is treated as a part of pore fluid and thus it has no significant effect on the sediment properties. Therefore, saturated modulus properties of hydrate bearing sediment can be calculated using Gassmann (1951) equation:

$$K_{sat} = K_{dry} + \frac{\left(1 - \frac{K_{dry}}{K}\right)}{\frac{\phi}{K_{fA}} + \frac{1-\phi}{K} + \frac{K_d}{K^2}} \tag{A.1}$$

and,

$$G_{sat} = G_{dry} \tag{A.2}$$

where, K_{dry} and G_{dry} are respective bulk and shear modulus of the dry sediment frame; K is the average bulk modulus of the soil grains; and ϕ is the porosity of the sediment. K_{fA} is the average bulk modulus of the fluid that can be calculated as (Ecker, 2001):

$$K_{fA} = \left[\frac{S_h}{K_h} + \frac{1 - S_h}{K_w}\right]^{-1} \tag{A.3}$$

where, K_h and K_w are respective bulk modulus of hydrate and water; and S_h is the degree of hydrate saturation in the pores.

The effective bulk (K_{dry}) and shear (G_{dry}) moduli of a dry sediment at different porosity can be calculated from the equation given by Dvorkin and Nur (1996):

At critical porosity ($\phi = \phi_c$)

$$K_{d\phi c} = \left[\frac{n^2\,(1-\phi_c)^2\,G^2}{18\,\pi^2\,(1-\nu)^2}\,P\right]^{\frac{1}{3}} \tag{A.4}$$

$$G_{d\phi c} = \frac{5 - 4\,\nu}{5\,(2-\nu)}\,\left[\frac{3\,n^2\,(1-\phi_c)^2\,G^2}{2\,\pi^2\,(1-\nu)^2}\,P\right]^{\frac{1}{3}} \tag{A.5}$$

where, $K_{d\phi c}$ and $G_{d\phi c}$ are, respective, K_{dry} and G_{dry} at critical porosity; G and ν are shear modulus and Poisson's ratio of the solid material respectively; n is the average number of contacts per grain; and P is the effective stress on the sediment.

At less than critical porosity ($\phi < \phi_c$)

$$K_{dry} = \left[\frac{\phi/\phi_c}{K_{d\phi c} + \frac{4}{3}\,G_{d\phi c}} + \frac{1 - \phi/\phi_c}{K + \frac{4}{3}\,G_{d\phi c}}\right]^{-1} - \frac{4}{3}\,G_{d\phi c} \tag{A.6}$$

$$G_{dry} = \left[\frac{\phi/\phi_c}{G_{d\phi c} + Z} + \frac{1 - \phi/\phi_c}{G + Z}\right]^{-1} - Z \tag{A.7}$$

where,

$$Z = \frac{G_{d\phi c}}{6}\,\left(\frac{9\,K_{d\phi c} + 8\,G_{d\phi c}}{K_{d\phi c} + 2\,G_{d\phi c}}\right)$$

At greater than critical porosity $(\phi > \phi_c)$

$$K_{dry} = \left[\frac{(1-\phi)/(1-\phi_c)}{K_{d\phi c} + \frac{4}{3}G_{d\phi c}} + \frac{(\phi-\phi_c)/(1-\phi_c)}{\frac{4}{3}G_{d\phi c}}\right]^{-1} - \frac{4}{3}G_{d\phi c} \tag{A.8}$$

$$G_{dry} = \left[\frac{(1-\phi)/(1-\phi_c)}{G_{d\phi c} + Z} + \frac{(\phi-\phi_c)/(1-\phi_c)}{Z}\right]^{-1} - Z \tag{A.9}$$

A.2 Frame supporting model

In this case, gas hydrate treated as a part of solid and thus it reduce the porosity and change the solid moduli of the sediment. the new reduced porosity ϕ_r can be calculated as (Ecker, 2001);

$$\phi_r = \phi\,(1 - S_h) \tag{A.10}$$

and, the bulk and shear moduli of the solids phase can be calculated using the Hill average formula for mixture of the sediment solid and the hydrate:

$$K' = \frac{1}{2}\left(f_h\,K_h + (1-f_h)\,K + [f_h/K_h + (1-f_h)/K]^{-1}\right) \tag{A.11}$$

$$G' = \frac{1}{2}\left(f_h\,G_h + (1-f_h)\,G + [f_h/G_h + (1-f_h)/G]^{-1}\right) \tag{A.12}$$

where, f_h is the volume fraction of hydrate in the solid phase and it can be calculated as:

$$f_h = \frac{\phi\,S_h}{1 - \phi\,(1 - S_h)} \tag{A.13}$$

Dry and saturated moduli of the sediment can be calculated by substituting ϕ_r, K', and G' as ϕ, K, and G respectively in Equations A.1 to A.9.

A.3 Cementation model

In this model, hydrate is formed at grain contacts and thus strongly reinforce the sediment. Using the contact cement theory (CCT) Dvorkin et al. (1991) proposed the effective shear and bulk modulus of a dry cemented sphere pack as:

$$K_{dry} = \frac{n\,(1-\phi_c)}{6}\,(K_c + \frac{4}{3}\,G_c)\,S_n \tag{A.14}$$

$$G_{dry} = \frac{3}{5}\,K_{CCT} + \frac{3\,n\,(1-\phi_c)}{20}\,G_c\,S_\tau \tag{A.15}$$

where, G_c and K_c are the shear and bulk moduli of the cement (in this case hydrate) respectively. Parameters S_n and S_τ relates to the normal stiffness of a cemented two grain combination. These parameters can be calculated as (Ecker, 2001):

$S_n = A_n\,\alpha^2 + B_n\,\alpha + C_n$

$A_n = -0.024153\,\Lambda_n^{-1.3646}$

$B_n = -0.20405\,\Lambda_n^{-0.89008}$

$C_n = -0.00024649\,\Lambda_n^{-1.9864}$

$S_\tau = A_\tau\,\alpha^2 + B_\tau\,\alpha + C_\tau$

$A_\tau = -10^{-2}\,(2.26\,\nu^2 + 2.07\,\nu + 2.3)\,\Lambda_\tau^{0.079\,\nu^2+0.175\,\nu-1.342}$

$B_\tau = (0.0573\,\nu^2 + 0.0937\,\nu + 0.202)\,\Lambda_\tau^{0.0274\,\nu^2+0.0529\,\nu-0.8765}$

$C_\tau = -10^{-4}\,(9.964\,\nu^2 + 4.945\,\nu + 3.1)\,\Lambda_\tau^{0.01867\,\nu^2+0.4011\,\nu-1.8186}$

$\Lambda_n = \frac{2G_c}{\pi\,G}\ \frac{(1-\nu)\,(1-\nu_c)}{1-2\,\nu_c}$

$\Lambda_\tau = \frac{G_c}{\pi\,G}$

$\alpha = \left[\frac{2\,S_h\,\phi}{3\,(1-\phi)}\right]^{0.5}$

where, G and ν are the shear modulus and Poisson's ratio of the grain material respectively; and G_c and ν_c are the shear modulus and Poisson's ratio of the

cement, respectively.

The saturated moduli of the sediment can be calculated using Equations A.1 to A.3.

A.4 Wave velocities

Primary (or compressional, V_p) and shear (V_s) wave velocities can be calculated using saturated moduli of the sediment:

$$V_p = \sqrt{\frac{\left(K_{sat} + \frac{4}{3}\,G_{sat}\right)}{\rho_b}} \tag{A.16}$$

$$V_s = \sqrt{\frac{G_{sat}}{\rho_b}} \tag{A.17}$$

where, ρ_b is bulk modulus of the sediment, and can be defined as:

$$\rho_b = (1 - \phi)\ \rho_s + \phi\,\rho_f \tag{A.18}$$

where, ρ_s and ρ_f are density of soil solids and pore fluid respectively.

Table A.1 presents the material properties used to model hydrate as pore filling, frame supporting, or cementing component within sand sediment.

Material	Material properties		
	Shear modulus GPa	Bulk modulus GPa	Density kg/m^3
Quartz (Helgerud et al., 1999)	45.0	36.60	2650
Methane hydrate (Helgerud et al., 2009; Sloan, 1998)	2.4	5.42	917
Water (Lee et al., 1996)	0.0	2.25	1000

Table A.1: *Material properties used in effective medium modelling of methane hydrate bearing sediment.*

Appendix B

Numerical analysis of specimen in the resonant column apparatus

This appendix reports a series of dynamic finite element numerical simulations of physical tests in the resonant column apparatus, carried out to model both the apparatus and an isotropic soil specimen. Forward modelling has been carried out to determine the impact of different degrees of anisotropy on the resonant frequencies of the specimens with their axes of anisotropy aligned in different directions relative to the vertical axis of the apparatus. Methods of determining the elastic parameters from these data are assessed.

B.1 Theory

For an isotropic material stiffness is constant in all directions. Only two soil parameters are required. Commonly the parameters are Young's modulus (E) with Poisson's ratio (ν), but in some applications shear modulus (G) and bulk modulus (K) are used. For an isotropic material the relationship ratio between shear modulus, G , measured in torsion, and Young's modulus, E , measured in either flexure of longitudinal vibration should be a function of Poisson's ratio, and since

$$E = G \times 2\,(1 + \nu) \tag{B.1}$$

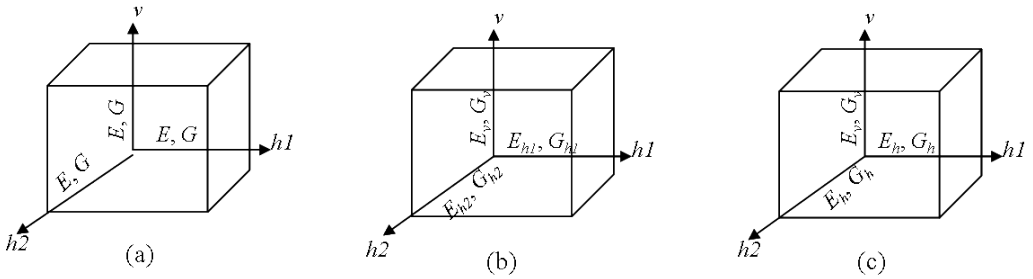

Figure B.1: *Material properties in different orthogonal directions (a) for isotropic, (b) for anisotropic, and (c) for cross-anisotropic materials.*

E/G can be expected to vary from about 2.5 for an unsaturated or dry material with isotropic stiffness (assuming $\nu \approx 0.25$) to 3 ($\nu = 0.5$) for a saturated, undrained isotropic material.

However, in general, soils are not isotropic. For a completely anisotropic behaviour, the stiffness in each orthogonal plane is different, that is $G_v \neq G_{h1} \neq G_{h2}$ and $E_v \neq E_{h1} \neq E_{h2}$, where v, $h1$ and $h2$ represent the vertical, first horizontal and second horizontal directions respectively, as shown in Figure B.1. A total of 21 independent parameters are required to describe the stiffness of a fully anisotropic material. However in most cases soils can be assumed to be transversely isotropic. In a transversely isotropic soil stiffness in the horizontal plane is assumed to be isotropic, and the vertical direction is the axis of anisotropy (such that $G_v \neq G_{h1}$, $G_{h1} = G_{h2}$ and $E_v \neq E_{h1}$, $E_{h1} = E_{h2}$). To describe a transversely isotropic elastic material five independent parameters are required (Love, 1927). Commonly these are Young's modulus (E_v and E_h); the Poisson's ratio linking strains in the horizontal directions to the vertical direction(ν_{vh}), Poisson's ratio linking strain in one horizontal direction to the other (ν_{hh}); and the shear modulus in the vertical plane (G_v). The shear modulus in the horizontal plane, G_h, is calculated from $G_h = E_h/2(1 + \nu_{hh})$. Since E_v and G_v are independent parameters, in theory the ratio E_v/G_v can adopt any value for a transversely isotropic material.

Resonant column apparatus

As discussed in Chapter 3, the test procedure for a fixed-free RC involves vibrating a cylindrical column of soil and measuring the amplitude of the vibration during a frequency sweep. The resonant frequency is then obtained from the frequency

response curve, determined from the peak amplitude observed. As shown in Figure B.2 various vibration modes can be applied to the soil (torsional, flexural (bending) and longitudinal) and from the resonant frequencies so obtained the shear modulus, flexural Young's modulus and vertical Young's modulus can be calculated.

For the routine interpretation of a fixed-free resonant column test the specimen is assumed to be elastic, homogeneous and isotropic and fixed at its base, with the drive system (drive mechanism, end platen, etc.) fixed to the top of the sample assumed to be a lumped mass. The solution for the torsional mode of vibration is shown in Equation B.2 (Richart et al., 1970),

$$\frac{I}{I_0} = \frac{\omega_n\, l}{V_s}\, tan\, \frac{\omega_n\, l}{V_s} \tag{B.2}$$

and,

$$G = \rho\, V_s^2 \tag{B.3}$$

where,I_0 is the mass polar moment of inertia of lumped mass attached to the free end, I is the mass polar moment of inertia of specimen, l is the length of the specimen ω_n is the circular resonant frequency ($= 2\pi f$) from torsional vibration of the specimen, V_s is the calculated shear wave velocity of the soil, ρ is the density of the specimen, and G is the inferred shear modulus of the specimen.

The solution for the flexural mode of vibration is shown in Equation 3.4 (Cascante et al., 1998),

$$\omega_f^2 = \frac{3\, E_{flex}\, I_b}{\left[\frac{33}{140}\, m_T + \sum m_i\, h(h_0, h_{1i})\right]\, l^3} \tag{B.4}$$

where,

$$h(h_{0i}, h_{1i}) = 1 + \frac{3\,(h_{1i} + h_{0i})}{2\, l} + \frac{3}{4}\, \frac{(h_{1i}^2 + h_{1i} h_{0i} + h_{0i}^2)}{l^2} \tag{B.5}$$

ω_f is the natural circular resonant frequency from flexural vibration of the specimen, I_b and E_{flex} are the second moment of inertia and Flexural modulus of the specimen respectively. h_{0i} and h_{1i} are the bottom and the top heights respectively of $i\,th$ mass (m_i), measured from the top of the specimen (Figure B.2); and m_T is the mass of the specimen.

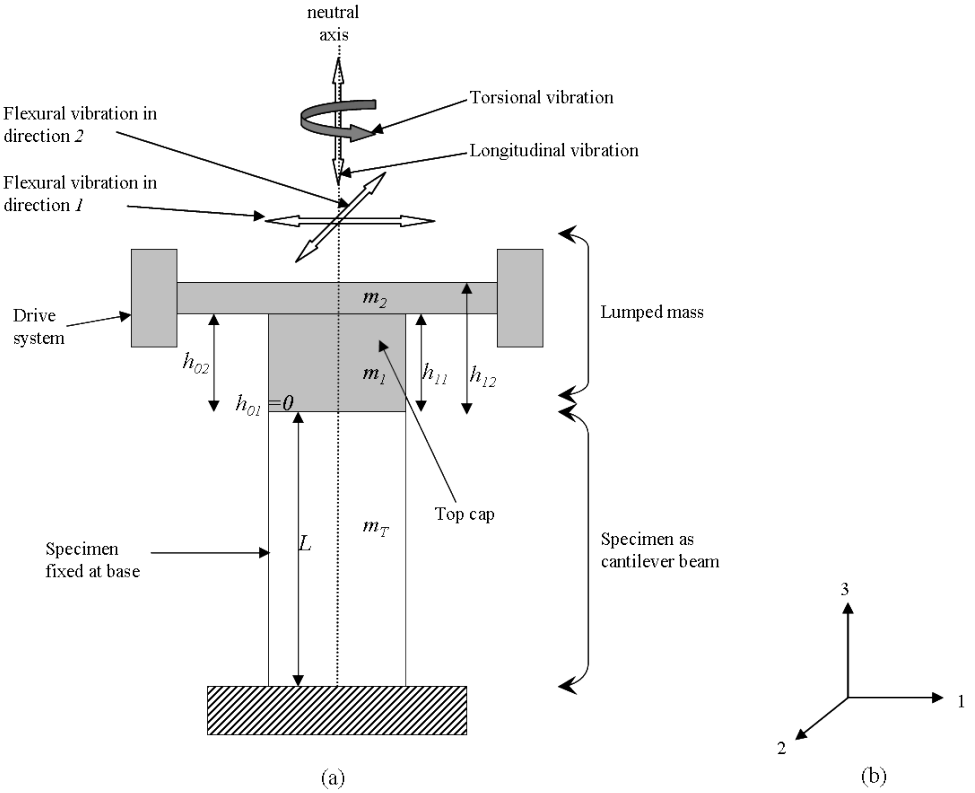

Figure B.2: *(a) Different modes of vibration of a specimen in resonant column apparatus (RCA). (b) Axis representation for RCA.*

Finally, the solution for the longitudinal mode of vibration is given as (Kohoutek, 1981),

$$\frac{m_T}{M} = \sqrt{\frac{m_T\, l\, \omega^2}{E\, A}}\, tan \sqrt{\frac{m_T\, l\, \omega^2}{E\, A}} \tag{B.6}$$

where, M is the total lumped mass attached at the free end of the specimen, E is the Young's modulus of the specimen, A is the cross sectional area of the specimen and ω is the circular resonant frequency from longitudinal vibration of the specimen.

B.2 Numerical modelling

To assess the effects anisotropy has on the stiffness values derived from a resonant column test a finite element model of the resonant column and a specimen with known cross-anisotropic properties was developed. Clayton et al. (2009) have previously developed an FE model of a Stokoe' resonant column using the finite element software ABAQUS (version 6.8). They were able to validate their model against measured laboratory test results on aluminium bars. They showed that the FE model accurately predicted the behaviour of a calibration bar of known properties. Their model was therefore adopted as a starting point for this work.

Modifications were made to include a specimen (diameter $70\,mm$ and length $140\,mm$) with defined elastic transversely isotropic properties. The geometry and density of the individual components of the drive mechanism (drive plate, magnets, accelerometer and counter weight) accurately replicate the complex geometry of the physical drive mechanism of a Stokoe resonant column apparatus (Figure B.3).

The specimen and drive mechanism were modelled separately and merged together to ensure all connections were rigid. The model was carefully partitioned such that the model was built using predominately hexagonal elements of size $4\,mm \times 4\,mm \times 4\,mm$; however some triangular prisms (wedges) were used in transition regions. 22646 elements were used, of which 12110 elements were for the specimen alone. The number of elements and element sizes were chosen to minimize the effect of meshing error on resonant frequency, as suggested by

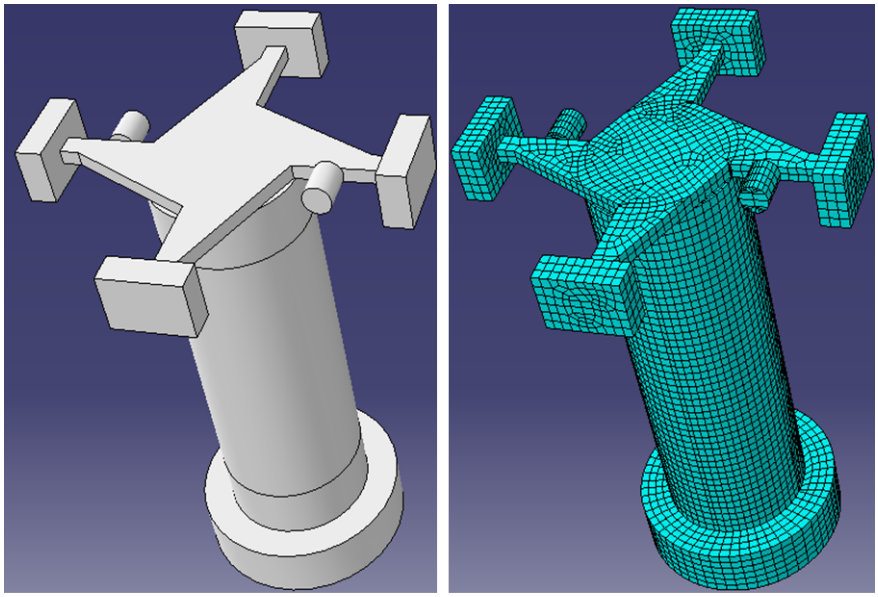

Figure B.3: *Modelled resonant column apparatus with a specimen, (a) before partition, and (b) after meshing.*

Clayton et al. (2009). Natural frequency extraction (sometimes referred to as 'frequency analysis') was used to calculate the natural modes of vibration and the corresponding natural frequencies by computing the eigenvectors and the eigenvalues of the model.

A number of different specimens were analysed. One set of analyses ('*iso*') modelled an isotropic specimen, with a further two sets being undertaken to include specimen anisotropy. In the first anisotropic model ('*vc*') the plane of isotropy was horizontal, equivalent to a specimen cut vertically from a typical transversely isotropic soil. In second anisotropic model ('*hc*') the plane of isotropy was vertical, equivalent to a specimen cut horizontally from a transversely isotropic soil, before being mounted vertically in the apparatus, as shown in Figure B.4.

B.3 Simulation results

The first set of analyses was conducted on isotropic specimens ('*iso*') with varying aspect (height to diameter) ratios. G_{iso}, E_{iso}, $E_{flex1iso}$ and $E_{flex2iso}$ were calculated from resonant frequencies for the respective torsional, longitudinal and flexural modes of vibration using Equations B.2 - B.6, where '*iso*' denotes iso-

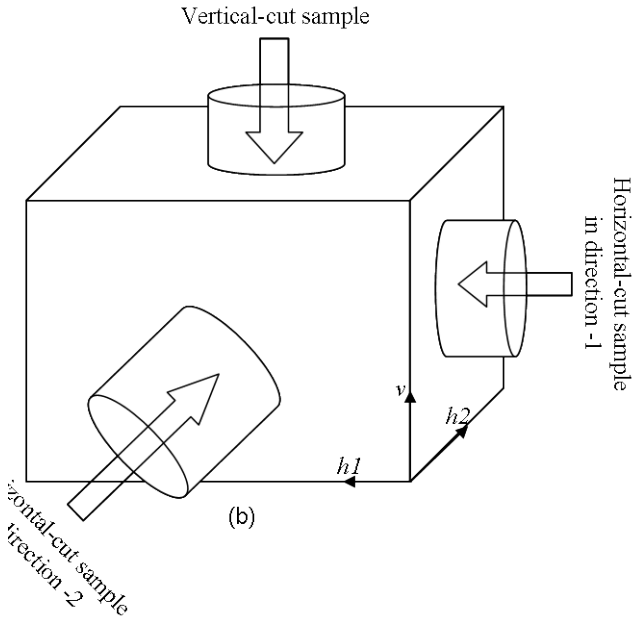

Figure B.4: *Sampling directions in a block sample. For a cross-anisotropic material sample extruded in horizontal direction 1 and 2 are same.*

tropic material, and '1' and '2' denote the two different flexural directions. Since the specimen was isotropic, $E_{flex1iso}$ and $E_{flex2iso}$ were equal and were denoted as $E_{flexiso}$.

In the derivation of Equation B.6 the effects of platen stiffness and lateral restraint are not taken into account. For short specimens it was thought that these might be significant, leading to over prediction of Young's modulus.

Figure B.5 shows the ratios of the $E_{flex1iso}$, E_{iso}, and G_{iso}, calculated from the extracted frequencies obtained from torsional, longitudinal and flexural mode of vibration respectively, by using Equations B.2 - B.6, to those input as material properties. It can be seen that the calculated value of $E_{flexiso}$ is dependent on l/d ratio, and for the conventional resonant column l/d ratio (=2) an error of around 10% will occur. The effect of aspect ratio on the shear modulus determined from torsional vibration appears negligible. The effect on Young's modulus derived from longitudinal vibration remains small down to aspect ratios of unity.

In the second set of numerical analyses, the specimen was modelled as a vertically cut transversely isotropic material ('*vc*'), with the axis of isotropy in the horizontal plane. G_{vc}, E_{vc}, $E_{flex1vc}$ and $E_{flex2vc}$ were calculated from Equations B.2 - B.6,

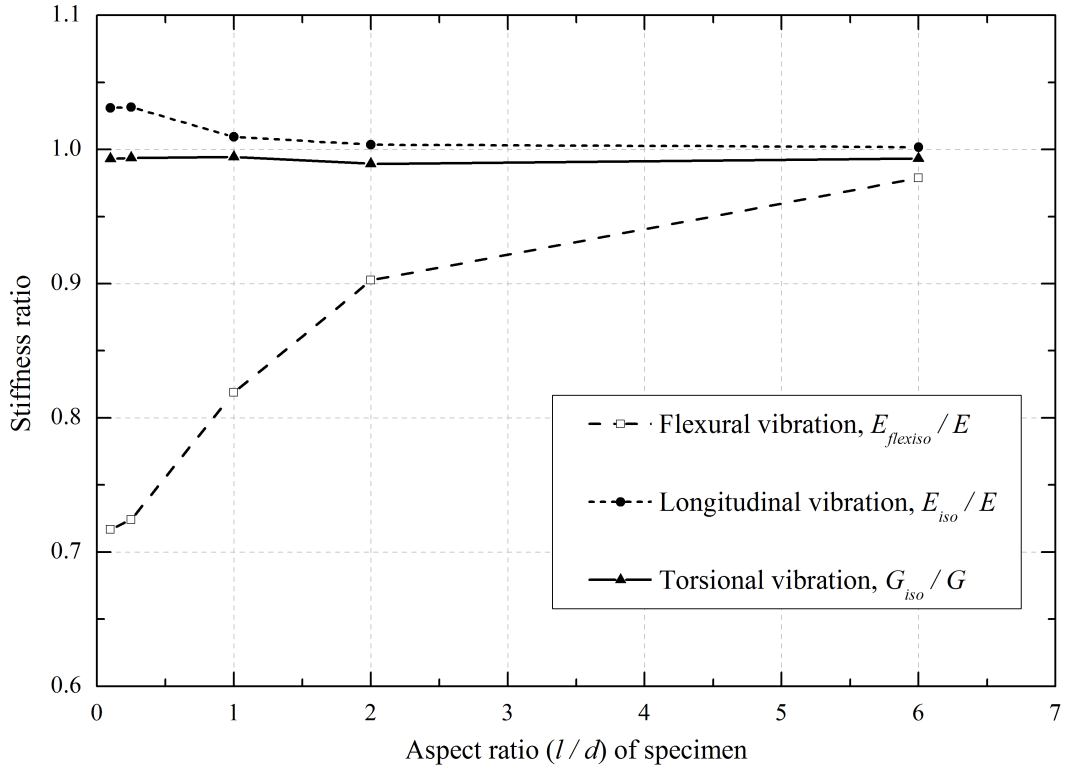

Figure B.5: *Ratio of calculated stiffness to the defined stiffness for an isotropic material with different aspect ratio.*

where the subscript 'vc' represents vertical cut sample. As might be expected, G_{vc} and E_{vc} values computed from the resonant frequencies in torsion and in longitudinal vibration were equal to the input values of G_v and E_v respectively. However, given the contribution of shear stiffness to the flexural stiffness of a 2:1 aspect ratio specimen identified (above) for the isotropic 'specimen', the values of Young's modulus calculated from the resonant frequency under flexural excitation (E_{flexvc}) differed from those in longitudinal excitation, and depended both on the input value E_v and G_v, as shown in Figure B.6.

A third set of numerical analyses were performed to model a horizontally cut ('hc') specimen where the plane of isotropy is perpendicular during resonant column testing, as shown in Figure B.4. Similar cross-anisotropic parameters to those used in the second set of analyses were chosen. G_{hc}, E_{hc}, $E_{flex1hc}$ and $E_{flex2hc}$ were calculated from Equations B.2 - B.6, where the subscript 'hc' represents horizontally cut specimen.

From these analyses it could be seen that, irrespective of the values taken by all other parameters, E_{hc} was equal to E_h. $E_{flex1hc}$ and $E_{flex2hc}$ were equal to

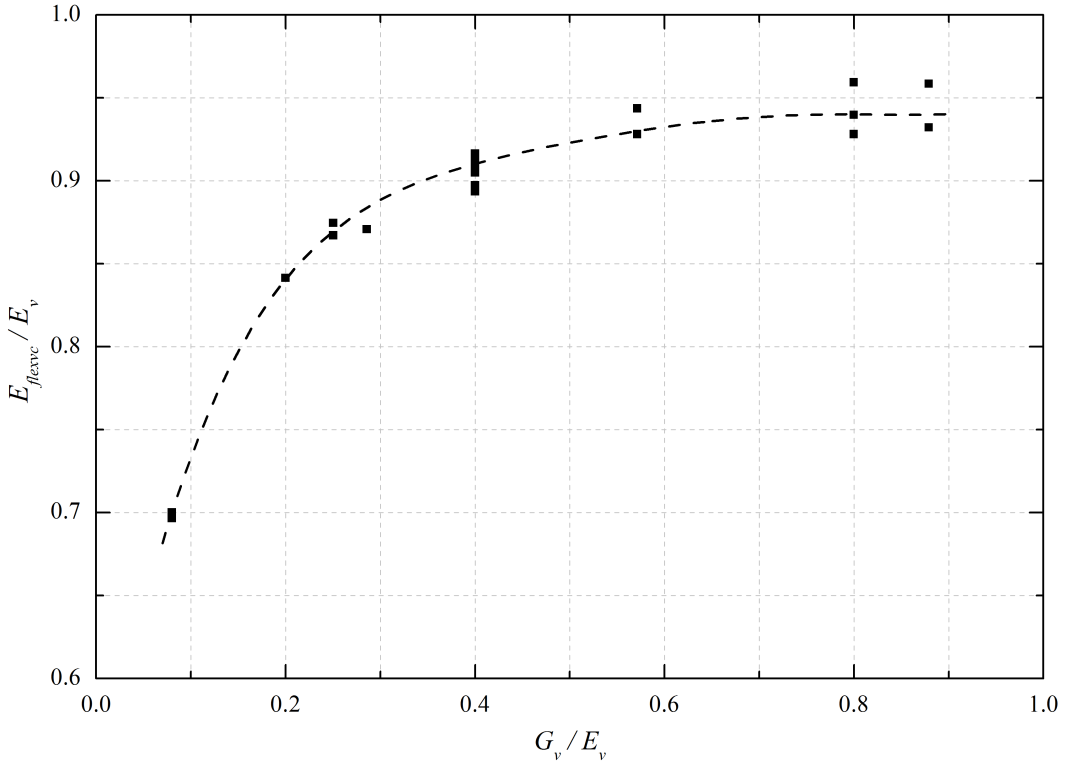

Figure B.6: *Effect of vertical shear modulus on Young's modulus of specimen inferred from flexural resonant frequency.*

$0.9 - 0.93\ E_h$ for the analyses that were conducted, but (by comparison with the effects shown in Figure B.6) shear stiffness in the plane of flexure may have a significant effect

G_{hc} was not equal to G_h or G_v. This stems from the fact that in the plane of torsional shear vibration, the shear properties of the specimen are not uniform, but vary from G_h to G_v. The value of G_{hc} inferred from the torsional resonant frequency results from a combination of shear moduli G_h and G_v, and from the analyses is approximately equal to the square root of the product of the shear moduli in the vertical and horizontal planes (Figure B.7).

These results suggest that, at least in principle, resonant column testing of both vertical and horizontal specimens cut from a transversely isotropic soil can allow the degree of anisotropy to be quantified. G_v can be determined from torsional resonance of vertically cut specimens, as usual. E_v can be determined from longitudinal resonance, and from flexural resonance and (with correction) Cascante's equation. E_h can be determined from horizontally cut specimens. The shear stiffness in the horizontal plane (G_h) can be deduced from G_v and the measured

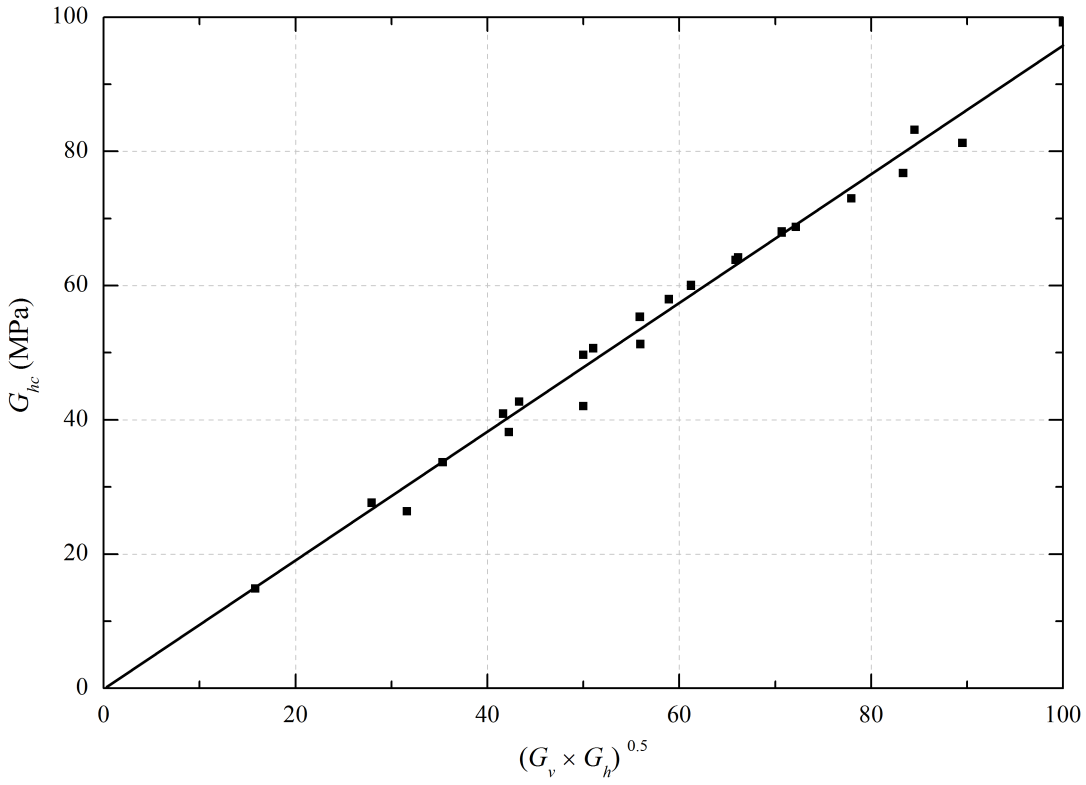

Figure B.7: *Relationship between shear modulus determined from torsional vibration of vertical cut specimen, and defined shear moduli values.*

value of G_{hc}, since

$$G_h = G_{hc}^2/G_v \tag{B.7}$$

In practice, values of shear moduli are likely to be more reliable than values of E, since the former are measured in torsion, and will be little affected by bedding effects, which may reduce measured values of Young's modulus for stiffer materials.

B.4 Summary

The standard (torsional) resonant column test determines the independent shear modulus in the vertical plane, G_v, when carried out on a conventional vertically-cut specimen. This value would equal one-third of the Young's modulus (E) for an isotropic undrained specimen, but the ratios G_v/E_v and G_v/E_h will vary if the material is transversely isotropic.

For an isotropic material the use of flexural vibration to derive E using Equation B.4 introduce errors of about 10% when the aspect ratio (l/d) of the specimen is (as usual) around 2. This error in E_{flex} occurs because no shear deformation is included in deriving Equations B.4 - B.5. However, although longitudinal vibration (and the use of Equation B.6) may provide a more accurate method for calculating E, more complex apparatus is required.

Numerical analyses of the resonant column apparatus with transversely isotropic soil shows that the degree of anisotropy of a soil can only be deduced if both vertical and horizontal cut specimens are tested. When this is done a maximum of four independent variables can be obtained with reasonable accuracy from flexural (or longitudinal) and torsional vibration of vertically and horizontally cut specimens. Values of E_v and E_h can be measured using longitudinal vibration of vertical and horizontal cut specimens respectively. Flexural vibration can also be used to calculate these stiffnesses, although the effect of shear stiffness in the plane of distortion needs to be borne in mind. Shear stiffness in the vertical plane can be obtained using torsional vibration of a vertical cut specimen. Shear stiffness in the horizontal plane can determined using Equation B.7, once the

values of G_v and G_{hc} have been obtained.

Appendix C

Analytical model to calculate increase in pore pressure during hydrate dissociation

This appendix discusses the analytical model that is developed to calculate the increase in pore pressure due to hydrate dissociation.

C.1 For general case

Consider a soil mass of volume (V_{in}) and porosity (ϕ_{in}) has a hydrate saturation (S_h). The hydrate is within the hydrate stability region at pressure (P_{in}) and temperature (T_{in}). If the temperature raised to T_{fin} such that hydrate dissociates, then the pore pressure within the sediment may increase. The increase in pore pressure can be calculated by following these steps.

At initial condition

There are three different initial conditions are identified with respect to water saturation;

- Water saturated hydrate bearing sediments: The sediment in which all the

pore spaces are filled with methane hydrate and water.

- Gas saturated hydrate bearing sediments: The sediment in which all the pore spaces are filled with methane hydrate and methane gas.
- Partially water saturated hydrate bearing sediments: The sediment in which all the pore spaces are filled with methane hydrate, methane gas, and water.

Water saturated hydrate bearing sediments

Since there are no free methane gas within water saturated sediments, initial moles of methane gas (n_{in}) for the water saturated sediment is zero ($n_{in} = 0$).

Gas saturated and partially water saturated sediments

Initial moles of methane gas (n_{in}) within gas saturated or partially water saturated sediments can be calculated from the gas law. As methane is a non-ideal gas, moles of methane gas present in the pore space at a given temperature and pressure can be calculated from Peng-Robinson gas equation (Peng and Robinson, 1976),

$$P = \left(\frac{R\,T}{V_m - b}\right) - \left(\frac{a\,\alpha}{V_m^2 + 2\,b\,V_m - b^2}\right) \tag{C.1}$$

where $V_m (= \frac{V_{va}}{n})$ is available molar volume for gas; V_{va} is the volume of voids available for gas; n is number of moles of gas in the voids; P is pressure (Pa); T is temperature (^oK); R is the universal gas constant (8.314472 Pa/K/mole); and a, b and α are Peng-Robinson's coefficients relating to gas as,

$$a = \frac{0.45724\,R^2\,T_c^2}{P_c} \tag{C.2}$$

$$b = \frac{0.07780\,R\,T_c}{P_c} \tag{C.3}$$

and

$$\alpha = \left(1 + \left(0.37464 + 1.54226\,\omega - 0.26992\,\omega^2\right)\left(1 - \sqrt{\frac{T}{T_c}}\right)\right)^2 \tag{C.4}$$

where, T_c and P_c are temperature and pressure at the critical point respectively, and ω is accentric factor. For methane gas; $T_c = 190.6\,K$ and $P_c = 4.656\,MPa$ and $\omega = 0.0108$. Substituting these values in Equations C.2 to C.4 yield $a = 0.24663$, $b = 2.64804 \times 10^{-5}$, and $\alpha = \left(1 + 0.39126\left(1 - \sqrt{\frac{T}{190.6}}\right)\right)^2$.

The Peng-Robinson's equation of state has four unknown parameters for a gas; pressure, temperature, number of moles and volume. If three parameters are known the fourth parameter can be calculated using Equation C.1.

At initial condition, pressure (P_{in}) and temperature (T_{in}) within the soil mass is known. Volume (V_1) available for methane gas can be calculated from initial conditions,

$$V_1 = V_{in} - (V_{solid} + V_{hy} + V_{w:in}) \tag{C.5}$$

where, V_{solid} is volume of soil solids ($= V_{in} \times (1 - \phi_{in})$), V_{hy} is volume of hydrate ($= V_{v:in} \times S_h$; S_h is hydrate saturation and is defined as volume of hydrate per unit of volume of the voids), $V_{v:in}$ is initial volume of voids ($= V_{in} \times \phi_{in}$), and $V_{w:in}$ is the initial volume of water ($= V_{v:in} \times S_{w:in}$; $S_{w:in}$ is initial water saturation). Thus Equation C.5 can be rewritten as,

$$V_1 = V_{v:in}(1 - S_h - S_{w:in}) \tag{C.6}$$

The initial moles of methane gas (n_{in}) within the pore spaces of gas saturated or partially water saturated sediments can be calculated using initial six soil properties (P_{in}, T_{in}, V_{in}, ϕ_{in}, S_h, and $S_{w:in}$) using Equations C.1 and C.6.

At the end of hydrate dissociation

As hydrate dissociates, it converts into its constituents parts of water and gas, the rise in pore pressure may occur under undrained condition. The final pore pressure (P_{fin}) can be calculated using final temperature (T_{fin}), moles of gas (n_{fin}), and available volume for gas (V_2) in Equation C.1.

Final moles of methane gas (n_{fin}) can be calculated as,

$$n_{fin} = n_{in} + n_d \tag{C.7}$$

where, n_d is the moles of methane gas from dissociation which is equivalent to the moles of methane hydrate (n_{hy}) within the specimen ($n_{hy} = \frac{V_{hy}\,\rho_{hy}}{M_{hy}}$; ρ_{hy} and M_{hy} are mass density and molar mass of methane hydrate respectively.

As hydrate dissociates some of the methane gas will dissolve in water (evolved from dissociation). Therefore, true moles of methane gas within pore spaces can be calculated from,

$$n_d = n_{hy} - (sol_m) \times n_{w:diss} \tag{C.8}$$

where sol_m is molar solubility of methane in water, and $n_{w:diss}$ is moles of water from dissociation ($= \frac{5.75}{(cage)} n_{hy}$, $cage$ is cage occupancy of methane within hydrate).

Final available volume for gas (V_2) can be calculated as,

$$V_2 = V_{in} - (V_{solid} + V_{w:in} + V_{w:diss}) + \frac{P_{fin} - P_{in}}{K}\, V_{in} \tag{C.9}$$

where, $V_{w:diss}$ is volume of water due to hydrate dissociation ($= \frac{5.75}{(cage)} \frac{n_{hy}\, M_w}{\rho_w}$; ρ_w and M_w are mass density and molar mass of water respectively, and $cage$ is cage occupancy of methane in methane hydrate), K is bulk modulus of soil mass at the end of dissociation. The third part in Equation C.9 $\left(\frac{P_{fin}-P_{in}}{K}\, V_{in}\right)$ is the volume expansion of soil mass due to change in effective stress.

It can be seen that V_2 is a function of P_{fin}, therefore P_{fin} is calculated through iteration of P_{fin} with respect to known properties (n_{in}, n_{fin}, P_{in}, ρ_{hy}, M_{hy}, ρ_w, M_w, $cage$, sol_m and K) in Equations C.1, C.7, and C.9.

Pore pressure due to temperature rise

As temperature rises from T_{in} to T_{fin}, pore pressure will increase irrespective of hydrate dissociation due to the expansion of methane gas. The rise in pore

pressure due to gas expansion (P_{temp}) is calculated through iteration of P_{temp} with respect to n_{in}, T_{fin}, and $V_{2:temp}$ in Equation C.1. Where $V_{2:temp}$ is defined as,

$$V_{2:temp} = V_1 + \frac{P_{temp} - P_{in}}{K} V_{in} \tag{C.10}$$

Then, the increase in pore pressure due to hydrate dissociation (P_{diss}) can be calculated as,

$$P_{diss} = P_{fin} - P_{temp} \tag{C.11}$$

C.2 For laboratory specimen

To calculate pore pressure evolution during dissociation within a specimen, two assumptions are made. All the water was converted into methane hydrate, and solubility of methane in water was negligible due to very low value (<0.0015 (Chapoy et al., 2004)) within applied range of pressure ($\leq 13\,MPa$) and temperature ($\leq 20^0C$).

After hydrate formation

As discussed in Chapter 3 the cell and back pressure are the only stresses applied to specimens. So, the radial strain can assumed to be equal to the axial strain for an isotropic, homogeneous specimen. Volume of the specimen at the end of hydrate formation (V_{sp1}) can be calculated using the initial specimen dimensions and the axial strain:

$$V_{sp1} = \frac{\pi}{4} \left(D_0 - \frac{\Delta L_1}{L_0} D_0 \right)^2 L_0 \left(1 - \frac{\Delta L_1}{L_0} \right) \tag{C.12}$$

where, D_0 and L_0 are specimen diameter and height at the start of the test respectively, ΔL_1 is the change in axial displacement at the end of the hydrate formation.

To calculate moles of methane gas after complete hydrate formation (or, before

the start of hydrate dissociation stage) using Equation C.1, pressure (P_{in}), temperature (T_{in}), and pore volume for gas (V_1) are required. Pressure (P_{in}) and temperature (T_{in}) within the specimen are back pressure and internal temperature values respectively to the specimen. Pore volume (V_1) available for the methane gas can be calculated using Equation C.5. Since, hydrate was formed using the excess gas method $V_{w:in}$ is equal to zero after complete formation. Therefore, Equation C.5 can be written as:

$$V_1 = V_{sp1} - (V_{solid} + V_{hy}) \tag{C.13}$$

where, V_{sp1} is current volume of the specimen, V_{solid} is volume of soil solids ($= m_s/G_s$; m_s is mass of dry soil within the specimen, G_s is specific density of soil solids, $G_s = 2.65$ for LBE sands). V_{hy} is the volume of total hydrate and can be calculated using the initial volume of added water ($V_{w:in}$) within the specimen,

$$V_{hy} = \frac{(cage)}{5.75} \times \frac{V_{w:in}\, M_{hy}\, \rho_w}{M_w\, \rho_{hy}} \tag{C.14}$$

cage is cage occupancy of methane within methane hydrate, ρ_w and ρ_{hy} are mass density of water ($= 1000\, kg/m^3$) and methane hydrate ($= 917\, kg/m^3$) respectively. M_w and M_{hy} are molar mass of water ($= 18.015\, g/mol$) and methane hydrate ($= 119.63\, g/mol$) respectively.

Then initial number of moles of methane gas (n_{in}) within the pore spaces is calculated using P_{in}, T_{in}, and V_1 in Equation C.1.

At the end of hydrate dissociation

In laboratory tests, hydrate was dissociated through increase in specimen temperature to T_{fin}. To calculate final pore pressure within the specimen, final moles of methane gas (n_{fin}) and the available volume for the gas (V_2) are required. These are calculated using modified equations C.7 and C.9 as given below,

$$n_{fin} = n_{in} + n_d \tag{C.15}$$

$$V_2 = V_{sp2} - (V_{solid} + V_w) \tag{C.16}$$

where, n_d is the moles of methane gas from dissociation which is equivalent to the moles of methane hydrate within the specimen ($= V_{hy} \times \rho_{hy}/M_{hy}$), and V_{sp2} is the current volume of the specimen. V_{sp2} is calculated similar to V_{sp1}, such as

$$V_{sp2} = \frac{\pi}{4}\left(D_0 - \frac{\Delta L_2}{L_0} D_0\right)^2 L_0 \left(1 - \frac{\Delta L_2}{L_0}\right) \tag{C.17}$$

where, ΔL_2 is the change in axial displacement at the end of the hydrate dissociation. As noted in Equation C.16, the volume expansion of the specimen due to changes in the effective stress is not considered. This is due to the fact that it has accounted in calculation of V_{sp2}.

Substituting n_{fin}, T_{fin}, and V_2 in Equation C.1, the expected final pore pressure (P_{fin}) after dissociation can be determined.

Pore pressure due to temperature rise

The increase in pore pressure (P_{temp}) due to gas expansion is calculated using n_{in}, T_{fin}, and V_1 in Equation C.1. So that the true expected pore pressure rise due to hydrate dissociation can be calculated as:

$$P_{diss} = P_{fin} - P_{temp} \tag{C.18}$$

References

Ahmadi, G., Ji, C. and Smith, D. (2004). Numerical solution for natural gas production from methane hydrate dissociation, *Journal of petroleum science and engineering* **41**(4): 269–285.

Ahmadi, G., Ji, C. and Smith, D. (2007). Natural gas production from hydrate dissociation: An axisymmetric model, *Journal of petroleum science and engineering* **58**(1-2): 245–258.

Alberty, M., Hafle, M. and Minge, J. (1997). Mechanisms of shallow waterflows and drilling practices for intervention, *Offshore Technology Conference*, p. OTC 8301.

Anderson, R., LLamedo, M. and Tohidi, B. (2004). Experimental investigation of methane hydrate growth and dissociation hysteresis in narrow pores, *European Geosciences Union 1st General Assembly*, Vol. 6, Nice, France, p. 07024. Geophysical Research Abstracts.

Anderson, R., Llamedo, M., Tohidi, B. and Burgass, R. (2003). Characteristics of clathrate hydrate equilibria in mesopores and interpretation of experimental data, *The Journal of Physical Chemistry B* **107**(15): 3500–3506.

Anderson, R., Tohidi, B. and Webber, J. (2009). Gas hydrate growth and dissociation in narrow pore networks: capillary inhibition and hysteresis phenomena, *Geological Society, London, Special Publications* **319**(1): 145.

ASTM-D4015 (1992). Standard test methods for modulus and damping of soils by the resonant-column method.

Bagirov, E. and Lerche, I. (1997). Hydrates represent gas source, drilling hazard, *Oil and Gas Journal* **95**: 99–104.

Beauchamp, B. (2004). Natural gas hydrates: myths, facts and issues, *Comptes Rendus-Geoscience* **336**(9): 751–765.

Berndt, C., Bunz, S., Clayton, T., Mienert, J. and Saunders, M. (2004). Seismic character of bottom simulating reflectors: examples from the mid-norwegian margin, *Marine and Petroleum Geology* **21**(6): 723–733.

Berndt, C., Mienert, J., Vanneste, M., Bunz, S. and Bryn, P. (2002). Submarine slope-failure offshore norway triggers rapid gas hydrate decomposition, *4th int. conf. on gas hydrates proc., Yokohama, Japan*.

Billy, M. (1980). A new simple method for measuring the velocities of sound in isotropic, nondispersive solids, *Journal of Physics D: Applied Physics* **13**: 767–771.

Biot, M. (1956). Theory of propagation of elastic waves in a fluid-saturated porous solid. i. low-frequency range, *J. Acoust. Soc. Am* **28**(2): 168–178.

Boswell, R. and Collett, T. (2010). Current perspectives on gas hydrate resources, *Energy Environ. Sci.* **4**: 1206–1215.

Briaud, J. and Chaouch, A. (1999). Hydrate melting in soil around hot conductor, *Journal of Geotechnical and Geoenvironmental Engineering* **123**(7): 645–653.

Brooks, J., Anderson, A., Sassen, R., Kennicutt, M. and Guinasso, N. (1994). Hydrate occurrences in shallow subsurface cores from continental slope sediments, *Annals of the New York Academy of Sciences* **715**(1): 381–391.

Bui, M. T. (2009). *Influence of Some Particle Characteristics on the Small Strain Response of Granular Materials*, PhD thesis, Civil Engineering and the Environment, University of Southampton, Southampton, UK.

Bui, T. M., Clayton, C. R. I. and Priest, J. A. (2010). The universal void ratio function for small strain shear modulus, *Fifth International Conference on Recent Advances in Geotechnical Earthquake Engineering and Soil Dynamics*, San Diego, California (USA).

Carcione, J. M. and Gei, D. (2004). Gas-hydrate concentration estimated from p- and s-wave velocities at the mallik 2l-38 research well, mackenzie delta, canada, *Journal of Applied Geophysics* **56**(1): 73–78.

Carpenter, G. (1981). Coincident sediment slump/clathrate complexes on the us atlantic continental slope, *Geo-Marine Letters* **1**(1): 29–32.

Carson, B., Westbrook, G. and Musgrave, B. (1993). Leg 146 preliminary report (cascadia margin), *Technical report*, Ocean Drilling Program, A&M University Research Park, 1000 Discovery Drive, College Station, Texas 77845-9547.
URL: *http://www-odp.tamu.edu/publications/prelim/146PREL.PDF*

Cascante, G., Santamarina, C. and Yassir, N. (1998). Flexural excitation in a standard torsional-resonant column device, *Canadian Geotechnical Journal* **35**: 478–490.

Chand, S. and Minshull, T. (2004). The effect of hydrate content on seismic attenuation: A case study for mallik 2l-38 well data, mackenzie delta, canada, *Geophysical research letters* **31**(14): L14609.

Chand, S., Minshull, T. A., Gei, D. and Carcione, Jose, M. C. (2004). Elastic velocity models for gas-hydrate-bearing sediments- a comparison, *Geophysical Journal International* **159**(2): 573–590.

Chapoy, A., Mohammadi, A., Richon, D. and Tohidi, B. (2004). Gas solubility measurement and modeling for methane–water and methane–ethane–n-butane–water systems at low temperature conditions, *Fluid phase equilibria* **220**(1): 111–119.

Chen, A. T. F., Lee, S. H. H. and Stokoe, K. H. (1979). Interpretation of strain dependent modulus and damping from torsional soil tests, *Technical Report USGS-GD-79-002, NTIS No PB-298479*, U. S. Geological Survey.

Circone, S., Stern, L. and Kirby, S. (2004). The role of water in gas hydrate dissociation, *J. Phys. Chem. B* **108**(18): 5747–5755.

Circone, S., Stern, L., Kirby, S., Durham, W., Chakoumakos, B., Rawn, C., Rondinone, A. and Ishii, Y. (2003). Co2 hydrate: synthesis, composition, structure, dissociation behavior, and a comparison to structure i methane hydrate, *J. Phys. Chem. B* **107**(23): 5529–5539.

Clarke, M. and Bishnoi, P. (2000). Determination of the intrinsic rate of ethane gas hydrate decomposition, *Chemical Engineering Science* **55**(21): 4869–4883.

Clayton, C., Kingston, E. and Priest, J. (2008). Testing of pressurised cores containing gas hydrate from deep ocean sediments, *Proceedings of the 6th International Conference on Gas Hydrates*, Vancouver, British Columbia (Canada).

Clayton, C., Priest, J. and Best, A. (2005). The effect of disseminated methane hydrate on the dynamic stiffness and damping of a sand, *Geotechnique* **55**(6): 423–434.

Clayton, C., Priest, J., Bui, M. and Kim, S. (2009). The stokoe resonant column apparatus: Effects of stiffness, mass and specimen fixity, *Geotechnique* **59**(5): 429–437.

Collett, T. (1994). Permafrost-associated gas hydrate accumulationsa, *Annals of the New York Academy of Sciences* **715**(1): 247–269.

Collett, T. and Dallimore, S. (2002). Detailed analysis of gas hydrate induced drilling and production hazards, *Proceedings of the 4th International Conference on Gas Hydrates*, Yokohama (Japan), pp. 47–52.

Collett, T., Riedel, M., Cochran, J., Boswell, R., Presley, R., Kumar, P., Sathe, A., Sethi, A., Lall, M., Sibal, V. and Scientists, T. N. E. . (2008). Indian national gas hydrate program expedition 01 initial report, *Technical report*, Indian Directorate General of Hydrocarbons.

Consoli, N., Foppa, D., Festugato, L. and Heineck, K. (2007). Key parameters for strength control of artificially cemented soils, *Journal of geotechnical and geoenvironmental engineering* **133**(2): 197–205.

Cortes, D., Martin, A., Yun, T., Francisca, F., Santamarina, J. and Ruppel, C. (2009). Thermal conductivity of hydrate-bearing sediments, *Journal of Geophysical Research-Solid Earth* **114**(B11): B11103.

Dallimore, S. R. and Collett, T. S. (1995). Intrapermafrost gas hydrates from a deep core hole in the mackenzie delta, northwest territories, canada, *Geology* **23**(6): 527–530.

Demirbas, A. (2010). Methane hydrates as potential energy resource: Part 1-importance, resource and recovery facilities, *Energy Conversion and Management* **51**(7): 1547–1561.

Dillon, W. P. (2001). *Encyclopedia of Physical Science and Technology*, Vol. 8, Academic Press, San Diego, California, chapter Gas hydrate in the ocean environment, pp. 473–486.

Dillon, W. P. and Max, M. D. (2003). *Natural Gas Hydrate in Oceanic and Permafrost Environment*, London: Kluwer Academic Publishers, chapter 6: Oceanic Gas Hydrate, pp. 61–76.

Driscoll, N., Weissel, J. and Goff, J. (2000). Potential for large-scale submarine slope failure and tsunami generation along the us mid-atlantic coast, *Geology* **28**(5): 407.

Durham, W., Kirby, S., Stern, L. and Zhang, W. (2003). The strength and rheology of methane clathrate hydrate, *J. Geophys. Res.* **108**(2182): 1–11.

Dvorkin, J., Berryman, J. and Nur, A. (1999). Elastic moduli of cemented sphere packs, *Mechanics of materials* **31**(7): 461–469.

Dvorkin, J., Helgerud, M., Waite, W., Kirby, S. and Nur, A. (2000). *Natural Gas Hydrate in Oceanic and Permafrost Environments*, Kluwer Academic Publishers, Netherlands, chapter 20: Introduction to physical properties and elasticity models, pp. 245–260.

Dvorkin, J., Mavko, G. and Nur, A. (1991). The effect of cementation on the elastic properties of granular material, *Mechanics of Materials* **12**(3-4): 207–217.

Dvorkin, J. and Nur, A. (1993). Dynamic poroelasticity: A unified model with the squirt and the biot mechanisms, *Geophysics* **58**(4): 524–533.

Dvorkin, J. and Nur, A. (1996). Elasticity of high-porosity sandstones: Theory for two north sea data sets, *Geophysics* **61**: 1363.

Ebinuma, T., Yasushi, K., Minagawa, H., Ohmura, R., Nagao, J. and Narita, H. (2005). Mechanical properties of sandy sediment containing methane hydrate, *Proceedings of the 5th International Conference on Gas Hydrates*, Vol. 3, Trondheim (Norway), pp. 958–961.

Ecker, C. (2001). *Seismic Characterization of Methane Hydrate Structures*, PhD thesis, Graduate Studies of Stanford University, Stanford University, Stanford, California (USA).

Ershov, E. and Yakushev, V. (1992). Experimental research on gas hydrate decomposition in frozen rocks, *Cold regions science and technology* **20**(2): 147–156.

Fernandez, A. and Santamarina, J. (2001). Effect of cementation on the small-strain parameters of sands, *Canadian Geotechnical Journal* **38**(1): 191–199.

Field, F. and Barber Jr, J. (1993). *Submarine Landslides: Selected Studies in the U.S. Exclusive Economic Zone*, U.S. Geological Survey, chapter A Submarine Landslide Associated with Shallow SeaFloor Gas and Gas Hydrates off Northern California, pp. 151–157.

Folger, P. (2008). Gas hydrates: Resource and hazard, *Technical report*, CRS Report for Congress.
URL: *http://www.fas.org/sgp/crs/misc/RS22990.pdf*

Francisca, F., Yun, T., Ruppel, C. and Santamarina, J. (2005). Geophysical and geotechnical properties of near-seafloor sediments in the northern gulf of mexico gas hydrate province, *Earth and Planetary Science Letters* **237**(3-4): 924 – 939.

Fredlund, D. (2000). The 1999 rm hardy lecture: The implementation of unsaturated soil mechanics into geotechnical engineering, *Canadian Geotechnical Journal* **37**(5): 963–986.

Fredlund, D. and Xing, A. (1994). Equations for the soil-water characteristic curve, *Canadian Geotechnical Journal* **31**(4): 521–532.

Freij-Ayoub, R., Tan, C., Clennell, B., Tohidi, B. and Yang, J. (2007). A wellbore stability model for hydrate bearing sediments, *Journal of Petroleum Science and Engineering* **57**(1-2): 209–220.

Gassmann, F. (1951). On elasticity of porous media (uber die elastizitat porosor medien), *Vierteljarhrsschrift der Naturforschenden Geselschaft,* **96**: 1–23.
URL: *http://citeseerx.ist.psu.edu/viewdoc/summary?doi=10.1.1.48.9319*

Glasby, G. (2003). Potential impact on climate of the exploitation of methane hydrate deposits offshore, *Marine and petroleum geology* **20**(2): 163–175.

Guerin, G. and Goldberg, D. (2002). Sonic waveform attenuation in gas hydrate-bearing sediments from the mallik 2l-38 research well, mackenzie delta, canada, *Journal of geophysical research* **107**(10.1029): 2088.

Guerin, G. and Goldberg, D. (2005). Modeling of acoustic wave dissipation in gas hydrate-bearing sediments, *Geochemistry Geophysics Geosystems* **6**(7): Q07010.

Handa, Y. P. and Stupin, D. Y. (1992). Thermodynamic properties and dissociation characteristics of methane and propane hydrates in 70-.ang.-radius silica gel pores, *The Journal of Physical Chemistry* **96**(21): 8599–8603.

Hardage, B., Remington, R. and Roberts, H. (2006). Gas hydrate - a source of shallow water flow?, *The Leading Edge* **25**(5): 634.

Hardin, B. and Black, W. (1966). Sand stiffness under various triaxial stressess, *Journal of the Soil Mechanics and Foundations Division* **92**(SM2): 27–42.

Hardin, B. and Drnevich, V. (1972a). Shear modulus and damping in soils: Design equations and curves, *Journal of the soil mechanics and foundations division* **98**(SM7): 667–692.

Hardin, B. and Drnevich, V. (1972b). Shear modulus and damping in soils: Measurement and parameter effects (terzaghi leture), *Journal of the soil mechanics and foundations division* **98**(6): 603–624.

Hashemi, S., Macchi, A., Bergeron, S. and Servio, P. (2006). Prediction of methane and carbon dioxide solubility in water in the presence of hydrate, *Fluid phase equilibria* **246**(1-2): 131–136.

Helgerud, M., Dvorkin, J., Nur, A., Sakai, A. and Collett, T. (1999). Elastic-wave velocity in marine sediments with gas hydrates: Effective medium modeling, *Geophysical Research Letters* **26**(13): 2021–2024.

Helgerud, M., Waite, W., Kirby, S. and Nur, A. (2009). Elastic wave speeds and moduli in polycrystalline ice ih, si methane hydrate, and sii methane-ethane hydrate, *Journal of geophysical research* **114**(B02212): 1–11.

Hobbs, N. (1975). Factors affecting the prediction of settlement of structures on rock: with particular reference to the chalk and trias (general report and state-of-the-art review for session iv), *Proc. Conf on Settlement of Structures*, BGS Cambridge, Pentech Press, London, pp. 579–610.

Holland, M., Schultheiss, P., Roberts, J. and Druce, M. (2008). Observed gas hydrate morphologies in marine sediments, *Proceedings of the 6th International Conference on Gas Hydrates*, Vancouver, British Columbia (Canada).

Hu, G. W., Ye, Y. G., Zhang, J., Liu, C. L., Diao, S. B. and Wang, J. S. (2010). Acoustic properties of gas hydrate-bearing consolidated sediments and experimental testing of elastic velocity models, *J. Geophys. Res.* **115**: B02102.

Huang, J. and Airey, D. (1998). Properties of artificially cemented carbonate sand, *Journal of geotechnical and geoenvironmental engineering* **124**: 492.

Huo, Z., Hester, K., Sloan Jr, E. and Miller, K. (2003). Methane hydrate non-stoichiometry and phase diagram, *AIChE journal* **49**(5): 1300–1306.

Hyndman, R. D. and Davis, E. E. (1992). A mechanism for the formation of methane hydrate and seafloor bottom-simulating reflectors by vertical fluid expulsion, *J. Geophys. Res.* **97**: 7025–7041. 10.1029/91JB03061.

Jayasinghe, A. and Grozic, J. (2008). Modeling dissociation behaviour of methane hydrate in porous soil media, *Proceedings of the 6th International Conference on Gas Hydrates*, Vancouver, British Columbia (Canada).

Johnston, D., Toksoz, M. and Timur, A. (1979). Attenuation of seismic waves in dry and saturated rocks; ii, mechanisms, *Geophysics* **44**(4): 691–711.

Jovicic, V. and Coop, M. (1997). Stiffness of coarse-grained soils at small strains, *Geotechnique* **47**(3): 545–61.

Kamath, V. and Holder, G. (1987). Dissociation heat transfer characteristics of methane hydrates, *AIChE Journal* **33**(2): 347–350.

Kawamura, T., Sakamoto, Y., Ohtake, M., Yamamoto, Y., Haneda, H., Yoon, J. and Komai, T. (2008). Dissociation behavior of hydrate core sample using thermodynamic inhibitor - part 2: Experimental investigation using long core samples, *International Journal of Offshore and Polar Engineering* **18**(2): 156–159.

Kayen, R. and Lee, H. (1991). Pleistocene slope instability of gas hydrate-laden sediment on the beaufort sea margin, *Marine Georesources & Geotechnology* **10**(1): 125–141.

Kim, H., Bishnoi, P., Heidemann, R. and Rizvi, S. (1987). Kinetics of methane hydrate decomposition, *Chemical engineering science* **42**(7): 1645–1653.

Kirchner, M. T., Boese, R., Billups, W. E. and Norman, L. R. (2004). Gas hydrate single-crystal structure analyses, *Journal of the American Chemical Society* **126**(30): 9407–9412.

Kneafsey, T. J., Tomutsa, L., Moridis, G. J., Seol, Y., Freifeld, B. M., Taylor, C. E. and Gupta, A. (2007). Methane hydrate formation and dissociation in a partially saturated core-scale sand sample, *Journal of Petroleum Science and Engineering* **56**(1-3): 108–126.

Koh, C. A. (2002). Towards a fundamental understanding of natural gas hydrates, *Chemical Society Reviews* **31**(3): 157–167.

Kohoutek, R. (1981). Natural longitudinal frequencies of a uniform rod with a tip mass or a spring, *Sound and Vibration* **77**(1): 147–148.

Kramer, S. L. (2004). *Geotechnical earthquake engineering*, Pearson education (Prentice-Hall Internation Series).

Kumar, A., Maini, B., PR, B., Clarke, M., Zatsepina, O. and Srinivasan, S. (2010). Experimental determination of permeability in the presence of hydrates and its effect on the dissociation characteristics of gas hydrates in porous media, *Journal of Petroleum Science and Engineering* **70**(1-2): 114–122.

Kvenvolden, K. (1988). Methane hydrate- a major reservoir of carbon in the shallow geosphere?, *Chemical Geology* **71**(1-3): 41–51.

Kvenvolden, K. (1993). Gas hydrates: geological perspective and global change, *Rev. Geophys* **31**(2): 173–187.

Kvenvolden, K. (1999). Potential effects of gas hydrate on human welfare, *in* PNAS (ed.), *Proceedings of the National Academy of Sciences*, Vol. 96, National Academy of Sciences, USA, pp. 3420–3426.

Kvenvolden, K. (2000). Gas hydrate and humans, *Annals-New York Academy of Sciences* **912**: 17–22.

Kvenvolden, K. A. (1994). Natural gas hydrate occurrence and issues, *Annals of the New York Academy of Sciences* **715**(1): 232–246.

Kvenvolden, K. A. and Barnard, L. A. (1983). Gas hydrates of the blake outer ridge, site 533, deep sea drilling project leg 76, *in* R. E. S. et al. (ed.), *Initial*

Reports of the Deep Sea Drilling Project, Vol. 76, U.S. Government Printing Office, U.S. Government Printing Office, Washington, USA, pp. 353–365.

Kwon, T., Cho, G. and Santamarina, J. (2008). Gas hydrate dissociation in sediments: Pressure-temperature evolution, *Geochemistry Geophysics Geosystems* **9**(3): Q03019.

Kwon, T.-H., Song, K.-I. and Cho, G.-C. (2010). Destabilization of marine gas hydrate-bearing sediments induced by a hot wellbore: A numerical approach, *Energy & Fuels* **24**(10): 5493–5507.

Lachet, V. and Behar, E. (2000). Industrial perspective on natural gas hydrates, *Oil & Gas Science and Technology* **55**(6): 611–616.

Lee, J., Francisca, F., Santamarina, J. and Ruppel, C. (2010). Parametric study of the physical properties of hydrate-bearing sand, silt, and clay sediments: 2. small-strain mechanical properties, *Journal of Geophysical Research* **115**(B11): B11105.

Lee, M., Hutchinson, D., Collett, T. and Dillon, W. (1996). Seismic velocities for hydrate-bearing sediments using weighted equation, *Journal of Geophysical Research* **101**(B9): 20347–20357.

Lee, M. W. and Collett, T. S. (2001). Elastic properties of gas hydrate-bearing sediments, *Geophysics* **66**(3): 763–771.

Love, A. (1927). *A treatise on the mathematical theory of elasticity, 1927*, Cambridge University Press.

MacKay, M. E., Jarrard, R. D., Westbrook, G. K. and Hyndman, R. D. (1994). Origin of bottom-simulating reflectors: Geophysical evidence from the cascadia accretionary prism, *Geology* **22**(5): 459–462.

Makogon, Y. (1981). *Hydrates of natural gas*, Moscow press.

Makogon, Y., Holditch, S. and Makogon, T. (2007). Natural gas-hydrates - a potential energy source for the 21st century, *Journal of Petroleum Science and Engineering* **56**(1-3): 14–31.

Malone, R. (1985). Gas hydrates topical report, *Technical Report DOE/METC/SP-218*, US Department of Energy.

Masui, A., Haneda, H., Ogata, Y. and Aoki, K. (2005). Effects of methane hydrate formation on shear strength of synthetic methane hydrate sediments, *Proceedings of the 5th International Conference on Gas Hydrates*, Vol. 2, Trondheim (Norway), pp. 657–663.

Matsumoto, R., Paull, C. and Wallace, P. (1996). Leg 164 preliminary report (gas hydrate sampling on the black ridge and carolina rise), *Technical report*, Ocean Drilling Program, A&M University Research Park, 1000 Discovery Drive, College Station, Texas 77845-9547.
URL: *http://www-odp.tamu.edu/publications/*

Matsumoto, R., Uchida, T., Waseda, A., Takeya, S., Hirano, T., Yamada, K., Maeda, Y. and Okui, T. (2000). 2. occurrence, structure, and composition of natural gas hydrate recovered from the blake ridge, northwest atlantic, *Proceedings of the Ocean Drilling Program. Scientific results*, Vol. 164, Ocean Drilling Program, pp. 13–28. Proceedings of the Ocean Drilling Program. Scientific results.

Matsushima, J. (2006). Seismic wave attenuation in methane hydrate-bearing sediments: Vertical seismic profiling data from the nankai trough exploratory well, offshore tokai, central japan, *Journal of geophysical research* **111**(B10): B10101.

Mavko, G. and Nur, A. (1975). Melt squirt in the asthenosphere, *Journal of Geophysical Research* **80**(11): 1444–1448.

Mavko, G. and Nur, A. (1979). Wave attenuation in partially saturated rocks, *Geophysics* **44**: 161.

McCann, C. (1969). Compressional wave attenuation in concentrated clay suspensions, *Acustica* **22**: 352–356.

McMullan, R. K. and Jeffrey, G. A. (1965). Polyhedral clathrate hydrates. ix. structure of ethylene oxide hydrate, *The Journal of Chemical Physics* **42**(8): 2725–2732.

Mienert, J., Vanneste, M., Bunz, S., Andreassen, K., Haflidason, H. and Sejrup, H. (2005). Ocean warming and gas hydrate stability on the mid-norwegian margin at the storegga slide, *Marine and Petroleum Geology* **22**(1-2): 233–244.

Mienert, J., Vanneste, M., Haflidason, H. and Bunz, S. (2010). Norwegian margin outer shelf cracking: a consequence of climate-induced gas hydrate dissociation?, *International Journal of Earth Sciences* pp. 1–19.

Mikami, J., Masuda, Y., Uchida, T., Satoh, T. and Takeda, H. (2000). Dissociation of natural gas hydrates observed by x-ray ct scanner, *Annals- New York Academy of Sciences* **912**: 1011–1020.

Minshull, T. A., Singh, S. C. and Westbrook, G. K. (1994). Seismic velocity structure at a gas hydrate reflector, offshore western colombia, from full waveform inversion, *J. Geophys. Res.* **99**(B3): 4715–4734.

Miyazaki, K., Masui, A., Sakamoto, Y., Aoki, K., Tenma, N. and Yamaguchi, T. (2011). Triaxial compressive properties of artificial methane-hydrate-bearing sediment, *Journal of Geophysical Research* **116**(B6): B06102.

Murphy III, W. (1982). Effects of partial water saturation on attenuation in massilon sandstone and vycor porous glass, *The Journal of the Acoustical Society of America* **71**: 1458.

Murphy III, W., Winkler, K. and Kleinberg, R. (1986). Acoustic relaxation in sedimentary rocks; dependence on grain contacts and fluid saturation, *Geophysics* **51**(3): 757.

Naioni, S. and Jahanfar, M. (2011). Effect of salt solution and plasticity index on undrain shear strength of clays, *World Academy of Science, Engineering and Technology* **73**: 982–986.

Nations, J. and Medley, Jr, G. (1997). Deepstar's evaluation of shallow water flow problems in the gulf of mexico, *Offshore Technology Conference*.

Nimblett, J., Shipp, R., Strijbos, F., Exploration, S. and Inc, P. (2005). Gas hydrate as a drilling hazard: Examples from global deepwater settings, *Offshore Technology Conference*.

Nixon, M. and Grozic, J. (2007). Submarine slope failure due to gas hydrate dissociation: a preliminary quantification, *Canadian Geotechnical Journal* **44**(3): 314–325.

Northern Aluminium Company Limited, . (1959). *Structural aluminium*, 4th impression, 1st edn, Cheney and Sons Ltd., Banbury, Oxon.

Olmos, B. and Roesset, J. (2010). Evaluation of the half-power bandwidth method to estimate damping in systems without real modes, *Earthquake Engineering & Structural Dynamics* **39**(14): 1671–1686.

Padden, M., Weissert, H. and De Rafelis, M. (2001). Evidence for late jurassic release of methane from gas hydrate, *Geology* **29**(3): 223–226.

Pallipurath, M. (2007). Dissociation of hydrated marine sediment. Oil and Gas Business, 2007.

Pang, W., Xu, W., Sun, C., Zhang, C. and Chen, G. (2009). Methane hydrate dissociation experiment in a middle-sized quiescent reactor using thermal method, *Fuel* **88**(3): 497–503.

Papagiannopoulos, G. and Hatzigeorgiou, G. (2011). On the use of the half-power bandwidth method to estimate damping in building structures, *Soil Dynamics and Earthquake Engineering* **31**: 1075–1079.

Parra, J. (2000). Poroelastic model to relate seismic wave attenuation and dispersion to permeability anisotropy, *Geophysics* **65**(1): 202–210.

Paull, C., Brewer, P., Ussler, W., Peltzer, E., Rehder, G. and Clague, D. (2003). An experiment demonstrating that marine slumping is a mechanism to transfer methane from seafloor gas-hydrate deposits into the upper ocean and atmosphere, *Geo-Marine Letters* **22**(4): 198–203.

Paull, C. K., Ussler III, W. and Dillon, W. K. (2000). *Natural Gas Hydrate in Oceanic and Permafrost Environment*, London: Kluwer Academic Publishers, chapter Potential Role of Gas Hydrate Decomposition in Generating Submarine Slope Failure: Natural Gas Hydrate in Oceanic and Permafrost Environment, pp. 149–156.

Pecher, I. and Holbrook, W. (2000). *Natural Gas Hydrate in Oceanic and Permafrost Environments*, Kluwer Academic Publishers, Netherlands, chapter 22: Seismic method for detecting and quantifying marine mathane hydrate/free gas reserviors, pp. 275–294.

Pecher, I., Minshull, T., Singh, S. and Huene, R. (1996). Velocity structure of a bottom simulating reflector offshore peru: Results from full waveform inversion, *Earth and Planetary Science Letters* **139**(3-4): 459–469.

Peng, D. and Robinson, D. (1976). A new two-constant equation of state, *Industrial & Engineering Chemistry Fundamentals* **15**(1): 59–64.

Pestana, J., Salvati, L. et al. (2006). Small-strain behavior of granular soils. i: Model for cemented and uncemented sands and gravels, *Journal of geotechnical and geoenvironmental engineering* **132**: 1071–1081.

Petres, D., Selim, M. S. and Sloan, E. D. (2000). Hydrate dissociation in pipelines by two-sided depressurization: Experiment and model, *Annals of the New York Academy of Sciences* **912**: 304–313. 10.1111/j.1749-6632.2000.tb06784.x.

Popenoe, P., Schmuck, E. and Dillon, W. P. (1993). *Submarine Landslides: Selected Studies in the U.S. Exclusive Economic Zone*, U.S. Geological Survey, chapter The Cape Fear Landslide: Slope Failure Associated with Salt Diapirism and Gas Hydrate Decomposition, pp. 40–53.

Priest, J. (2004). *The effect of methane gas hydrate on the dynamic testing of cohesive sand*, PhD thesis, Civil Engineering and the Environment, University of Southampton, Southampton, UK.

Priest, J., Best, A. and Clayton, C. (2006). Attenuation of seismic waves in methane gas hydrate-bearing sand, *Geophysical Journal International* **164**(1): 149–159.

Priest, J., Kingston, E. and Clayton, C. (2008). The structure of hydrate bearing fine grained marine sediments, *Proceedings of the 6th International Conference on Gas Hydrates*, Vancouver, British Columbia (Canada).

Priest, J., Rees, E. and Clayton, C. (2009). Influence of gas hydrate morphology on the seismic velocities of sands, *Journal of Geophysical Research-Solid Earth* **114**(B11): B11205.

Rampello, S., Viggiani, G. and Amorosi, A. (1997). Small-strain stiffness of reconstituted clay compressed along constant triaxial effective stress ratio paths, *Geotechnique* **47**(3): 475–489.

Reagan, M. and Moridis, G. (2007). Oceanic gas hydrate instability and dissociation under climate change scenarios, *Geophysical Research Letters* **34**(22): L22709.

Rees, E. V. (2009). *Methane Gas Hydrate Morphology and Its Effect on the Stiffness and Damping of some Sediments*, PhD thesis, Civil Engineering and the Environment, University of Southampton, Southampton, UK.

Richart, F., Hall, J. and Woods, R. (1970). *Vibrations of soils and foundations*, Wiley.

Ruppel, C. (1997). Anomalously cold temperatures observed at the base of the gas hydrate stability zone on the u.s. atlantic passive margin, *Geology* **25**(8): 699–702.

Sain, K., Minshull, T., Singh, S. and Hobbs, R. (2000). Evidence for a thick free gas layer beneath the bottom simulating reflector in the makran accretionary prism, *Marine Geology* **164**(1-2): 3–12.

Sakamoto, Y., Komai, T., Kawamura, T., Minagawa, H., Tenma, N. and Yamaguchi, T. (2007). Laboratory-scale experiment of methane hydrate dissociation by hot-water injection and numerical analysis for permeability estimation in reservoir: Part 1-numerical study for estimation of permeability in methane hydrate reservoir, *International journal of offshore and polar engineering* **17**(1): 47–56.

Santamarina, J. and Ruppel, C. (2008). The impact of hydrate saturation on the mechanical, electrical, and thermal properties of hydrate-bearing sand, silts, and clay, *Proceedings of the 6th International Conference on Gas Hydrates*, Vancouver, British Columbia (Canada).

Saxena, S., Avramidis, A. and Reddy, K. (1988). Dynamic moduli and damping ratios for cemented sands at low strains, *Canadian Geotechnical Journal* **25**(2): 353–368.

Saxena, S. and Reddy, K. (1989). Dynamic moduli and damping ratios for monterey no. o sand by resonant column tests, *Soils and Foundations* **29**(2): 37–51.

Schwab, W., Lee, H. and Twichell, D. (1993). *Submarine Landslides: Selected Studies in the U.S. Exclusive Economic Zone*, U.S. Geological Survey.
URL: *http://aquaticcommons.org/2050/*

Seed, H., Wong, R., Idriss, I. and Tokimatsu, K. (1984). Moduli and damping factors for dynamic analyses of cohesionless soils, *Technical Report UCB/EERC-84/14*, National Science Foundation.

Selim, M. S. and Sloan, E. D. (1989). Heat and mass transfer during the dissociation of hydrates in porous media, *AIChE Journal* **35**(6): 1049–1052. 10.1002/aic.690350620.

Selim, M. and Sloan, E. (1985). Modeling of the dissociation of an in-situ hydrate, *SPE California Regional Meeting*, Society of Petroleum Engineering, Bakersfield, California (USA).

Shaw, G. H. (1986). Elastic properties and equation of state of high pressure ice, *The Journal of Chemical Physics* **84**(10): 5862–5868.

Shipboard Scientific Party, . (2002). Leg 204 preliminary report (drilling gas hydrates on hydrate ridge, cascadia continental margin), *Technical report*, Ocean Drilling Program, A&M University Research Park, 1000 Discovery Drive, College Station, Texas 77845-9547.
URL: *http://www-odp.tamu.edu/publications/*

Sloan, E. D. (1998). *Clathrate Hydrates of Natural Gases*, New York: Marcd Dekker.

Song, Y., Yu, F., Li, Y., Liu, W. and Zhao, J. (2010). Mechanical property of artificial methane hydrate under triaxial compression, *Journal of Natural Gas Chemistry* **19**(3): 246–250.

Spangenberg, E. and Kulenkampff, J. (2003). Physical properties of gas hydrate bearing sediments, *Geophysical Research Abstracts*, Vol. 5, p. 09797.

Stern, L., Circone, S., Kirby, S. and Durham, W. (2001). Anomalous preservation of pure methane hydrate at 1 atm, *Journal of Physical Chemistry B* **105**(9): 1756–1762.

Stern, L., Circone, S., Kirby, S. and Durham, W. (2003). Temperature, pressure, and compositional effects on anomalous or "self" preservation of gas hydrates, *Canadian journal of physics* **81**(1-2): 271–283.

Stern, L., Kirby, S. and Durham, W. (1996). Peculiarities of methane clathrate hydrate formation and solid-state deformation, including possible superheating of water ice, *Science* **273**(5283): 1843–1847.

Stoll, R. D. (1979). Physical properties of sediments containing gas hydrates, *Journal of Geophysical Research* **84**(B4): 1629–1634.

Sun, R. and Duan, Z. (2005). Prediction of ch4 and co2 hydrate phase equilibrium and cage occupancy from ab initio intermolecular potentials, *Geochimica et cosmochimica acta* **69**(18): 4411–4424.

Tohidi, B., Anderson, R., Clennell, M., Burgass, R. and Biderkab, A. (2001). Visual observation of gas-hydrate formation and dissociation in synthetic porous media by means of glass micromodels, *Geology* **29**(9): 867–870.

Tsimpanogiannis, I. and Lichtner, P. (2007). Parametric study of methane hydrate dissociation in oceanic sediments driven by thermal stimulation, *Journal of Petroleum Science and Engineering* **56**(1-3): 165–175.

Uchida, T., Ebinuma, T. and Ishizaki, T. (1999). Dissociation condition measurements of methane hydrate in confined small pores of porous glass, *The Journal of Physical Chemistry B* **103**(18): 3659–3662.

Uchida, T., Ebinuma, T. and Narita, H. (2000). Observations of co2-hydrate decomposition and reformation processes, *Journal of Crystal Growth* **217**(1-2): 189–200.

Uchida, T., Ebinuma, T., Takeya, S., Nagao, J. and Narita, H. (2002). Effects of pore sizes on dissociation temperatures and pressures of methane, carbon dioxide, and propane hydrates in porous media, *The Journal of Physical Chemistry B* **106**(4): 820–826.

Uchida, T., Lu, H. and Tomaru, H. (2004). Subsurface occurrence of natural gas hydrate in the nankai trough area: Implication for gas hydrate concentration, *Resource Geology* **54**(1): 35–44.

Udachin, K. A. and Ripmeester, J. A. (1999). A complex clathrate hydrate structure showing bimodal guest hydration, *Nature* **397**(6718): 420–423. 10.1038/17097.

Ullerich, J., Selim, M. and Sloan, E. (1987). Theory and measurement of hydrate dissociation, *A.I.Ch.E.* **33**(5): 747–752.

Waite, W. F., Kneafsey, T. J., Winters, W. J. and Mason, D. H. (2008). Physical property changes in hydrate-bearing sediment due to depressurization and subsequent repressurization, *J. Geophys. Res.* **113**: B07102.

Waite, W., Winters, W. and Mason, D. (2004). Methane hydrate formation in partially water-saturated ottawa sand, *American Mineralogist* **89**(8-9): 1202–1207.

Walsh, J. (1966). Seismic wave attenuation in rock due to friction, *Journal of Geophysical Research* **71**(10): 2591–2599.

Walsh, J. (1969). New analysis of attenuation in partially melted rock, *Journal of Geophysical Research* **74**(17): 4333–4337.

Wang, Y., Cascante, G. and Santamarina, J. (2003). Resonant column testing: the inherent counter emf effect, *ASTM geotechnical testing journal* **26**(3): 342–352.

Warzinski, R. P., Gamwo, I. K., Rosenbaum, E. J., Myshakin, E. M., Jiang, H., Jordan, K. D., English, N. J. and Shaw, D. W. (2008). Thermal properties of methane hydrate by experiment and modeling and impacts upon technology, *Proceedings of the 6th International Conference on Gas Hydrates*, Vancouver, British Columbia (Canada).

Weaver, J. and Stewart, J. (1982). In situ hydrates under beaufort sea shelf, *in* H. French (ed.), *Proceedings Fourth Canadian Permafrost Conference*, National research Council of Canada, Calgary, Alberta, pp. 312–319.

Whiffen, B. L., Kiefte, H. and Clouter, M. J. (1982). Determination of acoustic velocities in xenon and methane hydrates by brillouin spectroscopy, *Geophys. Res. Lett.* **9**(6): 645–648.

White, J. (1975). Computed seismic speeds and attenuation in rocks with partial gas saturation, *Geophysics* **40**(2): 224–232.

Wilder, J. W. and Smith, D. H. (2002). Upper limits on the rates of dissociation of clathrate hydrates to ice and free gas, *The Journal of Physical Chemistry B* **106**(24): 6298–6302.

Winkler, K. and Nur, A. (1982). Seismic attenuation: effects of pore fluids and frictional sliding, *Geophysics* **47**(1): 1–15.

Winters, J. W., Pecher, I. A., Waite, W. F. and Mason, D. H. (2004). Physical properties and rock physics models of sediment containing natural and laboratory-formed methane gas hydrate, *American Mineralogist* **89**: 1221–1227.

Winters, W., Waite, W., Mason, D., Gilbert, L. and Pecher, I. (2007). Methane gas hydrate effect on sediment acoustic and strength properties, *Journal of Petroleum Science and Engineering* **56**(1-3): 127–135.

Winters, W., Waite, W., Mason, D. and Kumar, P. (2008). Physical properties of repressurized samples recovered during the 2006 national gas hydrate program

expedition offshore india, *Proceedings of the 6th International Conference on Gas Hydrates*, Vancouver, British Columbia (Canada).

Wu, L. and Grozic, J. P. (2008). Laboratory analysis of carbon dioxide hydrate-bearing sands, *Journal of Geotechnical and Geoenvironmental Engineering* **134**: 547–550.

Xu, W. and Germanovich, L. (2006). Excess pore pressure resulting from methane hydrate dissociation in marine sediments: A theoretical approach, *Journal of Geophysical Research-Solid Earth* **111**(B1): B01104.

Yakushev, V. and Collett, T. (1992). Gas hydrates in arctic regions: risk to drilling and production, *Proceedings of 2nd International Offshore and Polar Engineering Conference*, pp. 669–673.

Yun, T., Lee, C., Lee, J., Bahk, J. and Santamarina, J. (2011). A pressure core based characterization of hydrate-bearing sediments in the ulleung basin, sea of japan (east sea), *Journal of Geophysical Research* **116**(B2): B02204.

Yun, T., Narsilio, G., Santamarina, J. and Ruppel, C. (2006). Instrumented pressure testing chamber for characterizing sediment cores recovered at in situ hydrostatic pressure, *Marine Geology* **229**(3-4): 285–293.

Yun, T., Santamarina, J. and Ruppel, C. (2007). Mechanical properties of sand, silt, and clay containing tetrahydrofuran hydrate, *Journal of Geophysical Research* **112**(B4): B04106.

Zatsepina, O. Y. and Buffett, B. A. (1997). Phase equilibrium of gas hydrate: Implications for the formation of hydrate in the deep sea floor, *Geophys. Res. Lett.* **24**(13): 1567–1570.